Micro-inertial analysis of mechanical instability in granular materials with application to internal erosion.

A. Wautier

Aix-Marseille Université

Ecole doctorale 353 – Sciences pour l'ingénieur : mécanique, physique, micro et nanoélectronique

Thèse présentée pour obtenir le grade universitaire de docteur de l'université d'Aix Marseille

par

Antoine WAUTIER

Discipline : Mécanique des Solides
Laboratoires d'accueil : IRSTEA Aix-en-Provence, UR RECOVER et IRSTEA Grenoble, UR ETNA

Analyse micro-inertielle des instabilités mécaniques dans les milieux granulaires, application à l'érosion interne.

Micro-inertial analysis of mechanical instability in granular materials with application to internal erosion.

Soutenue le 17/09/2018 devant le jury :

Francesco DELL'ISOLA	Sapienza University of Rome	Rapporteur
Richard WAN	University of Calgary	Rapporteur
Félix DARVE	Laboratoire 3SR	Président
Elisabeth BOWMAN	The University of Sheffield	Examinateur
Farhang RADJAI	LMGC Université Montpellier	Examinateur
Noël LAHELLEC	LMA	Examinateur
François NICOT	IRSTEA	Co-Directeur de thèse
Stéphane BONELLI	IRSTEA	Directeur de thèse

"The recording of observable facts requires more than the reception of the stimuli [...]. It requires the knowledge of the appropriate conceptual scheme and how to apply it."
What Is This Thing Called Science? (1976) Alan F. Chalmers

"La montagna mi ha insegnato a non barare, a essere onesto con me stesso e con quello che facevo."
Montagne di una vita (1995), Walter Bonatti

Remerciements

J'aimerais tout d'abord remercier mes deux directeurs de thèse, Stéphane Bonelli et François Nicot pour m'avoir accompagné à la fois dans la construction de mon projet de thèse et dans sa réalisation. Je les remercie pour leur indéfectible optimisme et leur confiance en mon travail qui m'ont aidé à garder le cap pendant mes trois années de thèse. Merci de m'avoir considéré dès le début de la thèse comme un collègue. Je les remercie aussi pour m'avoir encouragé à élargir le spectre de mes travaux en m'investissant dans des projets de recherche connexes à la thèse, en enseignant à l'université et en école d'ingénieurs, en participant à l'animation de la vie scientifique du laboratoire, en participant à des actions de vulgarisation scientifique et tout récemment en organisant mon premier workshop scientifique.

Je tiens aussi à exprimer toute ma gratitude aux membres du jury pour l'intérêt qu'ils ont porté à mon travail de thèse et pour avoir accepté de l'évaluer. Merci à Francesco Dell'Isola et Richard Wan qui ont accepté de se prêter à l'importante tâche de rapporteur. Lors de ma soutenance, le temps de discussion qui a suivi ma présentation a été très riche. Après avoir couché par écrit trois année de recherche et tiré des conclusions, je ressors de ma soutenance avec de nombreuses nouvelles pistes à explorer et de belles perspectives de collaboration. Ma soutenance sera peut être moins une fin qu'un commencement !

Je voudrais aussi remercier chaleureusement Christian Geindreau, François Lacroix, Eric Vincens, Luc Sibille, Gérard Degoutte, Paul Royet et Guillaume Veylon qui ont accepté de faire partie de mon comité de thèse et qui ont porté un vif intérêt au suivi de l'avancement de mes travaux. Je les remercie pour le temps précieux qu'ils m'ont consacré et pour la qualité de leurs retours et de leurs conseils.

En amont de ce travail de thèse je n'oublie pas toutes les personnes qui ont soutenu mon projet de thèse et m'ont aidé à le construire. A ce titre, je remercie particulièrement Patrick Flammarion, Mohammed Naaim et Laurent Peyras qui se sont fortement mobilisés pour voir ce projet se concrétiser. Je remercie aussi la commission de la formation doctorale des IPEFs d'avoir cru en mon projet et le Ministère de l'Agriculture et de l'Alimentation d'avoir accepté de le financer.

Je remercie aussi tous mes collègues de Grenoble et d'Aix-en-Provence pour d'innombrables discussions, et pour la bonne ambiance qu'ils contribuent à faire régner à IRSTEA aussi bien pendant les heures de travail qu'en dehors. J'aimerais adresser une pensée particulière pour les habitués des sessions escalade du jeudi midi, pour les traileurs du Grand-Duc, pour les skieurs matinaux à Chamechaude et pour tous les habitués du départ CTP 12h10.

Sur un plan plus personnel, je voudrais souligner le soutien constant de ma famille tout au long de mes études sans qui je ne serai certainement pas arrivé où j'en suis aujourd'hui ! Merci à vous pour votre présence au quotidien (et en particulier lors de ma soutenance) et pour vos précieux conseils distillés pendant toutes ces années. Je terminerai ces remerciements par une pensée particulière pour Justine qui me supporte depuis déjà quelques années, et qui a partagé tout au long de ma thèse mes réussites comme mes doutes. Merci pour tes encouragements, ta bienveillance et ta patience à mon égard au quotidien, et surtout merci pour l'équilibre que tu apportes à ma vie !

Résumé

La France dispose d'un important parc d'ouvrages hydrauliques avec plus de 19 000 km de digues fluviales et maritimes, plusieurs dizaines de milliers de petits barrages, et environ 600 grands barrages. Ces ouvrages sont pour la plupart construits à base de matériaux granulaires compactés. Ce mode constructif en fait des ouvrages perméables qui sont par conséquent soumis en permanence à des écoulements d'eau dans leur volume pouvant altérer leur structure interne par érosion. Tant que les ouvrages endommagés ne sont pas soumis à aux chargements hydrauliques intenses pour lequels ils ont été dimensionnés (crues ou tempêtes par exemple), les conséquences de l'érosion interne peuvent passer inaperçues. Cependant, ces infiltrations d'eau sont susceptibles de générer des instabilités mécaniques responsables de ruptures inattendues lors de brusques modifications des conditions de chargement. Aujourd'hui, on observe en moyenne une rupture de digue par an en France, dont 45 % sont attribuées à l'érosion interne. Dans un contexte de changement climatique où la fréquence et l'intensité des tempêtes et de crues ne cessent d'augmenter, la compréhension des mécanismes de ruptures dans les digues et les barrages devient un enjeu de plus en plus important.

Localement, on distingue quatre types d'érosion interne : l'érosion de conduite, l'érosion régressive, l'érosion de contact et la suffusion. Ce dernier mécanisme, qui se définit par l'érosion sélective des plus petites particules d'un sol, est le seul pour lequel il n'existe aucune recommandation pratique pour prévenir de son occurrence. Cette thèse est consacrée à l'analyse des instabilités dans les matériaux granulaires soumis au phénomène de suffusion. Les objectifs de ce travail sont d'une part de comprendre les mécanismes élémentaires responsables des instabilités matérielles dans les matériaux granulaires et d'autre part de relier les changements de microstructure induits par un écoulement interne à l'existence de telles instabilités mécaniques.

Pour atteindre ces objectifs, une approche par homogénéisation est proposée. Elle consiste à prendre en compte la nature discrète des matériaux granulaires à l'échelle microscopique tout en considérant un nombre suffisamment important de grains pour être représentatif du comportement macroscopique. Le comportement mécanique de tels volumes élémentaires représentatifs peut alors être simulé grâce à une modélisation par éléments discrets permettant de rendre compte des interactions inter-grains, et un schéma de couplage fluide/grains. Grâce à des outils micromécaniques basés sur la définition de chaînes de force et de réseaux de pores, une première étape de ce travail de recherche permet de valider le caractère représentatif des échantillons granulaires utilisés vis-à-vis des mécanismes élémentaires de la suffusion.

Le cadre théorique général du travail du second-ordre est ensuite utilisé pour détecter l'existence d'instabilités mécaniques à l'échelle du point maté-

riel. Dans cette seconde étape, le couplage direct fluide/grains est ignoré pour se focaliser sur la mise en évidence des liens micro macro entre évolutions microstructurelles et leurs interprétations en termes d'instabilités mécaniques à l'échelle du milieu continu homogène équivalent. Nous avons montré que les instabilités observées résultent du déconfinement et de la flexion des chaînes de force. Leur effondrement déclenche une transition inertielle qui se traduit par un adoucissement transitoire. Ce régime dynamique prend fin lorsque la réorganisation de la microstructure permet de reconstruire de nouvelles chaînes de force stables. D'un point de vue macroscopique, ces réorganisations microstructurelles s'interprètent comme des déformations plastiques incrémentales. Grâce à l'utilisation d'une formulation non-associée du comportement élasto-plastique incrémental des matériaux granulaires, nous avons établi que l'intensité et la direction des incréments de déformation plastique pilotent l'existence d'instabilités mécaniques. En contrôlant le développement des déformations plastiques incrémentales, les particules libres jouent un rôle clé vis-à-vis de la stabilité mécanique des matériaux granulaires. Les particules libres étant aussi facilement transportables et érodables, ce résultat est d'autant plus important lorsque l'on s'intéresse à la suffusion.

Dans cette troisième étape, l'impact d'un écoulement interne sur la microstructure de matériaux granulaires est examiné en trois dimensions grâce à des simulations numériques intégrant un couplage complet avec le fluide. L'impact du fluide est double. D'abord, en introduisant des forces additionnelles, un écoulement interne génère une réorganisation de la transmission des efforts dans le squelette granulaire. Pour des matériaux instables, la réorganisation des contraintes locales peut suffire à provoquer la rupture globale du matériau. Dans ce processus, l'importance des fluctuations des forces fluides est soulignée, et comme pour le cas sec, les chaînes de force se retrouvent déconfinées et fléchissent en même temps que le matériau s'effondre sur lui-même. Le second impact du fluide concerne le transport des particules libres. De manière cohérente avec le rôle stabilisateur des particules libres, il est montré que lorsque le colmatage est prépondérant vis à vis de l'érosion, un écoulement interne est capable de restabiliser un matériau granulaire initialement instable au sens du critère du travail du second-ordre.

Mots clés : Instabilités mécaniques, matériaux granulaires, suffusion, DEM, PFV, micromécanique, travail du second-ordre, chaînes de force, réseaux de pores, érosion, colmatage.

Abstract

France owns a significant stock of hydraulic structures with more than 19,000 km of river and maritime dikes, several tens of thousands of small embankment dams and approximately 600 large dams. These hydraulic structures are most of the time built of granular compacted materials and are thus generally permeable. As a result, they are continuously subjected to internal fluid flows that can affect their internal structure through erosion. As long as the damaged structures are not subjected to the intense hydraulic loadings they are designed to resist to (flooding or storms for instance), the consequences of internal erosion are likely to remain unnoticed. However, internal fluid flows may generate mechanical instabilities that will lead to unexpected failures in case of sudden changes in the loading conditions. Today in France a yearly average of one dike failure is observed, with 45 % of the failures attributed to internal erosion. In a context of climate change in which the frequency and the intensity of storms and river floods increase, the understanding of dike and dam failure mechanisms has become a major issue.

Locally, internal erosion may be decomposed into four mechanisms: piping erosion, regressive erosion, contact erosion and suffusion. The latter, that consists in the selective erosion of the finest particles of a soil, is still the only one for which no practical recommendations have been proposed yet to prevent its occurrence. This PhD work is devoted to the analysis of instabilities in saturated granular materials subjected to internal fluid flows. The objectives of this work are i) to understand the elementary mechanisms responsible for material instability in granular materials and ii) to link flow induced microstructure modifications to the existence of such mechanical instabilities.

To achieve this, a homogenization approach is proposed. This consists in accounting for the discrete nature of granular materials at the microscale while considering a sufficiently large number of grains to be representative of the macroscopic behavior. The mechanical behavior of such representative elementary volumes can be simulated thanks to a discrete element method to account for the grain/grain interactions, and a fluid/grain coupling scheme. Taking advantage of micromechanical tools based on the definition of force chains and pore networks, the representativeness of numerical samples with respect to suffusion elementary mechanisms is assessed in the first step of this research work.

The general theoretical framework of the second-order work is then used to detect the existence of instabilities at the material point scale. In this second step, fluid/grain coupling is left aside to focus on the derivation of

micro to macro links between discrete evolutions of the microstructure and the associated continuum scale interpretations in terms of material stability. It is shown that instabilities result from the unjamming and bending of force chains. Force chain collapse results in an inertial transition characterized by a transient softening. This dynamic regime ends when microstructure reorganizations enable to build new stable force chains. At the macroscale, these rearrangements can be interpreted in terms of incremental plastic strains. Thanks to a non-associated elasto-plastic formulation of the constitutive behavior of granular materials, the intensity and the direction of incremental plastic strains are shown to drive the existence of mechanical instability. By controlling the development of incremental plastic strains, rattlers play a major role in the mechanical stability of granular materials. This key finding is of a particular significance in relation with suffusion as rattlers are privileged candidates to erosion.

The impact of an internal fluid flow on the microstructure of granular materials is eventually investigated numerically from fully coupled three dimensional simulations. The impact of the fluid is twofold. First, by introducing additional forces, an internal fluid flow induces stress reorganization in the primary fabric of granular materials. For unstable materials, these stress reorganizations can lead to material failure. In this process, the importance of fluid forces fluctuations is highlighted and as for the dry case, force chain deconfinement and bending occur together with the collapse. The second fluid impact concerns the transport of rattlers. Consistent with the stabilizing role played by rattlers, it is shown that, when clogging dominates over erosion, an internal fluid flow is able to restabilize unstable granular materials in the sense of the second-order work criterion.

Key words: mechanical instabilities, granular materials, suffusion, DEM, PFV, micromechanics, second-order work, force chains, pore networks, erosion, clogging.

Contents

Chapter 1

Introduction

1.1 General context of dike and dam failures

Water is in the meantime a vital natural resource and a source of important natural hazards. Nearly every human settlement developed in close connection to a river, and a significant proportion of the world population live by the seaside. However, these locations are also very sensitive to many kinds of natural hazards such as flooding or marine submersions. As a result, protective structures such as river or maritime dikes are commonly found and are essential to protect all these urbanized areas.

The example of The Netherlands is quite representative of the issues at stake as two thirds of the country could disappear in case of flooding or marine submersion. For a slightly larger country, France owns a significant stock of hydraulic structures. The linear length of dikes is indeed equivalent to 13 times the largest dimension of its territory, with more than 9,000 km of protection against flooding, 1,000 km of maritime dikes, 8,000 km of dikes for navigation canals and 1,000 km of hydroelectric canals (Bonelli, 2012). In total, this represents half of the earth circumference with 19,000 km. In addition to these elongated structures, several tens of thousands of small embankment dams (smaller than 15 m) and approximately 600 large dams are found in France.

These hydraulic structures whose primary function is to retain or transport water are essential for all sorts of human activities. However, as they are built to constraint water to flow in a counter natural direction, they must constantly resist the fluid flow which will take advantage of any fault in order to break loose. If the fluid does not succeed in the short term, in the long term these hydraulic structures are slowly but surely eroded. Similarly to

dikes of sand built by kids on beaches, without a constant care and regular reinforcements, they will eventually fail.

Dams and dikes are either built of natural compacted materials or of manufactured materials such as masonry or concrete. Because earthen hydraulic structures are much more permeable, they are more at risk. However, they are far more economical than their concrete counterparts. As a result, the great majority of dikes and some dams are built with natural compacted materials. For these earthen structures, statistics show that 90 % of the observed failure are caused by erosion (Bonelli, 2012). Between 1971 and 1995 in France, 71 incidents including 23 failures have been reported on only 550 large dams, a few thousands of small dams and only 1,000 km of dikes. Nowadays, an average of one failure per year is still observed in France (Arroux in 2001, Montambert in 2002, North canal in 2003, Rhine Rhone canal in 2005, Roanne canal in 2007, Xynthia in 2010, Ouches in 2013). On the international scale, examples of dikes and dams failure regularly hit the headlines such as in 2005 in New-Orleans (USA) during Katrina hurricane.

Flooding is known to be the most expensive natural hazard in terms of insurance cost. At the scale of Europe its yearly cost between 1980 and 2003 was estimated at three billion dollars. In France, it reached a billion euros in 2002 and 2003. By simply decreasing by a few percents the vulnerability of the hydraulic structures responsible for flooding, the sums at stakes justify the profitability of research projects aiming to understand the mechanisms responsible for dike and dam failures. In a context of climate change, the frequency and the intensity of storms and river floods is expected to increase and the understanding of these failure mechanisms will be even more critical.

1.2 Internal erosion and the particular case of suffusion

Applied to earthen hydraulic structures, erosion is the process by which a fraction of the material composing a dike or a dam is worn away under the action of water. For these permeable structures, two types of erosion may be defined depending whether erosion occurs on the surface or directly in the core of the structure. The first case corresponds to external erosion while the second one to internal erosion. Feedback on past failures shows that internal erosion is the major cause of 45 % of the failures of embankment dams (Foster et al., 2000), and contrary to external erosion, the consequences of internal erosion are more insidious as they are not always clearly visible from the outside of the damaged structure. This slow and invisible degradation of

the mechanical properties of the hydraulic structures is particularly critical when considering dikes as they are hardly ever subjected to the extreme loading they are supposed to resist to. Consequently, the internal erosion of dikes may be harmless most of the time when water level is low. But as soon as the level rises too much, failure may occur out of the blue. By contrast, the situation is less critical while considering embankment dams that are almost constantly subjected to their nominal load and for which a gradual degradation of their mechanical properties has better chances to be detected ahead of failure. In addition, contrary to dikes, dams are not very long structures (less than a few hundred meters compared to kilometers for dikes) and can be monitored more carefully than dikes. Consequently, dams will not systematically be mentioned together with dikes in the following, even though internal erosion mechanisms are identical.

Following the International Workshop on Internal Erosion of Embankment Dams and their Foundations held in Aussois, France from 25th to 27th July 2006 the international community agreed on the distinction between the four types of internal erosion illustrated in Figure 1.1 (Fell and Fry, 2007; Bonelli, 2012, 2013):

- Backward erosion that consists in the progressive erosion of the structure from downstream to upstream sides;

- Contact erosion that can occur when a fine layer of material in contact with a coarse one is eroded through the large pores in between coarse grains;

- Piping erosion that consists in the enlargement of an existing pipe in the hydraulic structure;

- Suffusion that is the selective erosion of the finest particles of a soil directly through the pore space of the material.

Among these four types of internal erosion process, suffusion is certainly the most complex and is still the only one for which no practical recommendations have been proposed yet to prevent its occurrence. Indeed the two most frequent criteria used in practice are not consistent and lead to contradictions in some cases (Li and Fannin, 2008). In addition suffusion often occurs for hydraulic gradients well below the critical value proposed by Terzaghi to account for soil liquefaction (Skempton and Brogan, 1994). Starting from these statements suffusion has received increased attention recently with several ongoing PhD thesis on this topic. In close connection with the present work, Rodaina Aboul Hosn proposed during her PhD thesis (2014-2017) an

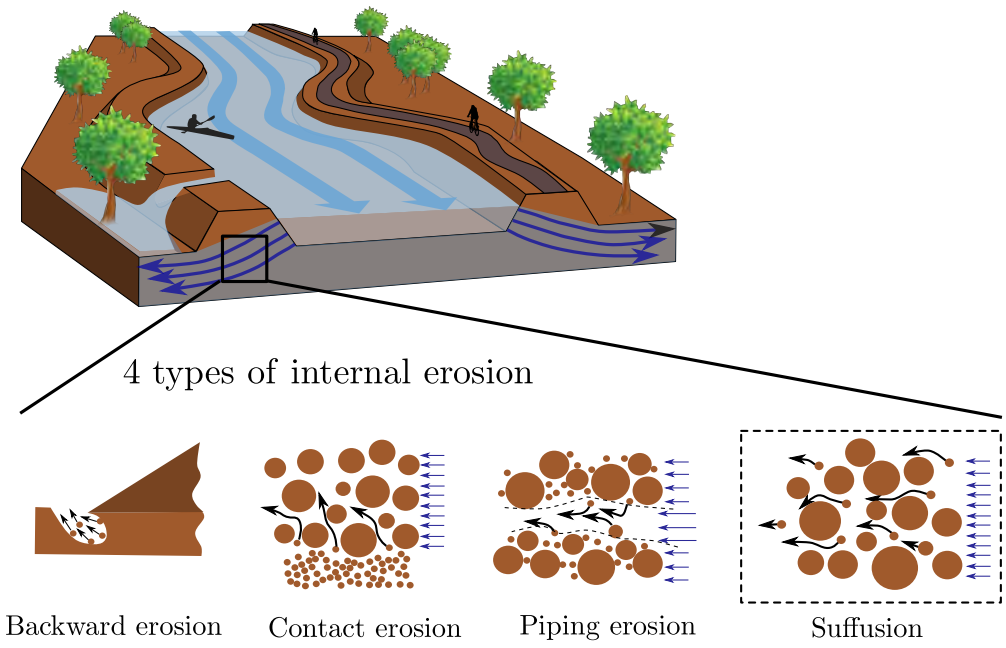

Figure 1.1 – The four types of internal erosion.

investigation of the effect of suffusion on the triaxial response of eroded soils. Her approach is based on the one side on a simplified numerical erosion procedure and on the other side on the conduction of post-erosion experimental triaxial tests. In parallel with the present thesis, a fully experimental thesis is conducted by Doan Nguyen (2015-2018). Together with the development of an erodimeter cell, the objective of this undergoing thesis is to provide experimental evidences of the impact of suffusion on the mechanical properties of soil.

A second particularity of suffusion compared to the three other types of internal erosion is that it cannot be modeled as a boundary value problem directly at the scale of the hydraulic structure. It is a material scale issue. Indeed, suffusion directly modifies the intrinsic mechanical properties of the material composing the hydraulic structure of interest by involving microstructure modifications (an increase in porosity for instance). From an engineering point of view, the effect of suffusion on the occurrence of failure has thus to be assessed through modifications of the constitutive behavior of the materials used in the modeling of the hydraulic structure. By contrast, the effect of piping or regressive erosion can be assessed by updating the internal geometry of the hydraulic structure (i.e. by defining an inner fluid domain) while keeping unchanged material constitutive behaviors. As for

contact erosion, it is indeed a hidden surface erosion problem which lead to the settlement of the coarse material into the finer one while keeping again unchanged material constitutive behaviors.

1.3 Justification for a numerical homogenization approach of suffusion

As a result, the understanding of suffusion is indeed an homogenization problem which involves multiple scales and physical processes. If we zoom into the dike body, soil may be modeled as a granular material, with grains interacting between each others through local contact laws. At this micro-scale, the macroscopic concept of erosion vanishes to the profit of fluid/grain interactions. Indeed, at this local scale the problem of interest consists in interactions between grains and a fluid flowing within the interstitial pore space.

This multi-scales and multi-physics view of suffusion lead to the formulation of two questions which are indeed the guidelines of all the work carried out during this PhD:

- What is the effect of an internal fluid flow on a granular material microstructure?

- What are the consequences of these microstructure modifications on the material constitutive behavior?

So far, most of the studies devoted to suffusion focused mainly on the first point with the objective to relate the particle size distribution (PSD) of a soil to the mass fraction of particles that can be moved out of the material by an internal flow. The occurrence of the loss of this fine fraction is usually referred to as *internal instability* (Kenney and Lau, 1985). For a long time, and still today for practical applications, the second question has often been eluded and suffusion is usually reputed to be harmful as soon as fine particles are eroded from the bulk of the material. This is however too conservative as sometimes, the withdrawal of some particles does not necessarily result in modifications of the mechanical constitutive behavior dangerous for the integrity of the whole hydraulic structure. This is why, considering these two questions together is essential to me. It is nevertheless a difficult guideline since it is much easier to stick to self-filtration processes. How can we characterize microstructure evolutions? How do we characterize the evolution of the mechanical behavior of an eroded material? What are the microstructure

evolutions responsible for dangerous alterations of the mechanical properties? What is indeed a *dangerous* evolution of the mechanical properties?

In order to provide some answers to these questions, different modeling strategies may be followed:

- A first modeling approach is to stick to a full continuum mechanics approach and to model a saturated soil as a the coexistence of a fluid phase, fluidized particles and a solid phase (see (Bonelli and Marot, 2011) for instance). The phase exchanges are then assessed through partial differential equations (mass conservation, transport, local erosion or deposition,...). Then, the change in the mechanical properties is related to the relative fractions of these different phases that are assumed to be internal state variables.

- A second approach consists in modeling the full fluid/grain interaction problem directly at the microscale. In this approach, grains are modeled individually, their interactions are accounted for through contact laws, the fluid flow is handled as a fluid mechanics problem in a complex pore space domain and the fluid forces applied on the grains are deduced from the local fluid velocities. In this approach, the full complexity of the microstructure geometry is accounted for and the evolving mechanical properties of the soil can be recovered at the macroscale (the scale of the continuum media) through numerical homogenization techniques.

One drawback of the first approach is that its validation strongly relies on experimental data. However, the different experimental works carried out today are still limited to fully answer to the two main questions formulated above. Indeed, most of the existing erodimeter cells are not able to impose simultaneously a hydraulic and a mechanical loading to investigate the coupling between both. Moreover, the use of rigid boundaries tends to induce large porosity close to the sample boundaries which results in localized transport of small particles along the sample boundary as visible in Figure 1.2. As a result, the microstructure of considered samples is no longer homogeneous in the end of experimental suffusion tests. The problem solved experimentally is thus always a boundary value problem and not a material point problem as necessary to investigate suffusion phenomenon. In order to overcome these limitations on the experimental side, some laboratories are currently developing erodimeter cells directly inside triaxial apparatus (Chang and Zhang, 2012), conducting post erosion triaxial test (Xiao and Shwiyhat, 2012) or acquiring X-ray tomography images of samples subjected to suffusion test to reckon the boundary influence in the sample volume (Nguyen et al., 2017).

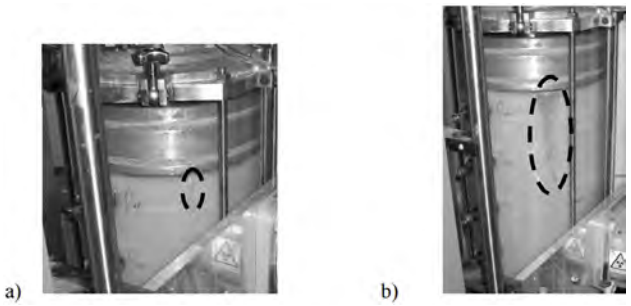

Figure 1.2 – Localization of erosion along the boundaries of erodimeter cells in laboratory tests (Sail et al., 2011).

In the present work, the choice was made to bypass the current laboratory limits by following the second modeling approach mentioned previously. By going down to the microscale, the modeling of suffusion is reduced to more elementary physical processes, the modeling of which is more documented and already validated. At this scale, suffusion consists in:

- modeling a fluid flow in a porous media;
- accounting for grain/grain interactions;
- accounting for fluid/grain interaction.

With use of existing and validated numerical codes to account for this two processes, a fully numerical work is conceivable in which real experiments are replaced by numerical ones. This particular bias is adopted in the present work with the objective to enhance the understanding of suffusion physics. Of course this second approach result in computationally expensive simulations and cannot be used directly to assess the occurrence of dike failure.

However, the result of this work is valuable to better interpret the macroscopic data obtained experimentally and to justify the underlying hypothesis adopted in the constitutive modeling of suffusion. To this last respect, the understanding of the micromechanics of suffusion is essential in the development of micro-mechanical models which are an alternative to direct numerical homogenization by use of mesostructures.

1.4 Outline and structure of the present work

This thesis summarizes three years of intense research that already led to four journal publications, two of which have already been published.

Chapter 2 introduces the necessary concepts and numerical tools to understand the following work. First the existing criteria used to assess the internal stability or instability of a soil are briefly reviewed. Then the notion of mechanical stability is introduced and substituted to the notion of internal stability to better link suffusion to potential material failure. To this respect, the second-order work criterion is introduced. Then, the specific DEM/PFV numerical modeling adopted in this work is introduced and justified.

Because suffusion occurs at the material point scale, its modeling at the microscale requires the introduction of a representative elementary volume (REV), i.e. a small volume of material sufficiently large to capture the physical processes at stake in a material subjected to an internal flow. In Chapter 3 different scales are introduced and numerical tools are developed to characterize the length scales associated with stress transmission and transport properties in granular materials. Fully coupled three dimensional fluid/grain simulations are carried out to estimate internal transport of free particles and validate the introduced length scales. Part of the results presented in this chapter were published in 2017 in "Scale separation between grain detachment and grain transport in granular media subjected to an internal flow" (Wautier et al., 2017).

In Chapter 4, fluid grain coupling is left aside to focus on the understanding of the micromechanics responsible for material instability. The results presented in this chapter are inspired by two research papers. The first paper "Micro-inertia origin of instabilities in granular materials" published in 2018 presents the systematic procedure used to assess the existence of material instability at the REV scale and relate this instability to micro mechanisms (Wautier et al., 2018b). The second paper "Rattlers contribution to granular plasticity and mechanical stability" that was recently submitted highlights the particular role played by free particles with respect to mechanical stability (Wautier et al., 2018c). As these free particles are very sensitive to internal flows, the impact of microstructure modifications resulting from erosion or clogging is intuited.

In Chapter 5, the impact of a fluid on the mechanical stability of a granular material is assessed thanks to fully coupled three dimensional fluid/grain simulations at the REV scale. Both the direct impact of a fluid flow on stress transmission and on the erosion or clogging of rattlers are considered. This chapter extends the results of the recently submitted paper "Flow impact on granular force chains and induced instability" (Wautier et al., 2018a).

Chapter 2

State of the art: suffusion impact on soils and numerical tools for its modeling

The objective of this chapter is to provide a minimal state of the art and introduce the necessary concepts and numerical tools to the understanding of the methodology and the results presented in the following chapters. The first section is dedicated to the current approaches deployed to assess soil susceptibility to suffusion. Based on this literature review the choice to consider suffusion susceptibility in terms of changes in mechanical properties is justified. The second section of this chapter is dedicated to the introduction of the concept of mechanical stability and instability that provide a relevant framework to assess whether the occurrence of suffusion may prove harmful. The second-order work criterion as introduced in continuum mechanics by Hill (Hill, 1958) is shown to provide a relevant indicator in the present case. The last two sections are dedicated to provide details on the available numerical methods able to simulate microscale mechanisms responsible for suffusion. A justification of the choice made to carry out the numerical experiments used in this thesis is provided.

2.1 Suffusion susceptibility: an internal stability approach

As recalled for instance by Garner and Fannin (2010), the occurrence of failure by internal erosion requires to fulfill three conditions illustrated in Figure 2.1: material susceptibility, hydraulic susceptibility and mechanical susceptibility.

In this Figure, it is recalled that failure is a combination of different factors and that suffusion as defined by the succession of grain detachment, grain transport and possibly grain attachment is neither a sufficient nor necessary condition for material failure. In the following subsections some of the main criteria used to prevent the occurrence of suffusion which corresponds indeed in Figure 2.1 to particle transport and possibly particle release are recalled. And the recent effort to relate macroscopic features of suffusion to micromechanical aspect is presented.

2.1.1 Geometrical criteria

By far the most common, geometrical criteria focus on material susceptibility (see Figure 2.1). Indeed, this class of criteria relies on the idea that in order to avoid particle transport a granular material, the pores of the coarse particles should not allow for the smaller particles to pass between them. This properties corresponds to the notion of self-filtration. For practical applications most of the criteria are constructed on particle size distributions

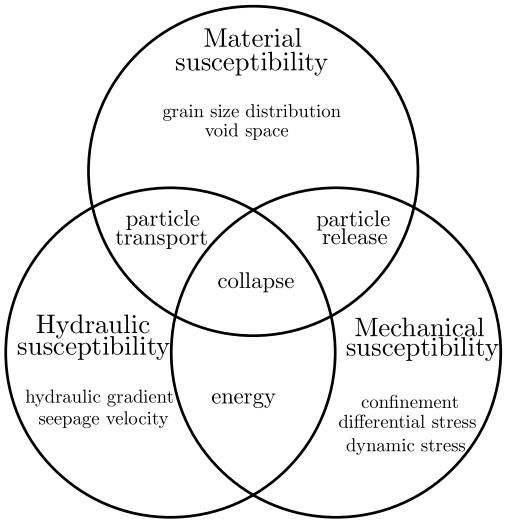

Figure 2.1 – Internal erosion conditions according to Garner and Fannin (2010).

(PSD) or more recently on constriction size distributions (CSD). An extensive description of the existing criteria may be found in the PhD thesis of Abdoulaye Hama (2016) or Le (2017). In this work only the two most widely used criteria are reviewed.

When two populations of grains may be identified, it is convenient to distinguish between coarse and fine grains. If the soil PSD is *gap-graded*, this distinction is straightforward but otherwise this requires an arbitrary threshold size to define the two grain populations. Based on this distinction between coarse grains composing a filter and potentially erodible fine grains, Peck and Terzaghi (1948) proposed $\frac{D_{15}}{4}$ to characterize the typical constriction size between the coarse grains where D_{15} is the particle diameter for which 15% of the mass of the coarse grains is finer than, and $\frac{1}{4}$ corresponds indeed to a typical constriction size in between the two geometrical configurations illustrated in Figure 2.2.

A soil retention criterion is then derived in the form of $\frac{D_{15}}{4} < d_{85}$, where d_{85} is the particle diameter for which 85% of the mass of the fine fraction is finer than (Peck and Terzaghi, 1948). Initially formulated by Terzhaghi for the design of filters, this criterion was reused later on by Kézdi (1979) to characterize the internal stability of a soil (i.e. the geometrical possibility for the smallest grains to move through the pore space defined by the largest grains). The definition of the so-called Kezdi's filter rule is illustrated in Figure 2.3 and is based on a splitting of the PSD between fine and coarse

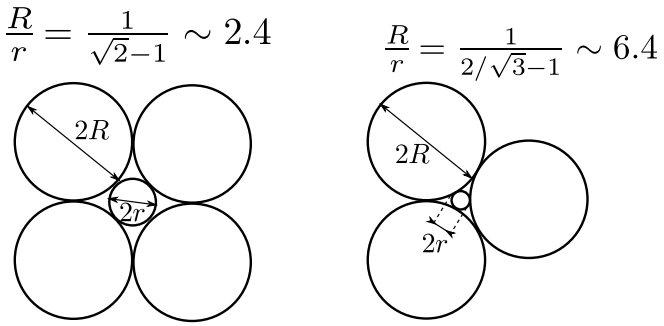

Figure 2.2 – Geometric justification of the ratio $\frac{1}{4}$ used in internal instability criteria.

particles around a varying grains diameter D. A soil is then reputed to be internally stable if the passing fraction between D and $4D$ is greater than 15 % whatever the chosen D value.

A widely used alternative to this criterion was proposed by Kenney and Lau (1985) based on the so-called "$\frac{H}{F}$" ratio illustrated in Figure 2.3. This criterion, always based on the PSD, defines F as the fraction of grains with a diameter smaller than an arbitrary value D. H corresponds then to the fraction of grain with diameters lying in the interval $[D, 4D]$. A low value of the ratio $\frac{H}{F}$ correspond to a soil with a *hole* in its PSD curve sufficiently large (again Figure 2.2 provide a justification for the factor 4 used here) to allow for grain transport. As a result, the lowest value of $\frac{H}{F}$ is sought for D describing the range of particle sizes constituting the considered soil. A threshold value of $\frac{H}{F} > 1$ was advocated for $F < 0.2$ in soils having a widely graded coarse fraction and for $F < 0.3$ in soils with a narrowly graded coarse fraction (Kenney and Lau, 1985). For fine fractions higher than 20 to 30 %, the material is considered as overfilled (Benahmed et al., 2015). In this case, the constriction sizes are driven by the fine particles and the filter rules are not relevant anymore.

These two criteria are the most used criteria for practical assessment of suffusion (Andrianatrehina et al., 2016), however, as shown by Fannin and Moffat (2006), Kezdi's filter rule proved to be too rough for some soils satisfying the criteria but experimentally internally unstable. Moreover, these two criteria show inconsistencies as shown Li and Fannin (2008) and recalled in Figure 2.4.

Since then, many authors have tried to improve these geometric criteria with validation on experimental suffusion tests in which soils are said to be internally unstable if there exists at least one combination between a

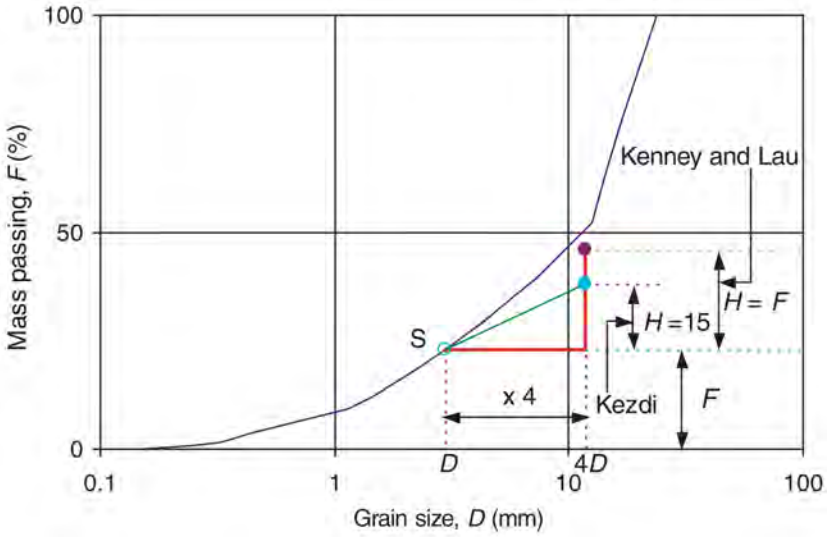

Figure 2.3 – Definition of the two main criteria used for practical applications (Li and Fannin, 2008).

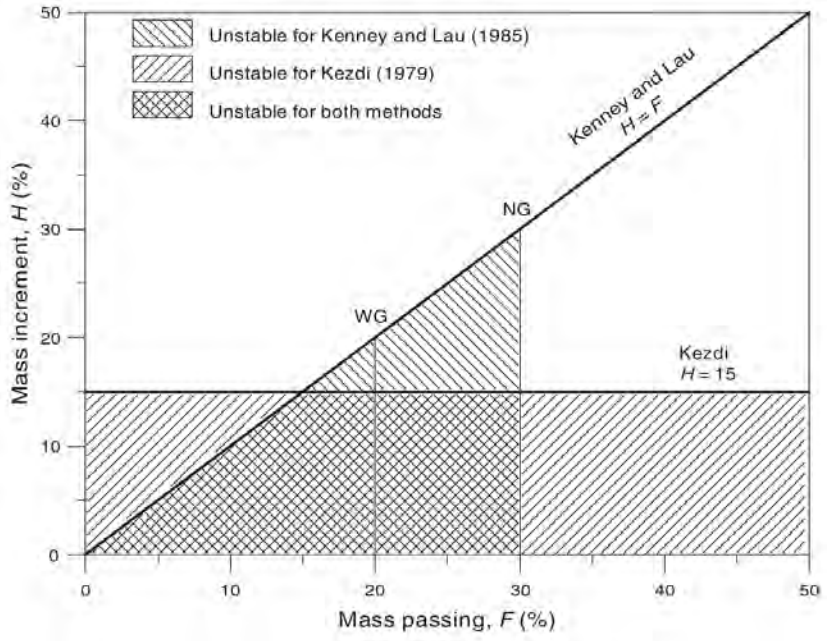

Figure 2.4 – Inconsistency of the two main criteria used for practical applications (Li and Fannin, 2008).

microstructure state, a stress state and an hydraulic loading leading to the washing of a fine fraction out of the sample. Among the different improved criteria, we can mention Wan and Fell (2008); Chang and Zhang (2013); Indraratna et al. (2015). Nevertheless, none of these criteria accounts for the effective occurrence of suffusion and the possible consequences in terms of material failure.

In a similar spirit to PSD based criteria, recent works proposed to assess the possibility to transport fine particles in the pore space based on the computation of constriction size distributions (CSD) (Silveira, 1965; Locke et al., 2001; Vincens et al., 2015). Reboul et al. (2010) and Vincens et al. (2012, 2015) summarized the methods for evaluating the constriction size distributions of a numerical assembly of spheres which were generated by the Discrete Element Method (DEM) and where the void geometry was evaluated by a radical Delaunay triangulation. Compared to PSD methods, the computation of CSDs enables to account for the particular arrangement of grains and to distinguish for instance between loose and dense sand. These methods are however computationally expensive and cannot be used for practical applications. Following the work of Silveira (1965), Locke et al. (2001) and Indraratna et al. (2015, 2007) improved self filtration criteria by deriving the CSD from the PSD plus some assumptions on the geometrical grain packing to account for the particular microstructure state.

2.1.2 Hydraulic and stress conditions

As recalled in Figure 2.1, the occurrence of suffusion also requires a sufficiently strong internal flow to transport and possibly detach grains in the material volume. Going back to the work of Terzaghi (1939), soil fluidization is related to the vanishing of the effective stress in the soil. As a result, provided the hydraulic gradient equals the effective stress, heave failure occurs. The critical vertical hydraulic gradient is then given by:

$$I_c = \frac{\gamma'}{\gamma_w} = (1-n)(\gamma_s - 1) \tag{2.1}$$

where n is the soil porosity and γ', γ_w and γ_s are respectively the specific gravity of the submerged soil, of water and of the soil particles.

Thanks to the combine use of photoelastic grains and numerical simulations, the overall behavior of granular materials was shown to rely on a limited number of grains (Drescher and De Jong, 1972; Liu et al., 1995; Radjai et al., 1998; Bardenhagen et al., 2000; Cambou et al., 2013). As a result,

the critical hydraulic gradient as introduced by Terzaghi largely over predicts the necessary hydraulic gradient to move some loosely loaded grains in a granular material.

Skempton and Brogan (1994) found indeed that for unstable materials, the critical hydraulic gradient could be roughly 1/3 to 1/5 of the normal predicted value based on the theory of Terzaghi for sand boil process. This deviation was accounted for by a stress reduction coefficient α such that:

$$I_c = \alpha \frac{\gamma'}{\gamma_w} \tag{2.2}$$

Skempton and Brogan (1994) proposed a grain-scale interpretation of this coefficient as most of the effective stress is carried by a matrix of coarse particles, leaving the loose finer particles under relatively low stress. Thanks to the use of discrete element simulations, Shire et al. (2014) provided a micromechanically based justification of this interpretation for idealized gap-graded samples with varying potential for internal stability. Based on the contact forces $\boldsymbol{f}^c$ applied on points $\boldsymbol{x}^c$ of a given particle p, the mean stress tensor $\bar{\boldsymbol{\sigma}}^p$ in each particle can be computed thanks to the Gauss theorem as (Love, 1927; Weber, 1966; Christoffersen et al., 1981; Mehrabadi et al., 1982; Nicot et al., 2013b)

$$\bar{\boldsymbol{\sigma}}^p = \frac{1}{V^p} \sum_{c=1}^{N_{c,p}} \boldsymbol{f}^c \otimes (\boldsymbol{x}^c - \boldsymbol{x}^p). \tag{2.3}$$

By volume averaging this tensor on two grain populations (coarse and fine grains) the stress reduction factor is linked to the ratio between the mean pressures computed on the fine grains only and on all the grains

$$\alpha_{\text{DEM}} = \frac{p'_{\text{fine}}}{p'} \tag{2.4}$$

where

$$\begin{cases} p' &= \frac{1}{V} \sum_{p=1}^{N_p} \frac{1}{3} \, \text{Tr}\bar{\boldsymbol{\sigma}}^p \, V^p \\ p'_{\text{fine}} &= \frac{1-n}{\sum_{p=1}^{N_{p,\text{fine}}} V^p} \sum_{p=1}^{N_{p,\text{fine}}} \frac{1}{3} \, \text{Tr}\bar{\boldsymbol{\sigma}}^p \, V^p \end{cases} . \tag{2.5}$$

and n the sample porosity.

Based on the fine content, Shire et al. (2014) show that the stress reduction factor increases as the microstructure of gap-graded materials changes

from underfilled (no fine particles are involved in stress transmission) to overfilled (many fine particles are involved in stress transmission).

Thanks again to the use of DEM, efforts were recently made to relate PSD based criteria to micromechanical features such as average number of contacts per particle, contact force distributions and the probability that a particle participates in stress transmission (Fonseca et al., 2014; Shire and O'Sullivan, 2013; Langroudi et al., 2015). Shire and O'Sullivan (2013) for instance used DEM to analyze the relationship between grain-scale fabric and the empirical criterion for assessing internal stability proposed by (Kézdi, 1979) for a series of idealized gap-graded soils with varying PSD and finer fractions at a single relative density level. They studied the degree of interlocking of fine particles with neighboring particles with respect to their participation in the stress transfer in the granular skeleton. The average coordination number decreases as internal instability increases which accounts for an increase in the proportion of loose, erodible fine particles. Similarly, the number of coarse particles participating in stress transfer falls as internal instability increases. Initially introduced with geometric considerations, Shire and O'Sullivan (2013) thus gave Kezdi's filter rule a micromechanical meaning by linking it to physical parameters.

In addition to gap graded soils, Langroudi et al. (2015) also considered a concave upward and a linear grading curves. The evolution of contact force networks confirms that internally stable soils have a more homogeneous network of contact forces compared to internally unstable soils. Force distribution analyses reflect higher percent of weak contacts and low connectivity for fine particles in internal instability.

Through the use of X-ray tomography, Fonseca et al. (2014) explored the link between PSD and the coordination number which provides an indicator of grain interlocking. The correlation between coordination number and internal stability was confirmed, with coordination number values being significantly higher for real material than model materials used in DEM.

2.2 Suffusion susceptibility: a mechanical stability approach

Despite abundant literature focused on the definition of criteria to assess the internal stability of a granular material, the consequences of suffusion in terms of mechanical stability have been surprisingly left aside. In this section the few attempts to characterize the consequences of suffusion on the mechanical behavior of granular materials are reviewed before introducing a

formal framework to precisely assess the mechanical stability of a soil through the use of the so-called *second-order work criterion*.

2.2.1 The drained triaxial test approach from experimental and numerical points of view

In order to investigate the mechanical consequences of suffusion, most of the studies found in the literature compare the drained triaxial response of a soil before and after suffusion either from an experimental (Chang and Zhang, 2011; Ke and Takahashi, 2012; Xiao and Shwiyhat, 2012; Ke and Takahashi, 2014a; Sibille et al., 2015b; Hosn et al., 2017) or a numerical point of view (Wood et al., 2008; Wood and Maeda, 2008; Scholtès et al., 2010; Sibille et al., 2015a; Hosn et al., 2016).

Experimental results

On the experimental side, Ke and Takahashi (2014a) evaluated the mechanical consequences of suffusion by conducting monotonic drained compression tests on eroded and non-eroded specimens. As large amounts of fines are washed out of the samples, the eroded specimens show contractive volumetric strains during the erosion phase which results in a less contractive behavior during triaxial loading as shown in Figure 2.5. As for the stress response, suffusion leads to a reduction of the soil strength during post-erosion drained triaxial tests (Figure 2.5). While applying larger effective confining pressure during the erosion step, the eroded mass of fine particles and the impact on the mechanical behavior decrease.

Similar observations were made by Chang and Zhang (2011), Chang and Zhang (2012) or Hosn et al. (2017) who noticed that after the loss of a significant amount of fine particles, the original dilative stress-strain behavior becomes contractive and the peak stress decreases. This may be explained by a global increase in the porosity when fine particles are washed out despite the small compaction observed during the suffusion test. As porosity is one of the key internal state variables which control the macroscopic strength of granular materials, an increase in porosity results in a decrease in the peak stress.

However, some researchers showed an opposite trend for the mechanical behavior of the eroded soil with larger deviatoric stresses for eroded specimen than for non-eroded ones at least for small axial strain values (Xiao and Shwiyhat, 2012; Ke and Takahashi, 2014b). Xiao and Shwiyhat (2012) attributed such behavior to the low degree of saturation as well as the occurrence of clogging. Whereas, Ke and Takahashi (2014b) suggested that such

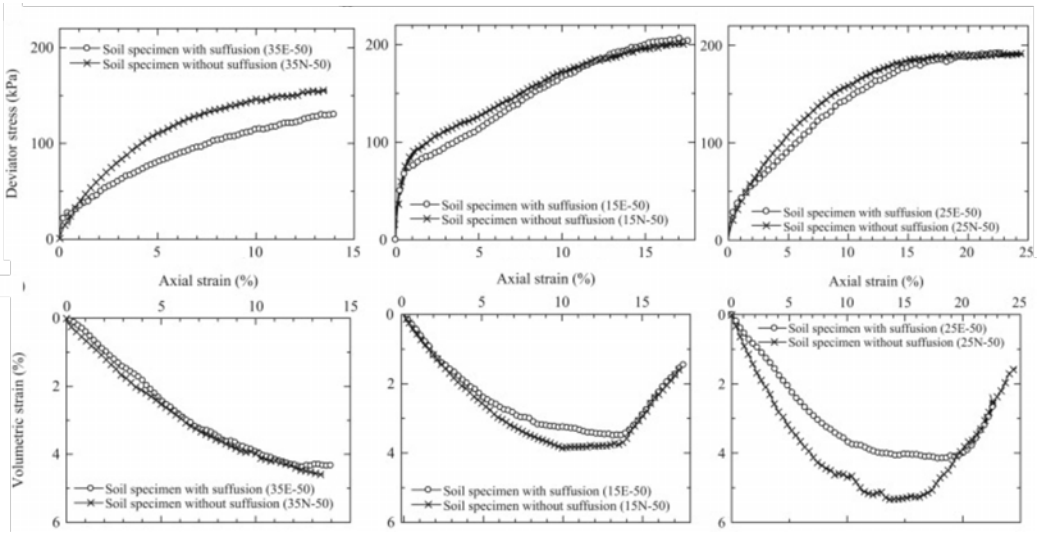

Figure 2.5 – Comparison of the drained triaxial responses of the three gap-graded specimens considered in Ke and Takahashi (2014a) with (circles) our without (crosses) suffusion. An effective confining pressure of 50 kPa is applied. The deviatoric stress (top) and the volumetric strain (bottom) evolutions with respect to the axial strain are shown.

an inconsistency of the eroded soil behavior might be related to changes in the soil fabric. Provided that the loss of particle is not too large, the observed compaction during the suffusion phase strengthens eroded specimens.

Numerical results

On the modeling side, hardly no study dare to account for the full fluid/-grain coupling problem. As a result, the consequences of suffusion on the soil microstructure are often mimicked through particle removal. For instance, Scholtès et al. (2010) simulated the degradation of dense granular assemblies through the progressive removal of the finest particles with the use of a discrete element model as well as an analytical micromechanical model (Chang and Hicher, 2005). Both models highlight a change from a dilative to a contractive behavior with the degradation and a strong dependency of the overall stability on the mobilized friction level is put forward. In particular, they show how failure is triggered when particle removal occurs for mobilized frictions greater than the one reached at the critical state. These results are consistent with those obtained previously by Wood et al. (2008) for two dimension biaxial tests in which the autors observed that the sta-

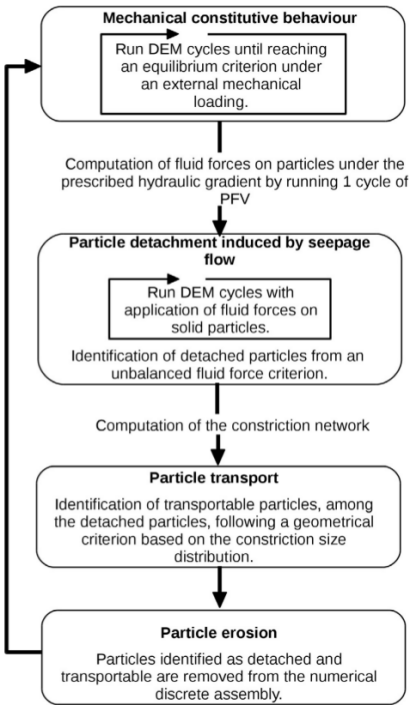

Figure 2.6 – One way coupling procedure developed by Hosn et al. (2018) to mimick suffusion by grain extraction.

bility of particle removal is related to the stress ratio which the sample is experiencing (this result will be revisited in Section 4.6).

More recently, Aboul Hosn (2017) developed in her PhD thesis a one way fluid/grain coupling (see Figure 2.6) to improve the selective extraction of erodible grains in DEM numerical simulations. By simulating an internal flow, fluid forces are estimated and applied to the small grains candidates to erosion. Provided that i) the intensity of the fluid forces is large enough to make these grains move and ii) these grains are smaller than a typical constriction size computed on the CSD, the particles are suppressed.

While subjected to different hydraulic gradients the numerical sample used in Hosn et al. (2018) shows that depending on the amount of eroded particles and depending on whether eroded particles are involved in stress transmission, two distinct responses are observed. The eroded medium either shows negligible deformations during erosion but then collapses suddenly once loaded in drained triaxial conditions, or it deforms significantly during erosion and exhibits a smaller peak strength once subjected to drained triaxial loadings. These two types of eroded behaviors are shown in Figure

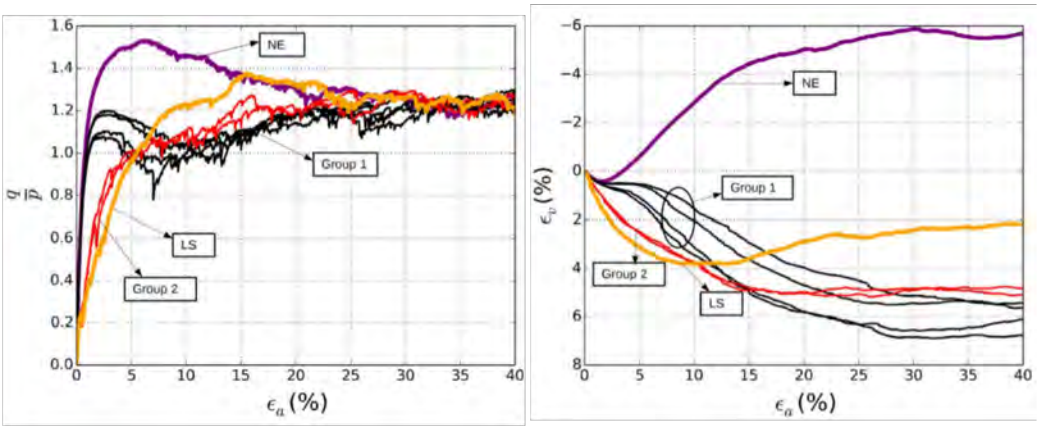

Figure 2.7 – Drained triaxial tests performed on a dense non-eroded numerical sample (NE) and on eroded samples exhibiting two types of behaviors: a peak stress reduction (group 1) or a change from a dense to a loose type behavior (group 2) Hosn et al. (2018).

2.7.

2.2.2 Triaxial testing limits to assess suffusion consequences on material resistance

A mechanical characterization of the effects of suffusion on soil simply based on triaxial tests in indeed a too rough approach. In classical soil mechanics theories, the interpretation of triaxial tests assume the homogeneity of the tested specimens in terms of microstructure. However, this assumption becomes questionable for eroded specimens in which erosion is far from homogeneous. As shown for instance in Sail et al. (2011) or more recently thanks to X-ray tomography by Nguyen et al. (2017), erosion tends to localize along the lateral boundaries of the tested specimen. These heterogeneities shown in Figures 2.8 and 2.9 prevent indeed easy interpretation of post erosion triaxial test. Indeed, as discussed in the introduction, the specimens should be considered as structures and no longer as representative elementary volumes.

In addition, the sole use of drained triaxial tests is not always representative of the changes in mechanical and hydraulic conditions that an eroded soil can undergo during flooding. To this respect, the work carried out during this PhD focused on providing a suitable framework to effectively assess the consequences of suffusion through the notions of mechanical stability and loss of stability.

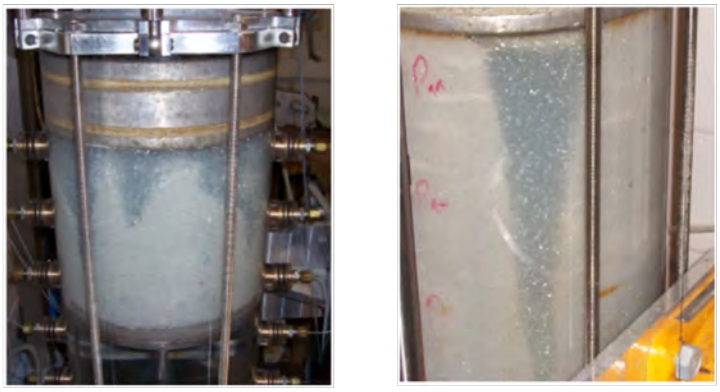

Figure 2.8 – Observation of microstructure heterogeneities in two experimental suffusion tests (Sibille et al., 2015b).

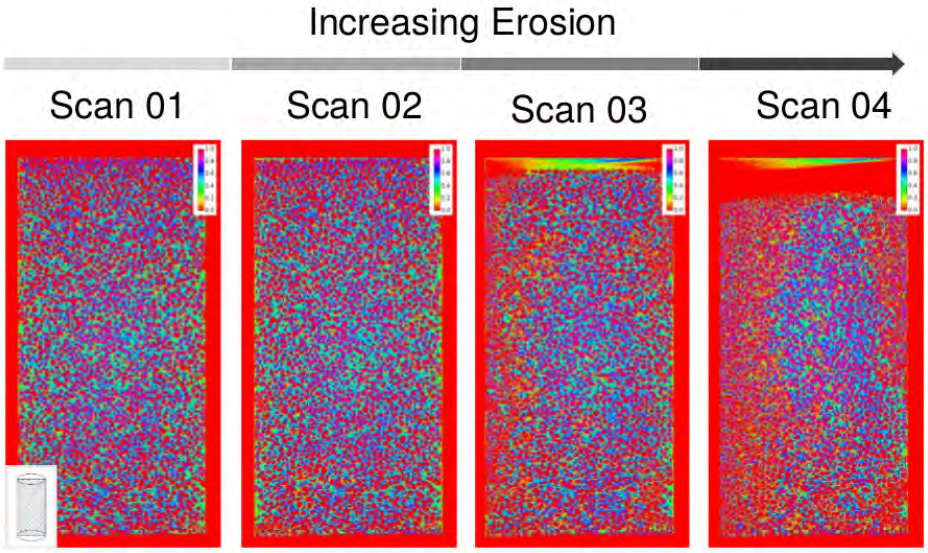

Figure 2.9 – Local porosity values along a slice of a specimen subjected to a suffusion test. Red colors correspond to the highest porosities concentrated along the lateral boundaries (Nguyen et al., 2017).

2.2.3 From an intuitive definition of instability to the second-order work criterion

In order to go a step forward in the understanding of the failure mechanisms in earthen hydraulic structures, there is a need for a precise definition of the notion of mechanical stability or conversely instability. This notion applies to a given phenomenon with respect to its evolution over time: a system is reputed unstable if and only if an infinitesimal perturbation induces finite changes in the response of the system.

Historically, in the field of solid mechanics, a formal mathematical definition was proposed by Lyapunov (1907) to study the stability of the trajectories of celestial bodies. Considering a body whose position and velocity at time t are $\boldsymbol{x}_1$ and $\boldsymbol{v}_1$ respectively, and assuming that a small perturbation is applied at this time on its position and its velocity, Lyapunov queried whether the new trajectory of this body $\boldsymbol{x}_2(t')$ and the new velocity $\boldsymbol{v}_2(t')$ remain *close* to the trajectory $\boldsymbol{x}_1(t')$ and the velocity $\boldsymbol{v}_1(t')$ it would have had without this perturbation for any $t' > t$. The formal mathematical formulation of this stability definition reads:

$$\begin{aligned}&\forall \varepsilon_x > 0 \text{ and } \forall \varepsilon_v > 0,\ \exists \eta_x(\varepsilon_x, \varepsilon_v) > 0 \text{ and } \exists \eta_v(\varepsilon_x, \varepsilon_v) > 0, \text{ such that}\\ &\text{if } ||\boldsymbol{x}_1(t) - \boldsymbol{x}_2(t)|| < \varepsilon_x \text{ and } ||\boldsymbol{v}_1(t) - \boldsymbol{v}_2(t)|| < \varepsilon_v,\\ &\text{then } \forall t' > t,\ ||\boldsymbol{x}_1(t') - \boldsymbol{x}_2(t')|| < \eta_x \text{ and } ||\boldsymbol{v}_1(t') - \boldsymbol{v}_2(t')|| < \eta_v.\end{aligned}$$

The extension of this definition to the continuum mechanics framework can be achieved by introducing adequate variables to describe the state of the system in place of the position and the velocity. In this particular context, the notion of stability relates to a stress/strain state of a given material with respect to its evolution under prescribed loading conditions (Darve et al., 1995).

However, the main difficulty with this general definition consists in formulating a related manageable criterion for practical use. If we limit our analyses to divergence instabilities (letting apart flutter instabilities), Hill's sufficient condition of stability (Hill, 1958) is often considered to describe the occurrence of material instability. A detailed derivation of this criterion from the writing of the energy balance can be found in the work of Nicot and Darve (2007c); Nicot et al. (2009, 2012) in the general framework of finite deformation. For the sake of simplicity, if we restrict here to small strain continuum mechanics, Hill's instability criterion applied to a material point states that:

> For a given equilibrium $(\boldsymbol{\sigma}, \boldsymbol{\varepsilon})$ reached after a given loading history, the material point is unstable if there exists at least one couple $(\mathbf{d}\boldsymbol{\sigma}, \mathbf{d}\boldsymbol{\varepsilon})$ linked by the constitutive law of the material such that $W_2 = \mathbf{d}\boldsymbol{\sigma} : \mathbf{d}\boldsymbol{\varepsilon} < 0$.

Let Ω denote a mechanical system of boundary $\partial\Omega$. Let $\mathbf{d}\boldsymbol{f}$ be the force per surface unit applied on $\partial\Omega$ and $\mathbf{d}\boldsymbol{u}$ the displacement acting on $\partial\Omega$. Starting from an initial equilibrium position, the variation of kinetic energy of this mechanical system is a second-order term d^2E_c equal to (Nicot and Darve, 2007c; Nicot et al., 2009, 2012)

$$\mathrm{d}^2E_c = |\Omega| \left(\overline{W}_2^{\mathrm{ext}} - \overline{W}_2 \right) = \int_{\partial\Omega} \mathbf{d}\boldsymbol{f} \cdot \mathbf{d}\boldsymbol{u} \, \mathrm{d}S - \int_{\Omega} W_2 \, \mathrm{d}V \tag{2.6}$$

where $\overline{W}_2^{\mathrm{ext}} = \dfrac{1}{|\Omega|} \int_{\partial\Omega} \mathbf{d}\boldsymbol{f} \cdot \mathbf{d}\boldsymbol{u} \, \mathrm{d}S$ is referred to as the mean external second-order work and $\overline{W}_2 = \dfrac{1}{|\Omega|} \int_{\Omega} W_2 \, \mathrm{d}V$ is the mean (internal) second-order work.

This fundamental equation states that the external work is always larger than the integral of the second-order work of the system. In the case of a nil external second-order work, a negative second-order work associated with an equilibrium position (at the first order $\mathrm{d}E_c = 0$) will automatically result in an increase in the kinetic energy of the system as $\mathrm{d}^2E_c > 0$. As a result, Hill's second-order work criterion may be seen as an energy criterion corresponding to a situation in which the deformation of the mechanical system can be pursued without any input of energy from the observer.

It is essential to note that the second-order criterion by itself does not provide a sufficient condition for failure. In other words, it is not a failure criterion but only a potential failure one. Some loading programs will lead to an effective failure but not every loading program will trigger off the underlying instability. By coming back to Equation 2.6, the vanishing of the second-order work leads to an increase in kinetic energy if and only if $\overline{W}_2 < \overline{W}_2^{\mathrm{ext}}$.

Recent papers have demonstrated the ability of this criterion to anticipate the occurrence of material instability characterized by an outburst of kinetic energy (Nicot et al., 2009; Daouadji et al., 2011; Nicot et al., 2012; Wan et al., 2013; Nicot et al., 2017). It has even been shown that the vanishing of the second-order work is indeed the first instability criterion to be encountered (Nicot et al., 2009; Daouadji et al., 2011; Wan et al., 2013; Challamel et al., 2010) and other instability criteria are simply particular cases associated to specific failure mechanisms such as localized failure (Rudnicki and Rice,

1975; Nova, 1994) or plastic limit failure. The main contributions to the field of geomechanics obtained thanks to the use of this criterion have been summarized in a recently published treatise (Wan et al., 2016).

2.2.4 Second-order work envelope based on directional analysis

Following the principle of incremental determinism, the incremental stress-strain response of a rate-independent material is only a function of the incremental stress $\mathbf{d}\boldsymbol{\sigma}$ and the incremental strain $\mathbf{d}\boldsymbol{\varepsilon}$. This statement can be formulated as the existence of a bijective function $\mathcal{L}$ depending on the past history of the material such that

$$\mathbf{d}\boldsymbol{\varepsilon} = \boldsymbol{\mathcal{L}}(\mathbf{d}\boldsymbol{\sigma}) \text{ or equivalently } \mathbf{d}\boldsymbol{\sigma} = \mathcal{L}^{-1}(\mathbf{d}\boldsymbol{\varepsilon}). \tag{2.7}$$

In the above relation (valid for rate-independent materials), $\mathcal{L}$ is a homogeneous function of degree 1. As a result, it can be rewritten by introducing a function $\mathcal{G}$ acting on the unit sphere in the stress space and such that

$$\mathbf{d}\boldsymbol{\varepsilon} = \boldsymbol{\mathcal{L}}(\mathbf{d}\boldsymbol{\sigma}) = ||\mathbf{d}\boldsymbol{\sigma}||\mathcal{G}(\boldsymbol{d}) \tag{2.8}$$

where $\boldsymbol{d} = \frac{\mathbf{d}\boldsymbol{\sigma}}{||\mathbf{d}\boldsymbol{\sigma}||}$ and $\mathcal{G}(\boldsymbol{d})$ has the dimension of the inverse of a pressure.

In in addition, if Euler's identity is used, the incremental constitutive relationship reads (Darve and Nicot, 2005)

$$\mathbf{d}\boldsymbol{\varepsilon} = ||\mathbf{d}\boldsymbol{\sigma}||\frac{\partial \mathcal{G}}{\partial \boldsymbol{d}} : \boldsymbol{d}. \tag{2.9}$$

As a result the incremental strain response depends only on the magnitude of the incremental stress increment $||\mathbf{d}\boldsymbol{\sigma}||$ and on the loading direction in the stress space $\boldsymbol{d}$. In Equation 2.9, it should be underlined that the constitutive operator $\frac{\partial \mathcal{G}}{\partial \boldsymbol{d}}$ depends only on the loading direction $\boldsymbol{d}$ but is generally not constant with respect to $\boldsymbol{d}$ which makes the incremental constitutive behavior non-linear.

Coming back to the definition of instability according to the second-order work criterion, Equation 2.9 shows that the sign of W_2 depends only on the loading direction, but generally through a non-linear relationship $W_2 = ||\mathbf{d}\boldsymbol{\sigma}||^2\boldsymbol{d} : \frac{\partial \mathcal{G}}{\partial \boldsymbol{d}} : \boldsymbol{d}$. As a result, the mechanical stability or instability assessment of a material requires the use of a directional analysis, as introduced for instance by Gudehus (1979). A directional analysis consists in loading a same initial material along several directions (either in the incremental stress or strain space). The material response is recorded and enables

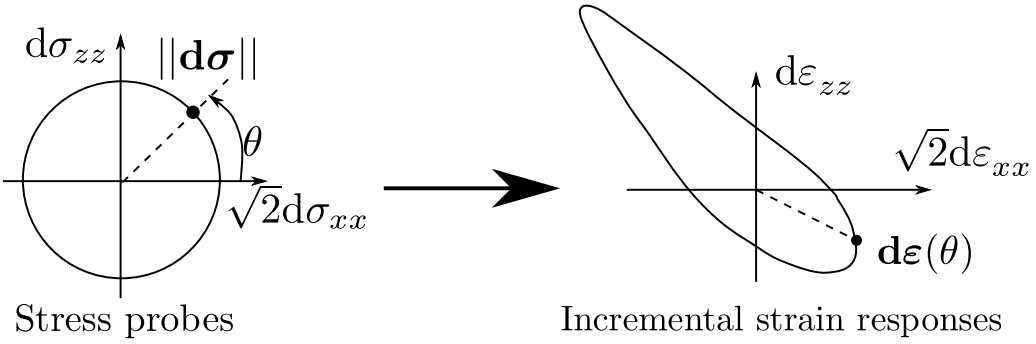

Figure 2.10 – Typical visualization of the incremental strain response of a granular material subjected to an incremental stress directional analysis conducted in axisymmetric conditions ($\mathrm{d}\sigma_{xx} = \mathrm{d}\sigma_{yy}$).

to compute the associated second-order work criterion. An example of the incremental strain response of a granular material subjected to an incremental stress directional analysis is shown in Figure 2.10.

The main difficulty consists in testing a sufficient number of loading directions to be able to detect the existence of a direction giving $W_2 < 0$. For numerical analysis, this question is only a computational cost issue. For real experiments, an other difficulty consists in preparing as many specimens as the number of tested loading directions because of the irreversible nature of each incremental loading. This is a reason why only very few experimental directional analyses exist (Royis and Doanh, 1998).

In many cases, granular materials can be assumed to exhibit an isotropic microstructure in a virgin state. Provided that they are subjected to axisymmetry loading conditions (for instance triaxial loading), the resulting constitutive behavior exhibits transverse anisotropy and directional analyses can be restricted to Rendulic's place of axisymmetry ($\sqrt{2}\mathrm{d}\sigma_{xx}, \mathrm{d}\sigma_{zz}$). In other words the unit sphere in the incremental stress or strain space reduces to a circle for these particular cases. In this case, polar (or circular) representations of the normalized second-order work

$$W_2^{\mathrm{norm}} = \frac{W_2}{||\mathbf{d}\boldsymbol{\sigma}||||\mathbf{d}\boldsymbol{\varepsilon}||} = \frac{\boldsymbol{d} : \frac{\partial \mathcal{G}}{\partial \boldsymbol{d}} : \boldsymbol{d}}{||\frac{\partial \mathcal{G}}{\partial \boldsymbol{d}} : \boldsymbol{d}||} \tag{2.10}$$

can be plotted as in Figure 2.11 for stress control. In this Figure, some particular incremental loading cases are shown with small schematic diagrams.

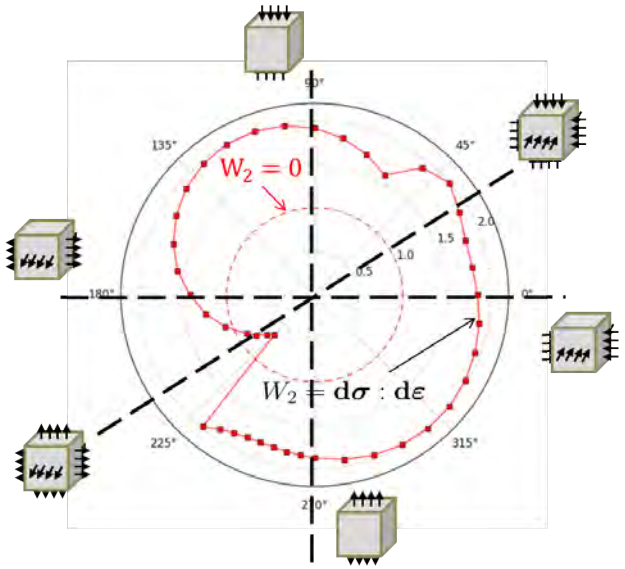

Figure 2.11 – Typical stress controlled circular envelope obtained for an unstable material. Some particular incremental loading cases are shown with schematic diagrams.

In Figure 2.12 circular representations of normalized second-order work envelopes found in the literature are shown for stress or strain controlled directional analyses in axisymmetic loading conditions.

In Figure 2.12 and for some stress states, the loading directions associated with the vanishing of the second-order work define a cone of instability (around 230° and 130° respectively for stress and strain controlled directional analyses). These directions are those that can lead to an effective failure of the material through an increase in kinetic energy and a transition from a quasi-static to a dynamic regime.

2.2.5 Flood induced loading and possible impact on mechanical stability

As seen in the previous subsection, directional analyses give more information than simply the existence or not of loading directions associated with $W_2 < 0$. Indeed, for unstable materials, directional analysis also provide the set of incremental loading directions that can lead to effective development of underlying instability. It is interesting here to estimate the incremental loading directions associated with flooding.

Contrary to the hydraulic loading associated with suffusion which is constant in time and result in a water pressure decrease through the dike or

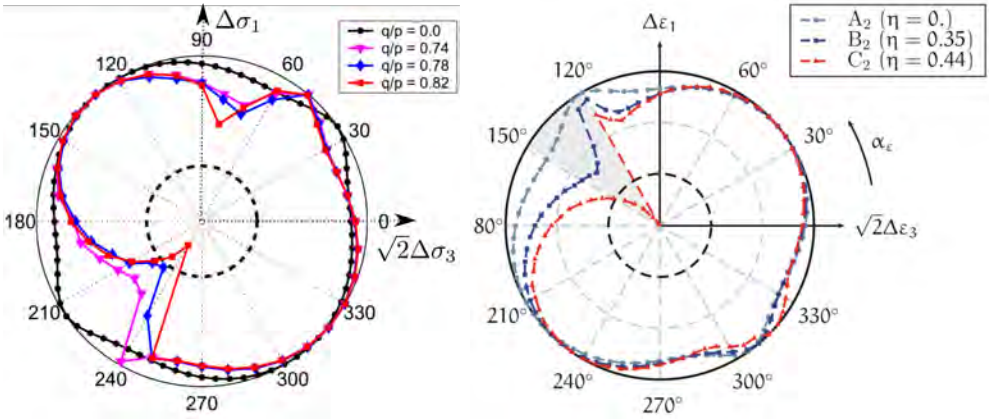

(a) Numerical sample (S1) (Sibille et al., 2007)

(b) Numerical loose granular assembly (Hadda et al., 2013)

Figure 2.12 – Typical circular representations of normalized second-order work envelopes resulting from stress (a) or strain (b) controlled directional analyses in axisymmetic loading conditions. In both cases, the envelopes are computed on numerical samples loaded in drained triaxial tests at different stress ratios $\eta = q/p$ and under a confining pressure of 100 kPa. The dashed circles correspond to $W_2 = 0$.

dam body (see Figure 2.13), flooding is associated with a sudden increase in the water level on the upstream side of the hydraulic structure. As a result, flooding imposes undrained conditions in the dike or dam body. In other words, the sudden rise in the water level imposes a global increase in interstitial water pressure in the short term as illustrated in Figure 2.13. In the short term the total stress remains approximately constant and the pore pressure increase results in a *drop* in the effective stress along a constant deviatoric stress loading direction (constant q-path). Consequently, the incremental stress loading associated with flooding is of the form $\mathbf{d\boldsymbol{\sigma}} = -\mathrm{d}p\mathbf{1}$. In Rendulic's plane $(\sqrt{2}\mathrm{d}\sigma_{xx}, \mathrm{d}\sigma_{zz})$, this corresponds to an incremental stress direction $\theta = \pi + \arctan\sqrt{2} \simeq 235°$ ($\mathrm{d}\sigma_{xx} = \mathrm{d}\sigma_{yy} = \mathrm{d}\sigma_{zz} = -\mathrm{d}p$ implies that $\theta \in [\pi, 3\pi/2]$ and $\tan\theta = \sqrt{2}$). Because this direction is usually close to the observed cones of instability in granular materials (see Figure 2.12(a)), flooding imposes indeed a potentially harmful loading for an unstable granular material in the sense of Hill's criterion. The proposal made in this PhD to characterize suffusion mechanical consequences in terms on mechanical stability through the second-order work criterion is thus very sensible.

In order to facilitate the interpretation of the stability analysis in terms of incremental loading from the hydraulic structure point of view, the choice

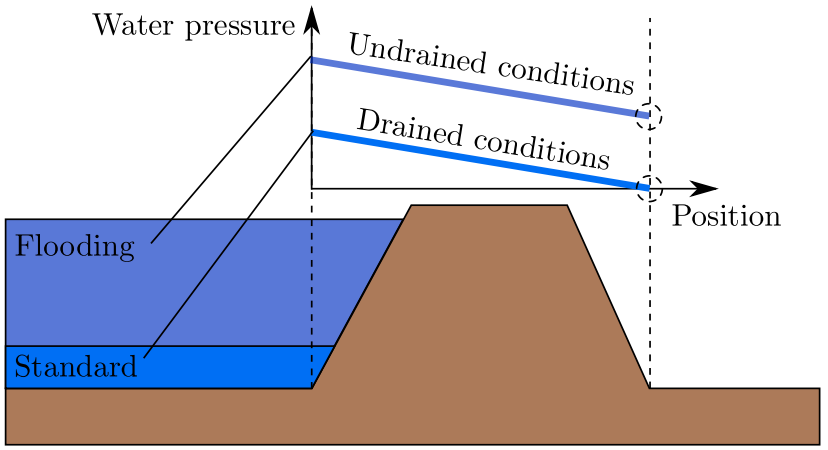

Figure 2.13 – Inner water pressure distribution for standard hydraulic loading conditions (drained conditions) and during flooding (undrained conditions).

was made in this work to consider only stress-controlled directional analyses.

2.3 Multiscale modeling of granular materials

Down to the microscale, granular materials can be described as a collection of particles interacting between each others through local contact laws. However, at the engineering scale, this discrete nature is not accounted for but hidden behind a macroscopic continuum description of their mechanical behavior. It is for instance unconceivable to model atoms in a metal beam or sand grains in earth dams and dikes. As a result, basically two approaches can be followed either i) by completely disregarding the discrete nature of the materials and proposing ad hoc constitutive equations to account for the macroscopic behavior of granular materials, or ii) by explicitly accounting for the local geometry and bridging the gap between the two scales thanks to homogenization techniques. Since one of the objective of this PhD work was to study the local physics of suffusion, the second approach was chosen and a discrete element modeling approach used in order to easily capture important microstructure modifications.

In this section, the used Discrete Element Method (DEM) computation scheme is briefly reviewed and the state of the art on the understanding of the local physics of granular materials is presented.

2.3.1 Microscopic modeling through discrete element methods (DEM)

First developments of Discrete Element Methods (DEM) are usually attributed to Cundall and Strack (1979). Since then, and thanks to increasingly powerful computing capability, DEM becomes widely accepted as an effective and efficient method to account for the complex behavior of granular materials. Indeed, by being able to simulate at a reasonable computational cost the collective behavior of tens to hundreds of thousands of particles, DEM offers the possibility to work at a scale at which discrete and continuum descriptions of granular material merge. This scale is known as the Representative Elementary Volume (REV) as introduced by Hill (1963) and enables direct comparison between experimental and simulation results. Consequently, recent studies show the ability of DEM methods to accurately account for characteristics of granular materials such as dilatancy/contractancy, anisotropy building, hardening/softening or shear band localization (Calvetti, 2003; Alonso-Marroquín, 2004; Luding, 2004; Sibille, 2006; Walker and Tordesillas, 2010; Zhu et al., 2016a).

In DEM, only two ingredients are needed to account for the evolution of a mechanical system: the geometry of the grains and the interaction forces between them. In DEM, contrary to molecular dynamics (MD), grains can only interact with their closest neighbors, provided that there exists a contact point between them. Among the existing discrete numerical approaches that have been developed, two families of models can be distinguished depending on how either contact forces are computed explicitly or implicitly. If grain inter-penetration is not allowed, a single geometric configuration can correspond to many different contact forces. As a result, the local contact forces can only be computed by considering the whole mechanical problem. Such approaches are referred to as non-smooth contact dynamics and rely on an implicit integration scheme. On the contrary, if grain inter-penetration is allowed, a small variation of the geometric configuration corresponds to a unique variation of the contact force. As a result, the local contact forces can be computed contact per contact. Such approaches are referred to as smooth contact dynamics and rely on an explicit integration scheme.

These two approaches are used in practice and have both advantages and drawbacks as underlined for instance in details in Dubois et al. (2017). On the one hand, smooth contact dynamics schemes are easier to implement, can handle large numbers of particles but face a CFL (Courant–Friedrichs–Lewy) condition for the choice of the integration time step, require the use of numerical damping and have to deal with hypo-elastic formulations of the contact law. On the other hand, non-smooth contact dynamics schemes show no CFL

conditions but each time step is computationally more expensive and they cannot yet handle large numbers of particles. For the sake of efficiency, a smooth contact dynamic approach is used in this work with contact stiffness sufficiently large so that grain inter-penetration remains limited. For most of the results presented in this PhD thesis, the choice is only a matter of numerical implementation but still for a few results this choice may slightly influence the physics (one example is detailed in the end of Section 4.2.4).

In practice, all simulations performed in this work have been using the open source code YADE (Yet Another Dynamic Engine) developed in 3SR lab in Grenoble (Šmilauer et al., 2015). The reason for the choice of this particular smooth contact dynamic code is mainly due to an existing efficient fluid/grain coupling scheme that is detailed in the next section.

Computation cycle

DEM relies on the integration of Newton's second law of motion for non-deformable solid bodies. For a single particle p the force and momentum balance equations read

$$\rho V_p \, \frac{\mathrm{d}^2 \boldsymbol{x_p}}{\mathrm{d}t^2} = \sum_{c_p} \boldsymbol{F}_{c_p} \tag{2.11a}$$

$$\frac{\mathrm{d}}{\mathrm{d}t} \left[\int_{V_p} (\boldsymbol{x} - \boldsymbol{x}_p) \times \frac{\mathrm{d}\boldsymbol{x}}{\mathrm{d}t} \, \rho \mathrm{d}V \right] = \sum_{c_p} (\boldsymbol{x}_{c_p} - \boldsymbol{x}_p) \times \boldsymbol{F}_{c_p} \tag{2.11b}$$

where ρ is the mass density of the particle, V_p its volume, $\boldsymbol{x_p}$ the position of its mass center, $\boldsymbol{x}_{c_p}$ the positions of the contact points of the particle and $\boldsymbol{F}_{c_p}$ the external contact forces applied on the particle at contact c_p.

If the particle shape is specified as a sphere, then Equation (2.11b) can be simplified by introducing the inertia momentum of a sphere $J = \frac{2}{5}\rho V_p R_p^2$ (R_p being the sphere radius) and the rotation speed $\boldsymbol{\omega}_p$ of the sphere. In this case, Equation (2.11b) reads

$$J \frac{\mathrm{d}\boldsymbol{\omega}_p}{\mathrm{d}t} = \sum_{c_p} R_p \boldsymbol{n}_{c_p} \times \boldsymbol{F}_{c_p} \tag{2.12}$$

where $\boldsymbol{n}_{c_p}$ is the outward normal vector to the sphere on point c_p.

For a time increment Δt, Equations (2.11a) and (2.12) are then discretized by use of a mid-point integration scheme with

$$\begin{cases} \left.\frac{\mathrm{d}\boldsymbol{x}_p}{\mathrm{d}t}\right|_{t+\Delta t/2} = \left.\frac{\mathrm{d}\boldsymbol{x}_p}{\mathrm{d}t}\right|_{t-\Delta t/2} + \left.\frac{\mathrm{d}^2\boldsymbol{x}_p}{\mathrm{d}t^2}\right|_t \Delta t \\ \boldsymbol{\omega}_p(t + \Delta t/2) = \boldsymbol{\omega}_p(t - \Delta t/2) + \left.\frac{\mathrm{d}\boldsymbol{\omega}_p}{\mathrm{d}t}\right|_t \Delta t \end{cases} \tag{2.13}$$

and

$$\boldsymbol{x}_p(t+\Delta t) = \boldsymbol{x}_p(t) + \left.\frac{\mathrm{d}\boldsymbol{x}_p}{\mathrm{d}t}\right|_{t+\Delta t/2} \Delta t. \tag{2.14}$$

Contrary to the position, the orientation of a particle cannot be simply described by a physical vector but through the three Euler's angles. In practice, the particle orientation is deduced from the second equation of (2.13) thanks to an efficient use of quaternion algebra (Šmilauer et al., 2015).

To sum up, each computation cycle is composed of the following four steps:

- Detect the contact points;
- Compute the contact forces;
- Integrate the force and momentum equations for each grain;
- Update the positions of the grains.

Contact law

The choice of the contact law is the second ingredient needed to perform DEM simulation with the choice of the grain geometry. Today, a large choice in contact laws have been developed and are implemented in DEM computation codes.

The most common contact law used in DEM is the elasto-frictional law, introduced by Cundall and Strack (1979). It assumes that a contact is created as two particles overlaps. The two contacting bodies are then assumed to be linked by two fictitious linear springs and a slider as illustrated in Figure 2.14. At time t, the normal spring defines a normal force $\boldsymbol{F}_n^t = -F_n^t \boldsymbol{n}^t$ ($\boldsymbol{n}^t$ being the outward normal unit vector to the contact) and the tangential spring associated with the slider define a tangential force $\boldsymbol{F}_\tau^t$.

The normal intensity F_n^t is defined at time t as proportional to the overlapping distance δ^t between the two particles through a contact stiffness k_n. As it is aligned with the normal direction (with opposite sense), it can be computed in a scalar form as

$$F_n^t = k_n \delta^t \tag{2.15}$$

In the above equation, the contact normal stiffness k_n depends on the size of the two contacting particles as it is proportional to the material's *Young*

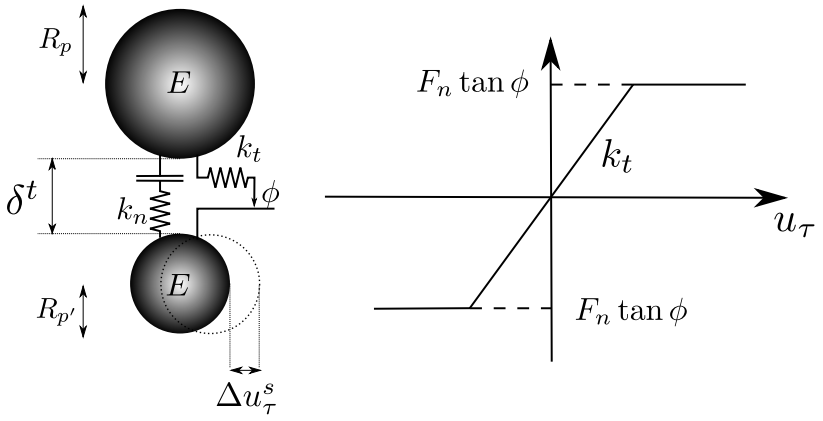

Figure 2.14 – Elasto-frictional law used in DEM simulations

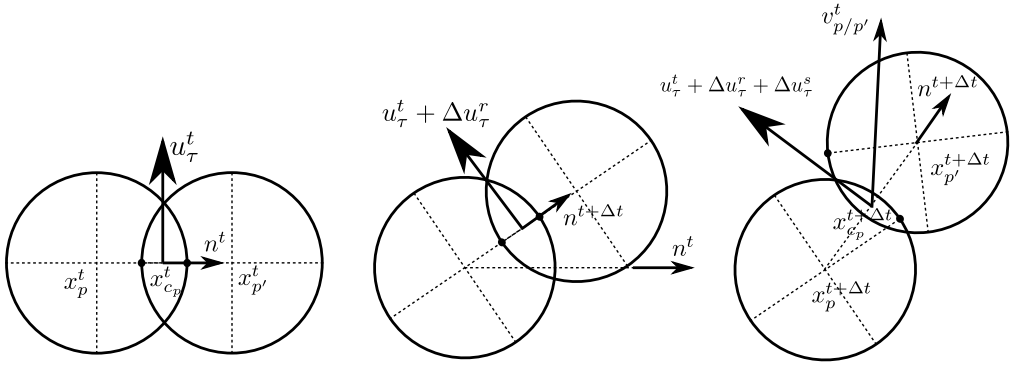

Figure 2.15 – Incremental update of the accumulated shear displacement $\boldsymbol{u}_\tau$ as implemented in YADE.

modulus E and to the harmonic average of the two particles radii R_p and $R_{p'}$

$$k_n = E\frac{2R_pR_{p'}}{R_p + R_{p'}}. \tag{2.16}$$

Contrary to its normal counterpart, the tangential force $\boldsymbol{F}_\tau^t$ cannot be simply defined based on the current geometrical configuration. It depends on the loading history and the accumulated shear displacement $\boldsymbol{u}_\tau^t$ at time t.

The incremental definition of $\boldsymbol{u}_\tau^t$ is not trivial and is illustrated in Figure 2.15.

Let consider two spheres p and p' in contact at time t. In this configuration

the outward normal vector for sphere p is

$$\boldsymbol{n}^t = \frac{\boldsymbol{x}_{p'}^t - \boldsymbol{x}_p^t}{||\boldsymbol{x}_{p'}^t - \boldsymbol{x}_p^t||} \tag{2.17}$$

and the contact point position $\boldsymbol{x}_{c_p}^t$ is located in the middle of the overlapping zone

$$\boldsymbol{x}_{c_p}^t = \boldsymbol{x}_p^t + (R_p - \frac{\delta^t}{2})\boldsymbol{n}^t \tag{2.18}$$

with $\delta^t = R_p + R_{p'} - ||\boldsymbol{x}_{p'}^t - \boldsymbol{x}_p^t||$.

Then, at time $t+\Delta t$, the two contacting spheres move to the new positions $\boldsymbol{x}_p^{t+\Delta t}$ and $\boldsymbol{x}_p^{t+\Delta t}$. Accordingly, the normal vector and the contact positions are updated as $\boldsymbol{n}^{t+\Delta t}$ and $\boldsymbol{x}_{c_p}^{t+\Delta t}$. The tangential displacement $\boldsymbol{u}_\tau^t$ is updated by introducing two correction terms $\boldsymbol{\Delta u}_\tau^r$ and $\boldsymbol{\Delta u}_\tau^s$.

Part of the update is simply linked to the solid rotation of the two spheres in contact and part of the update is coming from the relative motion between the spheres (Šmilauer et al., 2015). As a result, a first correction $\boldsymbol{\Delta u}_\tau^r$ is introduced to account for the rotation of the normal vector with a rotation velocity $\frac{\boldsymbol{\omega}_p^t + \boldsymbol{\omega}_{p'}^t}{2}$ without changing the norm of the shear displacement $||\boldsymbol{u}_\tau^t + \boldsymbol{\Delta u}_\tau^r|| = ||\boldsymbol{u}_\tau^t||$. The second increment accounts for the relative velocity $\boldsymbol{v}_{p'/p}^t$ of grain p' compared to grain p at the contact point $\boldsymbol{x}_{c_p}^t$

$$\boldsymbol{v}_{p'/p}^t = \left.\frac{\mathrm{d}\boldsymbol{x}_{p'}}{\mathrm{d}t}\right|_t - \left.\frac{\mathrm{d}\boldsymbol{x}_p}{\mathrm{d}t}\right|_t + \boldsymbol{\omega}_{p'}^t \times (\boldsymbol{x}_{c_p}^t - \boldsymbol{x}_{p'}^t) - \boldsymbol{\omega}_p^t \times (\boldsymbol{x}_{c_p}^t - \boldsymbol{x}_p^t) \tag{2.19}$$

The associated incremental shear displacement $\boldsymbol{\Delta u}_\tau^s$ at the contact point is then computed by integrating the shear component of the velocity with respect to the current normal vector $\boldsymbol{n}^{t+\Delta t}$

$$\boldsymbol{\Delta u}_\tau^s = \Delta t \left[\boldsymbol{v}_{p'/p}^t - (\boldsymbol{v}_{p'/p}^t \cdot \boldsymbol{n}^{t+\Delta t})\boldsymbol{n}^{t+\Delta t}\right]. \tag{2.20}$$

In the end, the shear displacement at time $t+\Delta t$ (perpendicular to $\boldsymbol{n}^{t+\Delta t}$) is updated as

$$\boldsymbol{u}_\tau^{t+\Delta t} = \boldsymbol{u}_\tau^t + \boldsymbol{\Delta u}_\tau^r + \boldsymbol{\Delta u}_\tau^s. \tag{2.21}$$

In the global framework, the tangential force $\boldsymbol{F}_\tau^t$ is then defined at time t as proportional to the shear displacement $\boldsymbol{u}_\tau^t$ through a contact stiffness $k_t = \alpha k_n$ expressed as a fraction α of its normal counterpart.

$$\boldsymbol{F}_\tau^t = -k_t \boldsymbol{u}_\tau^t \tag{2.22}$$

Table 2.1 – Mechanical parameters used in the elasto-frictional contact law implemented in YADE.

Parameters	Value
Density	3,000 kg.m^{-3}
Young Modulus (E)	356 MPa
Stiffness ratio (α)	0.42
Inter-particle friction angle (ϕ)	35°
Particle-wall friction angle	0°

Note that the tangential force $\boldsymbol{F}_\tau^{t+\Delta t}$ could have been defined equivalently in an incremental form by rotating $\boldsymbol{F}_\tau^t$ and adding the incremental contribution $\boldsymbol{\Delta F}_\tau = k_t \boldsymbol{\Delta u}_\tau^s$.

The above relation remains valid as long as contact sliding does not occur, which is assessed thanks to a Mohr-Coulomb criteria with an internal friction angle ϕ. As a result, the complete tangential force is expresses as

$$\boldsymbol{F}_\tau^t = \begin{cases} -k_t \boldsymbol{u}_\tau^t & \text{if } ||\boldsymbol{F}_\tau^t||/F_n^t < \tan\phi \\ -\tan\phi \; F_n^t \; \frac{\boldsymbol{u}_\tau^t}{||\boldsymbol{u}_\tau^t||} & \text{otherwise} \end{cases} \tag{2.23}$$

The input parameters used in this elasto-frictional contact law are reported in Table 2.1 and are similar to those used in Hadda (2006).

***Remark on the ratcheting effect*:** Because the relative velocity given in Equation (2.19) involves the non-constant length scales $||\boldsymbol{x}_{c_p}^t - \boldsymbol{x}_{p'}^t|| = R_{p'} - \frac{\delta^t}{2}$ and $||\boldsymbol{x}_{c_p}^t - \boldsymbol{x}_p^t|| = R_p - \frac{\delta^t}{2}$, the formulation of the shear force can result in granular ratcheting. This well known effect appears while considering cyclic loading during which a certain amount of permanent shear displacement is accumulated each cycle even in the elastic regime. For instance, let us consider two grains p and p'. p is fixed, and a displacement cycle is imposed to p' as follow:

- translation $\mathbf{d}\boldsymbol{x}_{p'}$ in the normal direction
- rotation $\Delta t \; \boldsymbol{\omega}_{p'}$
- translation $-\mathbf{d}\boldsymbol{x}_{p'}$ in the normal direction
- rotation $-\Delta t \; \boldsymbol{\omega}_{p'}$

If the branch vector used to define the relative shear displacement through grain rotation is not constant (as it is the case in Equation (2.19)), then the

shear displacement at the end of this cycle is not zero. It results in a finite contact force at the end of the cycle even though the positions and orientations are identical which contradicts the elastic nature of the problem. Given that DEM simulations tend to generate oscillations around equilibrium, it can have a significant impact on the evolution of the packings, resulting for instance in slow creep in iterations under constant load. The solution adopted in YADE to avoid ratcheting is inspired by the work of Mcnamara et al. (2008). Indeed, Equation (2.19) is replaced by

$$\boldsymbol{v}^t_{p'/p} = \alpha \left(\left.\frac{\mathrm{d}\boldsymbol{x}_{p'}}{\mathrm{d}t}\right|_t - \left.\frac{\mathrm{d}\boldsymbol{x}_p}{\mathrm{d}t}\right|_t \right) - \boldsymbol{\omega}^t_{p'} \times R_{p'}\boldsymbol{n}^t - \boldsymbol{\omega}^t_p \times R_p \boldsymbol{n}^t \tag{2.24}$$

with

$$\alpha = \frac{R_p + R_{p'}}{R_p + R_{p'} - \delta^t}. \tag{2.25}$$

Convergence conditions

As already mentioned in the comparison between smooth and non-smooth contact dynamics approaches, smooth contact dynamics is subjected to a CFL condition. This imposes a condition on the time step Δt that should be smaller than a critical time step Δt_c depending on the wave propagation velocity in the medium. For a granular system modeled as a collection of spheres linked by springs, the characteristic oscillation period T is equal to $2\pi\sqrt{\frac{m}{k}}$ with m the particle mass and k the spring stiffness. As m and $k \in \{k_n; k_t\}$ depend on the particle radius R_p, the critical time step Δt_c for the whole granular material must be strictly less than the minimum characteristic period over all particles for the stiffer spring k_n. By recalling that $k_n \simeq ER$ with R the radius of contacting particles and $m = \rho\frac{4}{3}\pi R^3$,

$$\Delta t_c \simeq R_{\min}\sqrt{\frac{\rho}{E}} \tag{2.26}$$

In case rolling resistance should be introduced, an other critical time step coming from the integration of (2.12) should also be considered.

In addition, in order to avoid permanent small oscillations in the system due to the absence of viscous damping in the used contact law, a numerical damping coefficient λ_d is used for numerical stabilization purpose. In practice, λ_d is set to 2%. The basic idea is to decrease the summary forces $\sum_{c_p} \boldsymbol{F}_{c_p}$ which increase the particle velocity and vice versa by comparing the current acceleration direction and particle velocity direction. The force

increment $\boldsymbol{\Delta F}_d$ corresponding to the numerical damping is computed component per component, which makes the damping scheme non-objective and clearly non-physical (Šmilauer et al., 2015)

$$\frac{\Delta F_d^i}{\sum_{c_p} F_{c_p}^i} = -\lambda_d \text{ sign} \left[\left(\sum_{c_p} F_{c_p}^i \right) \cdot \left(\left. \frac{\mathrm{d}x_p^i}{\mathrm{d}t} \right|_{t-\Delta t/2} + \left. \frac{\mathrm{d}^2 x_p^i}{\mathrm{d}t^2} \right|_t \frac{\Delta t}{2} \right) \right] \quad (2.27)$$

where i refers to vector components.

Computational efficiency in YADE

Before concluding on this short review of the DEM method that was used throughout this PhD work, it is important to tell a few words on the computational cost of DEM as implemented in YADE. It is indeed closely linked to the contact detection step and the critical time step.

Because contact detection requires basically to test for every couple of particles whether they intersect, the computation cost of this step strongly depends on the number of particles handled in the simulation. A brutal force algorithm predicts a complexity of $O(N_p^2)$, N_p being the number of particles. By sorting the particles by sub-domains and only checking the occurrence of contacts between particles belonging to a same domain, it is possible to speed up the contact detection. Dealing with each sub-domain in parallel on different processors also speeds up this step. However, if too many sub-domains are used, most of the contacts will concern particles belonging to different sub-domains. This will result in a decrease in computational efficiency as information exchange between processors will become too much time consuming. As a result, for tens of thousands of particles in 3D, no more than 6 to 10 processors should be used to speed up contact detection. A detailed performance test of YADE was carried out by Klaus Thoeni and is available on https://yade-dem.org/wiki/Performance_Test.

Because the critical time step $\Delta t_c \simeq R_{\min}\sqrt{\frac{\rho}{E}}$ is proportional to $R_{\min}$, the presence of a few small particles has dramatic consequences on the computation time needed to simulate the same physical time period.

As a result, the computational cost of a DEM simulation in YADE increases with

- the number of particles N;
- the aspect ratio $R_{\min}/R_{\max}$ between the smallest and largest particles.

If we come back to the numerical modeling of suffusion, these two comments predict very expensive numerical simulations as soils subjected to suf-

fusion exhibit i) a very wide particle size distribution (PSD) and ii) a significant mass fraction of fine particles. In order to account numerically for these PSD, both a large number of particles and a large aspect ratio are required. In addition, if we take into account the fact that the mechanical behavior of a soil is mainly dictated by the largest particles, the definition of a representative elementary volume also tends to increase the number of particles needed. Eventually, as it will be detailed in the next section, simulating the fluid flow increases significantly the computation cost also positively correlated with the number of particles.

For all these reasons, the PSD used during this PhD are not always associated with *internal instability* but they are still able to be used to account for fluid/grain interactions directly at the microscale.

2.3.2 Mesoscale structures and mechanics

The mechanical response of a granular material is a mixture between contact scale properties (rigidity, friction, ...) and geometrical effects linked to the specific arrangements of the grains (packing, void ratio, fabric, ...). In the end of the twentieth century, the combine use of photo-elastic grains and numerical simulations shows that the overall behavior of granular materials relies indeed on a limited number of grains organized in linear structures called force chains (Drescher and De Jong, 1972; Liu et al., 1995; Radjai et al., 1998; Cambou et al., 2013; Majmudar and Behringer, 2005; Peters et al., 2005). Such structures are shown in Figure 2.16 for photo-elastic grains and DEM contact force networks.

Besides these qualitative visualizations, the distributions of the contact forces magnitude have been investigated from microscale data. Both experimental and numerical results show that the probability density decays exponentially at large forces and shows a plateau or possibly a small peak near the average force (Cambou et al., 2013). As introduced for instance by Radjai et al. (1998), the contact network can be split into a strong and a weak contact networks depending whether contact forces are greater than the average contact force. The strong contact is responsible for the load bearing capacity of the granular material and the privileged orientation of the force transmission paths is aligned with the principal loading direction. On the contrary, the contacts belonging to the weak contact network are mainly perpendicular to the main loading direction and are responsible for the stability of the strong network as well as the energy dissipation (Radjai et al., 1998). During, a mechanical loading, granular material can thus be seen as a constantly evolving *complex network* that adapts to the changing boundary conditions (Walker and Tordesillas, 2010). The generation of

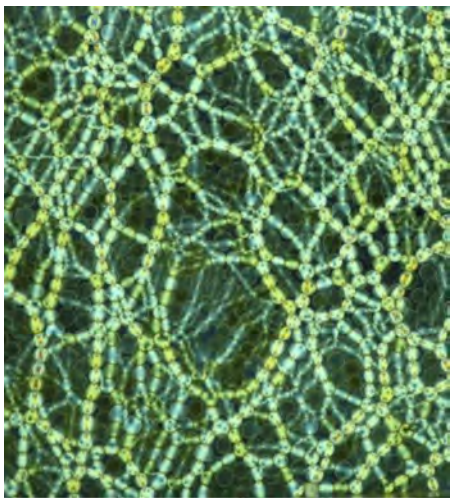

(a) Force chain visualization in a granular assembly of photoelastic disks (Majmudar and Behringer, 2005).

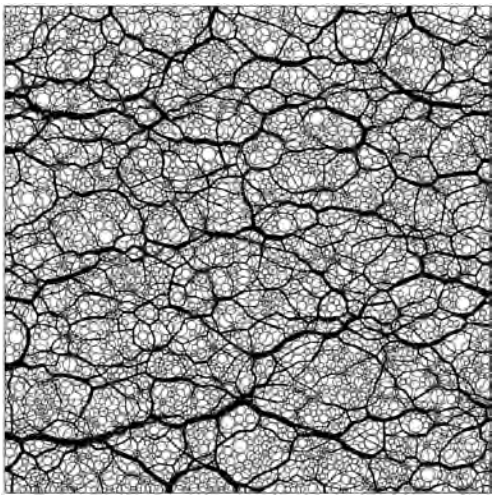

(b) The contact force network in a 2D packing of 4000 disks (Cambou et al., 2013).

Figure 2.16 – Experimental (a) and numerical (b) visualization of the heterogeneities in contact force networks.

column-like structures during a hardening phase followed by the collapse of these structures during a softening phase have been frequently observed in DEM simulations (Iwashita and Oda, 1998, 2000; Majmudar and Behringer, 2005).

From a slightly different perspective, some authors prefer to describe the two grain phases, not through contact networks at the scale of the whole specimens, but by introducing an intermediate scale between the grain scale and the REV scale. Such scale is referred to as mesoscale and two kinds of mesostructures composed of a few grains have been defined in the form of force chains and grains loops. This mesostructure approach has the advantage to be focused on the grains and not on the contacts. As a result, it is a more convenient approach to be used when considering suffusion as the fluid acts on the grains and not on the contacts.

In this work, the force chain definition[1] given in Peters et al. (2005) is adopted as well as the algorithm described to identify force chains in DEM simulations. This definition is illustrated in Figure 2.17 and reviewed here:

- From the definition of the mean stress in a grain recalled in Equation (2.3) the principal stress σ_1 of each grain is computed. Particles be-

[1]Following a discussion with the PhD jury, it appears that the wording *stress chain* should be preferred since the definition is based on the stresses and not forces.

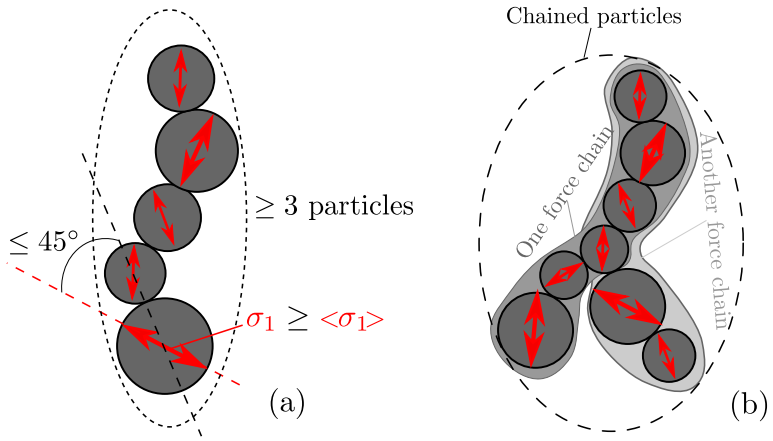

Figure 2.17 – Force chain definition according to Peters et al. (2005) (a). Force chain branching and definition of chained particles (b).

longing to a force chain are then searched among those having principal stress larger than the averaged particle principal stress ($\sigma_1 \geq <\sigma_1>$).

- Among these highly stressed grains, contacting grains having principal stress directions aligned with the geometrical contact direction forms column-like structures transmitting large stresses. As in Peters et al. (2005) a maximum angle of 45° is used to assess the stress/geometry alignment.

- Among the potential aligned groups of stressed grains, only those composed of more than 3 grains are eventually retained to define force chains.

As a result, force chain definition relies on three thresholds: the minimum principal stress ratio $\frac{\sigma_1^{\min}}{<\sigma_1>} = 1$, the maximum deviation angle between stress and geometric directions $\theta^{\max} = 45°$ and the minimum force chain length $L^{\min} = 3$. A justification of these thresholds will be provided in section 3.2.1 of the next chapter.

An other arbitrary aspect of the algorithm presented in Peters et al. (2005) is that force chain branching is not accounted for. As a result, and illustrated in Figure 2.17, force chains are not necessarily uniquely defined and two runs of the algorithm can identify different force chains. As a result, a distinction is made in this manuscript between force chains (mesostructures defined from running Peter's algorithm once) and chained particles (the set of all particles that can be part of force chains). While considering chained

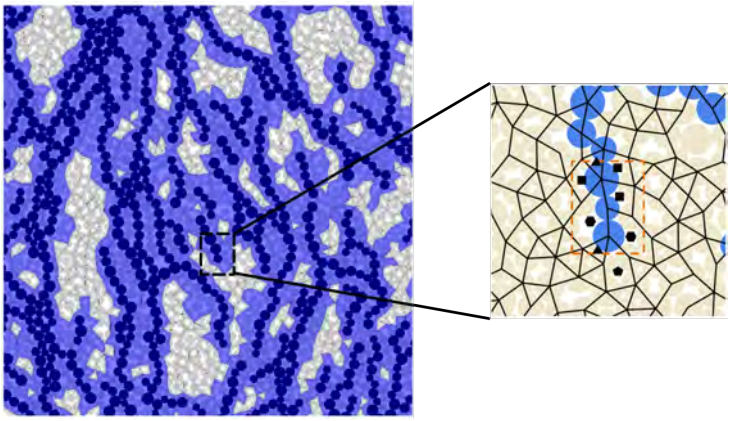

Figure 2.18 – Interplay between loops and force chains in a 2D numerical sample (Zhu, 2015). In the zoom (on the right) loop topology is shown by geometrical figures (triangle, square, ...).

particles, the notion of mesostructure is lost but in the meantime, branching is implicitly accounted for as shown in Figure 2.17.

Complementary to force chain grains, loops have been introduced in 2D to account for the properties of the loose phase. Indeed, in two dimensions the pore space is composed of isolated pores which are enclosed by grain cycles. These topological structures provide indeed a partition of the material domains into meso-scale loops. Compared to force chains that account for the load bearing capacity of the material, these mesostructures account for the deformability of the material. In his PhD, Zhu (2015) investigated in details the interplay between loops and force chains. By performing detailed analysis of DEM simulation, he showed how the surrounding loops around force chains ensure their mechanical stability (Zhu et al., 2016c,b). Loops and force chains in a 2D numerical specimen are illustrated in Figure 2.18.

2.4 Numerical modeling of internal fluid flows

In order to provide a full microscopic modeling of suffusion, the local fluid impact has to be simulated also at the local scale. From a conceptual point of view, accounting for fluid/grain interaction is not a new problem as it basically consists in the simulation of a laminar flow in a pore space which geometry is explicitly known. Under the additional assumption of fluid incompressibility, the fluid problem consists in solving Stokes and mass con-

servation equations

$$\begin{cases} \mu\nabla^2\boldsymbol{u} - \nabla p + \boldsymbol{f} = \boldsymbol{0} \\ \nabla\cdot\boldsymbol{u} = 0 \end{cases}, \tag{2.28}$$

where $\boldsymbol{u}$ is the fluid velocity, p the fluid pressure field, μ the fluid dynamic viscosity and $\boldsymbol{f}$ a body force (the gravity for instance).

From the knowledge of the fluid velocity field, the action of the fluid on the different grains of the material are deduced by integrating the shear and normal stresses on grain interfaces. Eventually, these additional forces can be used in the DEM computation to update the grain positions and the pore space geometry.

The real issue at stake when accounting for the fully coupled suffusion problem at the microscale is indeed a computational issue. Without very efficient numerical computation schemes, three dimensional problems are simply out of reach.

2.4.1 A comparative review of existing methods

A first approach is to simulate the fluid flow thanks to resolved Computational Fluid Dynamics (CFD) techniques. In this approach, the pore space is triangulated in order to solve Equation (2.28) thanks to Finite Element Methods (FEM). As tens to hundreds FEM elements per pore are required to get accurate results, the fluid solving step is extremely expensive and existing studies in the litterature are extremely scarce (Chareyre et al., 2012). Moreover, frequent remeshing is needed to account for the microstructure modifications.

As a result, much of the CFD approaches found in the litterature are indeed unresolved CFD approaches (Zeghal and El Shamy, 2004; El Shamy and Zeghal, 2005; Chen et al., 2011; Zhao and Shan, 2013; Shan and Zhao, 2014; Abdoulaye Hama et al., 2016; Kawano et al., 2017). Unresolved CFD is indeed hybrid between a micro and a macro scale modeling as the fluid problem is not solved at the pore scale but on finite elements, the size of which is much larger than the grains. As a result, Equation (2.28) has to be changed to account for the local porosity of the granular media. Compared to resolved CFD, unresolved CFD is computationally less expensive and requires no remeshing but in the meantime the microscale description of the problem is lost and ad hoc macroscopic assumptions are needed to account for the fluid flow (Darcy's law and Kozeny-Carman expression of the permeability for instance).

A third option to account for the fluid at the local scale is to use Lattice Boltzmann Methods (LBM) (Lallemand and Luo, 2000; Mansouri et al., 2009;

Yu and Fan, 2010; Cuellar et al., 2015; Jaeger et al., 2017; Ngoma et al., 2018). These methods rely on a statistical physics approach and Equation (2.28) is replaced by Boltzmann discrete equation to account for the fluid behavior through a collision-propagation scheme (Lallemand and Luo, 2000). As for resolved CFD approaches, this numerical scheme requires a discretization of the pore space but LBM relies on a fixed lattice that is not changed as grains move. Even if this numerical technique can be easily parallelized, its implementation in 3D is still very expensive. In addition, it should be noted that, incompressible flow represents a high difficulty for the conventional LBM, which is entirely based on density fluctuations.

A fourth class of approach lies in the use of pore network models (Bryant et al., 1993; Thompson and Fogler, 1997; Bakke et al., 1997; Hilpert et al., 2003; Abichou et al., 2004). Indeed, these methods (initially developed to predict the permeability of porous media) are based on a discretization of the void space into connected pores. The complexity of the fluid flow is then reduced to fluid exchange laws between adjacent pores. As a result, the accuracy of these approaches strongly relies on adequate definitions of how fluids are exchanged between pores in terms of the local pore geometry. A second difficulty consists in computing the fluid forces on the surrounding grains as the fluid state is defined as piecewise constant within each pore. However, provided that these difficulties can be overcome, these approaches provide a microscale fully coupled fluid/grain modeling at a relatively cheap computational cost.

So far, most of the existing studies in the literature did not dare to tackle suffusion problems in their full 3D complexity. Some studies propose 2D simulations, but 2D problems imply some arbitrary definition of the local conductivity, assuming virtual channels between adjacent voids as the pore space is not connected contrary to 3D. In this PhD work, the opportunity offered by the recent development of a promising pore network model embedded in the DEM code YADE has been seized to simulate suffusion at the representative elementary volume in 3D. The next subsection introduces in more details the coupled Pore-scale Finite Volume (PFV) - DEM model used in this PhD work (Chareyre et al., 2012; Catalano, 2012).

2.4.2 Pore-scale Finite Volume (PFV) method

Pore space discretization

The first ingredient of all pore network models is to simplify the geometry of the void space by defining a connected network of pores. In the PFV method, this is done by using a regular Delaunay triangulation which con-

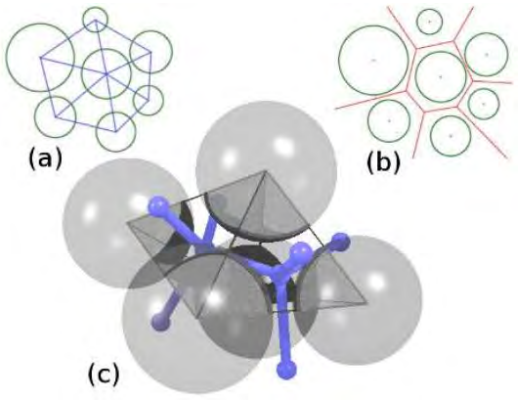

Figure 2.19 – Adjacent tetrahedra in the regular Delaunay triangulation and dual Voronoi network, in two dimensions (a,b) and three dimensions (c) (Chareyre et al., 2012).

sists in a weighted generalized form of the classical Delaunay triangulation (Edelsbrunner and Shah, 1996). This particular triangulation has the important property that all edges of the dual tessellation belong to the void space and do not intersect any grains. The result of this triangulation step is illustrated in Figure 2.19.

The partitioning described above results in a tethraedral mesh whose vertices coincide with the centers of the spheres. The dual tessellation system, defined by branches linking the Voronoi centers computed for each pore, represents the path along which the fluid is assumed to flow within the medium.

Before moving foreward, it is important to underline here that in the PFV method the size of the discretization is not controlled and is dictated by the microstructure. As a result, this method is well adapted to account for fluid flow in condensed granular materials. On the contrary, if granular suspensions or piping erosion are considered, the use of the PFV method will result in large pores which can lessen the method accuracy.

Fluid flow solving step

Following the work of Catalano (2012), let Ω_i be the domain defined by a tetrahedron i of the triangulation. The N_c tetrahedra define a partition of the total domain $\Omega = \cup_{i=1}^{N_c} \Omega_i$. As shown in Figure 2.20, Ω_i is composed of portions of spheres and of void space. Let Γ_i and Θ_i be the domains occupied respectively by the solid and the fluid (since we consider saturated granular materials): $\Omega_i = \Gamma_i \cup \Theta_i$.

In an integral form, the continuity equation (2.28) for an incompressible

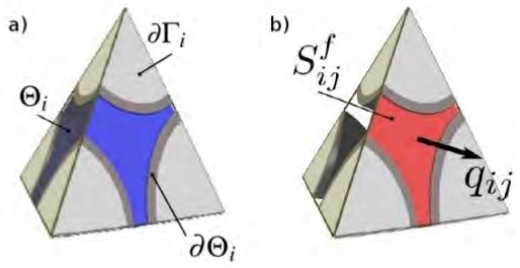

Figure 2.20 – Tetrahedron unit cell of the volume discretization (Chareyre et al., 2012). Pore volume (a) and constriction area (b).

fluid gives a relation between the time derivative of the fluid volume V_i^f contained in pore Ω_i, the fluid velocity $\boldsymbol{u}$ and the contour velocity $\boldsymbol{v}$

$$\frac{\mathrm{d}V_i^f}{\mathrm{d}t} = \int_{\partial\Theta_i} (\boldsymbol{v} - \boldsymbol{u}) \cdot \boldsymbol{n} \mathrm{d}S \tag{2.29}$$

where $\partial\Theta_i$ is the boundary of the fluid domain Θ_i and $\boldsymbol{n}$ the outward normal vector.

Because term $(\boldsymbol{v} - \boldsymbol{u}) \cdot \boldsymbol{n}$ acts on fluid grain interfaces, Equation (2.29) is the sum of four terms computed on the surfaces S_{ij} illustrated in Figure 2.20. If fluid fluxes q_{ij} from pores i to j are introduced, the continuity equation is expressed as

$$\frac{\mathrm{d}V_i^f}{\mathrm{d}t} = \sum_{j=j_1}^{j_4} \int_{S_{ij}^f} (\boldsymbol{v} - \boldsymbol{u}) \cdot \boldsymbol{n} \mathrm{d}S = -\sum_{j=j_1}^{j_4} q_{ij}. \tag{2.30}$$

As Stokes equation (2.28) predicts a linear relationship between the fluid velocity and the pressure gradient, the fluid exchange between two adjacent pores is sought in a Darcy (or Poiseuille) form. By assuming the fluid pressure to be constant in each pore, fluid fluxes are computed as

$$q_{ij} = g_{ij} \frac{p_i - p_j}{l_{ij}} \tag{2.31}$$

where g_{ij} is the hydraulic conductivity of constriction S_{ij}^f and l_{ij} is the inter-pore distance.

In the PFV model, Equation (2.28) is thus reduced to the two Equations (2.30) and (2.31) and the unknowns of the problem are the pore pressures p_i and the fluid fluxes q_{ij} where $(i, j) \in [\![1, N_c]\!]$. As a result, the fluid flow

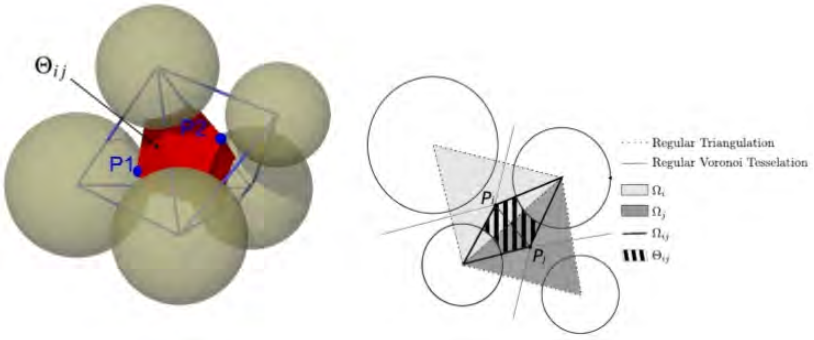

Figure 2.21 – Construction of subdomain Ω_{ij} and Θ_{ij}, defining the volume of the throat assigned to a facet for the definition of hydraulic radius R^h_{ij} (Chareyre et al., 2012).

problem is reduced to a linear algebra problem and basically to the inversion of a sparse matrix for which several efficient algorithms exist.

In Equation (2.31), the definitions of the geometrical parameters g_{ij} and l_{ij} are not given. The accuracy of the PFV model relies indeed on a savvy definition of these two parameters.

By analogy with the Hagen-Poiseuille relation, g_{ij} is defined based on the geometry of the facet ij. By introducing the hydraulic radius of the pore throat R^h_{ij}, the cross-sectional area A_{ij} and a dimensionless coefficient α, the hydraulic conductivity is expressed as

$$g_{ij} = \alpha \frac{A_{ij} R^h_{ij}}{\mu} \tag{2.32}$$

where μ is the fluid dynamic viscosity.

The geometric definition of R^h_{ij}, A_{ij} and l_{ij} are computed on a dual partitioning of the total domain Ω. Indeed, for two adjacent pores i and j, a domain Ω_{ij} is defined based on the center of the three common grains and the two Voronoi vertices P_i and P_j as illustrated in Figure 2.21. The corresponding fluid domain is designed as Θ_{ij}.

The hydraulic radius is then computed as

$$R^h_{ij} = \frac{|\Theta_{ij}|}{|\partial\Theta^s_{ij}|} \tag{2.33}$$

where $|\Theta_{ij}|$ is the fluid volume in Θ_{ij} and $|\partial\Theta^s_{ij}|$ is the surface of the fluid/-grain interface of Θ_{ij}.

The inter-pore distance is computed as $l_{ij} = ||P_iP_j||$ and the cross-sectional area as $A_{ij} = S^f_{ij}$.

The last remaining parameter to set is α that is set to $\alpha = 1/2$ in order to respect the analogy with the Hagen-Poiseuille law. It is worth noting that, this factor being the same for all constrictions, the pressure map is insensitive to α, and consequently do not affect the values of the forces applied on the particles.

The accuracy of the PFV scheme was tested and validated against CFD simulations in Chareyre et al. (2012); Catalano (2012).

Computing fluid forces acting on the grains

Through the triangulation of the void space, the grain impact on the fluid flow has been accounted for. The last step of the DEM-PFV coupling scheme is to compute the back effect of the fluid flow onto the grains. This is done by adding a fluid force into the force balance equation (2.11a). The total force $\boldsymbol{F}^f_k$ generated on particle k by the fluid includes the effects of absolute pressure $p^a = p + \rho_f \Phi$ (where Φ is a potential field) and viscous stress $\boldsymbol{\tau}$

$$\begin{aligned} \boldsymbol{F}^f_k &= \int_{\partial V_k} (p^a \boldsymbol{n} + \boldsymbol{\tau}) \, \mathrm{d}S \\ &= \int_{\partial V_k} \rho \Phi \boldsymbol{n} \, \mathrm{d}S + \int_{\partial V_k} p \boldsymbol{n} \, \mathrm{d}S + \int_{\partial V_k} \boldsymbol{\tau} \, \mathrm{d}S \\ &= \boldsymbol{F}^b_k + \boldsymbol{F}^p_k + \boldsymbol{F}^\nu_k \end{aligned} \tag{2.34}$$

where $\boldsymbol{n}$ is the outward normal vector to domain Ω_{ij} and V_k is the particle domain.

$\boldsymbol{F}^b_k$ is called the buoyancy force which is equal to Archimede's force in the case of gravitational body forces. It is not accounted for in the PFV method implemented in YADE.

In order to compute the last two terms, it is interesting to remark that the domains Ω_{ij} form a partition of the whole domain Ω. $\boldsymbol{F}^p_k$ and $\boldsymbol{F}^\nu_k$ are thus decomposed into $\boldsymbol{F}^{p,ij}_k$ and $\boldsymbol{F}^{\nu,ij}_k$ computed for each cell Ω_{ij}.

As derived in Chareyre et al. (2012),

$$\boldsymbol{F}^{p,ij}_k = \int_{\partial V_k \cap \Omega_i \cap \Omega_{ij}} p_i \boldsymbol{n} \mathrm{d}S + \int_{\partial V_k \cap \Omega_j \cap \Omega_{ij}} p_j \boldsymbol{n} \mathrm{d}S = A^k_{ij}(p_i - p_j)\boldsymbol{n}_{ij} \tag{2.35}$$

where A^k_{ij} is the area of particle k intersecting the common faces in between tetrahedra i and j and $\boldsymbol{n}_{ij}$ is the unit vector joining point P_i to P_j.

Derived from the momentum conservation, the surface integral over $\partial\Theta_{ij}$ of the stress vector $-p\boldsymbol{n} - \boldsymbol{\tau}$ applied on Θ_{ij} is equal to zero. As a result, by

decomposing $\partial\Theta_{ij}$ into a fluid/fluid interface $\partial\Theta_{ij}^f$ and a fluid/solid interface $\partial\Theta_{ij}^s$

$$\int_{\partial\Theta_{ij}} -p\boldsymbol{n}\mathrm{d}S + \int_{\partial\Theta_{ij}^f} -\boldsymbol{\tau}\mathrm{d}S + \int_{\partial\Theta_{ij}^s} -\boldsymbol{\tau}\mathrm{d}S = \mathbf{0} \tag{2.36}$$

By assuming that the shear stress in the fluid is negligible, we eventually get the total viscous force on Θ_{ij} as

$$\boldsymbol{F}^{\nu,ij} \simeq \int_{\partial\Theta_{ij}} -p\boldsymbol{n}\mathrm{d}S = A_{ij}^f(p_j - p_i)\boldsymbol{n}_{ij} \tag{2.37}$$

where $A_{ij}^f = S_{ij}^f$ is the area on the fluid domain on the common face between tetrahedra i and j.

Under the additional assumption that the force on sphere k is proportional to the surface γ_{ij}^k of that sphere contained in the subdomain Ω_{ij}, we eventually get

$$\boldsymbol{F}_k^{\nu,ij} \simeq \boldsymbol{F}^{\nu,ij}\frac{\gamma_{ij}^k}{\sum_{k=1}^3 \gamma_{ij}^k}. \tag{2.38}$$

In the end, the fluid forces acting on all the grains of the materials are computed by summing the contributions of all subdomains Ω_{ij}. This completes the DEM-PFV fully couple scheme.

Chapter 3

Micromechanical validation of the representativeness of numerical samples with respect to suffusion

At the microscale, suffusion consists in a rearrangement of particles driven by three elementary mechanisms, namely the detachment of grains from the granular skeleton, their transport through the pore network and possibly their reattachment to the granular skeleton farther away. In order to correctly simulate suffusion, there is a need to use a volume of granular material sufficiently large to simulate these three elementary processes. In this chapter, specific micromechanical tools are developed to investigate the susceptibility of a polydisperse assembly of spherical particles to grain detachment and grain transport. The possibility to provide a quantitative definition of the length scales associated with these two elementary mechanisms is shown thanks to the use of a Discrete Element Method (DEM) coupled with the Pore scale Finite Volume (PFV) fluid grain coupling scheme. The length scale analysis is addressed in this chapter thanks to the use of spatial autocorrelation between force chains and the definition of virtual transport paths. Most of the result presented in this chapter have been published in Wautier et al. (2017).

This chapter is organized as follows. In section 3.1, idealized virtual samples defined as poly-dispersed assemblies of spheres of varying void indices are generated and numerical experiments are considered in the form of drained triaxial tests. Based on the geometrical and micro-mechanical description of the samples under testing, two mesoscales (associated with force transmission and particle transport) are defined and quantified in sections 3.2 and 3.3 respectively.

3.1 Numerical experiments on widely graded samples with DEM

The micromechanical analysis is based on non-cohesive granular materials modeled as poly-disperse assemblies of spheres. The interaction between two particles is modeled by the classical elasto-frictional contact law proposed by Cundall and Strack (1979) and detailed in Section 2.3.1 with parameters of Table 2.1. Given all inter-particle contact forces, the induced particles displacements are then numerically integrated thanks to the DEM open source code YADE (Šmilauer et al., 2015).

3.1.1 Sample definition

Cubic assemblies of spheres are generated randomly with a uniform radius distribution between $r_{\min}$ and $r_{\max} = 10\, r_{\min}$. This particle size distribution is taken such that the smallest particles have a good geometrical chance of

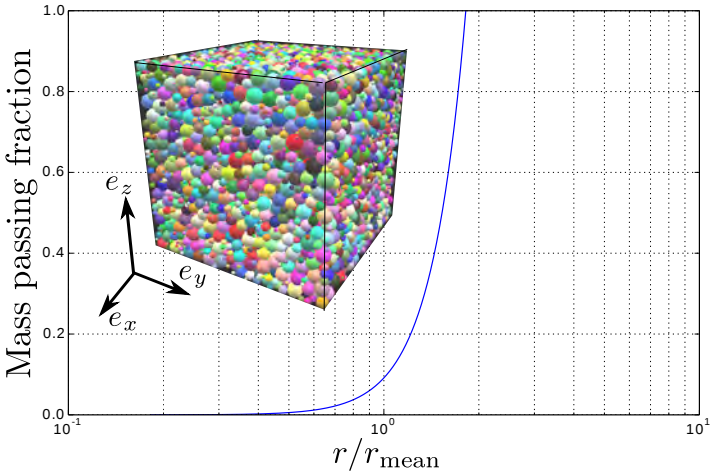

Figure 3.1 – Cumulative distribution in terms of mass corresponding to the generated samples. Particle radii are normalized by the mean radius value. An insight sample visualization is provided.

being transported through the voids created by the largest ones according to Therzaghi's filter rule: $r_{\mathrm{min}} \ll 4\, r_{\mathrm{max}}$ (Terzaghi, 1939). The corresponding cumulative distribution in terms of mass passing fractions is shown in Figure 3.1.

After generating a cloud of 10,000 non-overlapping spheres surrounded by six bounding planes defining a cube, the particles are inflated and allowed to rearrange according to the radius expansion technique. This process is stopped when the confining pressure applied on the bounding planes reaches an intermediate stress of 20 kPa. This stress is chosen such that it is large enough to obtained a jammed state while being still much smaller than the typical stress values that will be imposed in mechanical testing after the sample preparation step. From this point, the internal friction angle is artificially decreased by small steps, making it easier for particles to rearrange. Since the particle radii should be increased to keep the confining pressure constant, this procedure results in a densification process. Three geometrical configurations are generated during this process when the void ratio of the sample reaches the targeted values of 0.8, 0.7 and 0.6. These values were selected such that the resulting three samples exhibit macroscopic behaviors typical of loose, intermediate, and dense sands respectively. Accordingly, they are referred to as *loose sample*, *medium sample* and *dense sample* hereafter. Associated with the cubic grain assemblies thus generated, a Cartesian coordinate system $(\boldsymbol{e}_x, \boldsymbol{e}_y, \boldsymbol{e}_z)$ is defined such that the axis directions coincide

with the edges of the cube. This definition is recalled in Figure 3.5.

3.1.2 DEM simulation of drained triaxial tests

From the resulting forces applied on the bounding walls a macroscopic stress tensor $\boldsymbol{\sigma}$ is computed. The diagonal components σ_{xx}, σ_{yy} and σ_{zz} are obtained by dividing the total normal forces applied on each of the sample faces by their area. As frictionless bounding walls are considered, the off diagonal terms of $\boldsymbol{\sigma}$ are equal to zero. The resulting deviatoric stress q is then derived as

$$\left\{ \begin{array}{rcl} q & = & \sqrt{\frac{3}{2}\boldsymbol{\sigma}_{\text{dev}} : \boldsymbol{\sigma}_{\text{dev}}} \\ \boldsymbol{\sigma}_{\text{dev}} & = & \boldsymbol{\sigma} - \frac{1}{3}\text{Tr}(\boldsymbol{\sigma})\mathbf{1} \end{array} \right. \tag{3.1}$$

where $\mathbf{1}$ stands for the identity tensor and : stands for the double dot contraction product. Soil mechanics conventions are used with compression counted positive.

Likewise, the macroscopic homogeneous strain tensor $\boldsymbol{\varepsilon}$ is defined from the bounding walls displacements. Since no rotations are allowed for the bounding walls, the off diagonal terms of $\boldsymbol{\varepsilon}$ are equal to zero. The volumetric strain is then defined with the trace operator as

$$\varepsilon_v \;=\; \text{Tr}(\boldsymbol{\varepsilon}) = \varepsilon_{xx} + \varepsilon_{yy} + \varepsilon_{zz}. \tag{3.2}$$

A negative strain value correspond to contraction.

After the sample preparation phase, the internal friction angle of the inter-particle contact law (see Figure 2.14) is restored to its initial value of 35°. The same dry drained triaxial test is applied to the three prepared samples. This test consists in two steps:

- First an isotropic confining pressure of $\sigma_0 \;=\; 100\,\text{kPa}$ is applied by allowing the bounding walls to move;
- Then a vertical compression strain rate $\dot{\varepsilon}_{zz} \;=\; -0.01\,\text{s}^{-1}$ is applied up to 20 % of deformation while keeping a constant lateral confining pressure of σ_0; this strain rate is chosen such that the loading can be considered as quasi-static (Hadda, 2006).

The classical deviatoric stress and volumetric strain responses are shown for the three samples in Figure 3.2.

In Figure 3.2, the dense sample is characterized by a dilative behavior after a brief initial contracting phase. The stress response reaches a peak

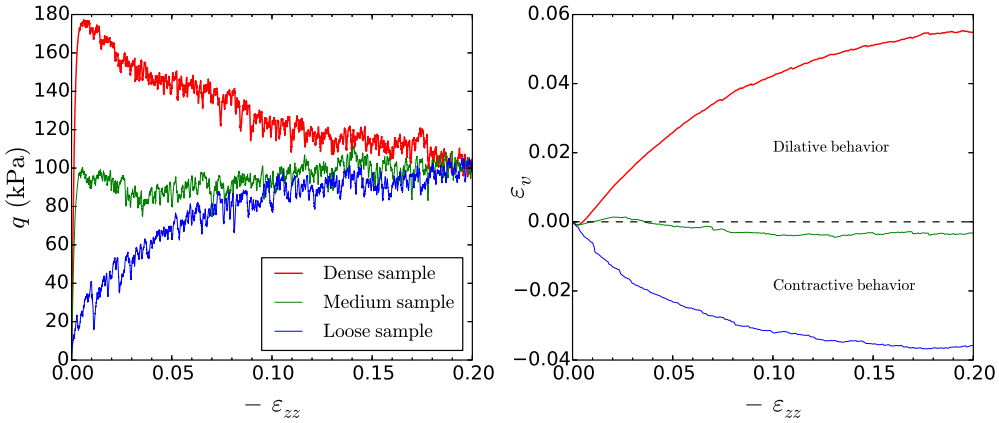

Figure 3.2 – Stress (left) and volumetric (right) responses of the prepared samples of different initial densities during a drained triaxial loading with confining pressure of 100 kPa and vertical strain $|\varepsilon_{zz}| \in [0, 0.2]$

followed by a softening phase. The loose sample is characterized by a contractive behavior and the absence of a stress peak. The medium sample evolves in an isochoric way with a stress peak immediately followed by a plateau. These three mechanical responses are consistent with those classically observed both in the laboratory (Terzaghi et al., 1996) and from discrete numerical simulations (Scholtès et al., 2010; Wang and Li, 2015). Moreover, one can highlight the existence of a unique critical state, as described in the classical critical state theory in soil mechanics (Schofield and Wroth, 1968).

3.2 Mesoscale analysis of force transmission

The microscale analysis of the force network in granular assemblies is underpinned by two governing ideas with respect to grain detachment. The first idea is that the most detachable grains do not transmit important forces. The second idea is that the typical length scale associated with the detachment process should be linked to the distance between the grains transmitting stresses through the granular assembly. As a result, the grains of the three samples presented in the previous section are first divided into two groups based on the force chain definition introduced by Peters et al. (2005). Then the spatial distribution of force chains is investigated using autocorrelation functions (Matheron, 1967; Kanit et al., 2003). This two steps analysis is conducted on the three samples presented in the previous section.

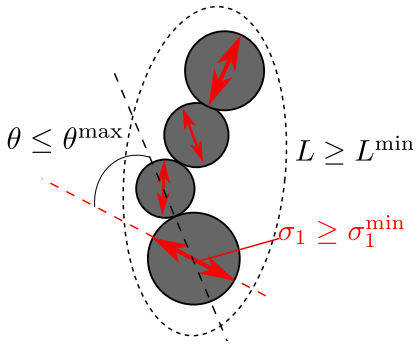

Figure 3.3 – Force chain definition according to Peters et al. (2005) based on the three threshold values $\sigma_1^{\min}$, $\theta^{\max}$ and $L^{\min}$.

3.2.1 Force chains and associated statistics

Force chains[1] are identified according to the same algorithm as Peters et al. (2005) reviewed in Section 2.3.2 of the state of the art. This definition is based on three threshold values recalled in Figure 3.3: the minimum principal stress $\sigma_1^{\min} =< \sigma_1 >$, the maximum deviation angle $\theta^{\max} = 45°$ and the minimum force chain length $L^{\min} = 3$. Before moving forward, a justification of these arbitrary thresholds can be given by performing a sensitivity analysis. In Figure 3.4, the evolution of the number of chained particles is given for different threshold values.

In Figure 3.4, the number of identified chained particles remains constant for $\sigma_1^{\min}$ smaller or greater than the mean principal stress $<\sigma_1>$ but around this particular value, a drop is observed. This behavior is typical of the existence of two grain populations (loose and stressed grains) and justifies *a posteriori* the used threshold value $\sigma_1^{\min} =< \sigma_1 >$ in Peters's definition. This value is also consistent with the alternative definition of the strong and weak contact networks (Radjai et al., 1998). For $\theta^{\max}$ and $L^{\min}$ the justification of the thresholds is less clear as the number of chained particles is an increasing function of $\theta^{\max}$ and a decreasing function of $L^{\min}$. Choosing $L^{\min} = 3$ corresponds to the minimum number of grains to define indeed a structure with non-trivial internal degrees of freedom. And choosing $\theta^{\max} = 45°$ corresponds to the largest angle that avoid to define force chains with geometric deviation larger than 90° between two successive contact orientations.

Based on these three threshold values, force chains can be identified in the three samples for several strain values. A typical visualization of the force chains in the dense sample can be found in Figure 3.5. At the beginning of

[1]Following a discussion with the PhD jury, it appears that the wording *stress chain* should be preferred since the definition is based on the stresses and not forces.

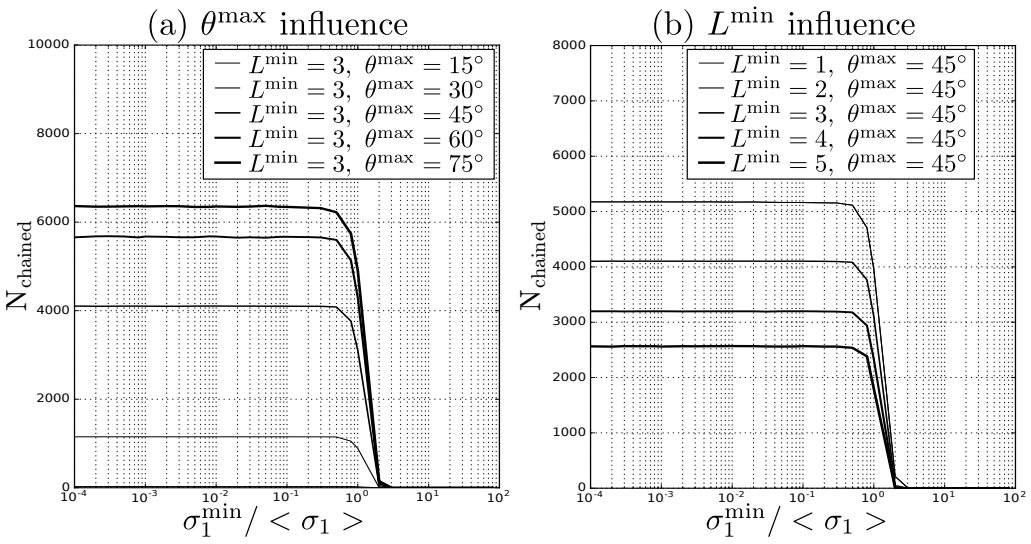

Figure 3.4 – Evolution of the number of chained particles for different threshold values. This sensitivity analysis is carried out for the dense sample under an isotropic confining pressure of 100 kPa ($\varepsilon_{zz} = 0$).

the triaxial test ($\varepsilon_{zz} = 0$), the force chains are distributed in an isotropic way which is consistent with the fact that no principal direction of loading exist. Once the deviatoric loading is applied, the force chains tend to align in the vertical direction of the macroscopic principal stress which is consistent with the previous results obtained in 2D with the combined use of fabric tensors and contact forces network (Radjai et al., 1998; Iwashita and Oda, 1998, 2000; Majmudar and Behringer, 2005).

In addition to these qualitative observations, some of the force chains' statistical properties can be analyzed. In Figure 3.6 the percentage of chained particles, the total number of force chains and the mean length of a force chain are plotted for the different samples during the triaxial test presented in the previous section.

As pointed out in Peters et al. (2005), only a small fraction of the total number of particles is involved in force chains. At the beginning of the triaxial test, the fraction of chained particles ranges from 23 to 31 % depending on the sample density (Figure 3.6 (a)). The higher the density, the more particles are involved in force chains. This should be related to the fact that for a dense sample the high number of contacts between particles enables a homogeneous distribution of the stress inside the sample. Conversely, a loose sample presents a more limited number of contacts, which results in the concentration of the stress onto a more limited number of particles. As the

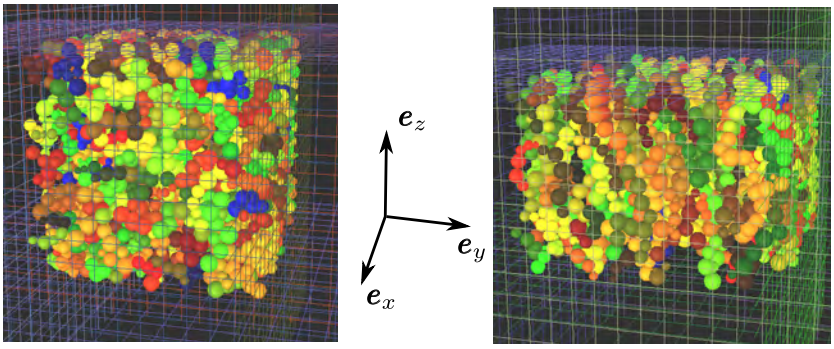

(a) $\varepsilon_{zz} = 0\%$ (b) $\varepsilon_{zz} = 20\%$

Figure 3.5 – Force chains visualisation for the dense sample under an isotropic confining pressure of 100 kPa (a) and at the end of the triaxial test (b).

deviatoric loading starts, force chains disappear, as illustrated in Figure 3.6 (a) and (b) for the dense and medium samples, respectively. After merely 10 % of strain, a critical state is reached with only 24 - 25 % of particles involved in force chains.

The evolution of the mean length of a force chain gives information on the ability of a material to withstand an incremental load. Indeed, granular assemblies containing long force chains are able to sustain high stress levels because most of the stiffness will result from the normal contact stiffness k_n (see Figure 2.14). In contrast, for granular assemblies containing short force chains the overall stiffness is more influenced by the tangential contact stiffness $k_t \leq k_n$ and the friction angle ϕ (see Figure 2.14). As a result, Figure 3.6 (c) accounts for the three typical macroscopic stress behaviors presented in dots. In particular, the softening experienced by the dense sample can be linked to the destruction of long force chains.

Overall, the three graphs in Figure 3.6 are consistent with the existence of a common critical state with respect to these meso-structures (Zhu et al., 2016a) given that the curves corresponding to the different samples collapse on a single curve for large strain values.

Another interesting statistical property of the chained particles with respect to grain detachment is the probability density that a particle of a given radius belongs to a force chain. The corresponding probability density for the dense sample in the isotropic initial state ($\varepsilon_{zz} = 0$) is shown in Figure 3.7. Probability densities corresponding to the two other samples and other axial strain levels are not shown as no noticeable evolutions have been observed. For comparison purposes, the uniform probability density for a grain of a given radius to be part of the different samples is plotted as a dashed line. It

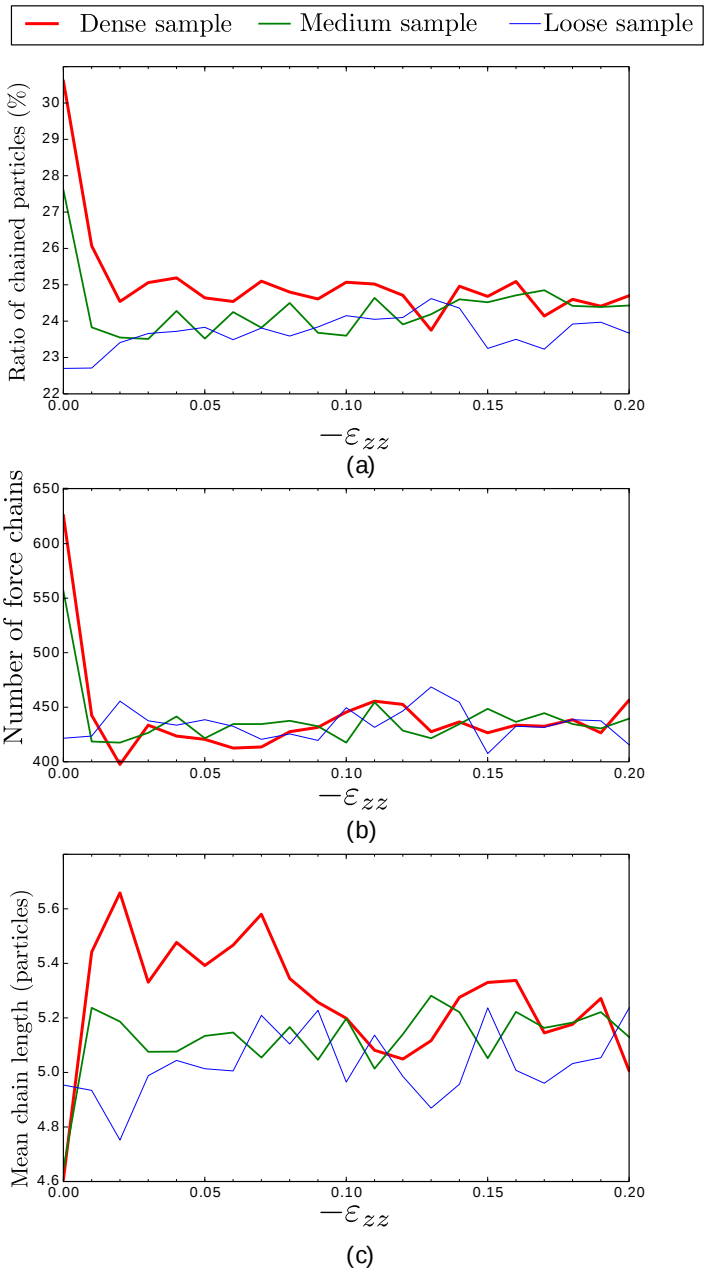

Figure 3.6 – Strain evolution of the ratio of chained particles (a), the number of force chains (b) and the mean chain length (c) for the three samples considered during the triaxial test.

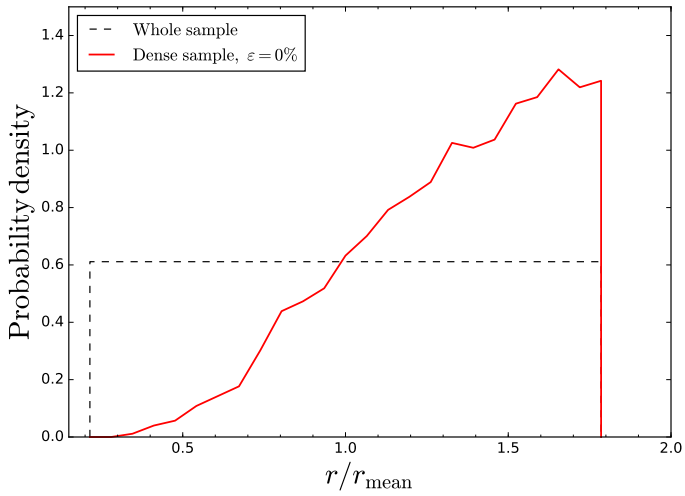

Figure 3.7 – Probability density for a grain of a given radius to be part of a force chain belonging to the dense sample in the isotropic initial state ($\varepsilon_{zz} = 0$). The dashed lines correspond to the uniform probability density for a grain of a given radius to be part of the whole sample.

should be noted here that the probability density functions are not bounded, but their integral over the whole range of radii is equal to 1.

In Figure 3.7, the probability densities corresponding to chained particles are very different from the reference horizontal probability density corresponding to Figure 3.1. Indeed, force chains are mainly composed of large particles (Voivret et al., 2009; Cambou et al., 2013) and particles smaller than $0.4\,r_{\text{mean}}$ are rarely involved in force chains. The dual comment is that the finest particles are the least loaded particles of the samples and therefore the most sensitive to internal fluid flows. Fine particles are also good candidates for being transported over large distances, which will be estimated in Section 3.3. However, no sharp transition is visible in the probability densities in Figure 3.7. As a result, no clear radius threshold exists between the loose particles of a granular assembly and the primary fabric responsible for stress transmission, as proposed in many suffusion susceptibility criteria. This result is consistent with the recent findings of To et al. (2015), proving the existence of an overlapping zone in the PSD curve in which a grain can either belong to the loose or the coarse phase of the resulting granular assembly.

As already mentioned, the probability density functions shown in Figure 3.7 do not depend on the strain level, which can result either from very stable force chains or from stable statistic rearrangements of chained particles. In

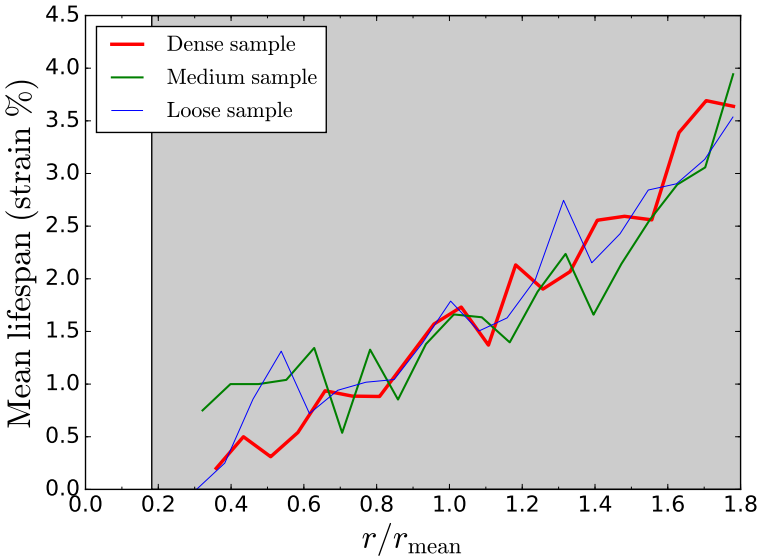

Figure 3.8 – Averaged lifespans of the chained particles existing in the isotropic state ($\varepsilon_{zz} = 0$) in terms of axial strain level $|\varepsilon_{zz}|$. The gray domain in the background corresponds to the range of radii for all the particles.

order to chose between these two options, the lifespan of a chained particle during the triaxial loading is introduced as the width of the strain interval during which this particle is continuously identified as belonging to force chains. In Figure 3.8, the average lifespan of the chained particles initially identified in the three samples under the isotropic confining pressure σ_0 is shown with respect to the grains' radii.

As seen in Figure 3.8, the average lifespan increases with the size of the particles from less than 1% up to 4 %. The force chains containing large particles are therefore less sensitive to an increase in the axial strain and have a longer lifespan than the force chains composed of small particles. However, it can be noted that even for the largest particles, the average lifespan remains limited to a few percent of strain. Overall, it can be concluded that the force chains are constantly rearranging to cope with the deviatoric loading. This dynamic process affects all the particles whatever their radii, but the largest chained particles are more stable than their smaller counterparts. The comparison between the three graphs in Figure 3.8 highlights the fact that the initial void ratio does not seem to have a strong influence on this rearrangement process.

3.2.2 Force chain spatial autocorrelation and associated length scales

Even if the statistical properties shown so far are able to describe several salient features of the chained particles, they do not capture the spatial distribution of the force chains. Based on the theoretical work of Matheron (1967); Lantuejoul (1991); Kanit et al. (2003), the spatial distribution of the chained particles can be described using autocorrelation functions.

Autocorrelation function definition

If Ω denotes the domain occupied by the chained particles of a given sample of volume V, the autocorrelation function C is defined for any vector $\boldsymbol{h} = (h_x, h_y, h_z)$ as the joint probability that a point $\boldsymbol{x}$ and the translated point $\boldsymbol{x} + \boldsymbol{h}$ simultaneously belong to chained particles (Matheron, 1967):

$$C : \left\{ \begin{array}{lcl} \mathbb{R}^3 & \mapsto & \mathbb{R} \\ \boldsymbol{h} & \mapsto & \mathbb{P}\{\boldsymbol{x} \in V \ / \ \boldsymbol{x} \in \Omega, \ \boldsymbol{x} + \boldsymbol{h} \in \Omega\} \end{array} \right. . \tag{3.3}$$

For $\boldsymbol{h} = 0$, the autocorrelation $C(0)$ corresponds to the chained particles volume fraction as $C(0) = \mathbb{P}\{\boldsymbol{x} \in \Omega\}$, and for $||\boldsymbol{h}|| \to \infty$, $C(\boldsymbol{h})$ converges towards $C(0)^2$ because of probability independence (no infinite range correlation exist in disordered media). Thus a normalized autocorrelation function $\tilde{C}$ can be introduced as

$$\tilde{C}(\boldsymbol{h}) \ = \ \frac{C(\boldsymbol{h}) - C(0)^2}{C(0) - C(0)^2}. \tag{3.4}$$

When $||\boldsymbol{h}||$ varies from 0 to ∞, $\tilde{C}$ varies from 1 to 0 and the rate of decrease characterizes the microstructure autocorrelation distance. A quantitative definition of this autocorrelation distance can be derived from the introduction of an approximate expression as

$$\tilde{C}_{\text{fit}}(\boldsymbol{h}) \ = \ \exp\left(-\sqrt{\left(\frac{h_x}{L_x}\right)^2 + \left(\frac{h_y}{L_y}\right)^2 + \left(\frac{h_z}{L_z}\right)^2} \right), \tag{3.5}$$

where L_x, L_y and L_z are three lengths scales that capture the decreasing rate of $\tilde{C}$. Even though this expression is empirical, the initial and final theoretical values of $\tilde{C}$ are recovered, the principal directions of geometrical anisotropy imposed by the mechanical loading along the axis x, y and z are respected (Radjai et al., 1998), and as predicted by the theoretical work of

Matheron (1967) and reviewed in Corson (1974) and in Jin et al. (2016), the initial tangent of the fit is not equal to zero and close to the specific surface of the samples. In 3D, and in case the autocorrelation function C depends only on $||\boldsymbol{h}||$, the initial tangent is

$$\left.\frac{\mathrm{d}C}{\mathrm{d}||\boldsymbol{h}||}\right|_{||\boldsymbol{h}||=0} = -\frac{s}{4}, \tag{3.6}$$

where s is the specific surface area defined as the ratio between the surface of the grains and the total volume of the sample (Jin et al., 2016).

A refinement of the definition of the three length scales introduced above can be derived from integral range theory (Matheron, 1975; Kanit et al., 2003). It was shown that the variance of a homogenized property Z of a biphasic material computed over a volume V is given by

$$D_Z^2(V) \;=\; \phi(1-\phi)\,(\Delta Z)^2\,\frac{A_3}{V} \tag{3.7}$$

where ΔZ is the property contrast between the two-phases of the material, ϕ is the material porosity and A_3 is the integral range defined as

$$A_3 \;=\; \iiint_{\mathbb{R}^3} \tilde{C}(\boldsymbol{h})\;\mathrm{d}h_x\mathrm{d}h_y\mathrm{d}h_z. \tag{3.8}$$

In our case, Z is simply the indicator function associated with force chains ($Z(\boldsymbol{x}) = 1$ if $\boldsymbol{x} \in \Omega$, 0 otherwise) and ϕ the porosity computed only by considering chained particles. The numerical estimation of A_3 in three dimensions is however out of reach in practice for two reasons:

- the numerical assessment of each value $\mathbb{P}\{\boldsymbol{x} \in \Omega \cap \boldsymbol{x}+\boldsymbol{h} \in \Omega\,\forall \boldsymbol{x} \in V\}$ relies on a large number of random samplings. Gathering enough values $\tilde{C}(\boldsymbol{h})$ for $\boldsymbol{h} \in \mathbb{R}^3$ to integrate $\tilde{C}$ is thus too expensive;
- moreover, as $\tilde{C}$ is integrated on $\mathbb{R}^3$, small numerical errors would result in non-integrability.

This is the reason why the fitted integrable function $\tilde{C}_{\mathrm{fit}}$ is used instead of $\tilde{C}$. In addition, to speed up the computation of $\tilde{C}(\boldsymbol{h})$, the central limit theorem is used. For a given $\boldsymbol{h}$ let us consider the random variable $Z_{\boldsymbol{h}}(\boldsymbol{x}) = \mathbb{1}(\boldsymbol{x} \in \Omega \text{ and } \boldsymbol{x}+\boldsymbol{h} \in \Omega)$ where $\mathbb{1}$ is the indicator function. For a large number N of random samplings, the central limit theorem predicts that the associated distribution converges toward a normal distribution whose average is equal to $\tilde{C}(\boldsymbol{h})$ and whose 95% confidence interval is

$$\left[\tilde{C}(\boldsymbol{h}) - 1.96\sqrt{\frac{\tilde{C}(\boldsymbol{h})(1-\tilde{C}(\boldsymbol{h}))}{N}}\;;\;\tilde{C}(\boldsymbol{h}) + 1.96\sqrt{\frac{\tilde{C}(\boldsymbol{h})(1-\tilde{C}(\boldsymbol{h}))}{N}}\right]. \tag{3.9}$$

For a fixed width δ of this interval, a controlled approximation of $\tilde{C}(\boldsymbol{h}) \simeq \sum_{n=1}^{N} Z_{\boldsymbol{h}}(\boldsymbol{x}_n)$ is thus obtained as soon as

$$1.96\sqrt{\frac{\sum_{n=1}^{N} Z_{\boldsymbol{h}}(\boldsymbol{x}_n)\left(1-\sum_{n=1}^{N} Z_{\boldsymbol{h}}(\boldsymbol{x}_n)\right)}{N}} < \frac{\delta}{2}. \tag{3.10}$$

With use of these two tricks, the integral range is approximated as a function of L_x, L_y and L_z:

$$A_3 \simeq A_3^{\text{fit}} \;=\; 8\pi\, L_x\, L_y\, L_z. \tag{3.11}$$

Thus a more physical definition of the autocorrelation lengths can be given as

$$\begin{cases} L'_x &= 2\pi^{1/3}\, L_x \\ L'_y &= 2\pi^{1/3}\, L_y \\ L'_z &= 2\pi^{1/3}\, L_z \end{cases}. \tag{3.12}$$

With this definition of the autocorrelation lengths, the integral range related to the chained particles can be seen as a volume of dimensions (L'_x, L'_y, L'_z). Combined with Equation (3.7), this gives a quantitative definition of the representative elementary volume (REV) associated with force transmission within a given sample as a multiple of the integral range. As a result, this also specifies the REV associated with grain detachment processes, namely a small volume which is structurally entirely typical of the whole material on average and for which the fluctuations due to the imposed boundary conditions can be ignored (Hill, 1963).

It is worth noting here that the integral range can be seen as a virtual unit cell inside which the microstructure is highly correlated. The whole grain assembly may therefore be seen as a collection of unit cells, the shape of which depends on the shape of the autocorrelation $C(\boldsymbol{h})$.

Autocorrelation distances between chained particles during triaxial loading

The autocorrelation functions corresponding to 0, 5, 10 and 20 % of deformation are plotted in Figure 3.10 for the dense sample together with equation (3.5). Analysis is restricted to the principal directions of loading $\boldsymbol{e}_x$, $\boldsymbol{e}_y$ and $\boldsymbol{e}_z$. Given that the samples used in this study are surrounded by bounding planes, the boundary particles tend to crystallize in the vicinity of these

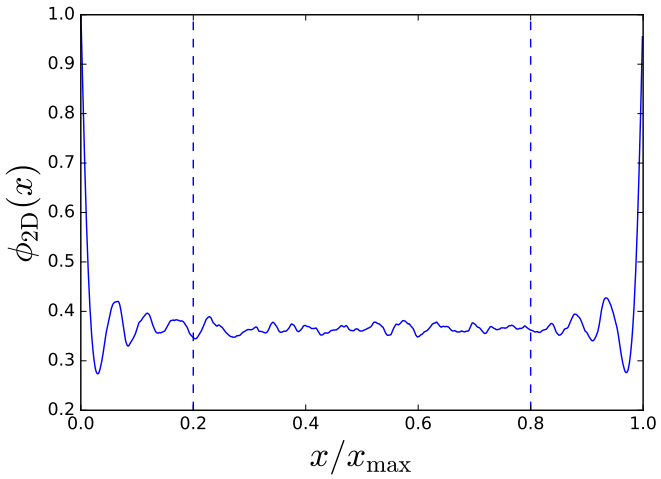

Figure 3.9 – 2D porosity $\phi_{2D}(x)$ computed in the x direction for the dense sample in the initial isotropic state ($\varepsilon_{zz} = 0$). The central zone of the sample used to compute spatial autocorrelation functions is shown by vertical dashed lines.

planes. This effect was highlighted in Reboul et al. (2008) for the local porosity. In Figure 3.9, this crystallization is shown for the dense sample in the initial isotropic state ($\varepsilon_{zz} = 0$). In this figure, the two dimensional porosity $\phi_{2D}(x)$ is computed in the plane $(\boldsymbol{e}_y, \boldsymbol{e}_z)$ for varying position x.

In Figure 3.9, $\phi_{2D}(x)$ is equal to 1 on the bounding walls as grains/wall contacts are limited to points. While going away from the walls, the porosity decreases with oscillations, the period of which corresponding to the typical grain size. In a central zone corresponding to $x/x_{max} \in [0.2, 0.8]$, the crystallization effect of the bounding walls disappears and the porosity remains constant. As a result, the autocorrelation analysis performed in the following is restricted to the core of the samples to get rid of these boundary effects (effective lengths of 0.8 times the total dimensions of the sample are adopted).

In the initial state, the autocorrelation points for $\boldsymbol{h} \propto \boldsymbol{e}_x$ and $\boldsymbol{h} \propto \boldsymbol{e}_z$ cannot be distinguished. Accordingly, the autocorrelation lengths L'_x and L'_z are very similar in this case, which is consistent with the fact that under the isotropic initial confining pressure the force chains tend to follow an isotropic distribution, as illustrated in Figure 3.5. In the final state, the autocorrelation function $\tilde{C}$ converges toward 0 much more slowly in the z direction than in the x direction. This is consistent with the fact that the force chains tend to align along the vertical principal direction of loading as seen in Figure

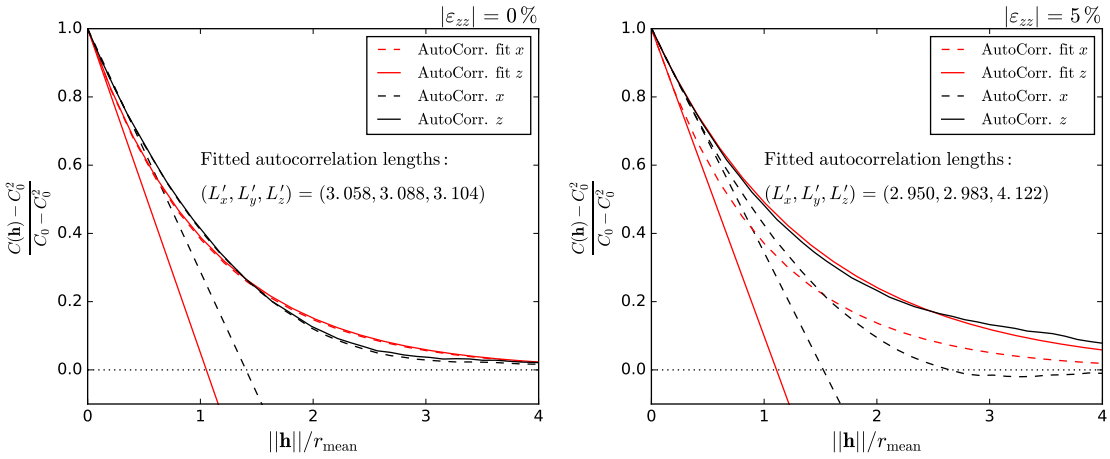

Figure 3.10 – Rescaled autocorrelation functions computed for the dense sample at two strain levels ($|\varepsilon| \in \{0, 0.05\}$). The plot of $\tilde{C}$ is restricted to $\boldsymbol{h} \propto \boldsymbol{e}_x$ and $\boldsymbol{h} \propto \boldsymbol{e}_z$. The corresponding fitted autocorrelation functions $\tilde{C}_{\text{fit}}$ are shown and the estimated autocorrelation lengths L'_i are given. The initial asymptote corresponding to Equation (3.6) is shown (dashed) together with the mean asymptote derived from the expression of $\tilde{C}_{\text{fit}}$ (solid).

3.5. Thus the autocorrelation lengths L'_x and L'_z are able to account for this anisotropic evolution of the microstructure. However, the proposed fit systematically overestimates the horizontal autocorrelation and cannot account for the negative values obtained for the horizontal autocorrelation function for $|\varepsilon_{zz}| \geq 5\%$. This latter *anti-correlation* feature should be related to an exclusion zone around force chains in the horizontal plane located at about $3\,r_{\text{mean}}$.

More comprehensively, the three autocorrelation lengths L'_x, L'_y and L'_z are plotted against the axial strain for the three samples in Figure 3.11 (a). A similar analysis is performed for the non-chained particles in Figure 3.11 (b) and for the whole set of particles in Figure 3.11 (c).

In Figure 3.11 (a), as the horizontal autocorrelation lengths remains more or less constant for all the samples around $3\,r_{\text{mean}}$ for the chained particles, the vertical autocorrelation length increases significantly between the initial and the final state. For the loose and the medium samples, the increase is monotonous whereas the vertical autocorrelation length for the dense sample reaches a peak value around $4.5\,r_{\text{mean}}$ for the chained particles. For $|\varepsilon_{zz}| > 15\%$, a critical state is reached as L'_z stabilizes for all the samples around $4\,r_{\text{mean}}$ for the chained particles. At this stage, the spatial distribution of chained particles can be characterized by a small volume, the size of which

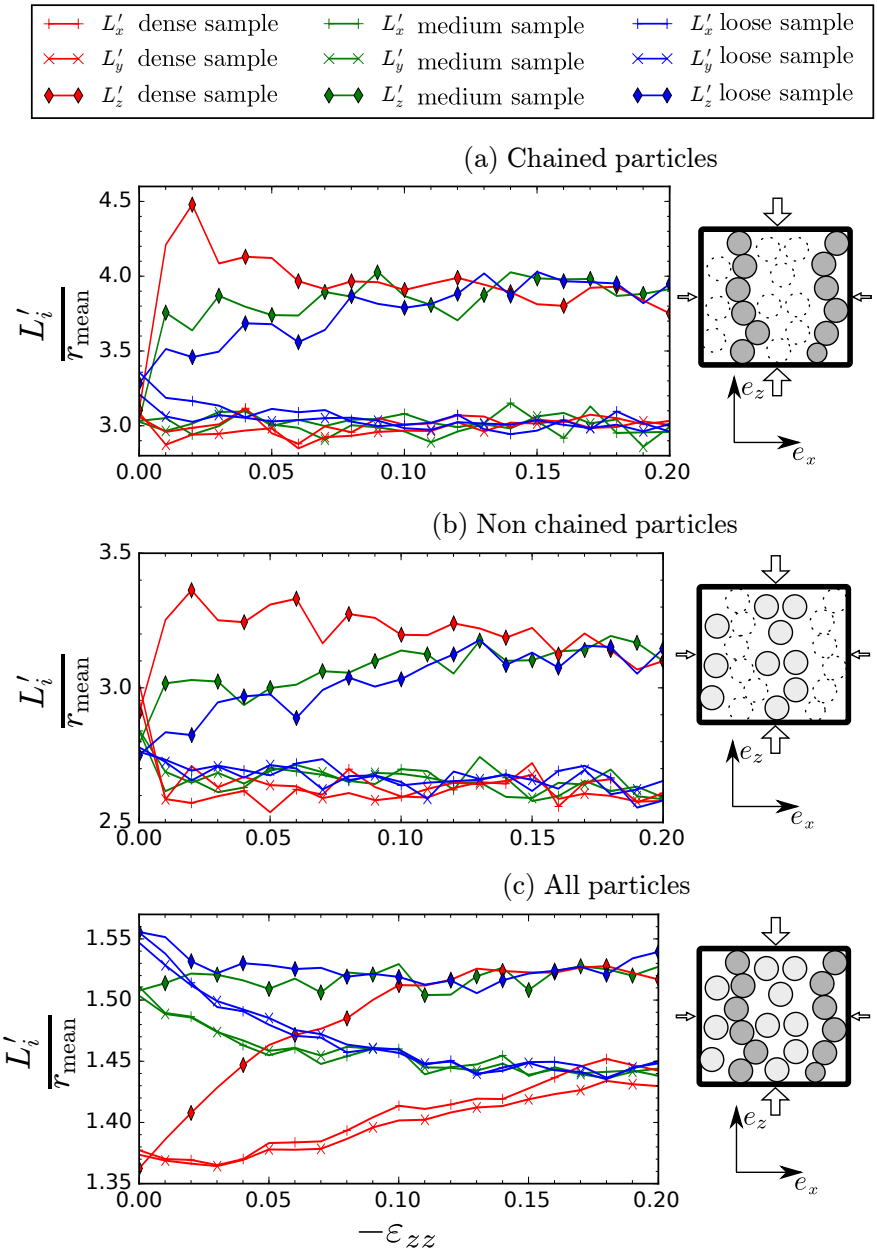

Figure 3.11 – Load induced anisotropy through the evolution of the three autocorrelation lengths L'_i ($i \in \{x, y, z\}$) during the drained triaxial loading. Autocorrelation analysis is restricted either to particles belonging to force chains (a), to particles not belonging to force chains (b) or to all particles (c).

is

$$(L'_x, L'_y, L'_z) \;=\; (3\,r_{\text{mean}}, 3\,r_{\text{mean}}, 4\,r_{\text{mean}}). \tag{3.13}$$

With reference to Equation (3.7), this gives the order of magnitude of the REV associated with the stress distribution within the different samples. For the sake of illustration, the volume fraction occupied by chained particles for the dense sample in the isotropic compression state is 30 %. An estimation of this volume fraction with a variance of 10^{-4} according to Equation (3.7) would require a volume V equal to roughly 2,000 times bigger than A_3 corresponding to a REV of dimensions $(38\,r_{\text{mean}}, 38\,r_{\text{mean}}, 50\,r_{\text{mean}})$ which is similar to the total size of the samples used in this chapter.

In Figure 3.11 (b) the evolution of the autocorrelation lengths computed for the non-chained particles is qualitatively similar to the one corresponding to chained particles. This argues in favor of the fact that the spatial distribution of loose particles can be effectively described by the spatial distribution of chained particles. However, the autocorrelation lengths L'_i are slightly smaller when considering the non-chained particles instead of the chained ones which could be related to the slight misfit observed in Figure 3.10 with respect to the horizontal autocorrelation for $|\varepsilon_{zz}| > 0\%$. When looking at the transient evolution of L'_z with respect to ε_{zz}, it can be noted that the dense sample is characterized by an initial increase in the vertical autocorrelation followed by a decrease toward the critical state. This can be closely related to the macroscopic response observed in Figure 3.2. Indeed the increase in the vertical autocorrelation corresponds to a lengthening of the force chains along the vertical direction which accounts for the initial hardening of the dense sample. The following decrease in the vertical autocorrelation accounts for the destruction of force chains and thus to the stress softening observed for the dense sample. For the medium and the loose samples, L'_z increases more or less continuously until reaching the critical state. This is consistent with the fact that these two samples do not experience any softening. In the end of the triaxial test, the three samples exhibit a common mesostructure associated with force chains whose size is characterized by equation (3.13). This provides a quantitative definition of the force chain pattern existing in the critical state as pointed out by Zhu et al. (2016a).

When considering the whole set of particles, the anisotropy with respect to z direction is still visible but the shapes of the curves are completely different from those obtained while considering only the force chains (Fig 3.11 (c)). Indeed they capture quite well the volumetric behavior of the different samples observed in Figure 3.2.

3.3 Mesoscale analysis of transport properties

The microscale analysis of the pore space is critical to assess the occurrence of grain transport. In this section, a simplification of the void phase of granular materials based on pore networks is presented. The geometrical and topological properties of these networks are used to propose estimations of the expected travel distances in the three samples introduced in Section 3.1.

3.3.1 Pore network definition

In the wake of the previous work of Reboul et al. (2008) and Vincens et al. (2015) for the transport of spherical cohesionless particles, the pore space can be reduced to the definition of a pore network. A regular triangulation of a spheres assembly (Edelsbrunner and Shah, 1996) is built from YADE software. This particular type of triangulation has the important property that all the edges of its dual tessellation belong to the pore space (Chareyre et al., 2012; Vincens et al., 2015).

This tessellation is the key ingredient in defining a pore network composed of pores (the nodes of the graph) and constrictions (the edges of the graph). The pores are defined following the level 0 analysis introduced in Reboul et al. (2008). Their positions are defined at the center of each tetrahedron of the regular triangulation in terms of power distances and their radii as the radius of the largest interior sphere in the associated tetrahedra. The constrictions are modeled as cylinders joining two adjacent pores (Reboul et al., 2008) and their radii are defined as the radius of the largest interior circle on the common face of the two tetrahedra defining the constriction. The definition of the pore and constriction radii is shown in Figures 3.12 (a) and (b). For the sake of illustration, three-dimensional visualizations of the pore network associated with two simple grain assemblies are shown in Figures 3.12 (c) and (d). It should also be noticed that the considered triangulation is built while considering all the particles, including the potentially migrating particles identified thanks to the force chains analysis. This choice is motivated by the idea that only a few non-chained particles will actually be detached under the action of a fluid, leading to few changes in the initial pore network. If this hypothesis is reasonable for the granulometry considered in this chapter, it becomes questionnable when larger fine particle contents are considered.

The bounding planes surrounding the samples locally induce a very different microstructure from that observed in the core of the samples (see Figure 3.9). Indeed, close to the boundary, a significant number of tetrahedra are found to be flat, which results in the estimation of very huge pore

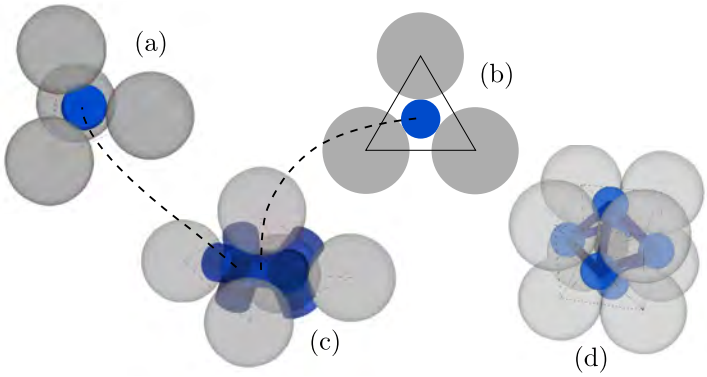

Figure 3.12 – Visualization of a tetrahedron with its inscribed pore sphere (a), a tetrahedron face with its inscribed constriction circle (b), a simple assembly of four spheres with the associated pore network (c), and an assembly of nine sphere with the associated pore network (d). In these figures, the spherical particles are represented in grey, the pore by blue spheres and the constrictions between two pores by blue cylinders. The tetrahedra resulting from the regular Delaunay triangulation are represented with black lines joining the different particles centers.

and constrictions radii. Consequently, as for the computation of autocorrelation functions, the pore network is only defined on a centered subvolume fraction of 0.8^3. A visualization of the pore network for the dense sample at the beginning and the end of the triaxial test is given in Figure 3.13.

In this figure the constrictions are represented by grey-scaled cylinders linking two pore centers. The lighter the cylinders, the larger the constrictions. The whole pore network is visible in snapshots (a_i) and (b_i) in Figure 3.13. The network is very dense and enables many possible paths connecting the different pores of the sample. To show only sufficiently large constrictions that allow particle transport, a radius threshold is applied. The two snapshots (a_{ii}) and (b_{ii}) correspond to a radius threshold $r = 0.3\, r_{\text{mean}}$, and the two snapshots (a_{iii}) and (b_{iii}) correspond to a radius threshold $r = 0.5\, r_{\text{mean}}$. Many constrictions larger than $0.3\, r_{\text{mean}}$ are still connected together which is no longer the case for constrictions larger than $0.5\, r_{\text{mean}}$ that are isolated from one another. These features give an idea of expected transport in the pore space for particles of different radii. The comparison between Figure 3.13 (a) ($|\varepsilon_{zz}| = 0\%$) and Figure 3.13 (b) ($|\varepsilon_{zz}| = 20\%$) highlights the fact that the number of large constrictions increases between the beginning and the end of the triaxial test for the dense sample, which is consistent with its dilative behavior observed in Figure 3.2.

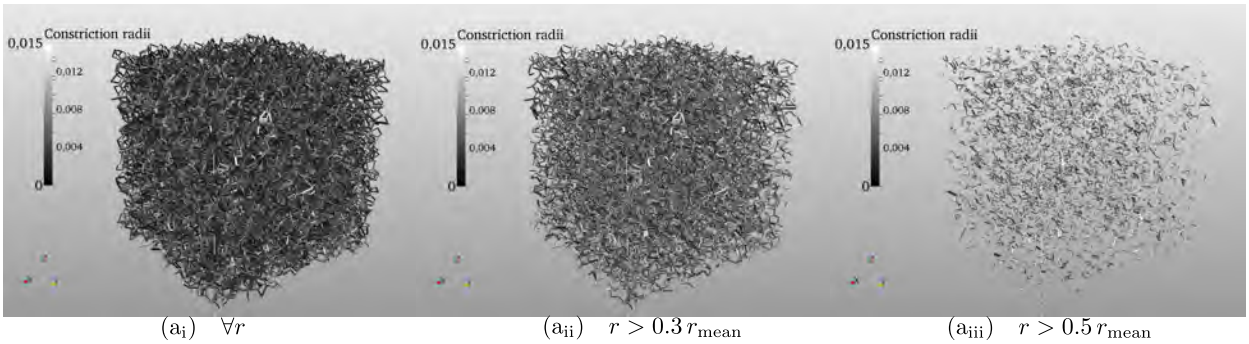

(a_i) $\forall r$ (a_{ii}) $r > 0.3\, r_{mean}$ (a_{iii}) $r > 0.5\, r_{mean}$

(a) $|\varepsilon_{zz}| = 0\%$

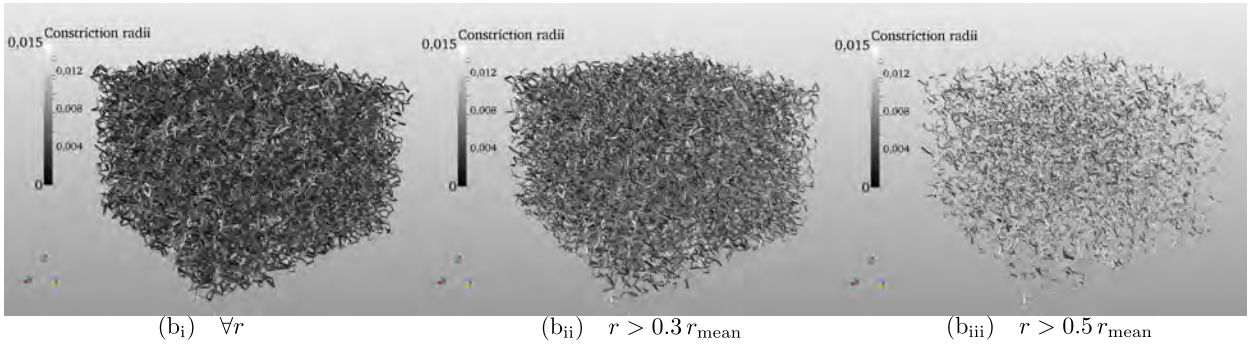

(b_i) $\forall r$ (b_{ii}) $r > 0.3\, r_{mean}$ (b_{iii}) $r > 0.5\, r_{mean}$

(b) $|\varepsilon_{zz}| = 20\%$

Figure 3.13 – Three dimensional visualization of the dense sample pore network under the initial isotropic loading (a) and after 20 % of deformation (b). Only constrictions are represented thanks to cylinders. The lighter the constrictions, the larger their radii. On the left, all constrictions are visible. In the middle, a radius threshold of $0.3\, r_{mean}$ is applied. On the right, a radius threshold of $0.5\, r_{mean}$ is applied.

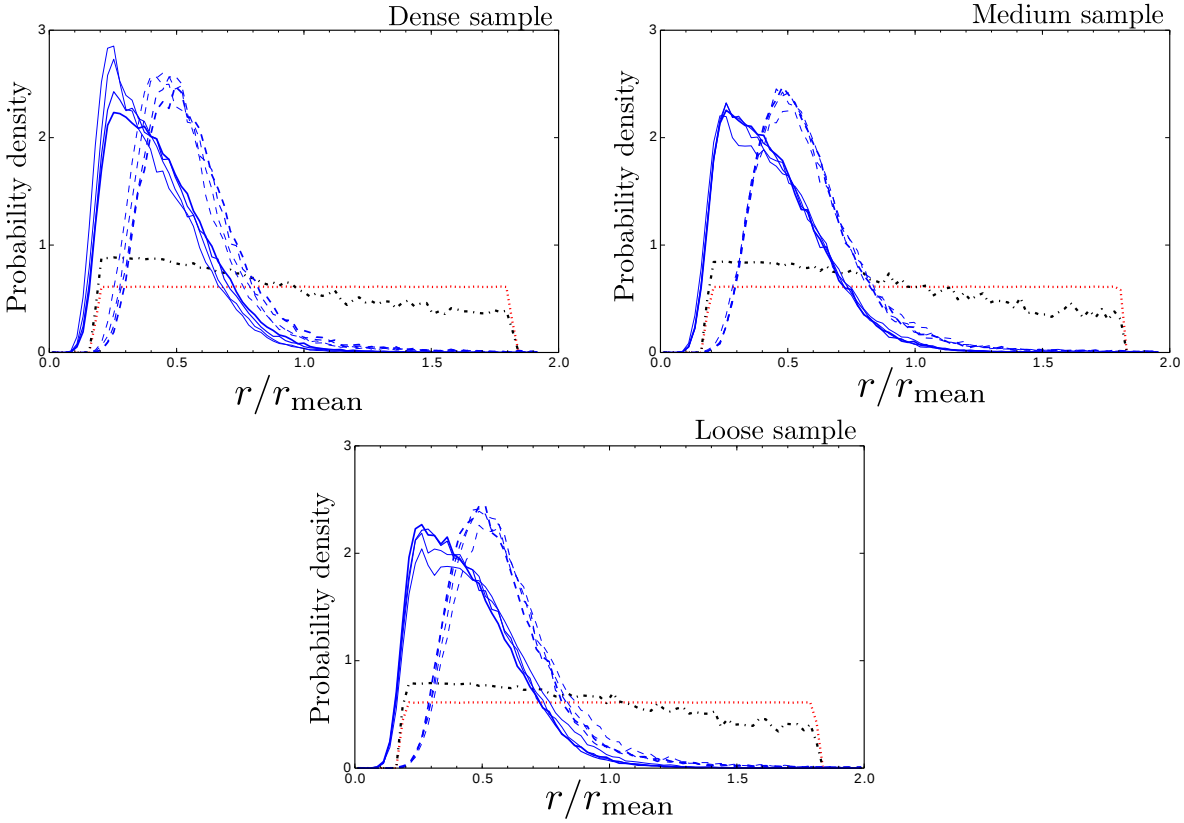

Figure 3.14 – Probability density for a pore (dashed blue), a constriction (solid blue), a grain (dotted red) or a non-chained grain (dash-dotted black) to be of a given radius. The three graphs correspond to the three samples used in this study. The line thickness corresponds to the strain level $|\varepsilon_{zz}| \in \{0, 0.05, 0.1, 0.2\}$ during the triaxial test. The thicker the line, the larger the strain.

3.3.2 Statistical identification of potentially transportable particles

From the pore network definition, the probability densities corresponding to pore and constriction radii are computed and plotted in Figure 3.14 for the three samples considered at four strain levels. To identify whether some particles of the sample could be transported within the pore space, the density probabilities that a grain and a non-chained grain would be of a given radius (see Figure 3.7) are also reported in Figure 3.14.

For every sample in Figure 3.14, the pore and the constriction probability density functions (pdfs) follow single-mode distributions around $r =$

$0.25\,r_{\text{mean}}$ and $r = 0.5\,r_{\text{mean}}$, respectively. Since the constriction mode value ($r = 0.2\,r_{\text{mean}}$) is significantly smaller than the pore value ($r = 0.5\,r_{\text{mean}}$), constriction sizes control the transport of particles. For the three samples, the comparison between the constriction and the grain pdfs highlights that a large number of grains are small enough to be transported through the pore network. An even larger fraction of the non-chained grains is concerned.

While observing how the strain of the pore and constriction probability densities evolve, the contractive/dilative behavior observed in Figure 3.2 is recovered. For the dense sample, the probability densities are shifted toward larger radius values, which is related to an overall increase of the pore space volume. On the contrary, for the medium and the loose samples, the probability densities are shifted toward slightly smaller radius values, which accounts for a decrease in the pore space volume.

3.3.3 Mean travel distances and associated length scales

Even though many particles are identified in Figure 3.14 as potentially detachable by analyzing the statistical properties of the pore network, determining the distance that a particle of a given radius can cover requires knowing the spatial distribution of pore and constriction radii. This distribution is accessible from the graph description of the pore space (see Figure 3.13). As constriction radii are smaller than their pore counterparts (Figure 3.14), only the constriction radii are considered while assessing the possibility for a grain to move from one pore to another.

Pore-to-pore transport criteria

In a granular material subjected to an internal flow, particle transport is not isotropic and is governed by the direction and intensity of the flow through the pore space. While keeping in mind the fact that in hydraulic structures, the fluid flow is perpendicular to the principal stress direction, the transport properties of the pore networks defined for the three samples are considered with a horizontal fluid flow imposed by a small pressure gradient of 10 Pa $\ll \sigma_0$ between the sample boundaries in the x direction. This fluid/-grain problem is addressed using the DEM/PFV model detailed in section 2.4.2. In this section it should be underlined that the PFV scheme is used as a *one way coupling* only to localize the macroscopic gradient onto the local pore network. An rougher option to the use of the PFV model to obtain a local pressure map would be simply to assume a linear decrease of the pressure from the upstream to the downstream sides of the sample. This option disregard local fluctuations but has the advantage that it does not need to

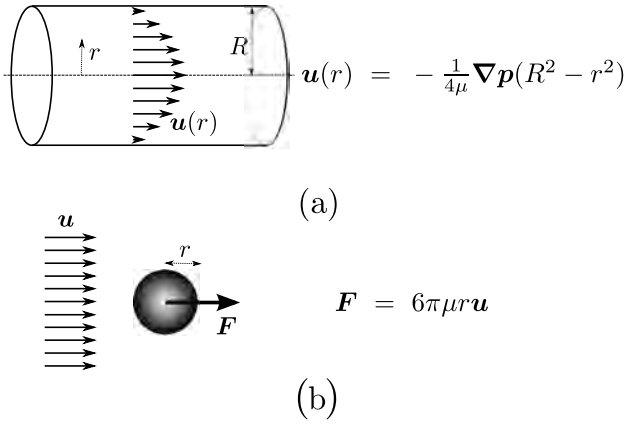

Figure 3.15 – Hagen-Poiseuille flow velocity profile in a circular tube (a) and Stokes drag force (b). In both cases viscous flow conditions are assumed.

use any numerical scheme to account for the internal fluid flow. It can also be used to perform a directional analysis of the transport properties of a given material. This rougher localization scheme will be used in Section 3.4.2 and 5.2.4 and the predicted travel distances will be compared with effective ones obtained thanks to *two ways coupling* DEM/PFV simulations.

From these simulations a pore pressure map is defined and used to study the transport of particles in the pore network. Based on the Hagen-Poiseuille flow velocity profile for a circular tube and the expression of the drag force of a uniform flow acting on a sphere for low Reynolds numbers (Figure 3.15), it can be assumed that the drag force acting on a particle of radius r in a constriction of radius R and subjected to a pressure gradient $\boldsymbol{\nabla p}$ scales as

$$\boldsymbol{F} \sim r\ \boldsymbol{\nabla p}\, R^2. \tag{3.14}$$

From this simple scaling law, a criterion for particle transport is proposed. Given a pore i connected to neighboring pores $\{j_1, j_2, j_3, j_4\}$, a transported particle of radius r in the pore i will move to a neighboring pore $k \in \{j_1, j_2, j_3, j_4\}$ if and only if

$$\begin{cases} R_{ik} > r \\ ||\boldsymbol{\nabla p}_{ij}||R_{ij}^2 \leq ||\boldsymbol{\nabla p}_{ik}||R_{ik}^2 \quad \forall j \in \{j_1, j_2, j_3, j_4\} \end{cases}, \tag{3.15}$$

where R_{ik} is the constriction radius of the connection between pores i and k. In other words, the particle propagates to the next accessible pore in the direction of maximum drag force.

Definition of expected travel distances

To estimate the average distance a particle of radius r can travel in the pore space, a propagation path $\mathcal{P}(n_0, r)$ is defined for every node n_0 of the pore network by repeated application of the propagation criterion introduced in Equation (3.15) (see Figure 3.16). For any node n_0, the farthest node n_k that the particle considered can reach is thus computed. From the list of the visited nodes $\{n_0, ...n_k\}$, the true travel distance $D^{\text{true}}(n_0, r)$, the shortest travel distance $D^{\text{short}}(n_0, r)$ and the tortuosity $T(n_0, r)$ corresponding to the path $\mathcal{P}(n_0, r)$ are then defined as

$$\begin{cases} D^{\text{true}}(n_0, r) &= \sum_{i=0}^{k-1} ||\boldsymbol{x}_{i+1} - \boldsymbol{x}_i|| \\ D^{\text{short}}(n_0, r) &= ||\boldsymbol{x}_k - \boldsymbol{x}_0|| \\ T(n_0, r) &= \dfrac{D^{\text{true}}(n_0, r)}{D^{\text{short}}(n_0, r)} \end{cases}, \tag{3.16}$$

where $\boldsymbol{x}_i$ stands for the vector position of node n_i. Figure 3.16 provides examples of propagation paths computed for the dense sample under the initial isotropic confining pressure σ_0 and for a radius threshold $r = 0$. On average, all the visible paths are aligned with the horizontal direction x corresponding to the imposed flow pressure gradient. As the radius threshold is chosen as $r = 0$, all the paths end on the sample boundaries, which is consistent with the fact that the pore space in 3D for a sphere assembly is a connected space.

The mean travel distance $\bar{D}^{\text{true}}(r)$ and the mean tortuosity $\bar{T}(r)$ are then deduced from statistical averaging of the above quantities over all the nodes of the pore network. In Figure 3.17 the mean travel distance is plotted together with the mean tortuosity for different radius values at four strain levels.

For the smallest radius values, the mean travel distance reaches a plateau, which is related to a percolation phenomenon. Indeed, the transport path can end up on the boundary of the sample for some nodes, as seen in Figure 3.16. In this case, the end of the propagation path does not coincide with the actual farthest point the particle would reach in a non-finite sample. In Figure 3.17 a percolation phenomenon is observed for r smaller than $0.2\, r_{\text{mean}}$ for all the samples. Conversely, no transport is possible for particles larger than $0.5\, r_{\text{mean}}$ for all the samples. This observation is consistent with the findings of Reboul et al. (2008) who highlighted the fact that the connectivity of the pores larger than the radius mode value of the probability density function on Figure 3.14 is too small to allow for the transport of such large particles. The grey zone on the graphs corresponds to the range of radius

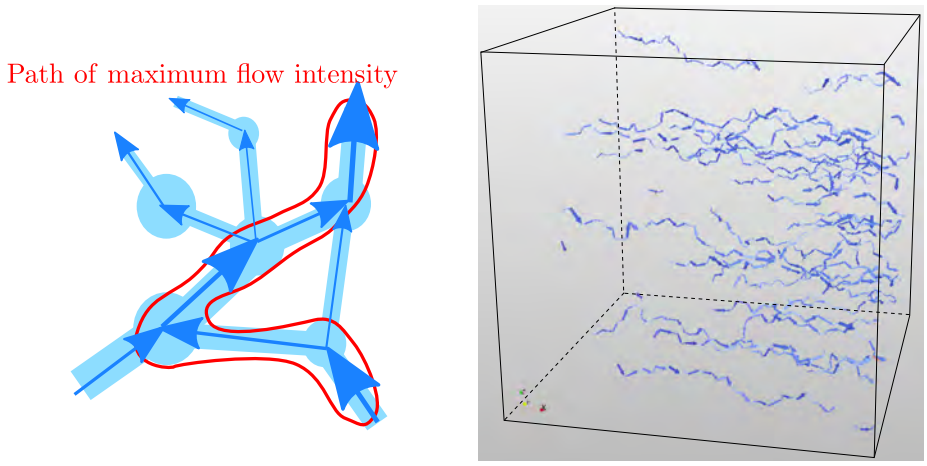

Figure 3.16 – Definition on a propagation path on the weighted pore network by flow intensity (left). Visualization of 60 propagation paths for the dense sample under the initial isotropic confining pressure σ_0 (right). The paths are chosen randomly for a radius threshold $r = 0$. The arrows indicate the propagation direction. The more intense the blue color, the larger the constriction radius. All paths end on the boundaries of the sample materialized by an empty cube.

values for the grains constituting the samples. If the largest grains cannot be transported, the smallest ones can be transported over long distances up to $25\, r_{\text{mean}}$. However, no percolation exists since there is no overlapping between the initial percolation plateau and grey zones on the graphs. Because of its dilative behavior (see Figure 3.2), transport appears to be greater in the dense sample after a few percent of vertical strain. For the loose and medium samples that exhibit a contractive behavior, the mean travel distance is reduced for the largest particles, but the mean travel distance of the smallest particles is slightly increased.

The dashed curves in Figure 3.17 represent the evolution of the tortuosity of the transport paths. No noticeable difference is visible between the three samples and the mean tortuosity decreases from 1.5 to 1 as the particle size increases following the mean change in travel distance. The limit value of 1 corresponds to the case where particles are so large that they are trapped in one or two pores. As the mean travel distance increases, the mean tortuosity increases and stabilizes around a finite value. This should be related to the fact that the propagation is driven by the flow direction, the mean direction of which is parallel to the x direction with limited fluctuations along the cross directions.

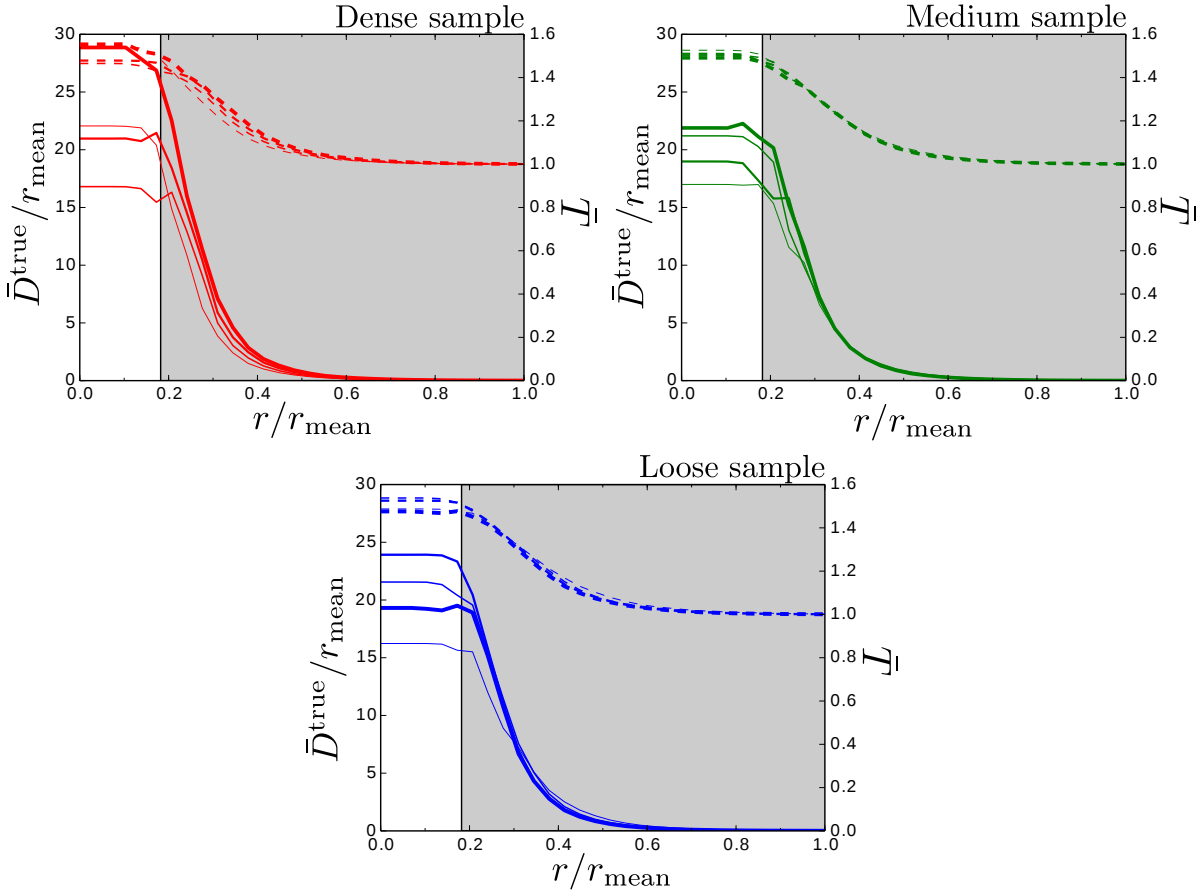

Figure 3.17 – Mean travel distance $\bar{D}^{\text{true}}$ (solid lines) and mean tortuosity $\bar{T}$ (dashed lines) for different radius thresholds. The three graphs correspond to the three samples used in this study and the line thickness corresponds to the strain level $|\varepsilon_{zz}| \in \{0, 0.05, 0.1, 0.2\}$ during the triaxial test. The thicker the line, the bigger the strain. The grey domain in the background corresponds to the accessible radius values for the grains composing the samples.

3.4 Numerical validation of expected travel distances thanks to DEM/PFV simulations

In the previous section, the expected transport distances are predicted without running fully coupled fluid grain simulations. Transport is indeed assessed first by localizing a macroscopic pressure gradient onto a pore network and then by using a simplified propagation criterion. In this section, a comparison with fully coupled DEM/PFV simulations is proposed.

3.4.1 Flow boundary value problem

Throughout this section, the dense sample prepared under an isotropic confining pressure $\sigma_0 = 100$ kPa is considered. Compared to the dry case, the problem of interest at the REV scale is modified to account for the hydraulic loading which is imposed in the form of a pressure drop in the direction $\boldsymbol{e}_x$ between an upstream face where the fluid pressure is set to p_0 and a downstream face where the fluid pressure is kept to 0. The pressure p_0 is set in order to impose an initial hydraulic gradient $I \in \{1, 2, 3\}$. By definition, the hydraulic gradient I is equal to the decrease in *hydraulic head* between the upstream and downstream sides of the sample. In the present case,

$$I = \frac{p_0}{\rho_f \; g \; \ell_x} \tag{3.17}$$

where $\rho_f = 1000$ kg.m^{-3} is the fluid density, $g = 9.81$ m.s^{-2} the gravitational acceleration and ℓ_x the sample length in the flow direction $\boldsymbol{e}_x$. It should be noticed here that the hydraulic gradient is only a dimensionless rescaling of the macroscopic pressure gradient p_0/ℓ_x as the PFV scheme relies only on the fluid dynamic viscosity $\nu = 10^{-3}$ Pa.s (see Section 2.4.2) and the gravity is not taken into account. On the four remaining faces of the sample, zero flux boundary conditions are imposed (details on the precise definition of such boundary conditions in the PFV scheme can be found in Catalano (2012). Because fluid forces scale with the square of the particle radii (in Section 2.4.2 pressure stresses are integrated over the sphere surfaces), it should be stressed that in comparison to the dry case, the dimensional PSD influences the results of coupled simulations and not only the dimensionless PSD presented in Figure 3.1. As a result, throughout this section the mean grain radius is set to $r_{\text{mean}} = 1$ mm.

Compared with the dry case, the existence of a fluid pressure gradient imposes consequently an effective stress gradient between the upstream and downstream boundaries. Indeed, the equilibrium at the sample scale imposes

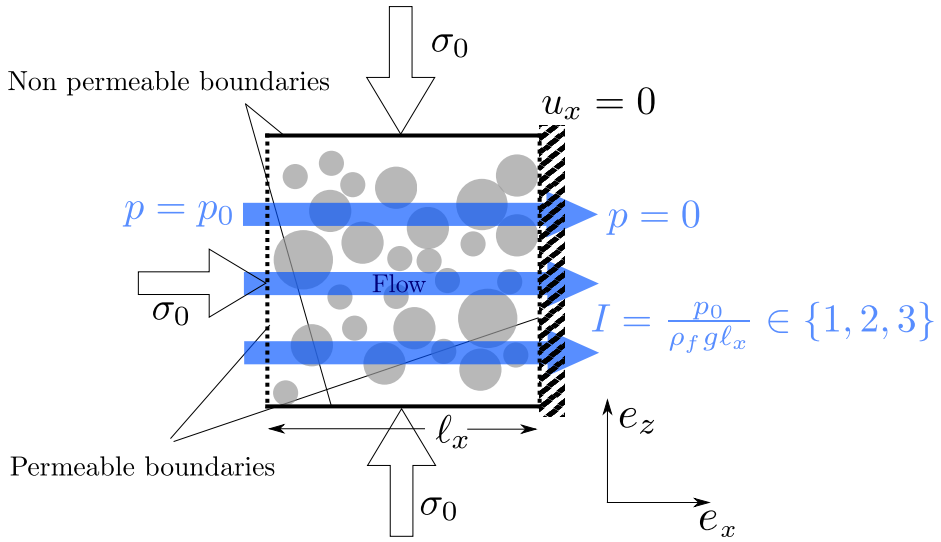

Figure 3.18 – DEM/PFV boundary value problem of interest at the REV scale. The used sample correspond to the dense sample prepared under an isotropic confinement $\sigma_0 = 100$ kPa and subjected to a hydraulic gradient $I \in \{1, 2, 3\}$.

that the total stresses are balanced but not the effective stresses. As a result, the normal effective stress on the downstream boundary is expected to be p_0 larger than the normal effective stress on the upstream boundary. Because the stress control in YADE considers the effective stress and not the total stress, the boundary conditions have to be adapted. As a result, the boundary condition on the downstream boundary is switched from stress to displacement control and a zero displacement condition is imposed on this boundary while effective stresses of $\sigma_0 = 100$ kPa are still imposed on all other faces of the sample. The full problem of interest is summarized in Figure 3.18. The introduction of a pressure gradient poses

During the DEM/PFV simulation the boundary conditions are kept unchanged and the system is let free to evolve under the action of the fluid forces. It should be underlined here the importance of non-periodic boundary conditions. Indeed, with periodic boundary conditions, the application of fluid forces would result in a collective motion of all the grains. To avoid such a non-physical situation, a possible numerical trick consists in not applying the fluid forces on some specific grains (Hosn et al., 2018). While looking at transport properties this numerical trick is acceptable, it is not relevant anymore to investigate the direct impact of a fluid flow on stress transmission as it will be considered in Chapter 5. For this later reason non-periodic

boundary conditions were selected by anticipation.

The simulation is stopped when all grains transported by the internal flow reach their farthest point and are either blocked in the sample volume by a too narrow constriction or reach the downstream side of the sample. In Figure 3.19 the sample is shown before and after the application on the internal fluid flow. In this figure the transportability of the particles is assessed thanks to coordination numbers Z_c:

- transportable particles are assumed to have a low coordination number ($Z_c < 3$) and are shown in blue;

- geometrically blocked particles are assumed to have a large coordination number ($Z_c > 4$) and are shown in red;

- clogged particles are assumed to be in contact with the three particles composing a too narrow constriction ($Z_c = 3$) and are shown in white. They remain blocked as long as the flow is kept in the same direction but they become free again if the flow is reversed.

In most of the cases, the use of Z_c to assess whether a particle can be transported by an internal fluid flow is sufficient but in some cases Z_c may not be a sufficient indicator as i) particles with 2 ou 3 contacts can be involved in stress transmission and ii) particles with 4 contacts may be part of a group of clogged particles. These particles status are illustrated in 2D in Figure 3.19 (c).

In Figure 3.20, the number of *transportable* ($Z_c < 3$) and *clogged* ($Z_c = 3$) particles are plotted with respect to time for the three hydraulic gradients $I \in \{1, 2, 3\}$.

After 0.8 s, most of the initially transportable particles have a coordination number larger than 3 and the sample reaches a new state in which the fluid does not induce particle transport anymore. While looking at the evolution of the curves in Figure 3.20, it should be underlined that the filtration process is faster when the hydraulic gradient is increased and that the fraction of transportable and clogged particles is not constant over time. This later observation means that some initially free particles have a final coordination number strictly larger than 3. As illustrated in Figure 3.19 (c), these particles may either be reattached to the primary skeleton and involved in stress transmission or belong to a group of clogged particles.

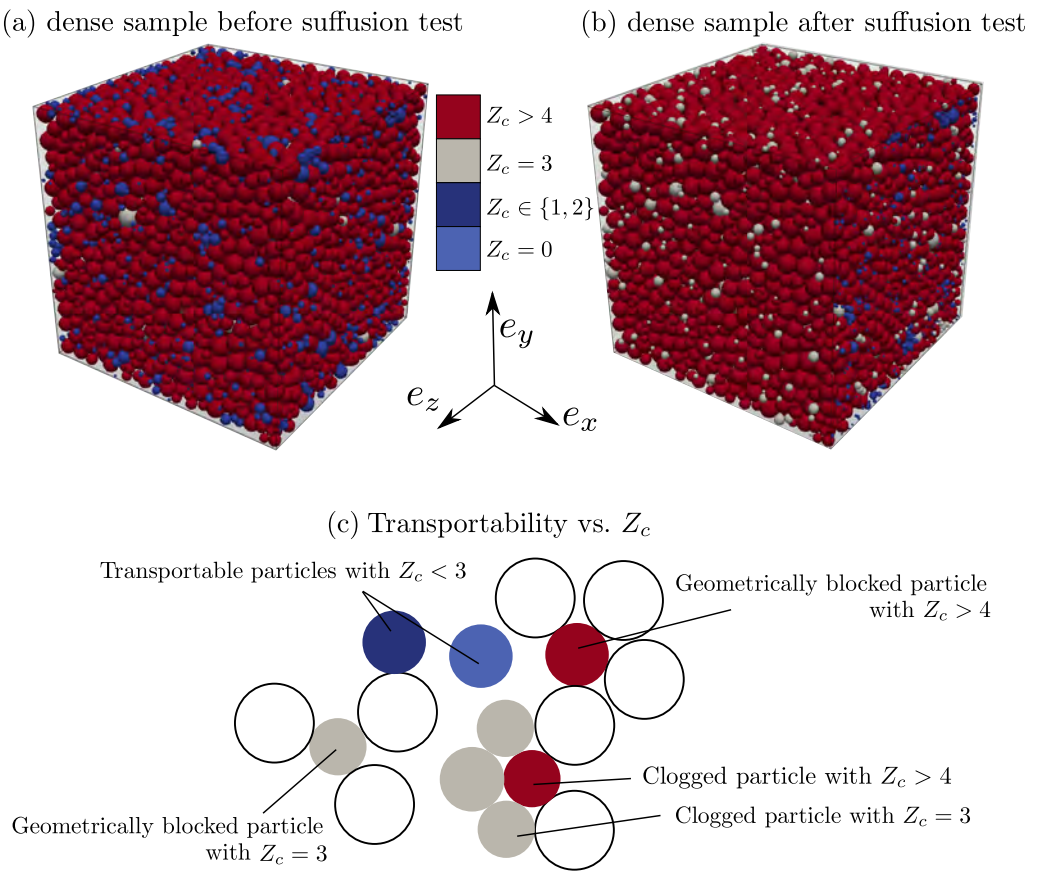

Figure 3.19 – Dense sample under isotropic confinement before (a) and after (b) the application of a hydraulic gradient $I = 1$ in direction $\boldsymbol{e}_x$. Particles are colored according to their coordination number Z_c in relation with their transportability (c).

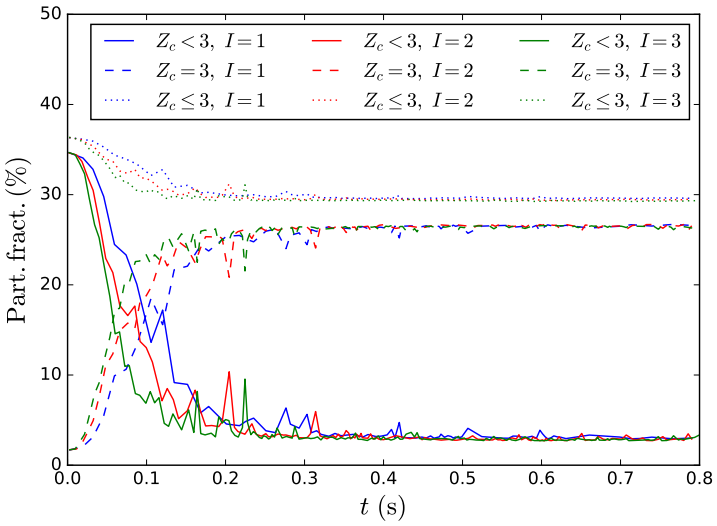

Figure 3.20 – Time evolution of the fractions of transportable (solid lines) and clogged (dashed lines) particles for the dense sample prepared under an isotropic confinement $\sigma_0 = 100$ kPa and subjected to three hydraulic gradients $I \in \{1, 2, 3\}$.

3.4.2 Numerical assessment of particle transport and erosion

By tracking the positions of all particles during the fluid flow simulations, the transport distances can be estimated from the fully coupled numerical simulations. For each particle k, the travel distance can be estimated either by comparing the final position $\boldsymbol{x}_k(t_f)$ and initial position $\boldsymbol{x}_k(t_0)$, or by incrementally summing the displacements observe during intervals $[t_i, t_{i+1}]$. Similarly to Equation (3.16), this leads to the definitions of the shortest travel distance $D_{\text{num}}^{\text{short}}$ and the true travel distance $D_{\text{num}}^{\text{true}}$ of a particle k with center $\boldsymbol{x}_k$:

$$\begin{cases} D_{\text{num}}^{\text{true}}(k) &= \sum_i ||\boldsymbol{x}_k(t_{i+1}) - \boldsymbol{x}_k(t_i)|| \\ D_{\text{num}}^{\text{short}}(k) &= ||\boldsymbol{x}_k(t_f) - \boldsymbol{x}_k(t_0)|| \end{cases} . \tag{3.18}$$

In Figure 3.21, the true and shortest displacements observed for all particles are plotted with respect to the particle radii for the three hydraulic gradients considered. Displacements are normalized by the mean radius r_{mean}.

In Figure 3.21 the particle displacements are not strongly influenced by the hydraulic gradient intensity as the three clouds of points superpose. As predicted by the transport model presented in the previous section, the smallest particles are transported over large distances up to $D_{\text{num}}^{\text{short}} = 45 r_{\text{mean}}$,

which is comparable to the sample dimension $\ell_x = 48r_{\text{mean}}$, and particles larger than $\sim 0.7r_{\text{mean}}$ hardly move. These observed transport distances are quite consistent with the pore and constriction size distributions shown in Figure 3.14 as $r > 0.7r_{\text{mean}}$ corresponds to the tails of the distributions.

While computing the mean observed displacements in Figure 3.21, it is interesting to compare these DEM/PFV estimates with the prediction of Section 3.3.3. This comparison is shown in Figure 3.22 for the mean true and shortest travel distances.

In Figure 3.22 the agreement between the predictions from Section 3.3.3 and the fully coupled numerical result is quite good. The proposed propagation criterion combined with the simplified description of the pore geometry is thus sufficient to capture the driving physical processes responsible for grain transport. However, it should be underlined that the effective transport is larger than the predicted values. This can be explained because the pore network used in the transport model of Section 3.3.3 is built on *all* the particles which includes particles transported by the flow. As a result, the pore and constriction sizes of the resulting pore network underestimate the *effective* pore sizes seen by the transported particles. The model prediction gives indeed a lower bound for $\bar{D}^{\text{short}}_{\text{num}}$ and $\bar{D}^{\text{true}}_{\text{num}}$.

The transport model used in Section 3.3.3 proposes a simplified approach to grain transport that does not need fully coupled fluid/grain simulations. A pore scale fluid model is however necessary to compute the pore pressure map which reduces the scope of applicability of the simplified transport model. To this respect, it is interesting to compare the mean travel distances obtained with a rougher pressure map deduced from the assumption of a linear decrease in the pore pressure between the upstream and downstream boundaries. The comparison between the two propagation model predictions in Figure 3.22 shows the importance of pressure fluctuations with respect to particle transport which affects mostly the smallest particles. The fluctuations are shown in Figure 3.22 to increase the mean travel distances.

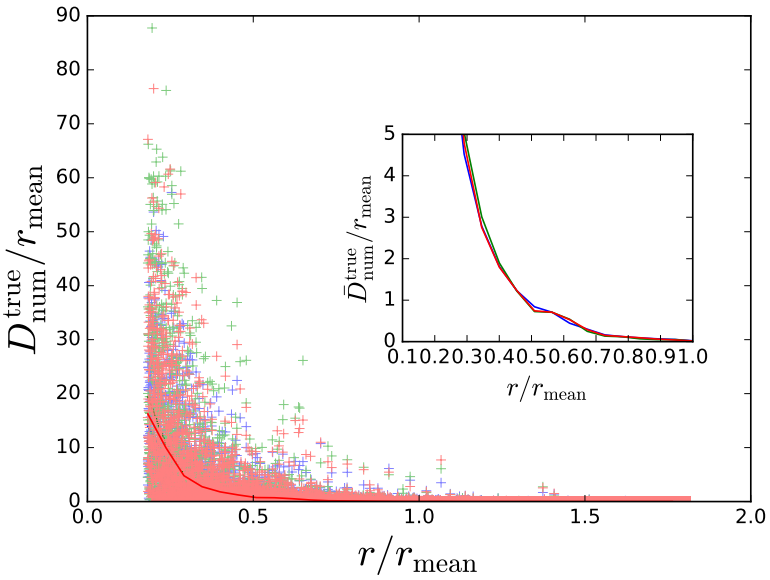

(a) Effective transport distances.

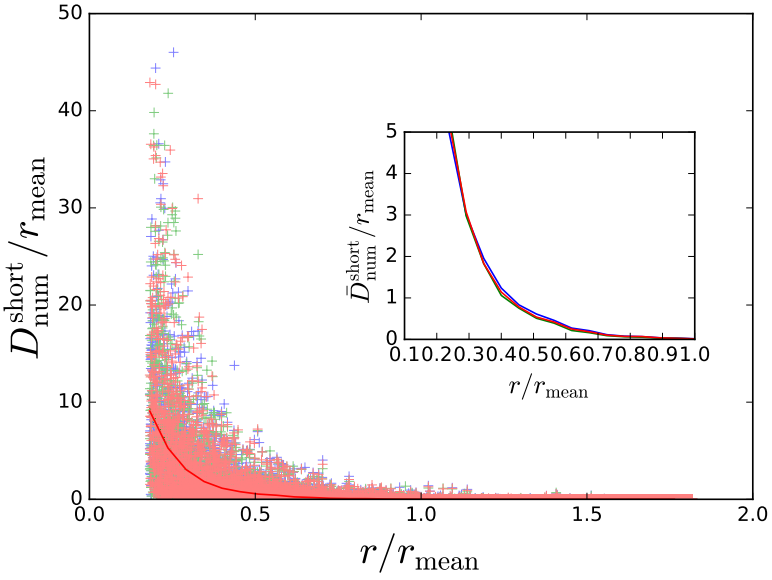

(b) Shortest transport distances.

Figure 3.21 – Numerical results for the shortest and true travel distances of all the particles of dense sample subjected to an isotropic confinement $\sigma_0 = 100$ kPa for three hydraulic gradients $I \in \{1, 2, 3\}$ (respectively in blue, red and green). The mean transport distances $\bar{D}^{\text{true}}_{\text{num}}$ and $\bar{D}^{\text{short}}_{\text{num}}$ are shown in solid lines.

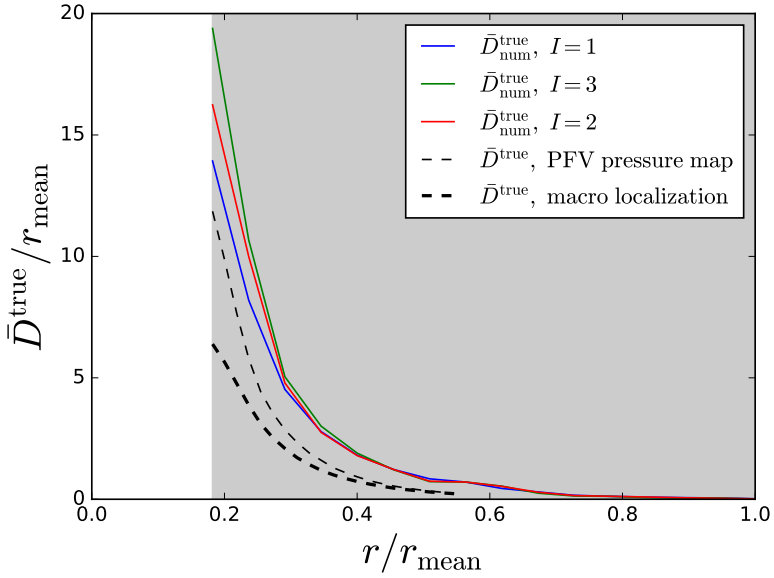

(a) Mean effective transport distances.

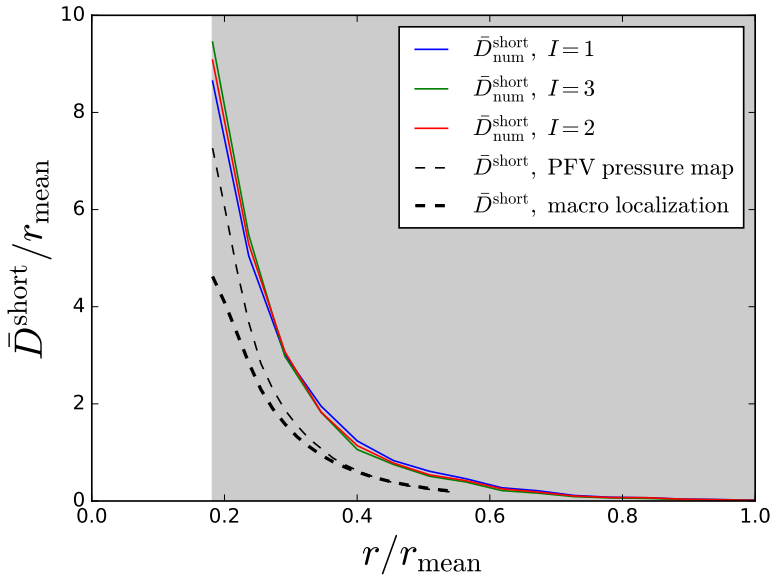

(b) Mean shortest transport distances.

Figure 3.22 – Comparison between the mean transport distances ($\bar{D}^{\text{true}}$ and $\bar{D}^{\text{short}}$) predicted with the transport model of Section 3.3.3 (thin dashed), this same model with a linear approximation of the pressure map (thick dashed), the numerical results obtained from DEM/PFV simulations for three hydraulic gradients $I \in \{1, 2, 3\}$ (solid lines). In all cases, the dense sample under an isotropic confinement $\sigma_0 = 100$ kPa is considered.

In Figure 3.23, the pressure fluctuations are quantified by looking at the difference between the pore pressure computed with the PFV model and the macroscopic linear regression $p_{\text{macro}} = p_0 - \frac{p_0}{\ell_x} x$. For the macroscopic fluid direction $\boldsymbol{e}_x$, the mean pressure $\bar{p}(x)$ is defined as the 2D average of the pore pressure p in directions $\boldsymbol{e}_y$ and $\boldsymbol{e}_z$ at a given position $x \in [0, \ell_x]$.

In Figure 3.23, the pore pressures fluctuate around the macroscopic prediction with a slight positive deviation close to the upstream boundary and a slight negative deviation close to the downstream boundary. These deviations are related to the larger porosity close to the sample boundaries shown in Figure 3.9 which induces a larger permeability close to the boundary and smaller local pressure gradients in these regions.

As illustrated in Figure 3.22 with the prediction of the travel distances, the fluctuations of a few percents of the pressure drop p_0 have a non-negligible influence on grain transport and justify the use of a *resolved* approach to model the fluid flow among the modeling options listed in Section 2.4.1.

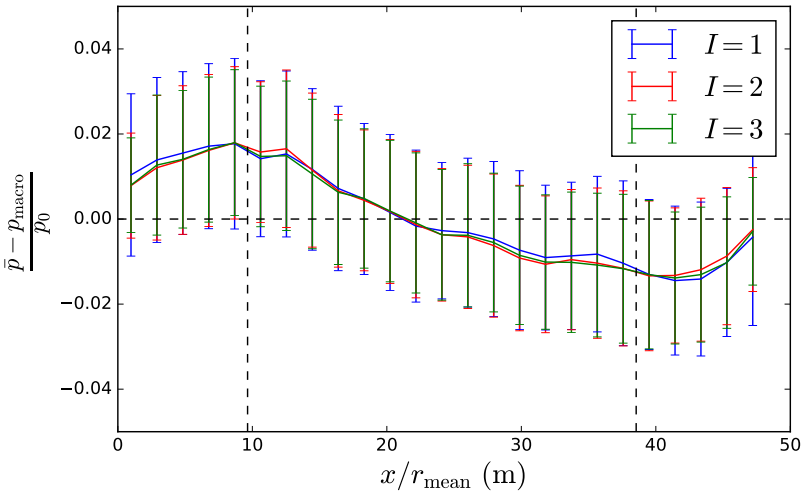

Figure 3.23 – Normalized difference between 2D averaged pore pressures $\bar{p}(x)$ and the linear regression $p_{\text{macro}} = p_0 - x\frac{p_0}{\ell_x}$ for the dense sample prepared under an isotropic confinement for $t = 0$ s (similar curves are obtained $\forall t > 0$). Three hydraulic gradients $I \in \{1, 2, 3\}$ are considered. Standard deviations are shown in the form of error bars. Two vertical dashed lines correspond to $x = 0.2\ell_x$ and $x = 0.8\ell_x$.

3.5 Summary of the main findings

Thanks to the use of specific micromechanical tools, partitions of both the solid and the void phases of granular materials have been proposed, motivated by the assessment of grain detachment and transport properties in granular materials subjected to suffusion. A partition of the solid fraction between chained particles and non-chained particles prefigures the susceptibility to grain detachment. Similarly, the void space is split into an accessible pore network and a non-accessible pore network. This dual partition is a fundamental ingredient to describe the grain transport process.

Based on DEM simulations, the microstructure evolutions of a numerical samples are recorded during a drained triaxial loading and the relevance of the proposed micromechanical tools in enhancing the comprehension of the macroscopic behavior is shown. In particular, the ability of the chained particle autocorrelation lengths to recover the hardening and softening behaviors of the dense sample confirms the relevance of this approach to describe the typical length scales associated with stress transmission. Likewise, the mean travel distance functions are shown to address the dilative and contractive behaviors of the specimen considered. Their relevance in correctly assessing

travel distances is validated thanks to fully coupled DEM/PFV simulations of the suffusion process.

By carefully considering the spatial distribution of particles participating in stress transmission and the spatial distribution of constrictions enabling particle transport within the pore space, two mesoscales are introduced in relation with the grain detachment and the grain transport processes. It was shown that the typical length scale associated with grain transport can be up to ten times larger than that associated with grain detachment. As a result, a scale separation exists between these two processes for the smallest particles in the present case. This implies that grain detachment and grain transport can be studied independently from one another for the particular granular material studied in this chapter. Macroscopically, if this separation of scales holds, suffusion may be described as the superposition of both detachment and transport processes.

Chapter 4

Micro to macro analysis of the elementary mechanisms responsible for mechanical instability in granular materials

---

In this chapter, fluid grain coupling is left aside to focus on the understanding of the micromechanisms responsible for the the onset of material instability in granular materials in the sense of the second-order work criterion as introduced in Section 2.2.3.

The aim of this chapter is twofold. A first objective is to investigate numerically the elementary mechanisms taking place in granular materials for a loading program leading to the vanishing of the second-order work. What is the micro-signature of an instability? What is the sequence of micromechanical mechanisms leading to the vanishing of the second-order work? A second objective is then to analyze the influence of some particular microstructure modifications on the overall mechanical stability.

This chapter is organized as follows. In Section 4.1, a representative elementary volume of an idealized loose granular material is generated and subjected to a drained triaxial test. For different stress states, the mechanical stability is assessed in Section 4.2 following a classical stress-controlled directional analysis procedure with use of the second-order work criterion. A particular care is paid to (i) the influence of the pre-stabilizing step of the procedure and (ii) the magnitude of the stress probe used in the directional analysis. Some of these results provide some insight on the standard numerical procedure used to assess the mechanical stability of a granular material thanks to the second-order work criterion. In Section 4.3, the microscale mechanisms leading to the vanishing of the second-order work are identified and a special care is paid to their chronology. For a particular stress state, the incremental constitutive behavior is then modeled in Section 4.4 within the framework of non-associated elasto-plasticity. This continuum mechanics modeling is used to relate plastic strain development and mechanical stability from analytical considerations. A conjecture on the particular role of rattlers is then formulated. In Section 4.5, the link between mechanical stability and plastic strain obtained at the macroscale is derived directly at the contact scale. Eventually, the stabilizing role of rattlers is confirmed numerically thanks to DEM simulations in Section 4.6.

4.1 Numerical experiments on narrowly graded samples with DEM

The micromechanical analysis performed throughout this chapter considers non-cohesive granular materials modeled as poly-disperse assemblies of spheres. The interaction between two particles is modeled by the classical elasto-frictional contact law detailed in Section 2.3.1 with parameters of

Table 2.1. Given all inter-particle contact forces, the induced particles displacements are then numerically integrated thanks to the DEM open source code YADE (Šmilauer et al., 2015).

4.1.1 Sample definition

A cubic assembly of spheres is generated randomly with a uniform radius distribution between $r_{\min}$ and $r_{\max} = 3.5\, r_{\min}$. After generating a cloud of 10,000 non-overlapping spheres surrounded by six bounding planes defining a cube, the particles are inflated and allowed to rearrange according to the radius expansion technique. This process is stopped when the confining pressure applied on the bounding planes reaches 20 kPa and the normalized unbalanced force (F_{unb}) of the system decreases below 10^{-5}. By definition F_{unb} is equal to the mean summary force on the N_p particles divided by the mean contact force magnitude on the N_c contacts:

$$F_{\text{unb}} = \frac{\frac{1}{N_p}\sum_{p=1}^{N_p} ||\sum_{c_p} \boldsymbol{F}_{c_p}||}{\frac{1}{N_c}\sum_{c=1}^{N_c} ||\boldsymbol{F}_c||}. \tag{4.1}$$

As a result F_{unb} has no units and provide an intrinsic measure of how close to equilibrium a mechanical system is. During this process, the inter-particle friction angle is maintained to its value of 35° in order to prepare a loose granular material with a void index of $e = 0.73$. The resulting sample may be visualized in Figure 4.1 together with the PSD curve corresponding to the used uniform radius distribution. Associated with the generated cubic grain assembly, a Cartesian coordinate system $(\boldsymbol{e_x}, \boldsymbol{e_y}, \boldsymbol{e_z})$ is defined such that the axis directions coincide with the edges of the cube.

4.1.2 DEM simulation of a drained triaxial test

From the obtained equilibrium state, a drained triaxial loading is then imposed to the sample in the form of a two step procedure as in Chapter 3. First, the confining pressure (σ_0) is increased from 20 kPa to 100 kPa by allowing the bounding walls to move. Once a new equilibrium state is reached ($F_{\text{unb}} < 10^{-5}$), a vertical compression strain rate $\dot{\varepsilon}_{zz} = 0.01\ \text{s}^{-1}$ is applied up to 6 % of deformation while keeping the same lateral confining pressure σ_0. This strain rate is chosen similar to the one used in previous numerical studies (Hadda et al., 2013; Nicot et al., 2012) and is supposed to be sufficiently small so that the loading can be considered as quasi-static.

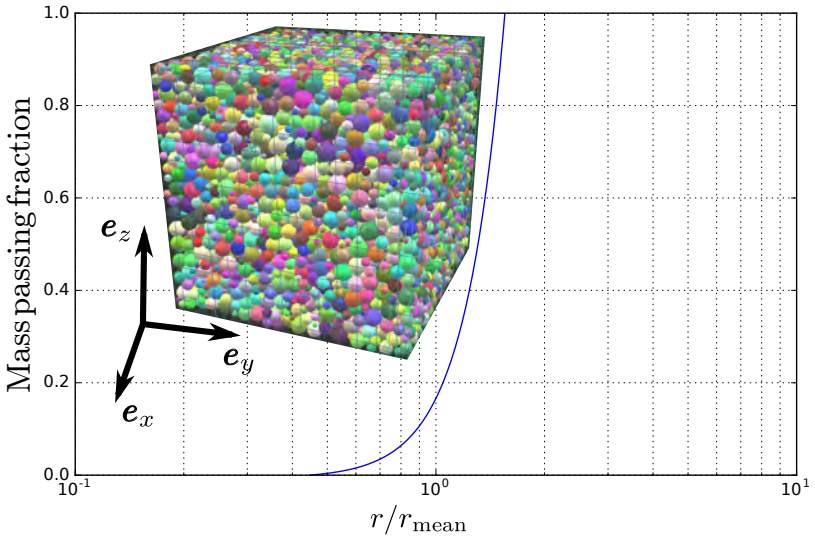

Figure 4.1 – Cumulative distribution in terms of mass corresponding to the generated sample. Particle radii are normalized by the mean radius value.

As in Chapter 3, the classical soil mechanics conventions are adopted with compressions counted positive. The homogeneous Cauchy stress tensor $\boldsymbol{\sigma}$ is defined at the REV scale from the forces applied on the bounding walls. The stress ratio η is then introduced as the ratio between the deviatoric stress q and the mean pressure p

$$\left\{\begin{array}{rcl} \eta & = & \dfrac{q}{p} \\ q & = & \sqrt{\frac{3}{2}\boldsymbol{\sigma}_{\text{dev}} : \boldsymbol{\sigma}_{\text{dev}}} \\ \boldsymbol{\sigma}_{\text{dev}} & = & \boldsymbol{\sigma} - p\,\mathbf{1} \\ p & = & \frac{1}{3}\text{Tr}(\boldsymbol{\sigma}) \end{array}\right. . \tag{4.2}$$

where $\mathbf{1}$ stands for the identity tensor, ":" stands for the double dot contraction product and Tr for the trace operator.

Likewise, a macroscopic homogeneous strain tensor $\boldsymbol{\varepsilon}$ is defined from the bounding walls displacements. In order to be consistent with the second-order work definition $W_2 = \mathbf{d}\boldsymbol{\sigma} : \mathbf{d}\boldsymbol{\varepsilon}$, compaction is counted positive. The volumetric strain is then simply defined as

$$\varepsilon_v \;=\; \text{Tr}(\boldsymbol{\varepsilon}). \tag{4.3}$$

In Figure 4.2, the stress ratio and volumetric strain responses are shown. A typical contractive behavior is observed as both η and ε_v monotonously

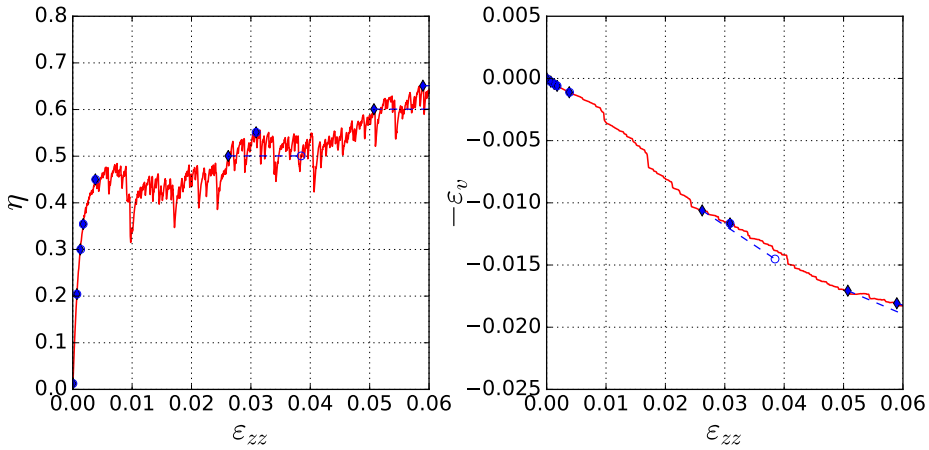

Figure 4.2 – Drained triaxial test response. The diamond points correspond to the mechanical states considered for the stability analysis. The circles corresponds to the stress-strain state reached after the pre-stabilization step (see subsection 4.2.1)

increase with the vertical compaction ($\varepsilon_{zz} > 0$). This behavior is typical of non-compacted granular material (recent gravel deposits or stocks of industrial materials for instance). After a sharp increase, the stress ratio slowly increases on average. This second phase of the mechanical response is characterized by a *bumpy* curve resulting from important grain rearrangement processes occurring from time to time. As a result, as soon as these sudden drops in η are observed the mechanical response of the sample becomes inherently dynamic and the quasi-static hypothesis becomes questionable over these short periods.

In order to study the mechanical stability of the particular sample under different mechanical stress states, 9 samples are saved during the triaxial loading for $\eta \in \{0.01, 0.20, 0.30, 0.35, 0.45, 0.50, 0.55, 0.60, 0.65\}$. The corresponding states are marked with diamonds in Figure 4.2.

4.2 Macroscopic assessment of bifurcation points

In this section, the mechanical stability of the 9 mechanical states saved during the triaxial loading presented in the previous section is assessed thanks to a classical stress-controlled directional analysis procedure with use of the second-order work criterion (Sibille et al., 2009; Nicot et al., 2007, 2009). This numerical procedure is composed of two steps which are reviewed in detail hereafter. First, a pre-stabilization is required to define a reference

equilibrium state. Then, an incremental stress probe is imposed at the scale of the whole sample which is accompanied by a transient mechanical response until a second equilibrium state is reached.

In addition to the directional analysis of the vanishing of the second-order work criterion (section 4.2.2), a particular care is paid to the influence of the pre-stabilizing step (section 4.2.1), to the transient response observed between the two equilibrium states (section 4.2.3) and to the influence of the magnitude of the stress probe (section 4.2.4).

4.2.1 Pre-stabilization step

Even if the vertical compression rate is set at a reasonably low value, the mechanical response recorded during the triaxial loading is inherently dynamic as it relies on particle rearrangements and the integration of Newton's second law of motion for each particle. As a result, a pre-stabilization step is required prior to study the mechanical stability of saved samples thanks to the second-order work criterion reviewed in Section 2.2.3.

This pre-stabilization step is achieved by keeping the lateral pressure to the constant value σ_0 and by imposing a vertical stress σ_{zz} corresponding to the stress ratio considered. The equilibrium state is assumed to be reached once $F_{\text{unb}} < 10^{-5}$.

Even if the stress state is kept constant, delayed deformations are observed during this pre-stabilization step. The final stress-strain states reached at the end of the pre-stabilization step are shown for each stress ratio in Figure 4.2 by blue circles. For $\eta \leq 0.45$ and $\eta = 0.55$, negligible delayed deformations are observed while for $\eta \in \{0.50, 0.60, 0.65\}$ delayed deformations are larger than 1 %. For stress ratios larger than $\eta = 0.45$, the quasi-static regime becomes questionable and sudden rearrangements in the microstructure yield fluctuations in the stress-strain response. These rearrangements are not instantaneous and continue to occur during the pre-stabilization step which result at the scale of the sample in delayed permanent deformations. A parallel can be drawn here with the concept of *delayed plasticity*[1] introduced by Di Prisco (di Prisco and Imposimato, 1996) and also mentioned in Froiio et al. (Froiio et al., 2010).These local particle reorganizations can affect the mechanical stability as the state variables obtained after the pre-stabilization step are different from the initial ones.

[1]Following a discussion with the PhD jury, it should be underlined that the timescales observed numerically and experimentally are different because i) the timescale linked to global rearrangement is not intensive (it increases with the size of the sample) and ii) other mechanisms such as grain plasticity or grain crushing can also contribute to plasticity on the experimental side.

4.2.2 Directional analysis step

As presented in Section 2.2.4, directional analysis is a convenient framework to track the existence of stress increments leading to the vanishing of the second-order work (Bardet, 1994; Sibille et al., 2009; Nicot et al., 2007, 2009; Harthong and Wan, 2013). In this study, we restrict our stability analysis to stress increments lying in the plane of axisymmetry such that $\mathrm{d}\sigma_{xx} = \mathrm{d}\sigma_{yy}$ (Rendulic plane). In this plane $(\sqrt{2}\mathrm{d}\sigma_{xx}, \mathrm{d}\sigma_{zz})$, a stress increment $\mathbf{d\boldsymbol{\sigma}}$ is fully described by its polar coordinates $||\mathbf{d\boldsymbol{\sigma}}||$ and θ such that

$$\left\{ \begin{array}{rcl} \sqrt{2}\mathrm{d}\sigma_{xx} & = & ||\mathbf{d\boldsymbol{\sigma}}|| \ \cos\theta \\ \mathrm{d}\sigma_{zz} & = & ||\mathbf{d\boldsymbol{\sigma}}|| \ \sin\theta \\ ||\mathbf{d\boldsymbol{\sigma}}|| & = & \sqrt{\mathrm{d}\sigma_{zz}^2 + 2 \ \mathrm{d}\sigma_{xx}^2} \end{array} \right. . \tag{4.4}$$

In practice, finite stress increments of $||\mathbf{d\boldsymbol{\sigma}}|| = 5$ kPa are imposed in the form of a stress loading rate of 142 kPa.s^{-1} (corresponding to 10,000 DEM time steps) followed by a stabilization phase letting the system evolves toward a new equilibrium position with $F_{\text{unb}} < 10^{-5}$. The size of the stress increment is similar to those classically used in the literature (Calvetti, 2003; Kishino, 2003; Sibille et al., 2009).

At the end, for each imposed stress increment $\mathbf{d\boldsymbol{\sigma}}$, a strain increment $\mathbf{d\boldsymbol{\varepsilon}}$ is obtained. A normalized second-order work is then defined at the material point scale (REV scale) as

$$W_2^{\text{norm}} = \frac{\mathbf{d\boldsymbol{\varepsilon}} : \mathbf{d\boldsymbol{\sigma}}}{||\mathbf{d\boldsymbol{\varepsilon}}|| \ ||\mathbf{d\boldsymbol{\sigma}}||} \tag{4.5}$$

Provided that the strain increment depends linearly on the applied stress increment for each direction θ (this will be investigated in section 4.2.4), the normalized second-order work introduced in Equation (4.5) depends only on θ and not $||\mathbf{d\boldsymbol{\sigma}}||$. For the considered stress increment $||\mathbf{d\boldsymbol{\sigma}}|| = 5$ kPa, the normalized second-order work envelopes for the 9 pre-stabilized samples are shown in Figure 4.3. A circular representation is used as the second-order work is positive outside the red dashed circle and negative inside.

In Figure 4.3, the normalized second-order work envelopes on the left correspond to the quasi-static regime ($\eta \leq 0.45$) while the ones on the right corresponds to the dynamic regime of the triaxial test ($\eta > 0.45$). For small stress ratios, no vanishing of the second-order work is observed. As the stress ratio increases, the second-order work gradually decreases for incremental stress directions around 210° and an instability cone (θ values such that $W_2 \leq 0$) is eventually obtained for $\eta = 0.45$. According to the second-order work criterion the sample becomes unstable while approaching the onset of

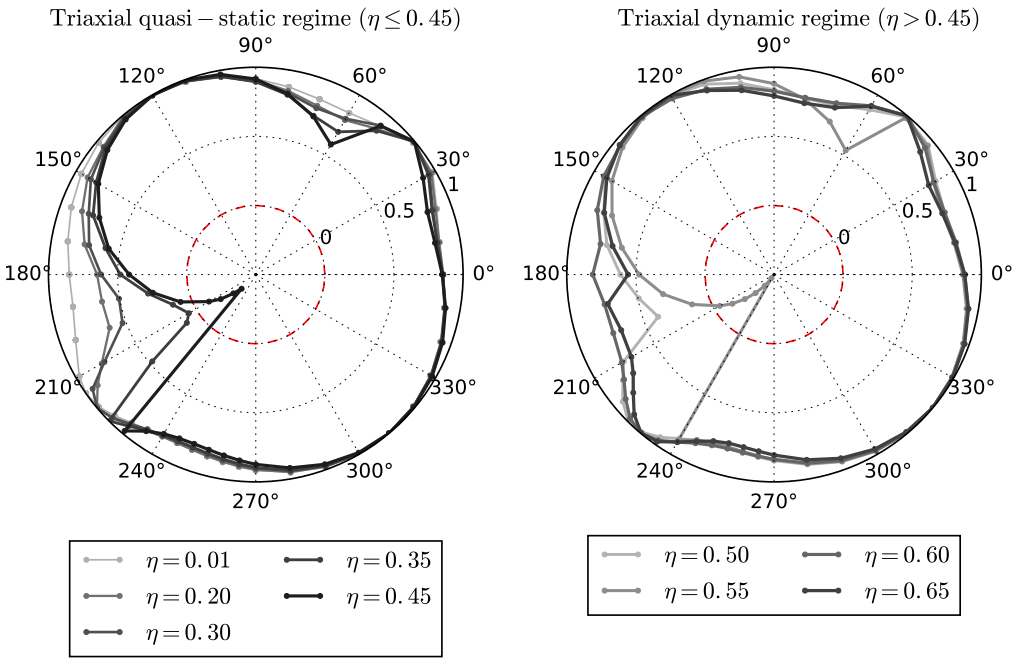

Figure 4.3 – Circular second-order work for different η values in quasi-static regime (left) and in dynamic regime (right). $W_2 = 0$ is indicated by a red dashed circle.

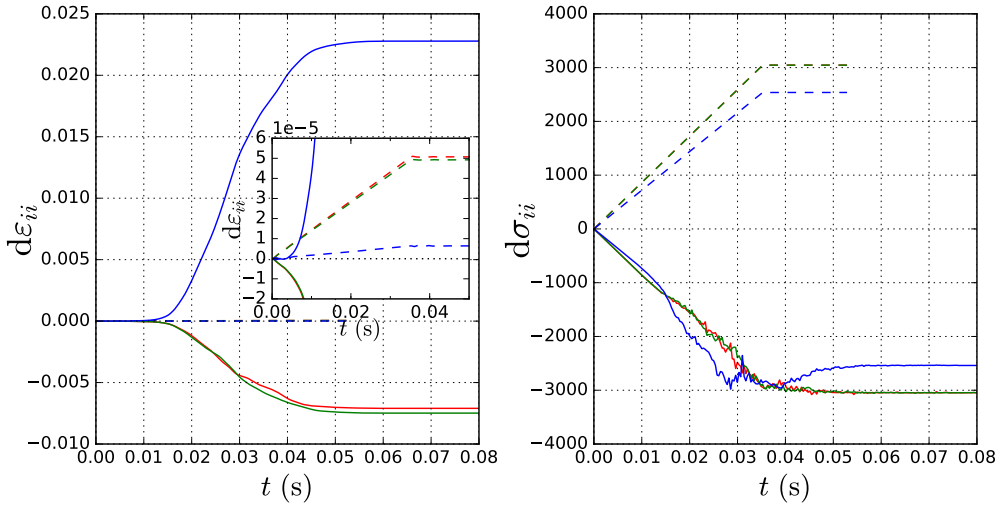

Figure 4.4 – Macroscopic strain (left) and stress (right) response for the two loading directions $\theta = 30.5°$ (dashed lines) and $\theta = 210.5°$ (solid lines). The vertical stress ($\mathrm{d}\sigma_{zz}$) and strain ($\mathrm{d}\varepsilon_{zz}$) components are plotted in blue while the horizontal ones are plotted in red ($\mathrm{d}\sigma_{xx}$ and $\mathrm{d}\varepsilon_{xx}$) and green ($\mathrm{d}\sigma_{yy}$ and $\mathrm{d}\varepsilon_{yy}$).

the dynamic regime during the triaxial loading as there exist incremental loading programs associated with negative W_2. Then, for higher stress ratio, the second-order work suddenly becomes positive again for all the incremental stress directions (except for $\eta = 0.55$ for which an instability cone is still visible). The non-vanishing of W_2 for $\eta \in \{0.5, 0.6, 0.65\}$ should be linked to the large delayed deformations observed for these stress state in Figure 4.2. The grain rearrangements result in a stable configuration for which no stress increments lead to the vanishing of the second-order work (at least for loading directions within the Rendulic plane).

4.2.3 Continuum scale analysis of the onset and development of instability

In the previous subsection, the second-order work has been systematically computed between two equilibrium states. In this subsection, transient evolutions induced by macroscopic stress probes are analyzed at the scale of the REV. In Figure 4.4, the incremental stress and strain time responses are presented for a stress ratio $\eta = 0.45$ and for the two loading directions $\theta = 30.5°$ (stable) and $\theta = 210.5°$ (unstable).

For the considered stable direction ($\theta = 30.5°$) the evolution of the incre-

mental stress follows perfectly the prescribed loading program in the form of a ramp over the first 10,000 numerical time iterations ($t < 0.035$ s). By contrast the measured stress increments corresponding to the unstable direction $\theta = 210.5°$ fails to follow prescribed ramp and a deviation is observed for $t \in [0.015, 0.04]$ s. Indeed, contrary to stable directions a transient loss of controllability (in the sense of Nova (Nova, 1994)) is observed for unstable directions. This has to be linked to the development of large incremental strains up to several percents whereas in the case of stable directions, the incremental strains are limited to approximately 10^{-5} (see inset graph in Figure 4.4).

The considered unstable direction ($\theta = 210.5°$) corresponds to a physical configuration in which the sample is slightly deconfined simultaneously in the vertical and horizontal directions ($\mathrm{d}\sigma_{zz} < 0$ and $\mathrm{d}\sigma_{xx} = \mathrm{d}\sigma_{yy} < 0$). For a stable material, this loading program should result in an increase in the volume of the sample which is only the case here for $t < 0.01$ s (before large strains develop). A sudden collapse of the sample in the vertical direction is observed and a densification of the sample is obtained as the horizontal dilatancy does not counterbalance the vertical contraction in Figure 4.4 ($\mathrm{d}\varepsilon_v = \sum_i \mathrm{d}\varepsilon_{ii} > 0$).

In Figure 4.5, the transient evolution of the second-order work is plotted for the two loading directions $\theta \in \{30.5°, 210.5°\}$ and for the same stress ratio $\eta = 0.45$. It should be noted here that as the sample does not follow a quasi-static evolution, the transient second-order work shown in Figure 4.5 is indeed the external second-order work which is an upper bound for the internal second-order work as $\mathrm{d}^2E_c \geq 0$ in Equation (2.6) (Nicot et al., 2017).

Initially positive, the second-order work vanishes after $t = 0.014$ s when the loss of controllability is observed. Then W_2^{ext} decreases, goes through a minimum and eventually stabilizes after $t = 0.05$ s around a negative value. This non-monotonic evolution should be underlined as for some stress ratios and some stress loading directions the final increase of the second-order work may rise above zero. Indeed this evolution is explained by the onset of a softening regime (the vanishing and the decrease of W_2) which is eventually stopped as the sample gets denser (the final increase in W_2^{ext}). Provided this softening regime is rapidly stopped (W_2^{ext} does not decrease too much), the final value for $W_2^{\mathrm{ext}} = W_2$ may become positive again.

In Figure 4.6, a circular representation of W_2^{ext} is shown in order to link the transient evolutions of $\mathbf{d}\boldsymbol{\sigma}$ and W_2^{ext} for a stress ratio $\eta = 0.45$.

In this Figure, the loss of controllability for unstable directions is visible as transient normalized second-order work does not follow a straight line. As the external second-order work decreases, the incremental stress loading direction

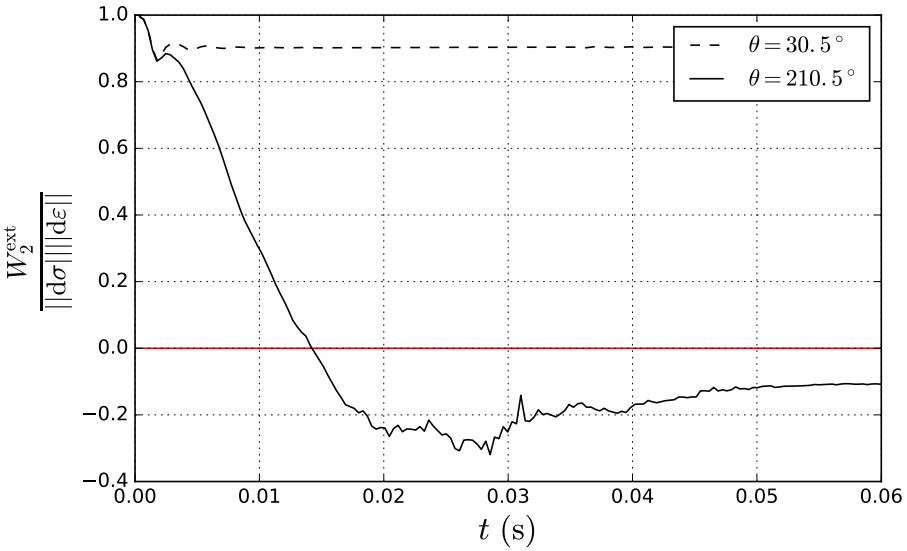

Figure 4.5 – External normalized second-order works for the two loading directions $\theta = 30.5°$ (dashed line) and $\theta = 210.5°$ (solid line). The vanishing of W_2 is indicated by the horizontal red line.

deviates toward the direction of the cone of instability slightly outside the normalized second-order work envelop computed in Figure 4.3 (as $W_2^{\text{ext}} > W_2$ according to Equation (2.6)) before getting back to its original position as soon as the softening regime is contained.

4.2.4 Influence of the stress increment on the onset of instability

As already pointed out in the literature concerning the numerical assessment of the mechanical stability of granular materials (Froiio et al., 2010; Sibille et al., 2009), the stress increment $||\mathbf{d\sigma}||$ used in the directional analysis cannot be infinitely small as assumed theoretically. This is usually assumed to be linked to the discrete nature of granular materials the mechanical behavior of which strongly rely on particle rearrangements and incorporate an internal length scale.

In this study, the specific influence of $||\mathbf{d\sigma}||$ on the normalized second-order work envelopes shown in Figure 4.3, has been explored for the stress ratio $\eta = 0.45$. In Figure 4.7, the normalized second-order work envelopes are shown for six stress increments $||\mathbf{d\sigma}|| \in \{0.5, 1, 2.5, 5, 7, 10\}$ kPa. For each stress increment, the testing procedure remains the same as in section 4.2.2.

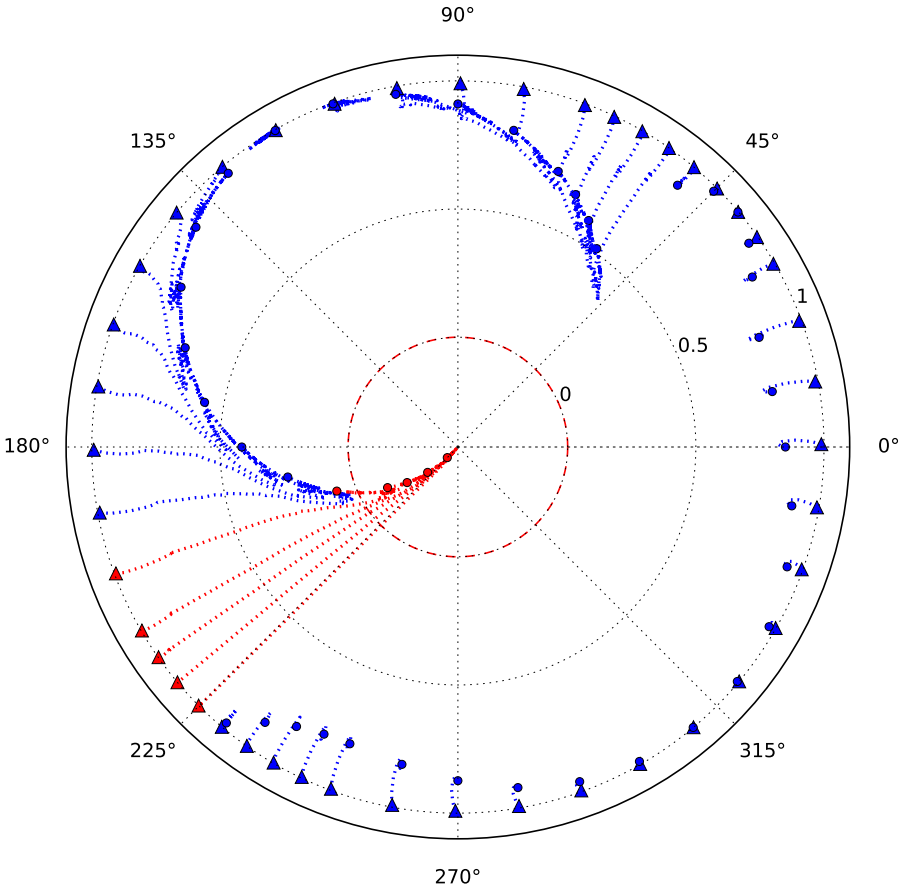

Figure 4.6 – Transient evolutions of the normalized second-order work for $\eta = 0.45$ and $||\mathbf{d}\boldsymbol{\sigma}|| = 5$ kPa (dotted lines). The initial states are shown with triangles while circles corresponds to the final ones. In case a transient vanishing of W_2^{ext} is observed these points appear in red. $W_2^{\text{ext}} = 0$ is indicated by a red dashed circle.

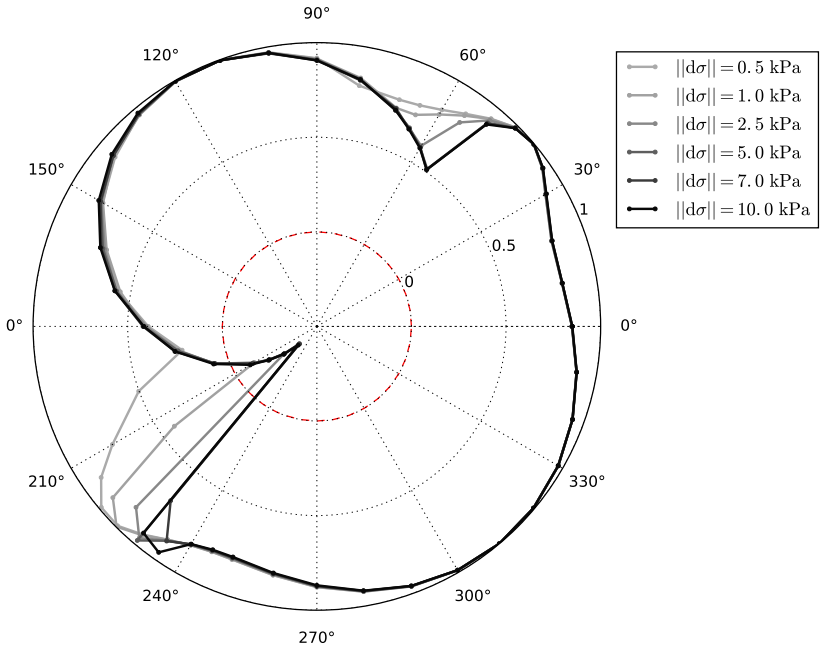

Figure 4.7 – Circular second-order work for $\eta = 0.45$ and different stress increment magnitudes. $W_2 = 0$ is indicated by a red dashed circle.

In particular, the same stress loading rate $||\mathbf{d\dot{\sigma}}|| = 142$ kPa.s^{-1} is used.

If no change is visible for stable directions, the magnitude of the applied stress increment has a noticeable impact on the width of the instability cone which can even disappear for small stress increments. Once underlying instability has been mobilized by the incremental stress perturbation, the normalized second-order work does not depend on $||\mathbf{d\sigma}||$ anymore. In the present case, a minimal value between 2.5 kPa and 5 kPa is required.

In order to explore this dependence on the stress increment at the microscale, it is interesting to define for each contact a sliding index I_p as

$$I_p = \frac{||F_t||/||F_n||}{\tan\phi} \tag{4.6}$$

where ϕ is the inter-particle friction angle, F_t and F_n are respectively the tangential and normal contact forces as defined in Figure 2.14. This sliding index is normalized between 0 and 1, $I_p = 1$ meaning that the Mohr-Coulomb criterion of the contact law is reached.

In Figure 4.8, probability density functions (pdf) associated with this sliding index are shown for the pre-stabilized sample corresponding to $\eta = 0.45$. The solid line corresponds to the reference pdf before the application of any stress increment while the dashed lines correspond to pdf reached after a

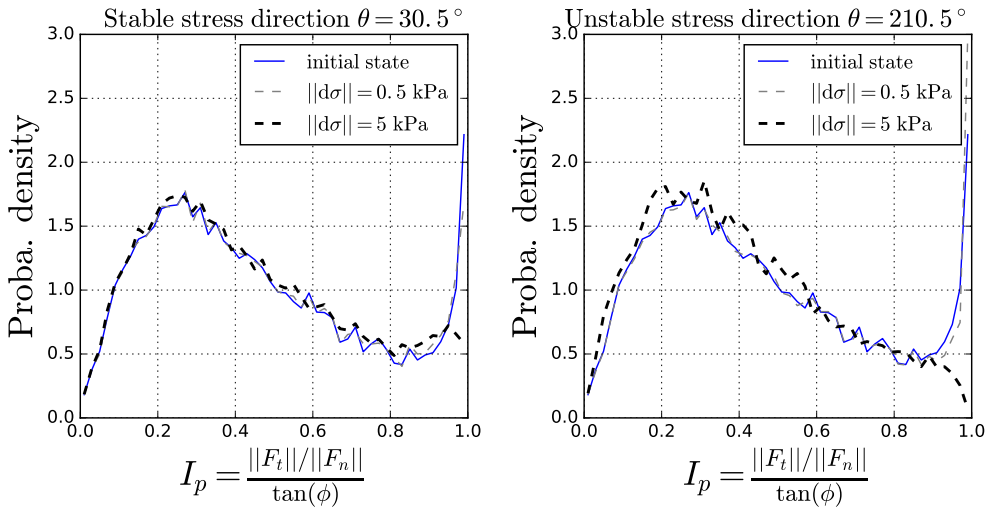

Figure 4.8 – Sliding index probability density functions before and after the application of an incremental stress for a stress ratio $\eta = 0.45$ and the two loading directions $\theta = 30.5°$ (left) and $\theta = 210.5°$ (right).

stress increment $||\mathbf{d\sigma}|| = 0.5$ kPa or $||\mathbf{d\sigma}|| = 5$ kPa. Two loading directions are considered as $\theta = 30.5°$ (stable direction) or $\theta = 210.5°$ (unstable direction).

In Figure 4.8, the initial pdf presents a "S" shape with a local maximum for $I_p \simeq 0.25$ and a maximum for $I_p = 1$. Indeed, in the initial configuration, a significant number of contacts have reached or are close to the Morh-Coulomb limit. For both θ directions, the application of a stress increments $||\mathbf{d\sigma}|| = 0.5$ kPa hardly changes the contact distribution whereas a larger stress increment of $||\mathbf{d\sigma}|| = 5$ kPa has a noticeable impact on the pdf as fewer contacts remain close to sliding. As a result, a finite stress increment is required to have an impact on the microstructure geometry which is required to observe the vanishing of the second-order work (Sibille et al., 2009; Froiio et al., 2010).

The comparison between the two loading directions for $||\mathbf{d\sigma}|| = 5$ kPa shows that for the unstable direction $\theta = 210.5°$, the probability density falls down to 0 for $I_p = 1$ which is not the case for $\theta = 30.5°$. Indeed, an incremental load in a stable direction will provoke a partial reorganisation of the microstructure through gain and loss of contacts, whereas an incremental load in an unstable direction will result in a complete microstructure reorganization. In both cases many contacts close to sliding are either lost or released and for $\theta = 210.5°$ no contacts remain close to sliding anymore.

In order to highlight the specific influence of the incremental stress $||\mathbf{d\sigma}||$

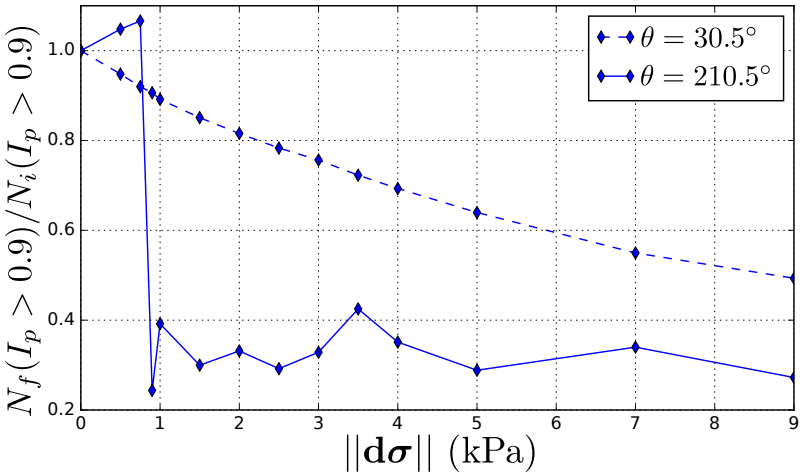

Figure 4.9 – Remaining fraction of contacts with a sliding index $I_p > 0.9$ with respect to the applied incremental stress magnitude for a stress ratio $\eta = 0.45$, an unstable direction $\theta = 210.5°$ (solid line) and a stable direction $\theta = 30.5°$ (dashed line).

on contact reorganizations, the fraction of contacts remaining close to sliding was investigated for $\theta \in \{30.5°; 210.5°\}$ and $\eta = 0.45$ for 14 values of $||\mathbf{d\sigma}||$. As in Figure 4.8 the shape of the pdfs remains mostly unchanged for $I_p < 0.9$, the contacts close to sliding are defined by $I_p > 0.9$.

In Figure 4.9, stable and unstable directions show completely different results. For $\theta = 30.5°$, the number of contacts remaining close to sliding smoothly decreases with $||\mathbf{d\sigma}||$ whereas a threshold value $||\mathbf{d\sigma^*}|| = 0.9$ kPa is observed for $\theta = 210.5°$. For $||\mathbf{d\sigma}|| < ||\mathbf{d\sigma^*}||$, the final number of contacts $N_f(I_p > 0.9)$ close to sliding increases monotonously by comparison with the initial one $N_i(I_p > 0.9)$. Then, for $||\mathbf{d\sigma}|| > ||\mathbf{d\sigma^*}||$ the remaining fraction of contacts close to sliding drops to a low value around 30 % and remains stable. These observations are consistent with the comments made previously and can be interpreted through a micromechanical approach of stability based on jamming analysis (Bagi, 2007). Indeed, an incremental loading along a stable direction will result in incremental modifications of the microstructure whereas an incremental loading along a unstable direction will result in a generalized unjamming/re-jamming process, provided that $||\mathbf{d\sigma}|| > ||\mathbf{d\sigma^*}||$. As a result, for unstable directions, there exists a threshold value responsible for the triggering of the observed instability. As soon as the threshold is reached, the size of the stress increment does not have any influence on the number of contacts close to sliding anymore. It should also be noted that

this value is found to depend on the loading rate and the direction of loading θ (not shown here).

The existence of a threshold value is consistent with DEM framework in which particle overlapping is allowed and controlled through a normal stiffness k_n. As a result, contact points are not limited to single points and the loss of contact requires a finite perturbation. In order to highlight the dependence of $||\mathbf{d}\boldsymbol{\sigma}^*||$ to k_n, a stiffening/softening experiment was carried out. k_n has been gradually increased or decreased from the initial value to a new value k_n^{new} while keeping constant the ratio k_n/k_t. After each incremental change in k_n^{new}/k_n the mechanical equilibrium is perturbed and the sample is let free to evolve until it re-stabilizes ($F_{\text{unb}} < 10^{-5}$) before changing again the normal stiffness. In Figure 4.10 the time evolution of k_n^{new}/k_n and the kinetic energy of the sample E_c are shown during the stiffening and softening experiments.

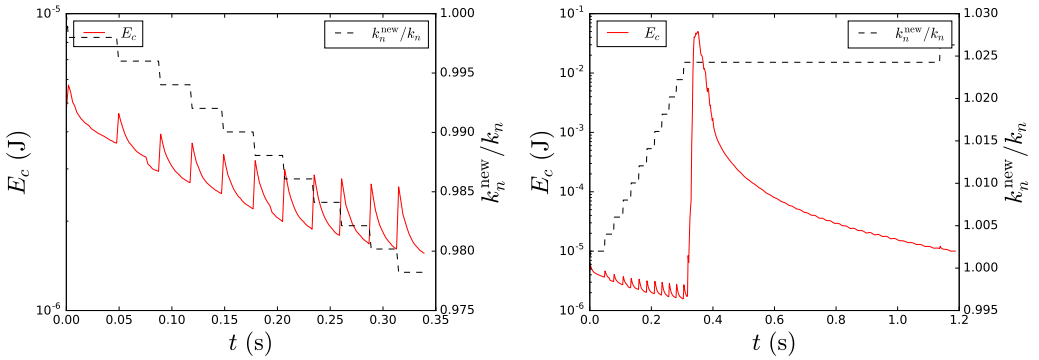

(a) Softening experiment

(b) Stiffening experiment

Figure 4.10 – Time evolution of k_n^{new}/k_n (dashed) and the kinetic energy of the sample E_c (solid) are shown during the stiffening and softening experiments.

In case where k_n^{new}/k_n is decreased, no inertial transition is observed and the small jumps in kinetic energy resulting from sudden changes in k_n^{new}/k_n rapidly vanish. On the contrary, when k_n^{new}/k_n is increased, the sample fails to adapt to the new stiffness value when k_n^{new}/k_n reaches 1.025. As a result, an outburst of kinetic energy is observed in Figure 4.10(b) as the sample collapses. This first observation shows that for a stiff material in an unstable state, a small perturbation can activate the underlying instability.

Complementary to Figure 4.10, a sensitivity analysis with respect to $||\mathbf{d}\boldsymbol{\sigma}||$ can be performed for the stabilized stiffer or softer samples. In Figure 4.11, the remaining fraction of contacts with a sliding index d smaller than 0.1 with respect to $||\mathbf{d}\boldsymbol{\sigma}||$ are given for different ratios k_n^{new}/k_n.

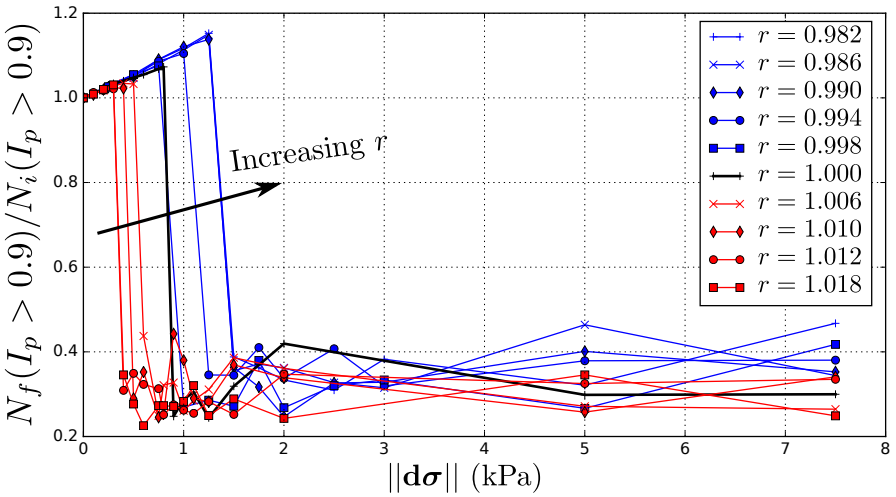

Figure 4.11 – Remaining fraction of contacts with a sliding index $I_p > 0.9$ with respect to the applied incremental stress magnitude for different ratios $r = k_n^{\text{new}}/k_n$ ($r > 1$ in red, $r = 1$ in black and $r < 1$ in blue). The unstable direction $\theta = 210.5°$ is considered.

In Figure 4.11, it can be seen that the stress threshold $||\mathbf{d\sigma}^*||$ depends on the normal stiffness. Without invoking non-linear effects coming from the geometry, this result is rather surprising as a larger k_n implies a smaller interpenetration but in the meantime a given incremental stress is expected to result in smaller changes in grain interpenetration. Since instability is considered, even small modifications of the sample geometry induced by changes in k_n or k_t can be sufficient to change the value of $||\mathbf{d\sigma}^*||$ necessary to trigger off microsructure modifications leading to the vanishing of the second-order work.

4.3 Micromechanical identification of driving mechanisms responsible for material instability

In the previous section, the mechanical stability of granular samples has been assessed at the scale of the REV and the onset of instability has been explained as the ability of an incremental load to trigger off microstructure reorganizations. If the mechanical state of the considered sample is in the bifurcation domain and loaded along an unstable direction, the incremental loading induces generalized microstructure reorganizations which result in a

macroscopic transient softening responsible for a loss of controllability. In the end, a new equilibrium is reached which is characterized by a contact population relatively far from sliding.

The purpose of this section is to provide a microscale investigation of the physical processes leading to the vanishing of the second-order work during the transient loss of controllability phase observed macroscopically in Figure 4.4. In all this section, the particular stress state $\eta = 0.45$ and the unstable loading direction $\theta = 210.5°$ are considered. A particular attention is paid to the chronology of events leading to the softening of the granular assembly.

4.3.1 Outbursts of kinetic energy

As regularly highlighted in the literature (di Prisco and Imposimato, 1997; Darve et al., 2004; Sibille et al., 2009; Nicot et al., 2012, 2009), the main ingredient enabling microstructure reorganizations in granular materials is the particles' kinetic energy. As a result, it is of particular interest to track the time evolution of the kinetic energy of the individual particles while applying a stress increment. In Figure 4.12, snapshots of the considered sample are shown for different time steps for two sufficiently large stress increments $||\mathbf{d}\boldsymbol{\sigma}|| \in \{1, 5\}$ kPa (see Figure 4.9). The particles are colored according to their kinetic energy, and the most energetic ones are highlighted. A threshold of $E_c^* = 10^{-8}$ J is chosen corresponding to the most energetic particles in the initial state.

In both cases, a localized burst of kinetic energy appears at the same spot and approximately at the same time (once $||\mathbf{d}\boldsymbol{\sigma}||$ reaches its targeted value in the 1 kPa case and during the transient increase of $||\mathbf{d}\boldsymbol{\sigma}||$ in the 5 kPa case). Then the local burst of kinetic energy propagates to the whole sample. In the case where $||\mathbf{d}\boldsymbol{\sigma}||$ is below the threshold value $||\mathbf{d}\boldsymbol{\sigma}^*||$ identified in section 4.2.4, no burst of kinetic energy is visible (not shown here). Indeed, the observed threshold value in direction $\theta = 210.5°$ corresponds to the minimal perturbation required to trigger off the burst of kinetic energy shown in Figure 4.12. Once initiated, the burst of kinetic energy propagate to the whole sample. The observed vanishing of the second-order work is thus a material property and not a structural one as the microstructure modifications do not stay localized in some regions of the sample with a length scale similar to the one of the whole sample.

The time evolution of the second-order work in Figure 4.6 can be reinterpreted in the light of these results. The initiation and the propagation of the burst of kinetic energy correspond to the decrease in W_2^{ext}. W_2^{ext} vanishes as soon as the burst of kinetic energy has propagated to the whole sample. This correlation is completely in line with Equation (2.6) that establishes the

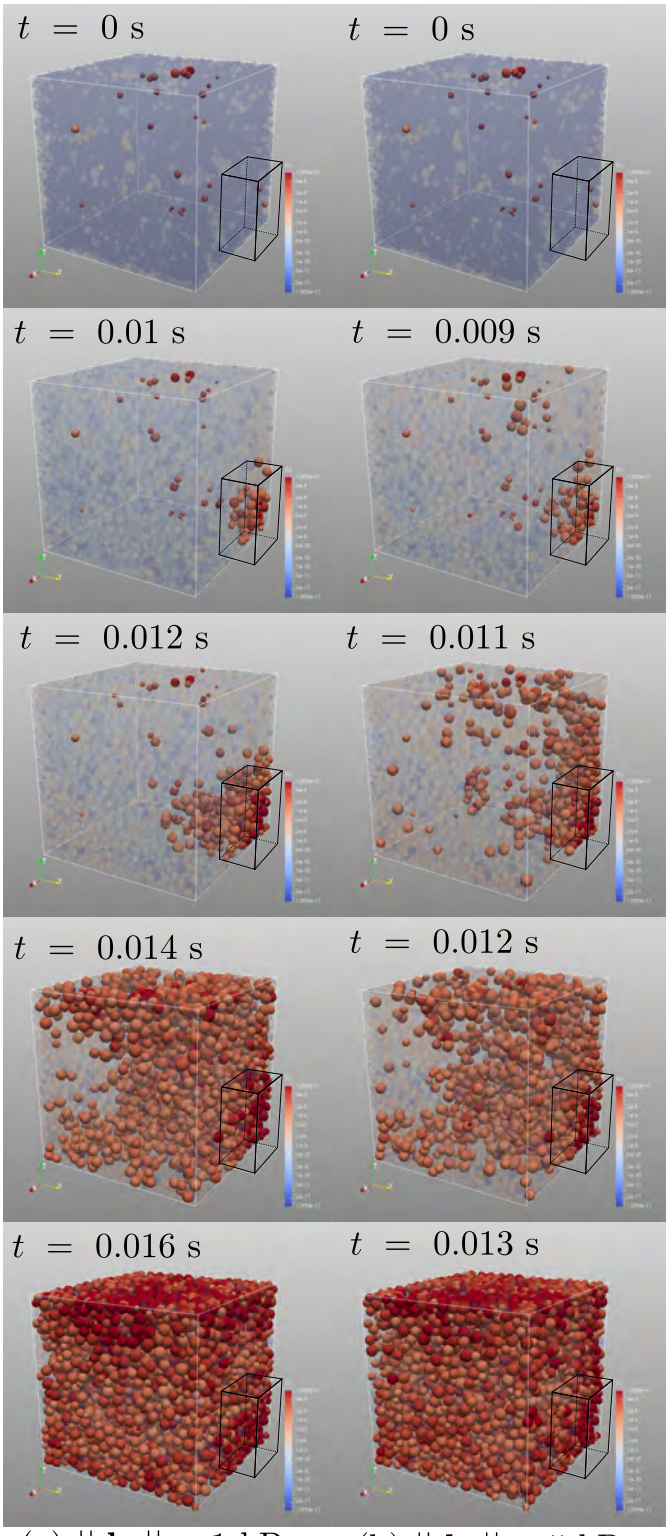

(a) $||\mathbf{d\sigma}|| = 1$ kPa (b) $||\mathbf{d\sigma}|| = 5$ kPa

Figure 4.12 – Onset and propagation of the burst of kinetic energy leading to the loss of controllability for $||\mathbf{d\sigma}|| = 1$ kPa (a) and $||\mathbf{d\sigma}|| = 5$ kPa (b). The sample considered is characterized by a stress ratio $\eta = 0.45$ and is loaded in an unstable direction $\theta = 210.5°$. Particles with $E_c > 10^{-8}$ J are highlighted. A control volume around the location of the kinetic burst is shown in black.

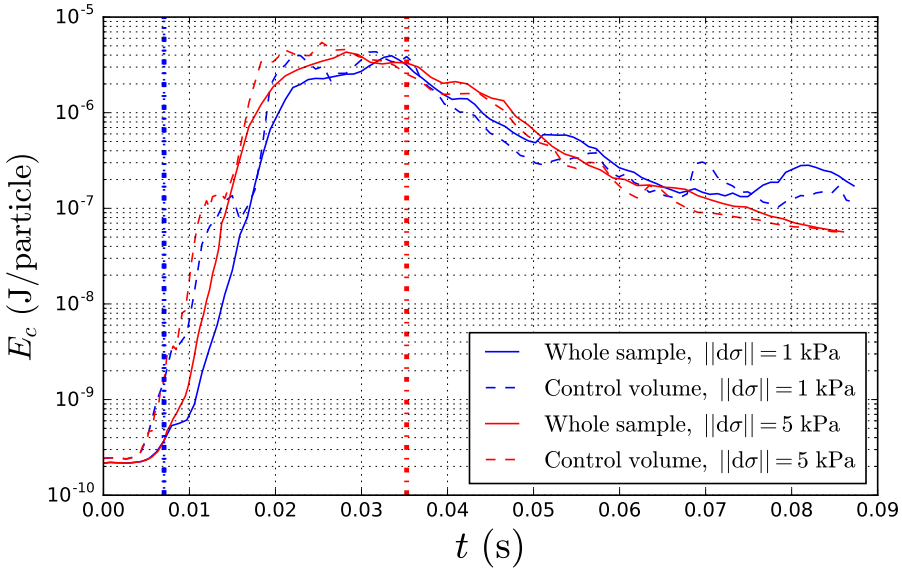

Figure 4.13 – Mean kinetic energy per particle for the whole sample and around the initiation of the kinetic burst. The sample considered is characterized by a stress ratio $\eta = 0.45$ and is loaded in an unstable direction $\theta = 210.5°$ with a stress increment $||\mathbf{d\sigma}|| = 1$ kPa (blue) or $||\mathbf{d\sigma}|| = 5$ kPa (red). The end of the imposed transient loadings (see Section 4.2.2) are shown by dash-dot lines.

close relation between the kinetic energy, the internal second-order work and the external second-order work.

In order to describe the onset and the propagation of the burst of kinetic energy, the time evolution of the mean kinetic energy per particle is plot in Figure 4.13 for the whole sample and for the small control volume visible in Figure 4.12.

In Figure 4.13, an early increase in the mean kinetic energy per particle occurs simultaneously in the control volume for $||\mathbf{d\sigma}|| = 1$ kPa and $||\mathbf{d\sigma}|| = 5$ kPa for $t \simeq 0.005$ s. This corresponds to the initiation of the burst of the kinetic energy shown in Figure 4.12. After $t \simeq 0.015$ s the kinetic energy per particle follows the same evolution in the control volume and for the whole sample. This marks the end of the propagation of the burst of the kinetic energy. For $||\mathbf{d\sigma}|| = 1$ kPa, the transient incremental loading is stopped before the end of the kinetic burst propagation (blue dotted line). As a result, a small plateau is observed in the general increase in the kinetic energy corresponding to the time needed for the instability to affect the whole sample. Such a plateau is not observed for $||\mathbf{d\sigma}|| = 5$ kPa as kinetic energy is

continuously provided through evolving boundary conditions (the end of the transient loading is reached even after the mean kinetic energy per particle reaches its maximum).

4.3.2 Chained particle populations renewal

As recalled in Section 2.3.2 and re-examined in Section 3.2.1, the macroscopic mechanical behavior of granular materials relies on a limited number of grains organized in mesostructures called force chains. It has been shown, that the strength of a granular material results from its ability to build relatively long force chains and to constantly rearrange the existing force chains to cope with any change in the boundary conditions (Tordesillas et al., 2011; Zhu et al., 2016a; Wautier et al., 2017).

Still based on the force chain definition of Peters et al. (2005), the chained particles responsible for stress transmission can be identified in the initial state and tracked while the incremental stress is applied. By comparing the current set of chained particles to the initial one, force chain renewal can be quantified as N_{born} current chained particles were not identified as such initially and N_{died} initial chained particles are no longer identified as such. A visualization of the force chains identified before and after the application of a stress probe leading to the vanishing of the second-order work is shown in Figure 4.14 as well as the time evolution of the total number of chained particles (N_{tot}) and the time evolution of the new and former ones (N_{born} and N_{died}).

In this figure the microstructure evolution induced by the applied incremental stress is visible. Between the initial and final states roughly 50 % of the chained particles are renewed while the total number of chained particles remains quasi-constant (a slight decrease from 2821 to 2661 chained particles is observed). In addition, in the final state the vertical anisotropy of the force chains seems visually to be less pronounced than initially.

4.3.3 Chained particles lifespan and life expectancy

In order to detect birth and death of force chains, the notions of lifespan and life expectancy are introduced similarly as in Zhu et al. (2016a). This analysis is not carried out directly on force chains but on groups of three chained particles that constitute the elementary bricks of force chains. For a given time t and a given group of three chained particles g, the lifespan $\ell_s(t, g)$ is defined as

$$\ell_s(t,g) \;=\; \frac{t - t_g^{\text{birth}}}{t - t_i}, \qquad \ell_s(t,g) \in [0,1] \tag{4.7}$$

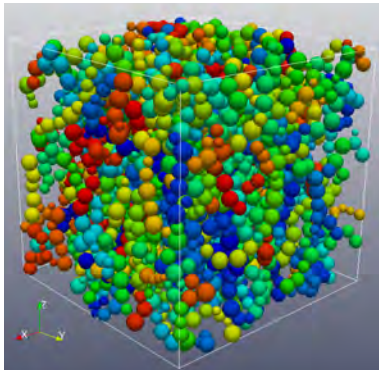

(a) Initial state, $\eta = 0.45$

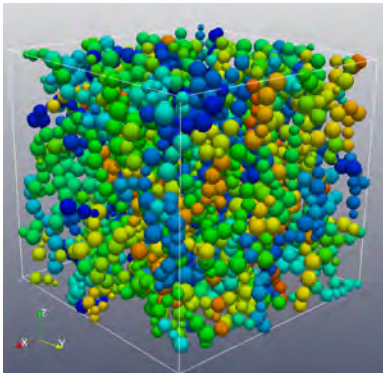

(b) Final state, $\eta = 0.45$
$\theta = 210.5°, ||\mathbf{d\sigma}|| = 5$ kPa

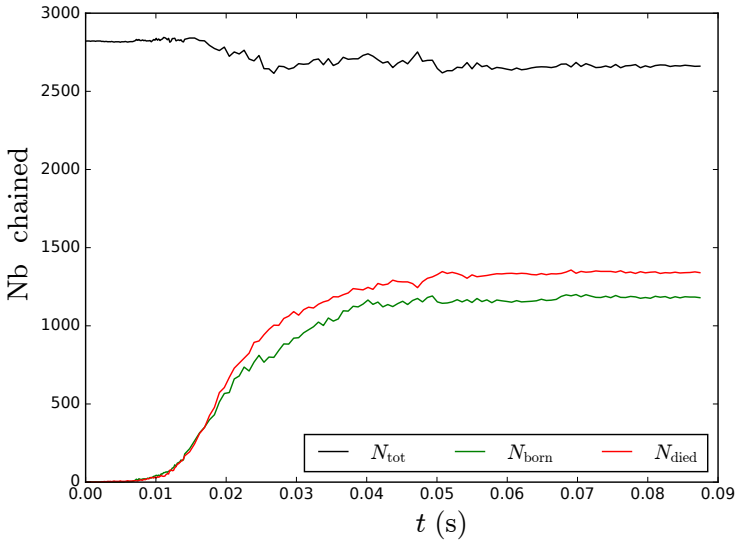

(c) Chained particles renewal, $\eta = 0.45$ $\theta = 210.5°$

Figure 4.14 – Visualization of force chains identified in the initial (a) and final (b) configurations for a stress ratio $\eta = 0.45$ in an unstable direction $\theta = 210.5°$ for $||\mathbf{d\sigma}|| = 5$ kPa. Force chains are composed of contacting particles of same color. (c) Time evolution of the number of chained particles (black), the number of new (green) and former (red) chained particles compared with the initial state.

where $t_i = 0$ is the time at which the incremental stress is applied and t_g^{birth} is the time at which the three particles composing g were first identified as chained particles and from which they remain continuously identified as such until the current time t. $\ell_s(t, g) = 1$ means that the group g of three chained particles have been existing since the initial configuration before the incremental stress is applied. On the contrary, $\ell_s(t, g) = 0$ means that g has just appeared.

Similarly, the life expectancy $\ell_e(t, g)$ of g computed at time t is defined as

$$\ell_e(t, g) \;=\; \frac{t_g^{\text{death}} - t}{t_f - t}, \qquad \ell_e(t, g) \in [0, 1] \tag{4.8}$$

where $t_f = 0.087$ s is the time at which a new equilibrium ($F_{\text{unb}} < 10^{-5}$) is reached after the application of the incremental stress $boldsymbol{\mathrm{d}\sigma}$ and t_g^{death} is the time at which the three particles composing g were last identified as chained particles starting from time t. $\ell_e(t, g) = 1$ means that the group g of three chained particles exists until the final stabilization of the sample. On the contrary, $\ell_e(t, g) = 0$ means that g is about to disappear.

In Figure 4.15, the probability density functions p_s and p_e are shown for different time $t \in [t_i, t_f]$ in order to identify whether the current force chains are rather young or old and whether they have a long life ahead or are about to disappear.

In the beginning of the incremental loading, the force chains are stable as all groups of three chained particles are old with a non-zero life expectancy. This statement remains true when the burst of kinetic energy identified in the previous subsection initiates and propagates to the whole sample ($t \in [0.005, 0.013]$ s). From the moment that the kinetic energy reaches its maximum level ($t = 0.0388$ s), groups of three particles start collapsing replaced by young force chains with a short life expectancy. Once the kinetic energy of the sample start decreasing (from $t = 0.0634$ s) some time after the targeted stress increment reaches its final value ($t = 0.035$ s), force chains become stable again as an aging population of force chains with a long life expectancy is encountered.

The main conclusions to be retained from this analysis are that:

- the initiation of the burst of kinetic energy is not due to the destruction of force chains;

- the loss of controllability appears prior to the generalized collapse of force chains;

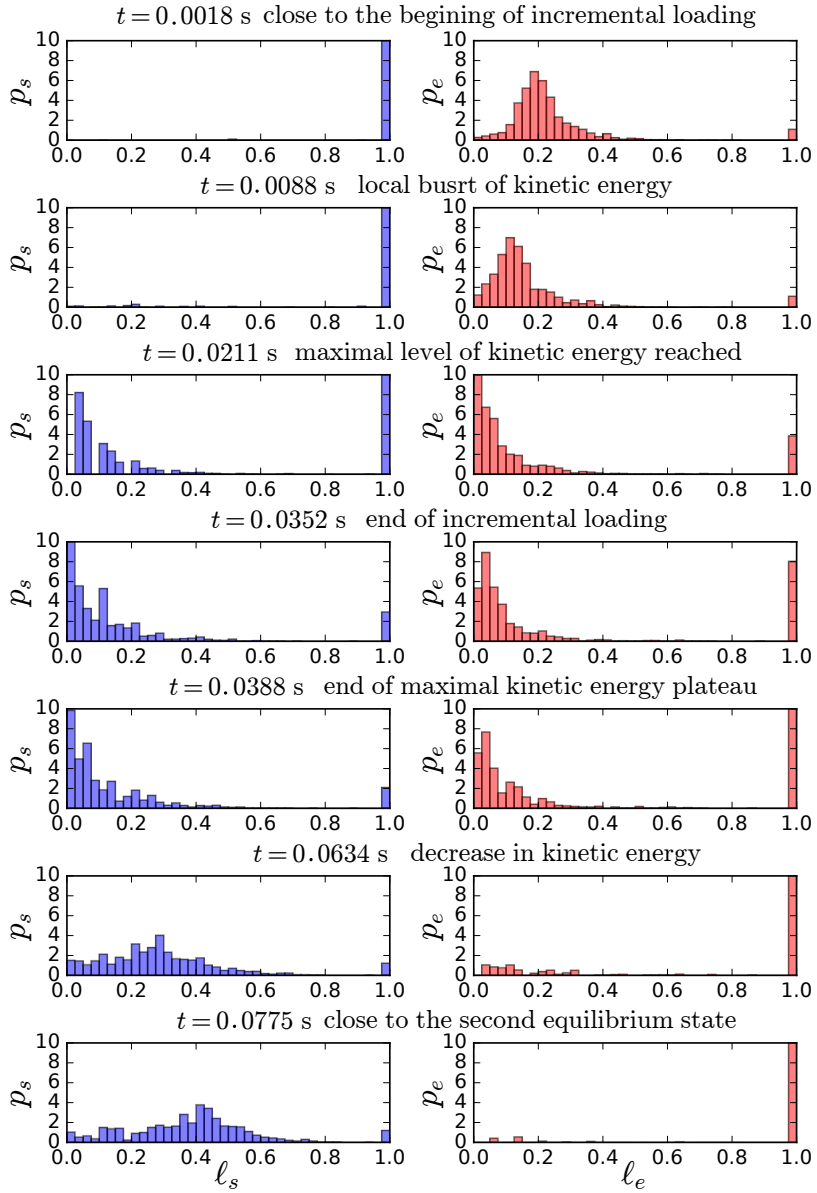

Figure 4.15 – Probability density histograms associated to the lifespan (left) and life expectancy (right) of the groups of three chained particles at different moments of the incremental loading. The sample considered is characterized by a stress ratio $\eta = 0.45$ and is loaded in an unstable direction $\theta = 210.5°$ with a stress increment $||\mathbf{d\sigma}|| = 5$ kPa. A high value of p_s around 1 corresponds to the presence of old force chains, a high value of p_e around 1 corresponds to the presence long lasting force chains.

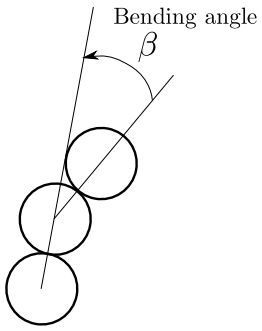

Figure 4.16 – Group of three chained particles (g) and geometric definition of the bending angle β.

- the force chains reorganization appears simultaneously with the maximum level of kinetic energy;

- the final stabilization of the sample is reached as soon as long lasting force chains appear.

4.3.4 Localized force chain bending

As the loss of controllability occurs prior to the destruction of force chains, their collapse should not be regarded as the triggering microscale mechanism responsible for the onset of the burst of kinetic energy (Tordesillas et al., 2010). Force chains are elongated column like structures loaded in compression. As a result, their effective failure is very likely to be related to the onset of bending, before destruction of any force chains (notice that the word bending is preferred to the term buckling frequently used in existing literature as it relies only on a geometric definition without any force or stress ingredients). Given a group of three chained particles g for which two contact directions form an angle $\beta \in [0, \pi]$, the bending rate $\dot{\beta}$ is simply the time derivative of β (see Figure 4.16). A strictly positive value $\dot{\beta} > 0$ characterize the bending of g.

In Figure 4.17, a zoom of the time evolution of the mean kinetic energy and the mean bending rate are shown for the whole sample and a small control volume around the location of the burst of kinetic energy (see Figure 4.12). On the first graph, the evolution of the difference between the actual incremental stress components and their prescribed values is shown.

In this figure, both the loss of controllability, the onset of the burst of kinetic energy and the increase in the bending rate in the control volume shown in Figure 4.12 occur simultaneously for $t \simeq 0.008$ s, approximately

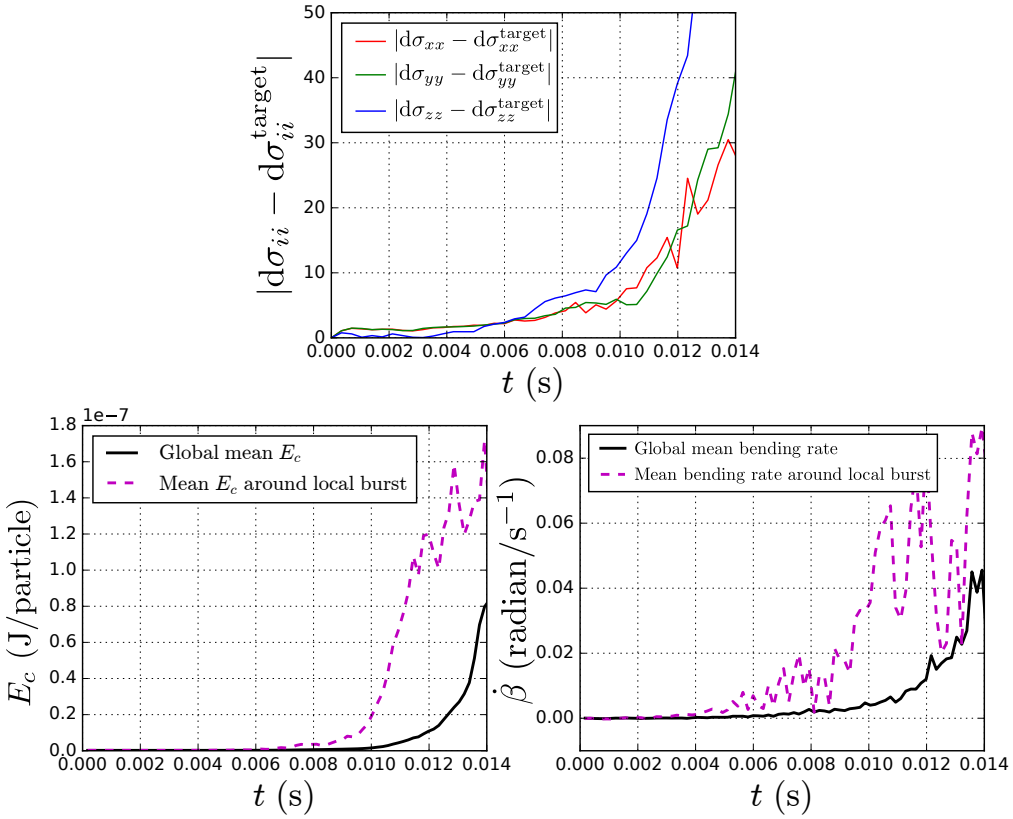

Figure 4.17 – Absolute error between the actual stress components and their targeted values during the incremental stress loading (top), mean kinetic energy per particle for the whole sample and close to initiation of the kinetic burst (bottom left), mean bending rate of the groups of three chained particles for the whole sample and around the kinetic burst (bottom right). The sample considered is characterized by a stress ratio $\eta = 0.45$ and is loaded along an unstable direction $\theta = 210.5°$ with a stress increment $||\mathbf{d\sigma}|| = 5$ kPa.

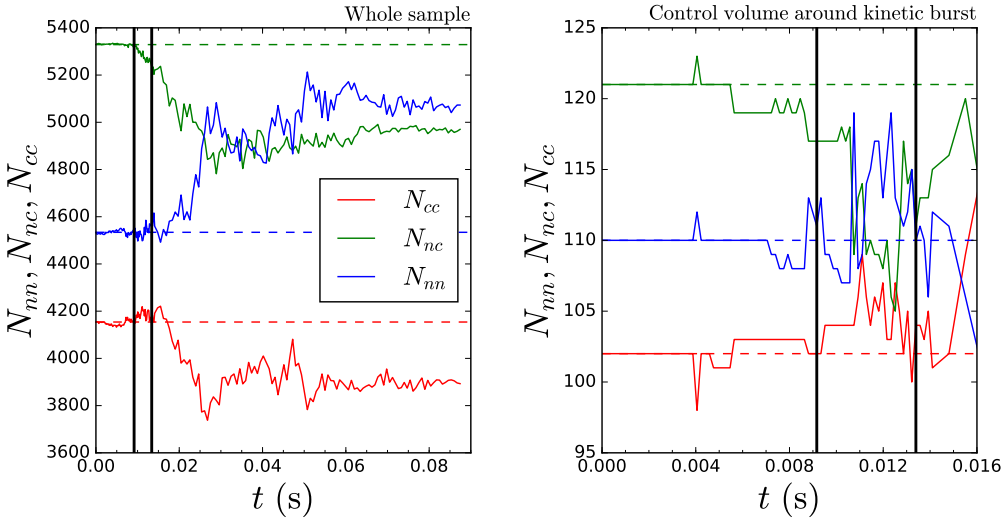

Figure 4.18 – Time evolution of the number of contacts between two chained particles (N_{cc}), two non-chained particles (N_{nn}) and a non-chained and a chained particle (N_{nc}). The evolution is given for the whole sample (left) and for the control volume shown in Figure 4.12 (right). The onset and the propagation of the burst of kinetic energy is delimited by two vertical lines. The sample considered is characterized by a stress ratio $\eta = 0.45$ and is loaded along an unstable direction $\theta = 210.5°$ with $||\mathbf{d\sigma}|| = 5$ kPa.

0.007 s prior to a general increase in mean kinetic energy per particle and mean bending rate for the whole sample (black solid curves in Figure 4.17). Indeed, the localized bending of a few force chains seems to be sufficient to generate a loss of controllability at the scale of the REV.

As recently shown for 2D granular assemblies, force chain loss of stability results from the opening of contacting grain cycles (Tordesillas et al., 2010, 2011; Zhu et al., 2016b). In order to investigate this feature in 3D, the time evolutions of the number of contacts between two chained particles (N_{cc}), two non-chained particles (N_{nn}) and a non-chained and a chained particle (N_{nc}) are represented in Figure 4.18. As in Figure 4.17, the time evolutions are given for the whole sample and for the same control volume around the location of the burst of kinetic energy (see Figure 4.12). The onset and the propagation of the burst of kinetic energy are indicated by two vertical solid lines.

In Figure 4.18, the number of non-chained/chained contacts (N_{nc}) decreases in the control volume even prior to the onset of the burst of kinetic energy while N_{nn} and N_{cc} remain more or less constant up to the end of the propagation of the burst of kinetic energy. This observation suggests that the

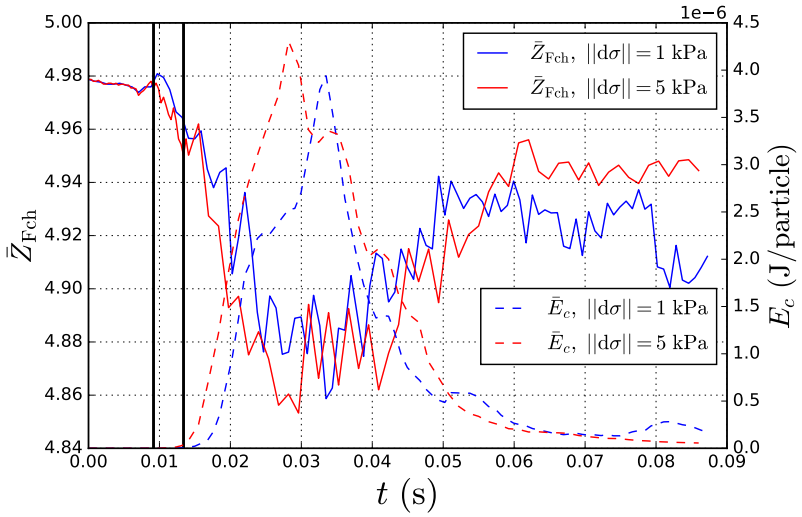

Figure 4.19 – Evolution of the mean coordination number of the chained particles for the two stress increments $||\mathbf{d\sigma}|| = 1$ kPa (blue) and $||\mathbf{d\sigma}|| = 5$ kPa (red). The onset and propagation of the kinetic energy burst are indicated by vertical lines while the mean kinetic energies are shown with dashed lines. The sample considered is characterized by a stress ratio $\eta = 0.45$ and is loaded in an unstable direction $\theta = 210.5°$.

localized bending highlighted in Figure 4.17 results from an early unjamming of force chains within the used control volume (and consequently a local dilatancy). The evolution of N_{cc}, N_{nn} and N_{nc} for the whole sample confirms this mechanism with a generalized drop in N_{nc} observed during the propagation of the burst of kinetic energy. This failure mechanism is consistent with the 2D opening of the three particles loops around force chains mentioned in Tordesillas et al. (2011) or Zhu et al. (2016b). In the end, following the generalized collapse of force chains, the initially loose sample gets denser and the number of contacts between non-chained particles increases. The decrease in N_{cc} follows qualitatively the trend mentioned in section 4.3.2 for the number of chained particles. However, as the number of chained particles is reduced by roughly 160, N_{cc} drops by approximately 260. This might result from changes in the topology of force chains (less branching or shorter chains for instance).

Complementary to Figure 4.18, the evolution of the mean coordination number of the particles belonging to force chains ($\overline{Z}_{\mathrm{Fch}}$) is shown in Figure 4.19 for $||\mathbf{d\sigma}|| \in \{1, 5\}$ kPa.

In Figure 4.19, the evolution of the mean kinetic energy for the whole sample is shown in dashed lines while the onset and propagation of the burst

of kinetic energy are still indicated by two vertical solid lines. As soon as the incremental load starts, $\overline{Z}_{\mathrm{Fch}}$ drops which is a signature of local dilatancy around force chains. This decrease in $\overline{Z}_{\mathrm{Fch}}$ appears before any noticeable increase in kinetic energy and its decreasing rate accelerates as the local burst of kinetic energy appears. These observations are consistent with the failure mechanism identified previously. In addition, it should be noted that drops in $\overline{Z}_{\mathrm{Fch}}$ occur simultaneously for $||\mathbf{d}\boldsymbol{\sigma}|| = 1$ kPa and $||\mathbf{d}\boldsymbol{\sigma}|| = 5$ kPa (both above the threshold value identified in section 4.2.4) so as the onset of the burst of kinetic energy. In the case $||\mathbf{d}\boldsymbol{\sigma}|| = 1$ kPa, the drop is observed after the end of the transient incremental loading while for $||\mathbf{d}\boldsymbol{\sigma}|| = 5$ kPa, the drop occurs during the transient increase of $||\mathbf{d}\boldsymbol{\sigma}||$ from 0 to 5 kPa (see Figure 4.13). As a result, the failure mechanism seems to be triggered off as soon as the incremental stress overcomes the threshold value $||\mathbf{d}\boldsymbol{\sigma}^*|| = 0.9$ kPa (see section 4.2.4). Then, the failure is not instantaneous and develops in an intrinsic timespan which is independent of the size of the stress increment. The concept of delayed instability observed experimentally in soils by di Prisco and Imposimato (1997) is recovered here at the microscale on a shorter timescale.

4.4 Phenomenological relation between plastic strain and mechanical stability

After detailed microscale analyses of the elementary mechanisms leading to the vanishing of the second-order work, this section focuses on the effect of changes in material properties on the existence of mechanical instability. In order to so, discrete and continuum modeling of granular materials are linked by fitting a non-associated elasto-plastic model based on DEM data to account for the incremental non-linearity of the material loaded under a stress ratio $\eta = 0.45$. This model is then used to exhibit the importance of plastic strain with respect to the existence of mechanical instability.

4.4.1 Elasto-plastic model fitting procedure based on DEM results

At the macroscale, irreversible microscale grain rearrangements are usually accounted for through plastic theory as long as they remain rate-independent. For frictional granular materials such as soils or rocks, it is well established that the normality of the flow rule as proposed by Drucker and Prager (1952) does not hold and the plastic behavior is non-associated. For such materials,

the volume change predicted by an associated flow rule is indeed significantly larger than that observed in experiments with soils or rocks. To account for these observations, the choice of a potential surface different from the yield surface is often used to accommodate a much smaller volume change. Such a continuum scale modeling is used in the following to account for the incremental behavior of granular materials. As a result, the incremental strain $\mathbf{d}\boldsymbol{\varepsilon}$ corresponding to an incremental stress $\mathbf{d}\boldsymbol{\sigma}$ is assumed to be additively broken down into an elastic part $\mathbf{d}\boldsymbol{\varepsilon}^e$ and a plastic one $\mathbf{d}\boldsymbol{\varepsilon}^p$ such that $\mathbf{d}\boldsymbol{\varepsilon} = \mathbf{d}\boldsymbol{\varepsilon}^e + \mathbf{d}\boldsymbol{\varepsilon}^p$. This is indeed an approximation as rigorously speaking this additive decomposition does not hold (Nicot and Darve, 2006b).

To extract the elastic part $\mathrm{d}\boldsymbol{\varepsilon}^e$ of the total incremental strain, one of the following two approaches found in the literature can be used:

- by successively imposing an incremental stress loading and unloading in the same direction. The residual strain is then considered to be equal to the plastic strain (Bardet, 1994; Kishino, 2003). This method is based on the hypothesis that only reversible deformations occur during the unloading and that no elastic unloading is prevented because of grain rearrangements during the loading phase.

- by performing the same incremental stress loading twice with two different contact friction angles: the material friction angle ϕ and a non-dissipative friction angle of 90°. This method prevents any plastic dissipation through friction when $\phi = 90°$ but does not prevent contact gain and loss which could result in non-reversible microstructure changes (the kinetic energy released form these events is partly dissipated through numerical damping). However, these irreversible changes do not impact the macroscopic behavior significantly as long as the amplitude of the loading increment remains small. Under this condition the observed strain can be considered to be fully elastic (Nicot and Darve, 2007a; Sibille et al., 2009; Calvetti, 2003).

Following the work of Nicot et al. (2007) and Calvetti (2003) the second method was used since no hysteresis was observed while performing incremental loading and unloading with a friction angle of 90°.

A systematic way to track the incremental behavior of a given material consists in performing a directional analysis as introduced by Gudehus (1979). By imposing, for instance, stress probes in different directions in the stress space and recording the corresponding strain responses, the incremental behavior is then given by the implicit relation between incremental stress and incremental strain. As previously shown by Nicot and Darve (2007a), the existence of a flow rule in granular materials is limited to axisymmetric

loading conditions. As a result, the directional analyses performed in this chapter are restricted to the Rendulic plane $(\sqrt{2}\mathrm{d}\sigma_{xx}, \mathrm{d}\sigma_{zz})$ (this corresponds to the plane $\mathrm{d}\sigma_{xx} = \mathrm{d}\sigma_{yy}$ in the stress space). By considering $\sqrt{2}\mathrm{d}\sigma_{xx}$ instead of $\mathrm{d}\sigma_{xx}$, scalar products in the Rendulic plane correspond to scalar products computed directly in the three dimensional stress space $(\mathrm{d}\sigma_{xx}, \mathrm{d}\sigma_{yy}, \mathrm{d}\sigma_{zz})$.

In the inset of Figure 4.20, incremental elastic strains are plotted in the axisymmetric plane $(\sqrt{2}\mathrm{d}\varepsilon^e_{xx}, \mathrm{d}\varepsilon^e_{zz})$ while incremental stress probes describe a circle in the Rendulic plane $(\sqrt{2}\mathrm{d}\sigma_{xx}, \mathrm{d}\sigma_{zz})$, the parametric equation of which is given by

$$\left\{ \begin{array}{rcl} \sqrt{2}\mathrm{d}\sigma_{xx} = \sqrt{2}\mathrm{d}\sigma_{yy} & = & ||\mathbf{d\boldsymbol{\sigma}}|| \ \cos\theta \\ \mathrm{d}\sigma_{zz} & = & ||\mathbf{d\boldsymbol{\sigma}}|| \ \sin\theta \\ ||\mathbf{d\boldsymbol{\sigma}}|| & = & \sqrt{\mathrm{d}\sigma_{zz}^2 + 2\ \mathrm{d}\sigma_{xx}^2} \end{array} \right. , \tag{4.9}$$

where $||\mathbf{d\boldsymbol{\sigma}}|| = 5$ kPa and $\theta \in [0, 2\pi]$.

Extending Bardet's 2D work (Bardet, 1994), the incremental elastic strain envelope shown in Figure 4.20 is typical of an incremental anisotropic elastic behavior. Let us assume that the sample behaves as a transverse isotropic material. This hypothesis is based on the following two points i) the sample preparation procedure results in an isotropic sample and ii) the triaxial loading introduces an anisotropy in the vertical direction (see Figure 3.11). Thus, in the Rendulic plane, the constitutive matrix relating the incremental strain to the imposed incremental stress reads as:

$$\begin{pmatrix} \sqrt{2}\mathrm{d}\varepsilon^e_{xx} \\ \mathrm{d}\varepsilon^e_{zz} \end{pmatrix} = \begin{pmatrix} \frac{1-\nu_h}{E_h} & -\sqrt{2}\frac{\nu_{hv}}{E_h} \\ -\sqrt{2}\frac{\nu_{hv}}{E_h} & \frac{1}{E_v} \end{pmatrix} \cdot \begin{pmatrix} \sqrt{2}\mathrm{d}\sigma_{xx} \\ \mathrm{d}\sigma_{zz} \end{pmatrix} \tag{4.10}$$

where E_h and E_v are the Young modulus in the horizontal and vertical directions respectively and ν_h and ν_{hv} are the Poisson ratios between horizontal directions and between the horizontal and the vertical directions, respectively.

While $\mathbf{d\boldsymbol{\sigma}}$ describes a circle in the Rendulic plane (Equation (4.9)), $\mathbf{d\boldsymbol{\varepsilon}}$ describes a tilted ellipse in the axisymmetric plane $(\sqrt{2}\mathrm{d}\varepsilon^e_{xx}, \mathrm{d}\varepsilon^e_{zz})$ with the following parametric equation:

$$\left\{ \begin{array}{rcl} \sqrt{2}\mathrm{d}\varepsilon^e_{xx} = \sqrt{2}\mathrm{d}\varepsilon^e_{yy} & = & ||\mathbf{d\boldsymbol{\sigma}}|| \left[\frac{1-\nu_h}{E_h}\cos\theta - \frac{\sqrt{2}\nu_{hv}}{E_h}\sin\theta \right] \\ \mathrm{d}\varepsilon^e_{zz} & = & ||\mathbf{d\boldsymbol{\sigma}}|| \left[-\frac{\sqrt{2}\nu_{hv}}{E_h}\cos\theta + \frac{1}{E_v}\sin\theta \right] \end{array} \right. . \tag{4.11}$$

By minimizing the quadratic error between the numerical points and Equation (4.11), a very good prediction of the numerical results is achieved

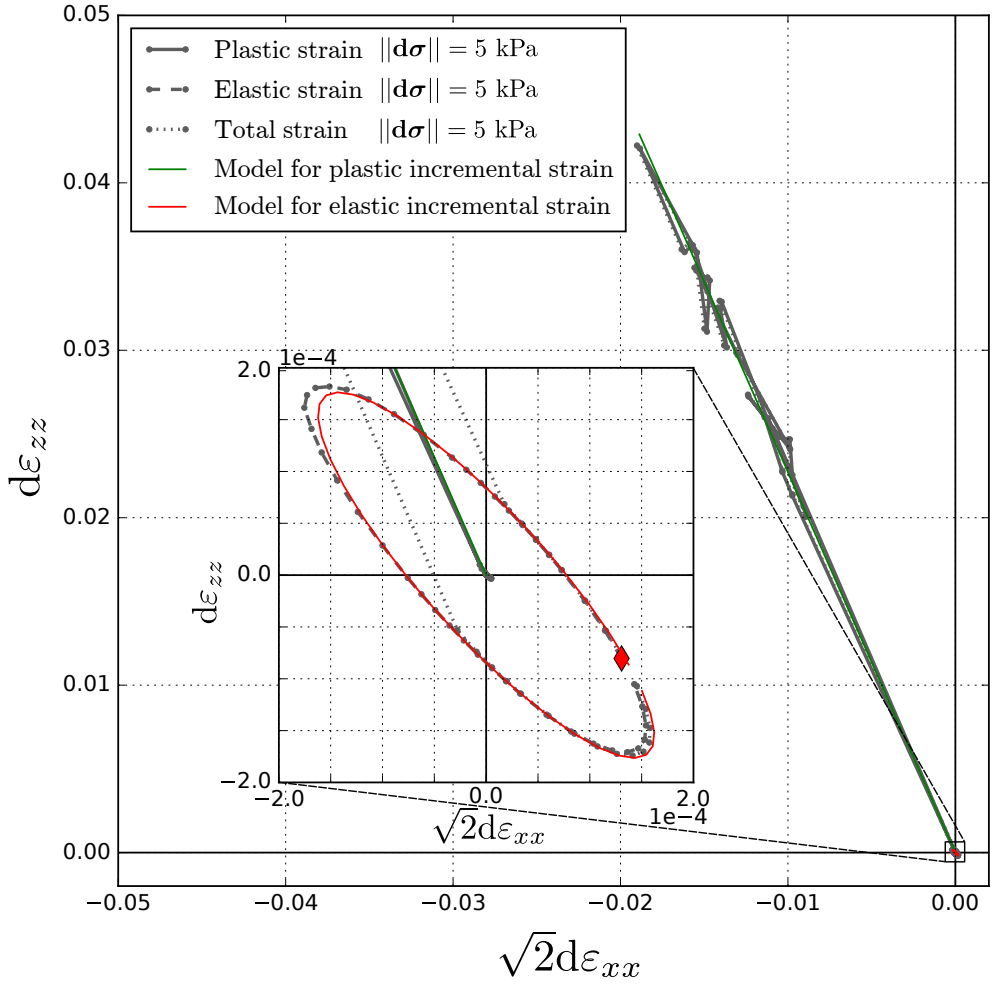

Figure 4.20 – Incremental strain responses in axisymmetric plane for the sample corresponding to $\eta = 0.45$ while incremental stress probes describe a circle in the Rendulic plane (Equation (4.9)). The total incremental strain (dotted line) is broken down into its elastic (dashed line) and plastic parts (solid line). The point corresponding to $\theta = 0$ is shown with a diamond in the inset plot. Fitted elastic and plastic models for incremental strains are shown with thin solid lines.

by choosing $E_h = 25.2$ MPa, $E_v = 32.5$ MPa and $\nu_h = \nu_{hv} = \nu = 0.31$. The resulting fitted model is shown in Figure 4.20[2].

As summarized in Figure 4.23, the elastic incremental behavior is accounted for in the Rendulic plane through three material constants E_h, E_v and ν. It must be stressed here that the choice $\nu_h = \nu_{hv}$ is arbitrary and has no reason to hold. Indeed, the three independent material constants at stake in Equation (4.10) are $\frac{1-\nu_h}{E_h}$, $\frac{\nu_{hv}}{E_h}$ and E_v. However, assuming $\nu_h = \nu_{hv}$ is though convenient to benchmark the present material parameters to classical Young modulus obtained for uniformly distributed loose sands that range from 10 to 30 MPa. Based on the load history, the vertical compaction induces the building of force chains mainly aligned in this direction (see Figure 3.11). As a result, the sample is expected to be stiffer in the vertical direction than in the horizontal one which is consistent with $E_v > E_h$.

As discussed in Bardet (1994) in 2D, the inclination of the ellipse is linked to the ratio between E_h and E_v. In order to compute the tilt angle of the ellipse, let us first compute the square of the distance between a point from the ellipse and the origin in Equation (4.11):

$$r^2/||\mathbf{d}\boldsymbol{\sigma}||^2 = (a^2+b^2)\cos^2\theta + (c^2+b^2)\sin^2\theta - 2b(a+c)\cos\theta\sin\theta \quad (4.12)$$

where $a = \frac{1-\nu_h}{E_h}$, $b = \sqrt{2}\frac{\nu_{hv}}{E_h}$ and $c = \frac{1}{E_v}$.

The major and minor directions of the ellipse correspond to extremal values. As a result they correspond to the vanishing of the derivative

$$\frac{\mathrm{d}r^2/||\mathbf{d}\boldsymbol{\sigma}||^2}{\mathrm{d}\theta} = (c^2-a^2)\sin(2\theta) - 2b(a+c)\cos(2\theta) \quad (4.13)$$

By introducing an angle $\tilde{\theta}$ such that

$$\begin{cases} \cos\tilde{\theta} &= \frac{2b(a+c)}{\sqrt{(c^2-a^2)^2+4b^2(a+c)^2}} \\ \sin\tilde{\theta} &= \frac{c^2-a^2}{\sqrt{(c^2-a^2)^2+4b^2(a+c)^2}} \end{cases}, \quad (4.14)$$

Equation (4.13) can be written as

$$\frac{\mathrm{d}r^2/||\mathbf{d}\boldsymbol{\sigma}||^2}{\mathrm{d}\theta} = -\sqrt{(c^2-a^2)^2+4b^2(a+c)^2}\cos(2\theta+\tilde{\theta}). \quad (4.15)$$

As a result, major θ_t^+ and minor θ_t^- directions are given by

$$\theta_t^{\pm} = -\frac{\tilde{\theta}}{2} \pm \frac{\pi}{4} \quad (4.16)$$

[2]It should be underlined here that the fitting procedure assumes the major symmetry of the constitutive tensor. This is not necessarily the case for granular materials for which the rigorous definition of a strain energy is not possible as soon as contact gain and loss occur.

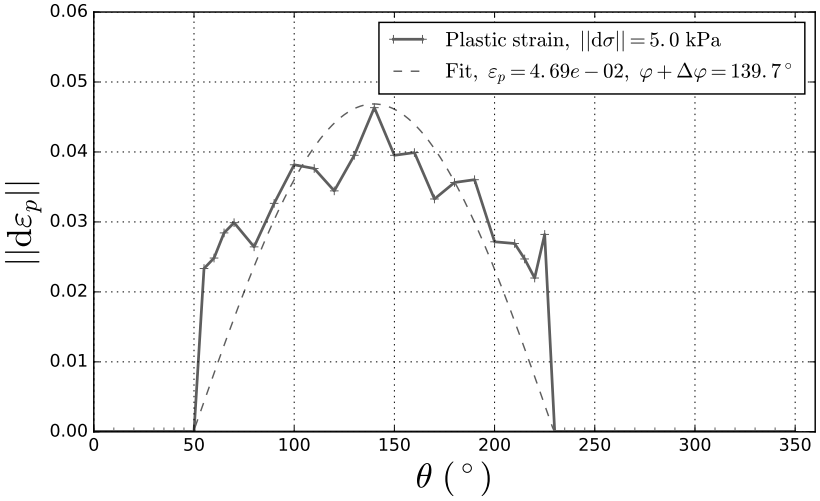

Figure 4.21 – Evolution of the norm of the incremental plastic strain $||\mathbf{d}\boldsymbol{\varepsilon}^p||$ with respect to the loading angle θ. Numerical results are shown as a solid line while the fitted truncated cosine function is shown as a dashed line.

By using the fitted values recalled in Table 4.1, we found in our case $\theta_t^+ = -50.4°$. Compared with the isotropic case ($E_h = E_v = E$), the isotropic tilted angle is found to be independent of E and ν as

$$\left\{ \begin{array}{rcl} \cos\tilde{\theta}_{\text{iso}} & = & \frac{2\sqrt{2}}{3} \\ \sin\tilde{\theta}_{\text{iso}} & = & \frac{1}{3} \end{array} \right. , \tag{4.17}$$

which corresponds to $\theta_t^{\text{iso}+} = -54.7°$.

By subtracting the incremental elastic strain from the total strain, the plastic contribution is then recovered. In Figure 4.20, $\mathbf{d}\boldsymbol{\varepsilon}^p$ is plotted in the axisymmetric plane whereas the norm $||\mathbf{d}\boldsymbol{\varepsilon}^p||$ is plotted against the stress probe angle θ in Figure 4.21.

In Figure 4.20, the plastic strain concentrates in a single direction φ whatever the loading direction θ. This indicates a typical flow rule the direction of which is φ in the plane $(\sqrt{2}\mathrm{d}\varepsilon_{xx}, \mathrm{d}\varepsilon_{zz})$. In Figure 4.21, the plastic flow intensity can be approximated by a truncated cosine function with a maximum intensity ε_p in the stress loading direction $\theta = \varphi + \Delta\varphi$ normal to the plastic yield surface:

$$\left\{ \begin{array}{rcl} \sqrt{2}\mathrm{d}\varepsilon_{xx}^p = \sqrt{2}\mathrm{d}\varepsilon_{yy}^p & = & \varepsilon_p \max\left(0, \cos(\theta - \varphi - \Delta\varphi)\right)\cos(\varphi) \\ \mathrm{d}\varepsilon_z z^p & = & \varepsilon_p \max\left(0, \cos(\theta - \varphi - \Delta\varphi)\right)\sin(\varphi) \end{array} \right. . \tag{4.18}$$

By minimizing the quadratic error between the numerical points and Equation (4.18), a reasonable prediction of the numerical results is achieved

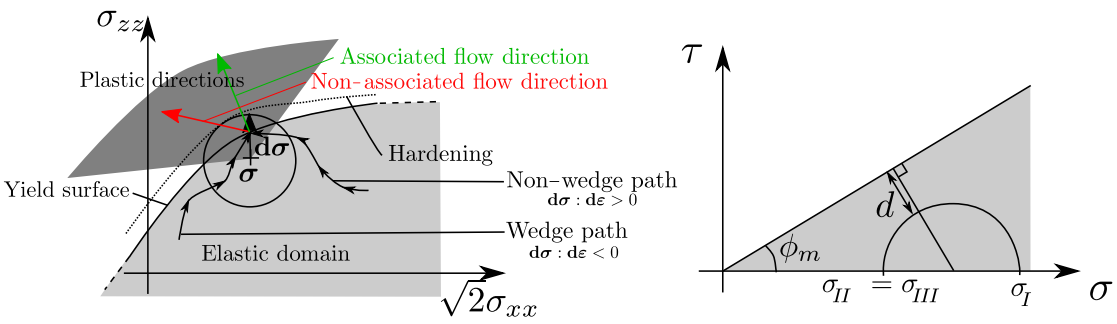

(a) Non–associated flow rule

(b) Distance to Mohr–Coulomb limit

Figure 4.22 – (a) Illustration of an associated and non-associated flow rule in the Rendulic plane. Starting from a state $\boldsymbol{\sigma}$, an incremental load $\mathbf{d\sigma}$ is applied. In case the plastic limit is crossed, a plastic increment exists and the plastic limit may move if hardening occurs. (b) Illustration of the distance d to Morh-Coulomb plastic limit thanks to Mohr circle.

by choosing $\varphi = 113.8°$, $\Delta\varphi = 25.9°$ and $\varepsilon_p = 4.69\ 10^{-2}$. The resulting fitted model is included in Figure 4.20.

The non-zero value for $\Delta\varphi$ is a signature of the non-associated character of the flow rule (Nicot and Darve, 2007b; Sibille et al., 2009). Indeed, in the case of associated plasticity, the direction of the plastic flow rule is given by the perpendicular direction to the yield surface in the stress space as illustrated in Figure 4.22 (a). If the reference stress state is close enough to the plastic limit, the angular range of incremental loadings $\mathbf{d\sigma}$ able to activate plasticity is close to 180° (see Figure 4.22 (a)). In Figure 4.21, the loading angles for which $||\mathbf{d\varepsilon}^p|| \neq 0$ are such that $\theta \in [49.7°, 229.7°]$. The reference state $\eta = 0.45$ therefore belongs to the yield surface. As a result, in our case $\varphi + \Delta\varphi$ corresponds to the normal to the plastic limit surface, which is equal to 139.7°. The observed flow direction in Figure 4.20 equal to $\varphi = 113.8°$ and not to 139.7°, however, which is incompatible with the existence of an associated flow rule.

If a Mohr-Coulomb plastic limit is assumed, the half-plastic plane ($\theta \in [\varphi + \Delta\varphi - \frac{\pi}{2}, \varphi + \Delta\varphi + \frac{\pi}{2}]$ can be linked to the material friction angle ϕ_m (at the continuum scale). Indeed, for stress states in the Rendulic plane, the distance d between the Mohr-Coulomb straight line and the Mohr circle representing the stress state (see Figure 4.22 (b)) reads

$$d = \frac{\sigma_{III} + \sigma_I}{2} \sin\phi_m - \frac{\sigma_I - \sigma_{III}}{2}. \tag{4.19}$$

where $\sigma_I = \sigma_{zz}$ and $\sigma_{II} = \sigma_{III} = \sigma_{xx}$ and σ_{III} are the principal stresses in decreasing order.

Remembering the fact that initially the stress state is given by a horizontal confinement σ_0 and a vertical stress characterized by the stress ratio η, the total stress components to be considered during the directional analysis given in Equation (4.9) are

$$\left\{ \begin{array}{rcl} \sigma_{xx} & = & \sigma_0 + \frac{||\mathbf{d\sigma}||}{\sqrt{2}} \cos\theta \\ \sigma_{zz} & = & \frac{2\eta+1}{1-\eta}\sigma_0 + ||\mathbf{d\sigma}|| \sin\theta \end{array} \right. , \tag{4.20}$$

which leads to

$$d(\theta) = \sigma_0 \frac{(2+\eta)\sin\phi_m - 3\eta}{2(1-\eta)} + ||\mathbf{d\sigma}|| \frac{\sqrt{3-2\sin\phi_m+3\sin^2\phi_m}}{2} \cos(\theta+\theta_0) \tag{4.21}$$

with θ_0 defined such that

$$\left\{ \begin{array}{rcl} \cos\theta_0 & = & \frac{1+\sin\phi_m}{\sqrt{3-2\sin\phi_m+3\sin^2\phi_m}} \\ \cos\theta_0 & = & \frac{\sqrt{2}(1-\sin\phi_m)}{\sqrt{3-2\sin\phi_m+3\sin^2\phi_m}} \end{array} \right. . \tag{4.22}$$

As a result, directions corresponding to non-zero plastic increments are given by $d(\theta) < 0$. When the initial state belongs to the yield surface ($d = 0$ for $||\mathbf{d\sigma}|| = 0$) the suitable range for θ is $[\frac{\pi}{2} - \theta_0, \frac{3\pi}{2} - \theta_0]$, whose amplitude is 180°. In our case, this assumption is likely to hold true as the amplitude of non-zero values for the plastic incremental strain in Figure 4.21 is 180° which is a consequence of the hardening observed during the drained triaxial loading in Figure 4.2. As a result, the vanishing of d for $||\mathbf{d\sigma}|| = 0$ corresponds to a material friction angle $\phi_m = 33.4°$. For such a material friction angle, the half-plastic plane predicted by Equation (4.21) is $[\frac{\pi}{2} - \theta_0, \frac{3\pi}{2} - \theta_0] = [68°, 248°]$, which is different from the one observed in Figure 4.21 $[\varphi + \Delta\varphi - \frac{\pi}{2}, \varphi + \Delta\varphi + \frac{\pi}{2}] = [50°, 230°]$. The difference observed might stem from the fact that the material does not follow a perfect Mohr-Coulomb plastic criterion as assumed to derive Equation (4.21).

In the end, the fitting procedure described in this subsection and summarized in Figure 4.23 is based on the identification of six parameters. For the sample prepared in the mechanical state $\eta = 0.45$ the fitted parameters are given in Table 4.1.

4.4.2 Plastic strain intensity and vanishing of the second-order work

The phenomenological model introduced in the previous subsection and fitted in the Rendulic plane, is convenient to interpret the vanishing of the second-order work in terms of macro variables such as the maximum level of plastic

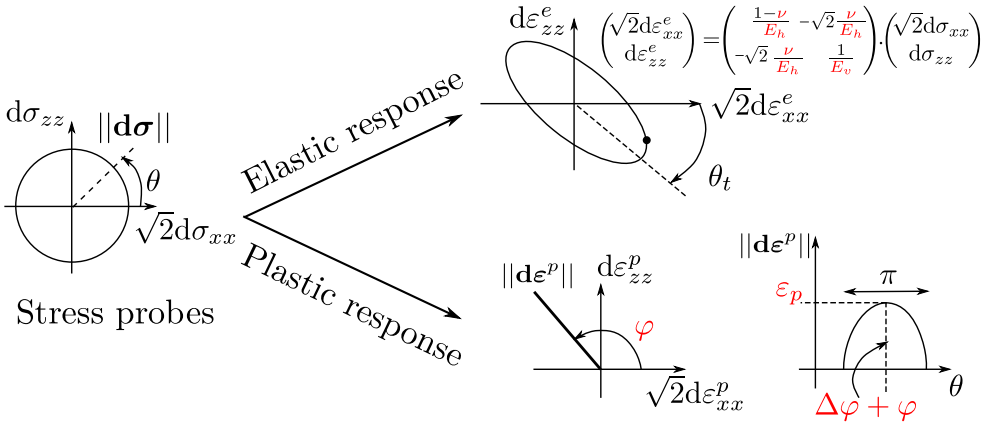

Figure 4.23 – Non-associated elastoplastic fitted response in the incremental strain space corresponding to stress probes describing a circle in the Rendulic plane. The strain response is broken down into an elastic part characterized by three parameters and a plastic one described with three parameters.

Table 4.1 – Fitted parameters for the incremental non-associated elastoplastic behavior of the sample saved in the mechanical state $\eta = 0.45$.

Elastic behavior	Plastic behavior
$E_h = 25.2$ MPa	$\varphi = 113.8°$
$E_v = 32.5$ MPa	$\Delta\varphi = 25.9°$
$\nu = 0.31$	$\varepsilon_p = 4.69\ 10^{-2}$

strain ε_p. Indeed, based on Equations (4.9), (4.11) and (4.18), in the plastic domain $\theta \in [\varphi + \Delta\varphi - \frac{\pi}{2}; \varphi + \Delta\varphi + \frac{\pi}{2}]$, the second-order work reads

$$\begin{aligned} W_2 &= \mathbf{d\sigma} : (\mathbf{d\varepsilon}^e + \mathbf{d\varepsilon}^p) \\ &= ||\mathbf{d\sigma}|| \sqrt{\beta^2 + \gamma^2} \left(\frac{\alpha}{\sqrt{\beta^2+\gamma^2}} + \cos(2\theta - \varphi_0) \right) \end{aligned} \tag{4.23}$$

with

$$\left\{ \begin{array}{rcll} \alpha &=& \frac{1}{2}||\mathbf{d\sigma}|| \left(\frac{1-\nu}{E_h} + \frac{1}{E_v} \right) & + \quad \frac{\varepsilon_p}{2} \cos(\Delta\varphi) \\ \beta &=& \frac{1}{2}||\mathbf{d\sigma}|| \left(\frac{1-\nu}{E_h} - \frac{1}{E_v} \right) & + \quad \frac{\varepsilon_p}{2} \cos(2\varphi + \Delta\varphi) \\ \gamma &=& -||\mathbf{d\sigma}|| \frac{\sqrt{2}\nu}{E_h} & + \quad \frac{\varepsilon_p}{2} \sin(2\varphi + \Delta\varphi) \\ & & \cos\varphi_0 = \frac{\beta}{\sqrt{\beta^2+\gamma^2}} & \text{and} \quad \sin\varphi_0 = \frac{\gamma}{\sqrt{\beta^2+\gamma^2}} \end{array} \right. . \tag{4.24}$$

In Figure 4.24 the analytical expression (4.23) (parameters from Table 4.1) is compared with the DEM results obtained in Section 4.2 (sample corresponding to $\eta = 0.45$).

In Figure 4.24, the fitted model is shown to account nearly perfectly for the shape of the circular envelopes obtained numerically. The relative contribution of the elastic and plastic strains to the normalized second-order work are shown with dashed lines ($W_2 = W_2^e + W_2^p$). For the set of parameters in Table 4.1, two half-planes can be defined in which $W_2 \simeq W_2^e$ or $W_2 \simeq W_2^p$. The second-order work vanishes in the half-plastic plane $[\varphi + \Delta\varphi - \frac{\pi}{2}; \varphi + \Delta\varphi + \frac{\pi}{2}]$ which is a signature of material instability by divergence. The discontinuity observed for $\theta = \varphi + \Delta\varphi + \frac{\pi}{2}$ is linked to the activation of the plasticity along a *wedge path* as illustrates in Figure 4.22. For $\theta = \varphi + \Delta\varphi - \frac{\pi}{2}$, $\mathbf{d\sigma}$ is changed in $-\mathbf{d\sigma}$ while $\mathbf{d\varepsilon}$ is kept the same as imposed by the flow rule. As a result, no discontinuity is observed in the circular envelope for the direction $\theta = \varphi + \Delta\varphi - \frac{\pi}{2}$. This difference between the two sides of the plastic domain stems from the non-associated character of the flow rule is visible because the normal direction $\varphi + \Delta\varphi$ to the half-plastic plane (dashed line) differs from the direction of plastic increment in the axisymmetric plane φ (solid line).

As a result of Equation (4.23), a necessary condition for having a loading direction leading to the vanishing of the second-order work reads

$$\text{If } \exists\theta \text{ such that } W_2(\theta) < 0, \text{ then } \alpha^2 \leq \beta^2 + \gamma^2. \tag{4.25}$$

If this condition is satisfied and if the directions θ giving $W_2 < 0$ lie in the plastic half-plane $[\varphi + \Delta\varphi - \frac{\pi}{2}; \varphi + \Delta\varphi + \frac{\pi}{2}]$ (otherwise Equation (4.23) is not

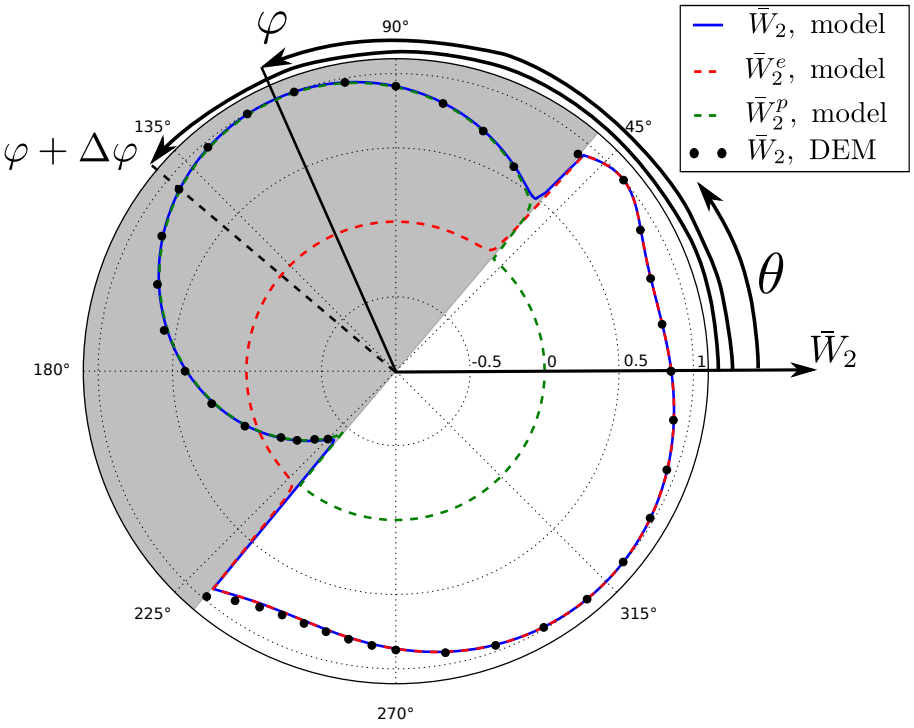

Figure 4.24 – Comparison between analytical (solid lines) and numerical (dots) normalized second-order work envelopes for the initial sample corresponding to $\eta = 0.45$. The model parameters are taken from Table 4.1. The relative contribution of the elastic and plastic incremental strain in the computation of W_2 are shown with dashed lines. The plastic half-plane $[\varphi + \Delta\varphi - \frac{\pi}{2}; \varphi + \Delta\varphi + \frac{\pi}{2}]$ corresponds to the grey domain. The maximum plastic intensity direction $\varphi + \Delta\varphi$ (black dashed line) and the plastic flow direction φ (black solid line) are also shown.

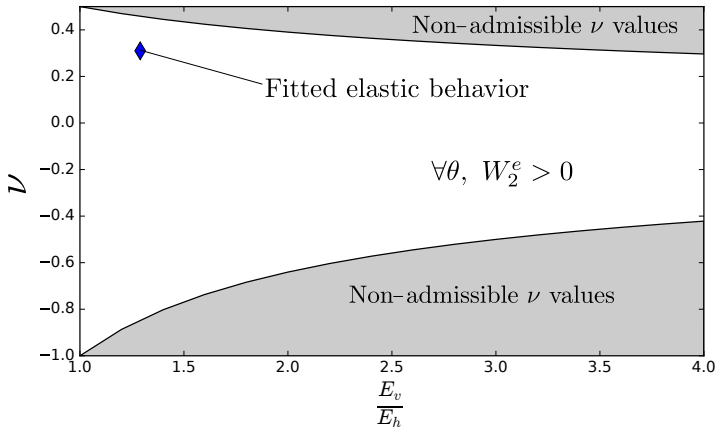

Figure 4.25 – Phase diagram of couples $(\nu, \frac{E_v}{E_h})$ leading to the positive definition of the constitutive tensor. The point corresponding to the fitted parameters in Table 4.1 is indicated.

valid), the granular material considered is at a bifurcation point. In other words, even if the considered material is at equilibrium in the current state (defined by the geometry of its microstructure and its stress state), incremental loading programs exist that will lead to the material failure through an abrupt increase in kinetic energy.

If we assume that the material behavior is fully elastic ($\varepsilon_p = 0$), then condition (4.25) can be written in terms of material constants ν and E_v/E_h as

$$\nu \leq -\frac{1+\sqrt{1+8E_v/E_h}}{4E_v/E_h} \quad \text{or} \quad \nu \geq \frac{-1+\sqrt{1+8E_v/E_h}}{4E_v/E_h}. \tag{4.26}$$

This condition corresponds indeed to the positive definition of the constitutive tensor and define the admissible bounds for ν. The set of admissible parameters $(E_v/E_h, \nu)$ is illustrated in Figure 4.25.

The positive definition of the constitutive tensor results in the fact that the elastic contribution to the second order work is always positive. As a result, the size of the plastic increment is expected to play an important role with respect to the vanishing of the second-order work. This sensitivity to ε_p is explored in Figure 4.26 in which normalized circular envelopes of the second-order work are shown for different ε_p values while keeping other parameters of Table 4.1 constant.

The plastic strain intensity ε_p has a great influence on the existence and the width of the cone of instability resulting from Equations (4.23) and (4.24).

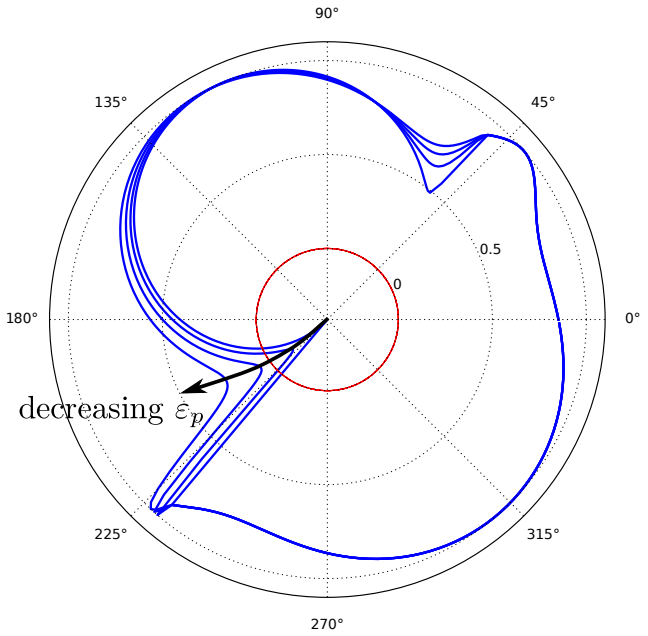

Figure 4.26 – Analytical normalized second-order work envelopes for different plastic intensities $\varepsilon_p \in \{\varepsilon_p^\circ, \varepsilon_p^\circ/20, \varepsilon_p^\circ/50, \varepsilon_p^\circ/100\}$ where $\varepsilon_p^\circ = 4.69\ 10^{-2}$. The six other parameters of the model are selected from Table 4.1.

The larger ε_p, the larger the instability cone. This close relationship between the vanishing of the second-order work and the size of the plastic increments was also recently accounted for by Zhang et al. (2016) while considering the occurrence of *strain bursts*.

4.4.3 A conjecture for the stabilizing role played by rattlers

When looking back to the microscale, the plastic strain intensity can be linked to the presence of rattlers, i.e. free particles not participating in stress transmission[3]. Indeed, from the results illustrated in Figure 4.26 combined with the schematic diagram in Figure 4.27, we conjecture that rattlers (particles with no contacts in absence of gravity) play the particular of limiting the development of plastic strain when the existing contact network fails to adapt to the newly imposed mechanical loading and induces microstructure rearrangements. Given that large incremental plastic strain development is a necessary condition for the onset of macroscopic instability, rattlers play a fundamental role in mitigating material instability by divergence. This issue will be discussed from micromechanical considerations in the following two sections.

4.5 A contact scale explanation for the stabilizing role played by rattlers

Complementary to the previous section, the particular role played by rattlers in mitigating plastic strain development can be examined analytically and qualitatively using the micro-formulation of the second-order work introduced for granular materials (Nicot et al., 2007; Hadda et al., 2013). In this section, the contact scale necessary condition to observe the vanishing of the second-order work contact scale necessary condition to observe the vanishing of the second-order work (Nicot and Darve, 2006a; Nicot et al., 2013a) is revisited in terms of rattlers influence to provide an analytical proof of the conjecture formulated in Section **??**. This section is kept qualitative on purpose but a quantitative assessment of the role played by rattlers directly at the contact scale is proposed in **??** through DEM simulations.

[3]In the absence of gravity, rattlers are floating particles. When gravity is accounted for, rattlers deposit in the bottom of pores with three contacts with non-rattler particles. The name rattlers come from the verb to rattle. When a sample is shaken, rattlers rattle!

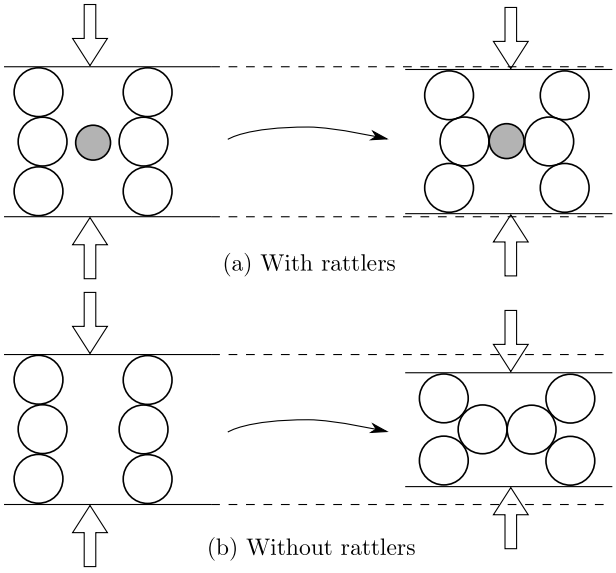

Figure 4.27 – Schematic diagram of the particular role played by rattlers with respect to plastic strain development. Comparison between a microstructure with rattlers (a) and the same microstructure without rattlers (b).

Let $\boldsymbol{\ell}^c$ be the branch vector connecting the centers of two contacting spherical particles at contact c, $\boldsymbol{F}^c$ the inter-particle contact force, $\boldsymbol{F}^p$ the resultant contact force on particle p and $\boldsymbol{x}^p$ the position of its mass center. Then the volume integral of the second-order work on a sample of domain Ω can be computed from micro-quantities as

$$\int_\Omega W_2 \mathrm{d}V = \sum_c \boldsymbol{\Delta F}^c \cdot \boldsymbol{\Delta \ell}^c + \sum_p \boldsymbol{\Delta F}^p \cdot \boldsymbol{\Delta x}^p \tag{4.27}$$

where $\boldsymbol{\Delta}$ correspond to incremental variations and $\cdot$ to the scalar product.

Provided that only inertial terms can be ignored ($\forall p, \boldsymbol{\Delta F}^p = \boldsymbol{0}$), the second term vanishes and the second-order work computed at the REV scale reads:

$$W_2 = \frac{1}{|\Omega|} \sum_c \boldsymbol{\Delta F}^c \cdot \boldsymbol{\Delta \ell}^c. \tag{4.28}$$

Consequently a microscopic second-order work can be defined at the contact scale as $w_2^c = \boldsymbol{\Delta F}^c \cdot \boldsymbol{\Delta \ell}^c$ (Nicot and Darve, 2006a).

By further breaking down $\boldsymbol{\Delta F}^c$ and $\boldsymbol{\Delta \ell}^c$ into normal and tangential components, w_2^c can be expressed as

$$w_2^c = \boldsymbol{\Delta F}_n^c \cdot \boldsymbol{\Delta \ell}_n^c + \boldsymbol{\Delta F}_t^c \cdot \boldsymbol{\Delta \ell}_t^c. \tag{4.29}$$

The definition of the different vectors at stake in this equation appears more clearly in Figure 4.28.

Using the contact law recalled in Section 2.3.1, the first term reads $k_n||\boldsymbol{\Delta\ell}_n^c||^2$ and is always positive, as is the second one as long as $||\boldsymbol{F}_t^c||/||\boldsymbol{F}_n^c|| < \tan\phi$. As a result, $w_2^c \geq 0$ if the contact behaves elastically. If sliding occurs, the sign of w_2^c is difficult to predict and two cases should be considered (see Figure 4.28 and Nicot and Darve (2006a); Nicot et al. (2013a)).

(a) $\boldsymbol{F}_n^c$ remains constant and $\boldsymbol{\Delta F}_t^c$ is such that $\boldsymbol{F}_n^c + \boldsymbol{F}_t^c + \boldsymbol{\Delta F}_t^c$ reaches the Mohr-Coulomb limit cone. In this case the tangential relative displacement $\boldsymbol{\Delta\ell}_t^c$ is positively collinear to $\boldsymbol{F}_t^c + \boldsymbol{\Delta F}_t^c$ and for a sufficiently small increment $\boldsymbol{\Delta F}_t^c$, $\boldsymbol{\Delta F}_t^c \cdot \boldsymbol{\Delta\ell}_t^c \geq 0$. As a result $w_2^c \geq 0$.

(b) $||\boldsymbol{F}_n^c||$ decreases such that $\boldsymbol{F}_n^c + \boldsymbol{\Delta F}_n^c + \boldsymbol{F}_t^c$ violates Mohr-Coulomb limit cone as $||\boldsymbol{F}_t^c|| > (||\boldsymbol{F}_n^c|| - ||\boldsymbol{\Delta F}_n^c||)\tan\phi$. In this case, the tangential force decreases as

$$\boldsymbol{\Delta F}_t^c = -\Big[||\boldsymbol{F}_t^c|| - (||\boldsymbol{F}_n^c|| - ||\boldsymbol{\Delta F}_n^c||)\tan\phi\Big]\frac{\boldsymbol{F}_t^c}{||\boldsymbol{F}_t^c||} \tag{4.30}$$

whereas the relative displacement $\boldsymbol{\Delta\ell}_t^c$ is positively collinear to $\boldsymbol{F}_t^c$. In this case, the tangential term in w_2^c is negative and

$$w_2^c = \frac{1}{k_n}||\boldsymbol{\Delta F}_n^c||^2 - \left[\frac{||\boldsymbol{F}_t^c||}{||\boldsymbol{F}_n^c||} - \left(1 - \frac{||\boldsymbol{\Delta F}_n^c||}{||\boldsymbol{F}_n^c||}\right)\tan\phi\right]||\boldsymbol{F}_n^c||\;||\boldsymbol{\Delta\ell}_t^c|| \tag{4.31}$$

As a result, it should be underlined that the occurrence of contact sliding is *not* a sufficient condition to observe the vanishing of w_2^c. If a contact slides under an "increase" in the tangential force, for instance, the scalar product $\Delta\boldsymbol{u}_t \cdot \Delta\boldsymbol{F}_t$ is positive. Contact sliding through normal unloading is thus a *necessary* condition to observe the vanishing of the local second-order work w_2^c. Then the vanishing of the second-order work W_2 at the scale of a representative elementary volume requires the following two conditions:

- A sufficient number of contacts have to slide through normal unloading;
- A large proportion of these contacts has to exhibit a sufficiently large tangential displacement $\Delta\boldsymbol{\ell}_t^c$ such that the local second-order work w_2^c vanishes.

By imposing internal geometrical constraints to a granular material, rattlers can contribute to limiting the size of the tangential increment $||\boldsymbol{\Delta\ell}_t^c||$

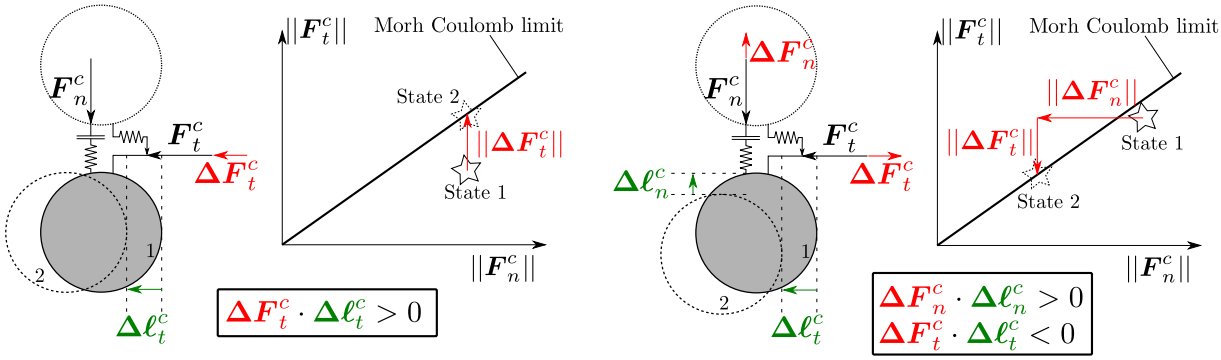

(a) Sliding through increase in $||\boldsymbol{F}_t^c||$

(b) Sliding through decrease in $||\boldsymbol{F}_n^c||$

Figure 4.28 – Two incremental loadings leading to contact sliding with different consequences on the sign of w_2^c. While configuration (a) results in $w_2^c > 0$, configuration (b) can result in $w_2^c < 0$ depending on $||\boldsymbol{\Delta \ell}_t^c||$.

when contact sliding occurs as illustrated in Figure 4.29. Consequently, the presence of rattlers will result in a decrease in the number of contacts with $w_2^c < 0$ and an increase in W_2 which imposes mechanical stability at the macroscopic scale. This constitutes a micromechanical proof of the conjecture formulated in Section 4.4.3.

4.6 DEM inspection of rattlers' stabilizing role

In this section, the two samples corresponding to $\eta = 0.35$ and $\eta = 0.45$ in Figure 4.2 are considered. By referring to Figure 4.3 the sample corresponding to $\eta = 0.35$ is reputed stable whereas the sample corresponding to $\eta = 0.45$ is reputed unstable.

Based on these two samples, in this section we focus on the role played by the loose phase (i.e. the least stressed grains of the assembly) with respect to the mechanical stability of granular materials. In particular we focus on the role played by rattlers, i.e.particles with no contacts with their neighbors. Given that these particles do not carry any load, they can be easily removed from the saved samples, without decaying the their bearing capacity. Similarly, rattlers can be artificially added to existing interstitial voids. These two artificial microstructure modifications will be considered in the following two subsections and may be representative of massive erosion or clogging induced by an internal flow.

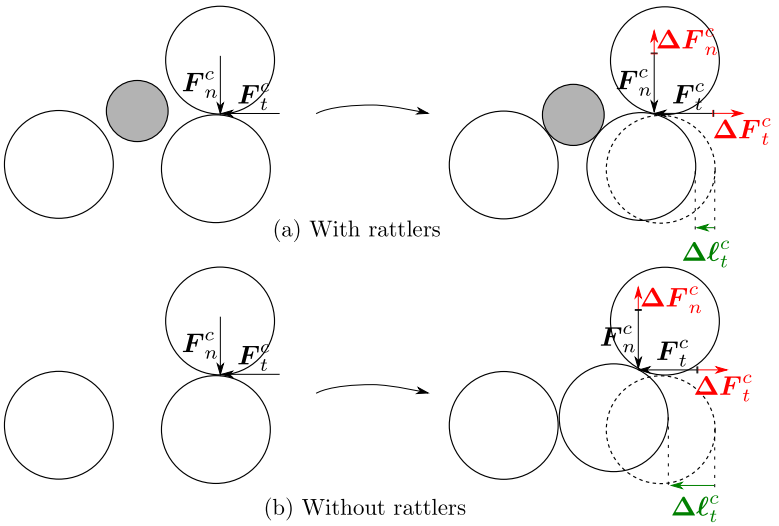

Figure 4.29 – Schematic diagram of the particular role played by rattlers with respect to the size of the tangential increment $||\boldsymbol{\Delta \ell}_t^c||$ for the incremental loading of Figure 4.28 (b).

4.6.1 Mechanical stability assessment for samples without rattlers

In Figure 4.30 (a) the sample corresponding to the mechanical state $\eta = 0.45$ is shown with the free particles highlighted in white. In this case, artificial removal of rattlers concerns 3,480 particles out of 10,000 and the resulting microstructure is shown in Figure 4.30 (b). A similar extraction procedure was performed on the sample corresponding to the mechanical state $\eta = 0.35$ in which 3,458 particles are found to be rattlers.

As for the virgin microstructure, a stress-controlled directional analysis (see Equation (4.9)) with 5 kPa stress probes is performed with artificially eroded microstructures. In Figure 4.31, circular representations of the resulting normalized second-order work are shown for the two samples saved and compared with those obtained before any particle are removed.

In the case corresponding to $\eta = 0.35$, the sample initially identified as stable with respect to the second-order work criterion ($\forall \theta,\ W_2 > 0$) enters the bifurcation domain when rattlers are removed ($\exists \theta$, such that $W_2 < 0$). In the case corresponding to $\eta = 0.45$, both samples are in the bifurcation domain. Removing rattlers results in a wider cone of instability (the set of loading directions leading to $W_2 < 0$). These observations show that rattlers play an important role with respect to mechanical stability even though they did not initially contribute to supporting the mechanical load. Indeed, if the

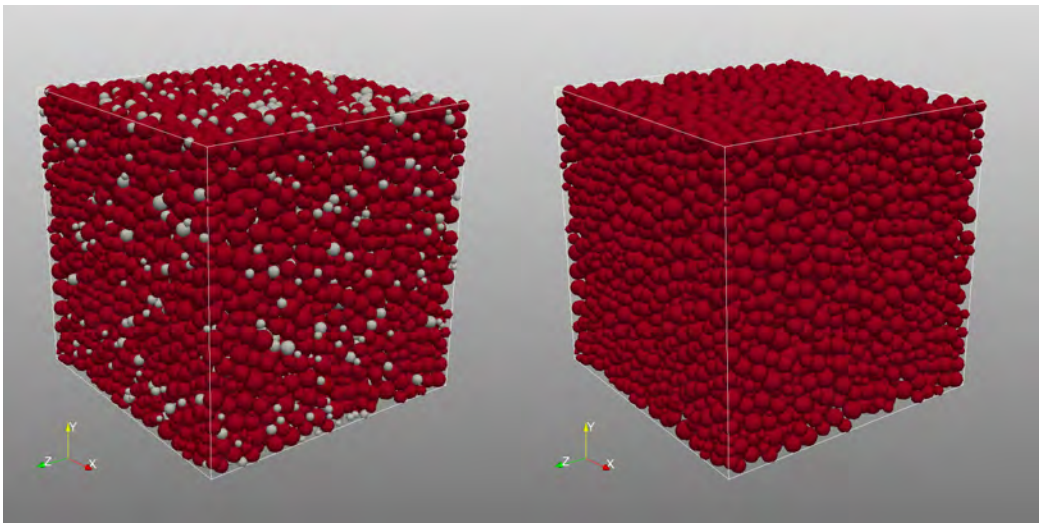

(a) with rattlers (b) no rattlers

Figure 4.30 – Microstructure evolution induced by removing free particle for the sample corresponding to the mechanical state $\eta = 0.45$. Free particles are shown in the initial sample (a) in grey. After these 3,480 particles are removed, the resulting microstructure is shown in (b) without rattlers.

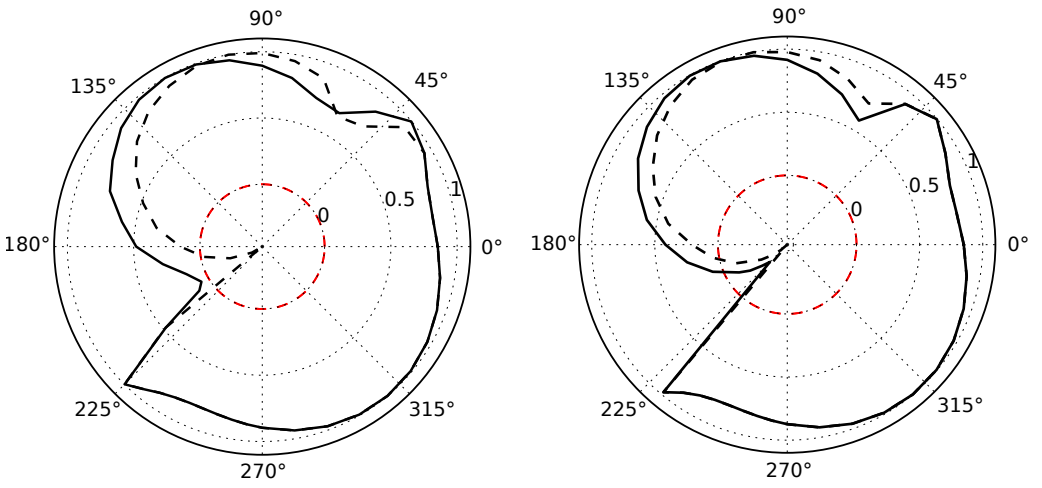

(a) $\eta = 0.35$ (b) $\eta = 0.45$

Figure 4.31 – Circular envelopes of normalized second-order work for $\eta = 0.35$ (a) and $\eta = 0.45$ (b). The initial microstructure containing rattlers corresponds to solid lines while the microstructure without rattlers corresponds to dashed lines.

existing contact network fails to transmit the imposed incremental stress, the microstructure is forced to rearrange until a more robust contact network is built, possibly by mobilizing free particles. As a result, free particle removal reduces rearrangement possibilities, which is consistent with an increase in the number of unstable loading directions. At the macroscale, this results in larger plastic increments. For instance, in the case of $\eta = 0.45$, the maximum plastic intensity ε_p introduced in Section 4.4.1 rises from 4% to 21% when rattlers are removed. The corresponding incremental strain envelopes observed during the directional analyses performed are shown in Figure 4.34.

These observations are consistent with previous studies in which particle removal is considered (including particles involved in stress transmission). For instance, Scholtès et al. (2010) show that granular samples loaded in a drained triaxial state with a sufficiently large η value cannot adapt to substantial particle removal. In some cases, removing some stressed particles is sufficient to induce the collapse. Indeed, destabilized contact networks cannot find any new stable configurations by incorporating new particles into force chains. Even if particle removal does not lead to instantaneous failure, Scholtès et al. (2010) and Hosn et al. (2018) observed considerable reduction of the peak stress in drained triaxial tests resulting from the decrease in the number of accessible microstructure configurations.

4.6.2 Mechanical stability assessment for samples with added rattlers

Following the pore network analysis shown in Wautier et al. (2017), an artificial increase in the number of rattlers is achieved as follows:

- define a pore network using a regular Delaunay triangulation of the media (Chareyre et al., 2012);

- for every pore defined as a tetrahedron linking the center of four particles, compute the radius of the inscribed sphere together with the position of its center;

- check whether such a sphere intersects any other existing particles not belonging to the tetrahedron considered. If yes, decrease the computed inscribed sphere radius until no intersection exists;

- include a particle inside every pore where the inscribed radius is larger than a threshold value r_{th}.

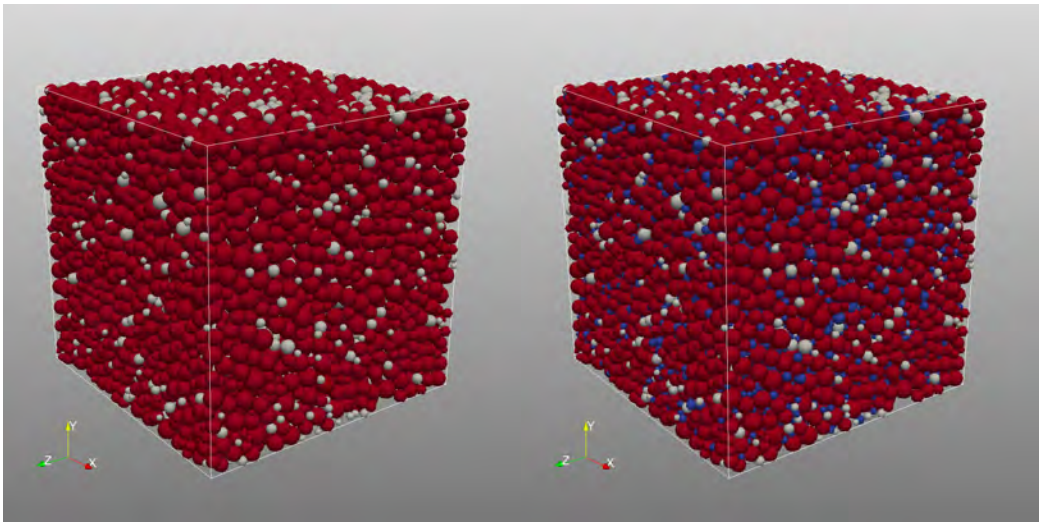

(a) with rattlers (b) more rattlers

Figure 4.32 – Microstructure evolution induced by inclusion of free particles for the sample corresponding to the mechanical state $\eta = 0.45$. Free particles are shown in the initial sample (a) in white. The 12 805 added particles are shown in blue in the enriched sample (b).

The result of the above procedure with $r_{\text{th}} = \frac{r_{\text{min}}}{2}$ is shown for the sample corresponding to $\eta = 0.45$ in Figure 4.32 (b). A total of 12,805 particles have been added to existing voids (in addition to pre-existing rattlers).

As in the previous subsection, a stress-controlled directional analysis was performed with this artificially enriched microstructure. In Figure 4.33, circular representations of the normalized second-order work are shown for (i) the initial sample with $\eta = 0.45$, (ii) this sample without rattlers and (iii) this same sample in which additional rattlers are incorporated.

In Figure 4.33, the role played by rattlers with respect to mechanical stability is clearly shown and confirms the conjecture proposed in Section 4.4.3. Indeed, adding new rattlers offers new possibilities in rebuilding contact networks. In the case $\eta = 0.45$, the maximum plastic intensity ε_p is reduced from 4% to 0.8% when additional rattlers are considered as shown in Figure 4.34. As a result, fewer incremental loading directions are associated with a negative value of the second-order work as observed in Figure 4.33. However, despite the large number of newly incorporated rattlers, a cone of instability persists for the sample considered. These additional rattlers do not get jammed into a new contact network quickly enough to prevent the existence of macroscopic instability.

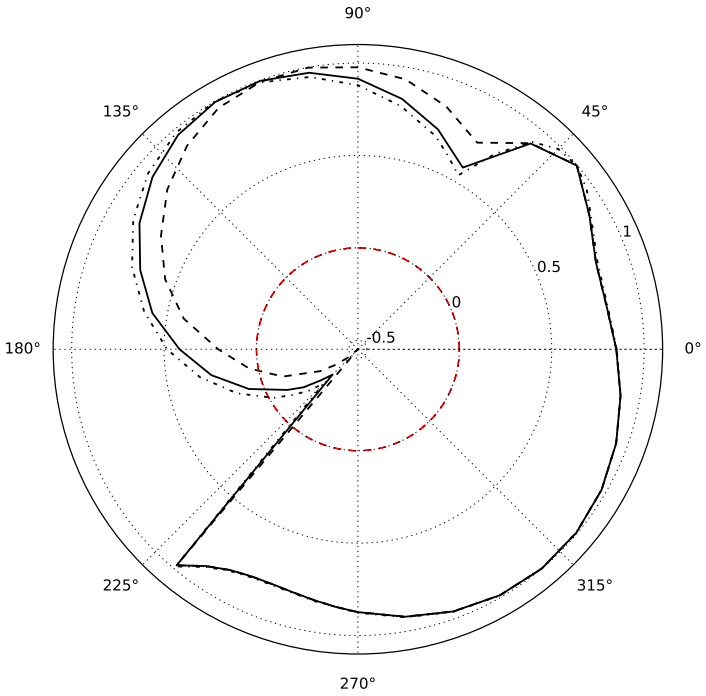

Figure 4.33 – Circular envelopes of normalized second-order work for $\eta = 0.45$. Three microstructures are considered: the initial microstructure (solid line), the initial microstructure without rattlers (dashed line) and the initial microstructure enriched with more rattlers (dotted-dashed line).

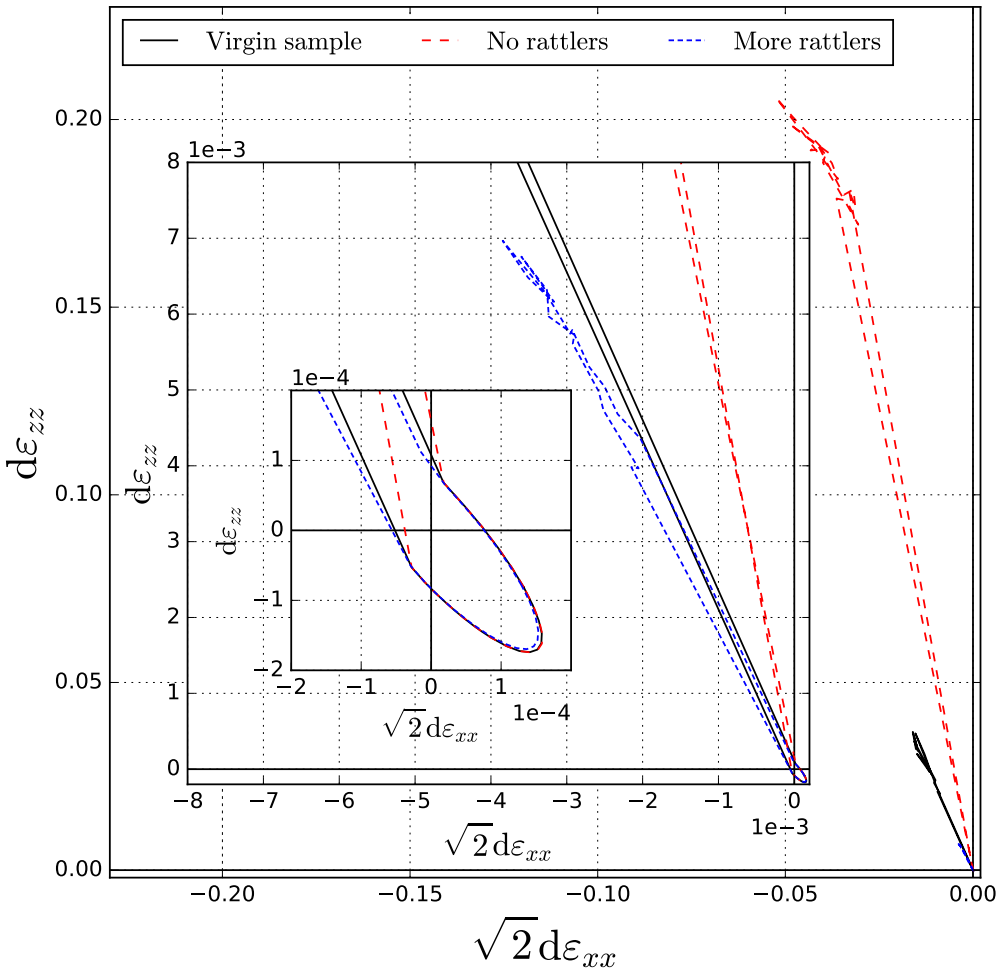

Figure 4.34 – Incremental strain envelopes associated with directional analyses in the case of $\eta = 0.45$. The three microstructures shown in Figures 4.30 and 4.32 are considered: virgin (solid line), with rattlers removed (large dashed line), with more rattlers (small dashed line). Two levels of zoom are provided in the inset plots.

4.6.3 Rattlers' influence on the macroscopic direction of the non-associated flow rule

As shown in the previous subsection, rattlers have a significant impact on the mechanical stability of the samples considered. For the sample corresponding to $\eta = 0.45$ it is interesting to reconsider the model parameters of Table 4.1 while updating the plastic flow intensity ε_p to account for the removal or addition of rattlers considered in this section ($\varepsilon_p = 21\ 10^{-2}$ and $\varepsilon_p = 8\ 10^{-3}$ respectively). The comparison between the resulting envelopes and the numerical data is given in Figure 4.35.

As shown in Figure 4.35, the change in the plastic intensity explains most of the change in the W_2 circular envelope in the case where new rattlers are incorporated but does not account for the modification induced by the removal of rattlers. Indeed, the presence or absence of rattlers may have an other impact on the plastic behavior at the continuum scale through the plastic flow direction as illustrated in the schematic diagram of Figure 4.36. The macroscopic activation of the plastic behavior corresponds locally to substantial grain rearrangements following the collapse of pre-existing force chains. Initially these force chains are oriented in the principal stress direction along z axis. Once they fail, the sample contracts in this direction while slightly dilating in the horizontal directions x and y as a consequence of vertical to lateral force transmission. When rattlers are removed, the vertical contraction is stopped later while the horizontal dilation is less influenced. Since incremental plastic strains result from the collapse of mesostructures mostly oriented along the z axis, the impact of rattlers is expected to be greater along $\mathrm{d}\varepsilon_{zz}$ than along $\mathrm{d}\varepsilon_{xx}$ and $\mathrm{d}\varepsilon_{yy}$. This asymmetric influence results in a clockwise rotation of the plastic flow in the axisymmetric plane $(\sqrt{2}\mathrm{d}\varepsilon_{xx}, \mathrm{d}\varepsilon_{zz})$ as observed numerically in Figure 4.34. However, since the onset of the plastic behavior is governed by the primary fabric, the plastic half-plane is however not affected by the modification of the population of rattlers.

As shown in Figure 4.35, a decrease in the plastic flow direction φ while keeping $\varphi + \Delta\varphi$ constant precisely accounts for the new circular envelopes when rattlers are removed from the sample. On the contrary, when adding rattlers, a small increase in the plastic flow direction φ provides a better fit of the numerical data. The modified plastic parameters are given in Table 4.2

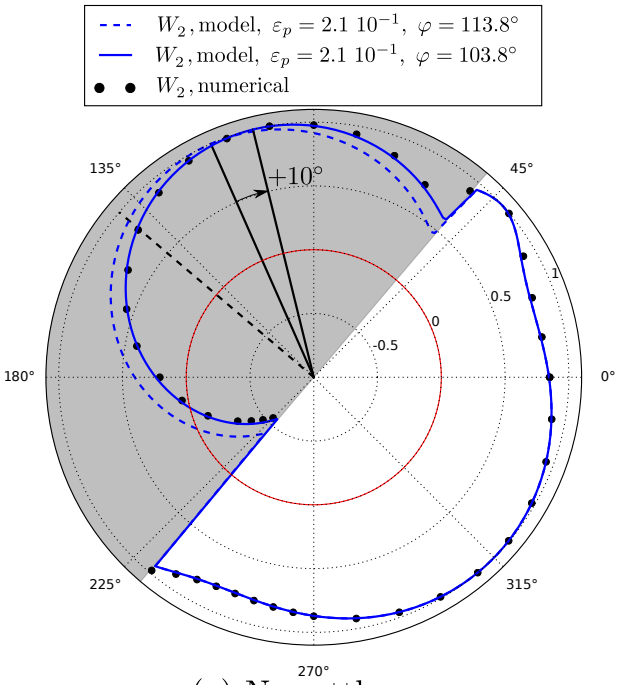

(a) No rattlers

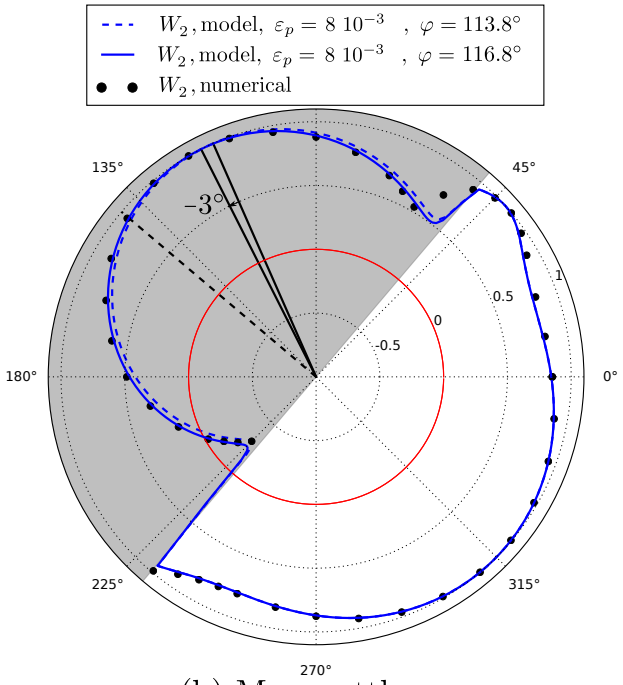

(b) More rattlers

Figure 4.35 – Circular envelopes of normalized second-order work for $\eta = 0.45$ corresponding to the sample without rattlers (a) and in which additional rattlers are incorporated (b). The phenomenological fits coming from the elastoplastic model presented in Section 4.4.1 are shown with a dashed line with parameters from Table 4.1 and updated ε_p values, and as a solid line for the updated plastic parameters from Table 4.2. The maximum plastic intensity direction $\varphi + \Delta\varphi$ (the black dashed line segment) and the plastic flow direction φ (two thick solid line) are also shown for both fits.

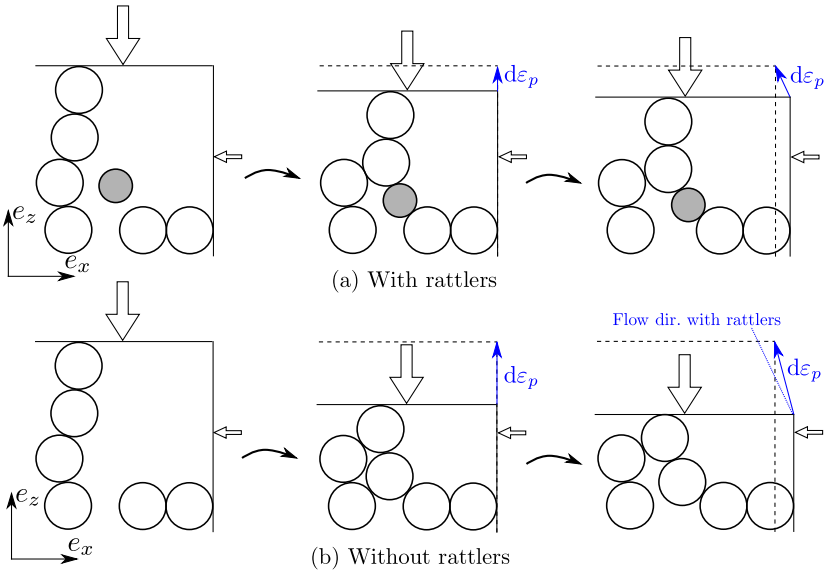

Figure 4.36 – Illustration of the plastic flow rotation induced by rattler removal with anisotropically oriented force chains in the z direction.

Table 4.2 – Updated plastic parameters for the incremental non-associated elastoplastic behavior for the mechanical state $\eta = 0.45$ in case of removal or addition of rattlers.

No rattlers	More rattlers
$\varphi = 113.8° - 10°$	$\varphi = 113.8° + 3°$
$\Delta\varphi = 25.9° + 10°$	$\Delta\varphi = 25.9° - 3°$
$\varepsilon_p = 21\ 10^{-2}$	$\varepsilon_p = 8\ 10^{-3}$

4.7 Summary of the main findings

Thanks to the combine use of the second-order work theory at the macroscale and the force chain concept at the microscale, physical mechanisms responsible for the onset and development of instability in granular materials have been identified at the microscale. It was shown that an incremental stress loading leading to the vanishing of the second-order work provokes the unjamming of force chains. This results in their bending accompanied by an increase in the kinetic energy. At the macroscale, force chain bending is visible through softening behavior and loss of controllability as the measured incremental stress rotates toward the direction of the instability cone. The correlation between the increase in kinetic energy and the vanishing of the second-order work predicted by the writing of the kinetic energy balance (2.6) is verified, but it is shown here that this is the consequence of the propagation of a burst of kinetic energy to the whole sample. Once the kinetic energy of the whole sample is large enough, existing force chains collapse and important microstructure reorganizations are observed resulting in a macroscopic densification (for loose granular materials). This densification is eventually stopped as soon as new stable force chains are built. Macroscopic softening ends and the incremental stress rotates back to its prescribed direction.

In addition to this physical interpretation of the vanishing of the second-order work, a particular attention has been paid to the pre-stabilization step required to define a reference equilibrium state as well as to the magnitude of the stress increments required to trigger off instability. Even for quasi-static evolutions, it was shown that localized micro-inertia crisis occur during this pre-stabilization step. As a consequence, threshold values exist for stress increments below which the sign of the normalized second-order work depends on the magnitude of stress increments. These observations are hardly ever reported in the literature and could provide clues to carry out systematic numerical assessment of the bifurcation domain of granular materials.

By going back to a continuum mechanics perspective, the local grain rearrangements were linked to the macroscopic concepts of plasticity and material instability. To this respect, a particular attention was paid to provide physical interpretations of the phenomenological parameters used in non-associated elasto-plastic constitutive modeling. A necessary condition for the occurrence of material instability within granular materials (detected by the second-order work criterion) lies in the development of large plastic strains. Provided that the current contact network fails to withstand an incremental load, the mechanical stability of a granular material at the macroscale is closely related to the ability of free particles to get jammed into new force chains. Indeed, removing free particles results in an increase in in-

cremental plastic strain. When the loading history induces microstructure anisotropy, local microstructure rearrangements occur in a specific direction which affects macroscopically the direction of the flow rule. As a consequence of these two microstructure effects, the removal of rattlers leads to an increase in the number of loading directions associated with a vanishing second-order work. On the contrary, adding free particles inside the pores of an unstable granular assembly is shown to have a stabilizing effect.

These latter results are of a particular significance in relation with suffusion as rattlers are privileged candidates to erosion. Indeed, if rattlers are too big to be transported through the pore space, they remain trapped inside the soil and ensure mechanical stability. On the contrary, if the soil loses some rattlers, a mechanical instability is more likely to appear. Clogging and erosion are thus expected to have antagonist effects with respect to mechanical stability. These two effects can be invoked for instance to comfort the interpretations of experimental triaxial tests performed on eroded soils (see Section 2.2.2). If the post-erosion peak stress is unchanged or increases, clogging of rattlers is certainly the privileged mechanism. On the contrary, if the post-erosion peak stress decreases, erosion of rattlers is certainly the privileged mechanism. The competition between these two mechanisms will be analyzed from fully coupled simulations in Section 5.2 in the following chapter.

Chapter 5

Numerical assessment of the impact of an internal fluid flow on the mechanical stability of granular materials

As reviewed in the state of the art chapter of this manuscript, the occurrence of suffusion has been mostly been considered through geometric considerations. Indeed, the notion of *internal stability* has been introduced in the geomechanics community as the ability of a granular material to self prevent the loss of the smallest particles under the action of disturbing forces such as seepage or vibration (Kenney and Lau, 1985). The notion of self filtration follows, and most of the criteria used for practical applications are constructed on particle size distributions (PSD) (Kenney and Lau, 1985; Skempton and Brogan, 1994; Li and Fannin, 2008) or more recently on constriction size distributions (CSD) (Sjah and Vincens, 2013; Vincens et al., 2015; Li et al., 2014). Only few of them take into account the mechanical or hydraulic loading to assess the occurrence of the phenomenon (Shire et al., 2014; Jaeger et al., 2017; Kawano et al., 2017) and none account for the resulting evolutions in terms of mechanical stability as deduced from the literature review in Section 2.1.

For cohesionless granular materials, an internal flow does not directly modify the mechanical properties at the contact scale but induces geometrical changes in the microstructure following two kinds of mechanisms.

- A first change lies in the transport of rattlers, i.e. particles with no contacts with their neighbors in the absence of gravity. Under the action of an internal fluid flow, these particles move through the pore space and are either eroded or clogged depending on their size with respect to those of pores and constrictions (Reboul et al., 2008; O'Sullivan et al., 2015; Wautier et al., 2017).

- The second flow impact consists in introducing additional forces on the primary skeleton of the granular material (Mahabadi and Jang, 2017; Beguin et al., 2012). This results in stress redistribution and possibly to grain detachment if the existing contact network is forced to rearrange.

The first aspect has been widely accounted for through filtration tests (O'Sullivan et al., 2015; Vincens et al., 2015) and the relative impact of clogging and erosion can artificially be obtained by modifying the population of rattlers (see Section 4.6). The second aspect has been much less investigated and grain detachment is usually assessed thanks to a *Shield criterion* at the scale of a single grain and not at the scale of the whole contact network.

The objective of this chapter is twofold. First, by considering a granular sample without rattlers prepared in an unstable mechanical state, the direct impact of a fluid flow on the primary skeleton is investigated and the ability of the internal flow to trigger off underlying instability is shown. Then, the

relative influence of erosion and clogging is considered for a widely graded sample in an unstable state subjected to an internal flow.

Similarly to the previous chapers, the micromechanical analysis performed in this chapter considers non-cohesive granular materials modeled as polydisperse assemblies of spheres. The interaction between two particles is modeled by the classical elasto-frictional contact law proposed by Cundall and Strack (1979) and presented in Section 2.3.1. The input parameters used in this elasto-frictional contact law are reported in Table 2.1. After computing all inter-particle contact forces, induced particles displacements are integrated based on Newton's second law of motion using the open source code YADE (Šmilauer et al., 2015) based on a discrete element method (DEM). The fluid grain coupling is accounted for thanks to the use of the pore scale finite volume (PFV) scheme developed by Chareyre et al. (2012) and reviewed in Section 2.4.2. Compared to most of fluid-grain problems discussed in the literature, this study dares to account for the fluid phase connectivity in 3D (Robinson et al., 2014; Jaeger et al., 2017; Kawano et al., 2017).

This chapter is organized as follows. In Section 5.1, the ability of a fluid to trigger off underlying instability on a sample in which rattlers are initially removed is shown and microscale mechanisms are investigated. In Section 5.2 the relative influence of erosion and clogging is considered for a widely graded sample.

5.1 Direct flow impact on stress transmission

5.1.1 Sample definition with no rattlers

In this section, the loose granular sample used in Chapter 4 is considered for which the grain radii follow a uniform distribution between $r_{\min}$ and $r_{\max} = 3.5\, r_{\min}$. After being prepared in an isotropic state following the radius expansion technique, this sample was subjected to a drained triaxial test (see Section 4.1) which is recalled in Figure 5.1. In this section, the sample saved for a stress ratio $\eta = 0.35$ (marked with a diamond in Figure 5.1) and no rattlers is considered. As shown in Figure 4.31, the resulting sample is known to be mechanically unstable in the sense of the second-order work criterion. Indeed, some incremental loading programs will result in an unbounded increase in kinetic energy which is a signature of an inertial transition. However, knowing whether additional forces resulting from an internal fluid flow can trigger of this inertial transition still remains an open question.

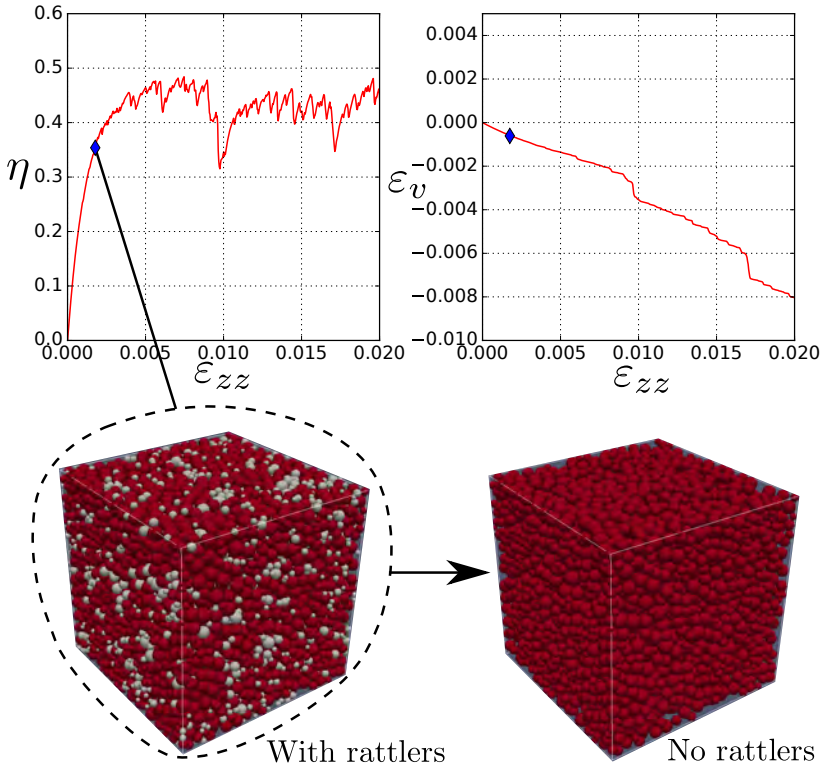

Figure 5.1 – Drained triaxial test response with respect to axial strain ε_{zz} (top). The stress ratio η is defined as the ratio between the deviatoric stress and the mean stress and ε_v stands for the relative volume change. The diamond point corresponds to the mechanical state $\eta = 0.35$ considered for the fluid/grain coupled problem. The two bottom images illustrate the microstructure changes resulting from the removal of rattlers (particles with coordination number $Z_c = 0$). The 3,458 removed particles are shown in white.

5.1.2 Fully coupled DEM/PFV numerical experiments

The numerical sample resulting from the preparation procedure presented in the previous subsection is subjected to a macroscopic pressure gradient. During this mechanical testing, the stress state is kept constant ($\eta = 0.35$) and the microstructure is let free to evolve (in particular, new rattlers are not removed). Two flow directions are considered:

- parallel to the principal loading direction (along z axis) and referred to as *vertical flow case* hereafter;
- perpendicular to the principal loading direction (along x axis) and referred to as *horizontal flow case* hereafter.

Figure 5.2 summarizes the boundary value problem solved in the two flow cases. On upstream faces, the fluid pressure is set to p_0 while on downstream faces null fluid pressure and null displacement are imposed. On the remaining faces of the sample, zero flux conditions are imposed ($q_x = q_y = 0$ for the vertical case and $q_z = q_y = 0$ for the horizontal one). The upstream pressure p_0 is prescribed such that the hydraulic gradient $I = \frac{p_0}{\rho g \ell}$ is set to 0.1 with $\rho = 1000$ kg.m^{-1} the fluid density, $g = 9.81$ m.s^{-2} the earth gravity and $\ell \in \{\ell_x, \ell_z\}$ the sample length in the flow direction. In the vertical case, $p_0 = 151$ Pa while in the horizontal one $p_0 = 152$ Pa. Since the effective stress is now varying at the scale of the sample, the problem of interest is no longer a homogenization problem and the concept of REV vanishes. However, as the fluid pressure drop p_0 is small compared to the effective stress σ_0 and if we neglect the flow induced microstructure heterogeneities at the scale of the sample, the concept of REV is restored approximatively. Under this hypothesis, the fluid can be seen as an external perturbation that makes the microstructure evolve without any change in the stress state. As already mentioned in Section 3.4, it should be emphasized that the additional fluid pressure p_0 applied only the upstream wall generates an effective stress gradient between the upstream and downstream walls of the sample. As a result, in the direction of the pressure gradient, the downstream effective stress is p_0 higher than the upstream one. In practice, the control on the downstream wall is switched from effective stress to displacement and a zero displacement condition $u_x = 0$ or $u_z = 0$ is imposed to the downstream wall depending on the flow case.

As also mentioned by anticipation in Section 3.4 the use of non-periodic boundary conditions is capital here in order to study the direct fluid impact on stress transmission as no particles have to be fixed in order to prevent collective motion of the sample (contrary to the use of periodic boundary conditions).

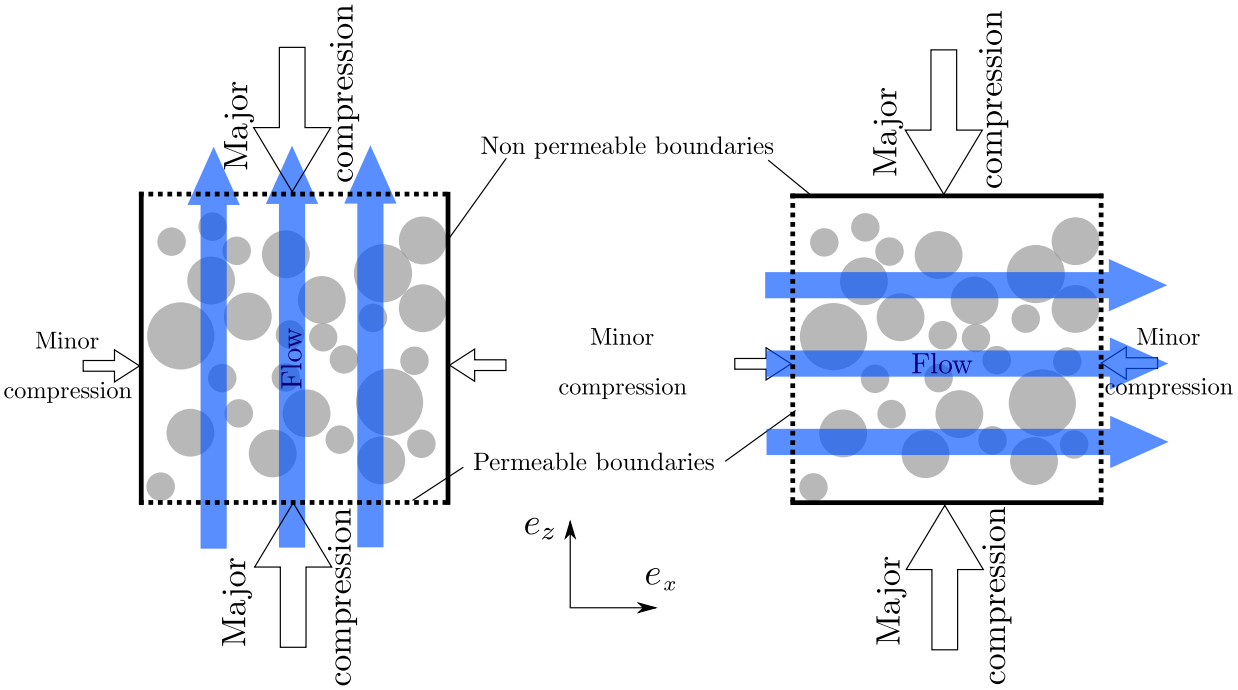

(a) Vertical flow case (b) Horizontal flow case

Figure 5.2 – Boundary value problems solved for two flow directions. In the vertical case (a), zero flux boundary conditions are applied in directions x and y while on the top face a pressure p_0 is imposed while keeping $p = 0$ on the bottom face. In the horizontal case (b), zero flux boundary conditions are applied in directions z and y while on the left face a pressure p_0 is imposed while keeping $p = 0$ on the right face. In both case the mechanical loading correspond to the stress state $\eta = 0.35$ reached during the triaxial loading of Figure 5.1. In x and y directions a confining stress $\sigma_{xx} = \sigma_{yy} = 100$ kPa is imposed while in z direction a compression $\sigma_{zz} = \frac{2\eta+1}{1-\eta}\sigma_{xx}$ is applied.

5.1.3 Flow induced material failure

In Figure 5.3, the incremental strain responses are shown for the two flow directions while the initial and final microstructures are shown in Figure 5.4. In both cases, the collapse of the sample is observed with very large final incremental strains in the principal direction of loading whatever the flow direction ($|\mathrm{d}\varepsilon_{zz}| \simeq 12 - 14\%$). The failure direction is indeed governed by the stress state. In our case ($\eta > 0$), the compression in the direction z is larger than the transverse compression in the directions x and y. When material failure occurs, the sample undergoes a transient liquefaction during which it cannot withstand anymore the imposed mechanical loading (see section 4.2.3). During this transient period, it shrinks along the direction of major compression (z in the present case). The deformation stops when the new microstructure is able to resist again to the imposed stress state. The collapse direction could switch provided that the additional fluid pressure p_0 imposed in the horizontal direction was such that $p_0 + \sigma_{xx} > \sigma_{zz}$. This is however unlikely to occur as in practice $p_0 \simeq 10^2$ Pa $\ll \sigma_{xx} = \sigma_{yy} \simeq 10^5$ Pa.

Indeed, the internal flow acts as a small perturbation that is sufficient to trigger off the collapse but it does not control the failure direction. In addition, the flow direction does not seem to have any influence on the occurrence of failure.

In Figure 5.3, the collapse of the sample is visible as $\mathrm{d}\varepsilon_{zz}$ suddenly drops below -0.1 which corresponds to a decrease in more than 10% of the sample length in the principal stress direction (see Figure 5.4). Laterally, a little dilation of roughly 1% is observed in the meantime. In the inset plot of Figure 5.3 small strain jumps corresponding to small microstructure evolutions are observed before the global collapse. Indeed, the fluid impact on the granular skeleton is incremental and the flow induced modifications of the contact network develop with a characteristic time up to the global failure.

5.1.4 Influence of fluid force fluctuations

In the boundary value problems recalled in Figure 5.2 the confining stresses applied through grain contacts by the bounding walls are kept unchanged while a fluid pressure drop is imposed to generate an internal fluid flow. As presented in Section 2.4.2, the flow impact is then taken into account in the DEM computation through additional fluid forces applied on every particle. As a result, these additional fluid forces are at the origin of the sample collapse. In Figure 5.5, their micro influence is assessed by plotting the statistical distributions of their three components F_x^f, F_y^f and F_z^f for the two flow cases at the beginning of the flow simulation ($t = 0$ s). The

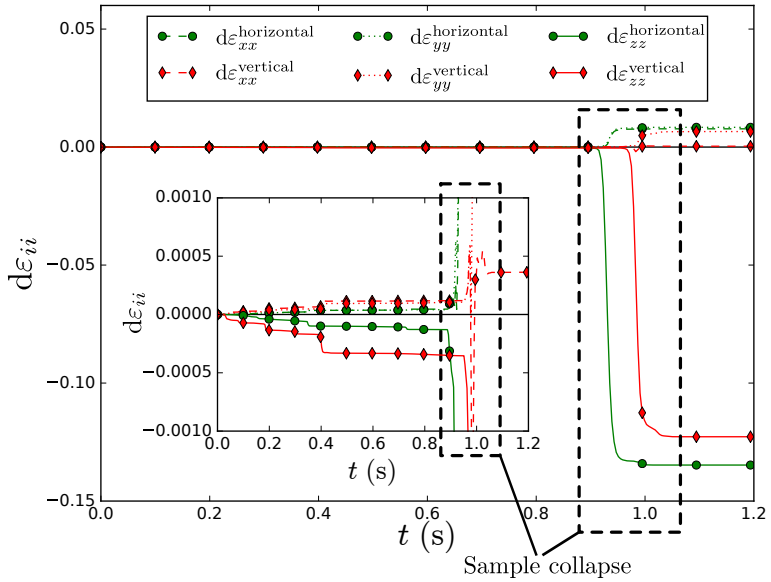

Figure 5.3 – Incremental strain response with respect to time after a fluid pressure drop p_0 is applied in the vertical direction (red curves) or in the horizontal direction (green curves) while keeping a stress state constant ($\eta = 0.35$).

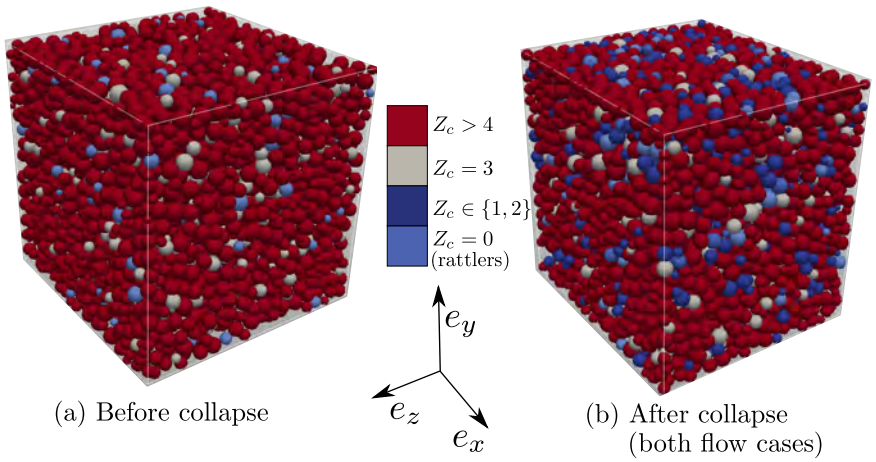

Figure 5.4 – Sample visualization before and after fluid flow is applied. Particles are colored according to their coordination number Z_c.

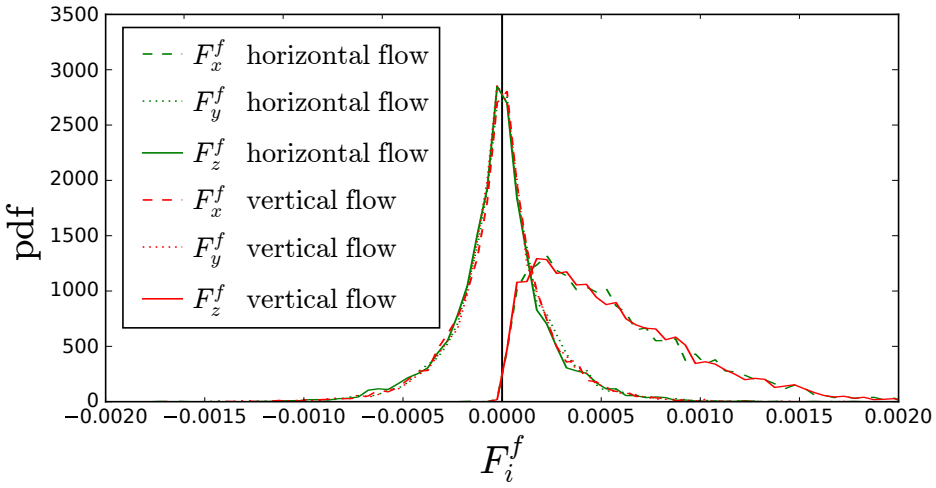

Figure 5.5 – Probability density functions (pdfs) associated to fluid forces components F_x^f, F_y^f and F_z^f acting on individual grains after a fluid pressure drop p_0 is applied in the vertical direction (red curves) or in the horizontal direction (green curves) while keeping a stress state constant ($\eta = 0.35$). The pdfs are plotted for $t = 0$ s but remains unchanged until the global failure of the sample.

probability density functions (pdfs) shown in Figure 5.5 remain unchanged until the global failure of the sample (not shown here).

In Figure 5.5 only two functions are sufficient to describe the six pdfs:

- One to account for fluid forces along the direction of the macroscopic pressure gradient (x or z). These pdfs have strictly positive mode and mean values, which is consistent with the macroscopic flow direction;

- One to account for fluid forces perpendicular to the macroscopic pressure gradient (y and z or x and y). These pdfs are symmetric with zero mean values, which is also consistent with the macroscopic flow direction.

As a result, the pore network driving the fluid force distributions remains isotropic even if the stress state is anisotropic. This is indeed due to the fact that the axial strain levels reached during the triaxial loading are too small to lead to microstructure anisotropy (see Figure 3.11 (c) for axial strain lower than 1%).

The similarities between pdfs of Figure 5.5 and those measured experimentally (Rashidi et al., 1996; Johns et al., 2000; Beguin et al., 2012) or numerically using other coupling schemes (Magnico, 2003; Maier et al., 1999)

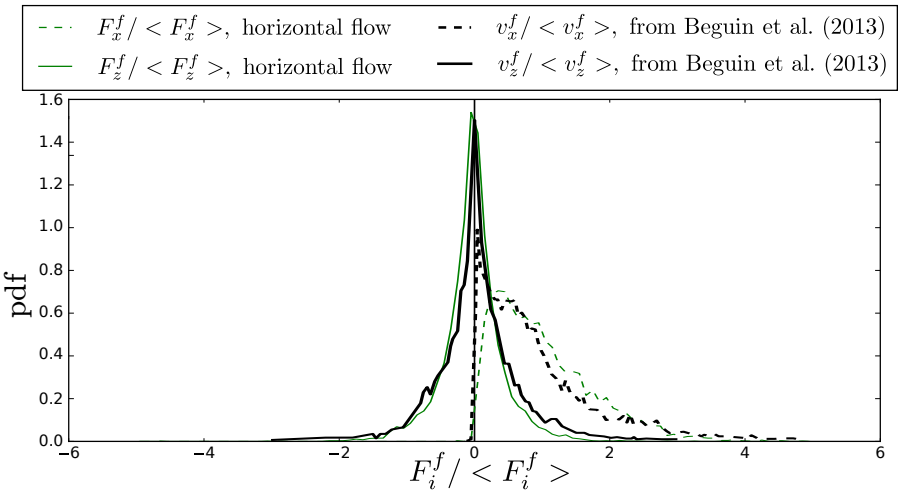

Figure 5.6 – Probability density functions (pdfs) associated to normalized fluid forces $F_x^f/ < F_x^f >$ and $F_z^f/ < F_x^f >$ in the horizontal direction (green lines) compared to the pdfs obtained in Beguin et al. (2012) for dimensionless fluid velocities $v_x^f/ < v_x^f >$ and $v_z^f/ < v_x^f >$ (black thick lines).

are striking. In case of Stoke drag force, the fluid force is proportional to the flow velocity. As a result a comparison between velocity and force pdfs may be attempted by rescaling the fluid forces by the mean fluid force in the macroscopic flow direction. The comparison between pdfs from Figure 5.5 and those obtained by Beguin et al. (2012) is shown in Figure 5.6.

The pdfs for the direction perpendicular to the macroscopic flow are very close to each other while a larger difference can be observed in the macroscopic flow direction. In particular, the experimental mode is much smaller than the one obtained numerically. This can be explained because the pdfs obtained in Beguin et al. (2012) are computed from velocity fields at a resolution finer than the pore size. Indeed, the statistical analysis of Beguin et al. (2012) accounts for the variations of the fluid velocity in boundary layers around grains. As a result, a more important contribution of small velocity values is expected as the fluid velocity is nil on the grain boundaries.

The comparison between the two functions describing the pdfs in Figure 5.5 also gives important clues to understand why the fluid flow direction does not influence the occurrence of macroscopic failure. Indeed, even if fluid forces perpendicular to the macroscopic pressure gradient have a zero mean value, the corresponding pdf shows a standard deviation which is non-negligible compared to the pdf mode value corresponding to the component along the macroscopic flow direction. As a result, whatever the macroscopic flow direction, local fluid force fluctuations can result in incremental loading

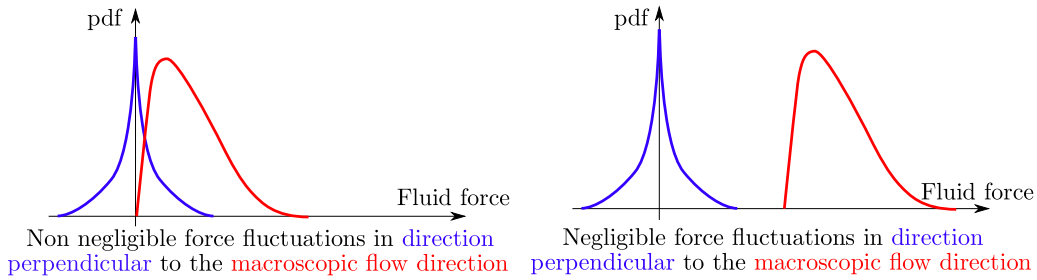

Figure 5.7 – Two possible cases for the fluid force pdfs in the direction of the macroscopic flow and perpendicular to it. In the top case (observed situation), pdfs overlap means that force fluctuations cannot be neglected. In the bottom case (hypothetic situation), no overlapping exists and force fluctuations around the macroscopic flow direction can be neglected.

to particles such that some of the current contacts will reach Mohr-Coulomb limit sliding condition. This situation is illustrated in Figure 5.7. From a quantitative point of view, imagine for instance that a given particle contact is about to slide provided that an additional fluid force $F_z > 0.0002$ N is applied. Based on the statistical results shown in Figure 5.5, the probability for this contact to slide is 80 % in the vertical flow case and 15 % in the horizontal one. As a result, even for the horizontal flow case, this contact has a non-negligible chance to slide. The local non-sensitivity to the macroscopic flow direction is however only true for low magnitude forces. Large fluid forces are more aligned to the macroscopic flow direction as shown by the pdfs in Figure 5.5. The ability of both flow directions to trigger off the sample collapse means that the required magnitude of the fluid forces is quite small for the considered microstructure and the considered stress state.

5.1.5 Contact scale signature for the sample collapse

For a material in the bifurcation domain, some incremental loadings will result in rapid increase in kinetic energy as illustrated for instance in Figure 4.12. The local evolutions of the kinetic energy are shown in Figures 5.8(b) and 5.8(a) in which particles are colored according to their kinetic energy, and the most energetic ones are highlighted thanks to the use of an arbitrary threshold E_c^*.

For both flow directions the sample collapse is preceded by a double burst of kinetic energy. The two bursts initiate locally and then propagate to the whole sample in quite a similar pattern visible in Figure 4.12 for an incremental loading associated with the vanishing of the second-order work.

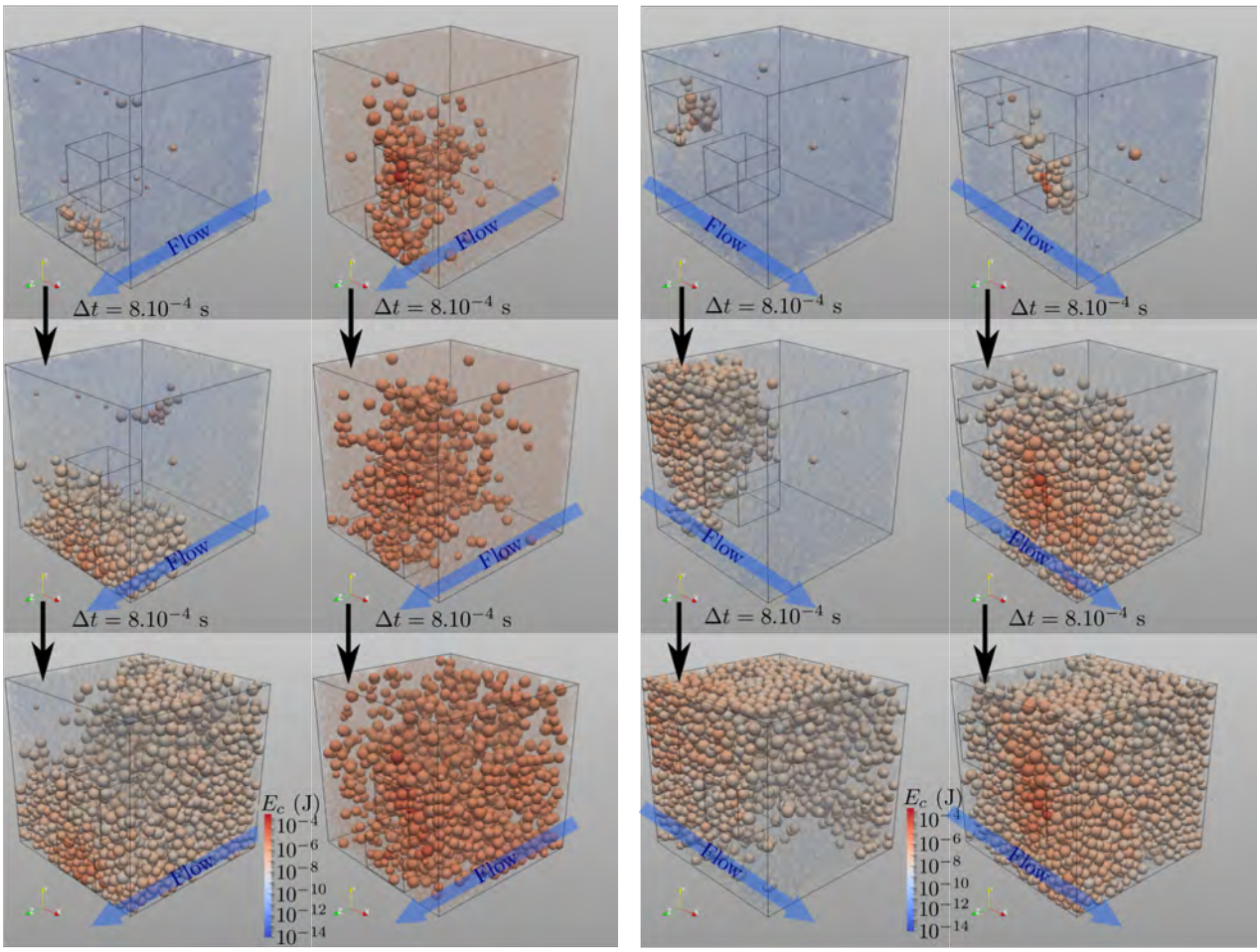

First burst $E_c^* = 10^{-8}$ J — Second burst $E_c^* = 10^{-6}$ J

(a) Vertical flow case

First burst $E_c^* = 10^{-8}$ J — Second burst $E_c^* = 10^{-8}$ J

(b) Horizontal flow case

Figure 5.8 – Visualization of the two outbursts of kinetic energy propagation for the two flow cases. Particles are colored according to their kinetic energy (log scale). Those with kinetic energy higher than E_c^* are highlighted.

If the first bursts initiate in different locations for the two flow directions, the second bursts start at the same spot. For the vertical flow case the two bursts follow in a row while for the horizontal flow case, the sample temporarily restabilizes between the two outbursts of kinetic energy. As a result, the second burst is more intense in the vertical case and a higher kinetic threshold $E_c^* = 10^{-6}$ J was used to highlight its propagation in Figure 5.8.

The burst mechanism is a signature of a local failure of the existing contact network under the action of additional fluid forces. Even if the failure remains localized, this can affect the whole contact network as stresses are forced to redistribute. In order to assess the impact of this stress redistribution on the contact network, it is interesting to analyze whether contact forces get closer to the Mohr-Coulomb limit. At the contact scale the sliding index $I_p = \dfrac{||\boldsymbol{F}_t||/||\boldsymbol{F}_n||}{\tan\phi}$ introduced in Equation (4.6) is reconsidered. This sliding index compares the ratio between the tangential and normal contact force magnitudes ($||\boldsymbol{F}_t||$ and $||\boldsymbol{F}_n||$) with the Mohr-Coulomb limit value $\tan\phi$, ϕ being the inter-particle friction angle.

I_p values sufficiently closed to 1 (contact close to sliding) is a necessary condition to observe the local the vanishing of the second-order work (Nicot and Darve, 2006a; Wautier et al., 2018c). A large population of contacts with I_p close to 1 is thus a necessary condition to obtain a material instability, i.e. a macroscopic vanishing of the second-order work (Wautier et al., 2018b). In Figure 5.9, the time evolution of the fraction of contacts close to sliding $\frac{N_c(I_p>0.9)}{N_c^{\text{tot}}}$ is plotted for the two flow cases during the sample collapse identified in Figure 5.3 by large strain jumps. It is recalled here that the condition $I_p > 0.9$ used to define contacts close to sliding is justified in Section 4.2.4. In this figure, the initiation of the two outbursts of kinetic energy detected in Figures 5.8(b) and 5.8(a) are shown with vertical solid lines.

In Figure 5.9, the two identified bursts of kinetic energy have two very different signatures in terms of $\frac{N_c(I_p>0.9)}{N_c^{\text{tot}}}$ evolutions. While the first burst is associated with a decrease in $\frac{N_c(I_p>0.9)}{N_c^{\text{tot}}}$, the second burst is associated with an increase in $\frac{N_c(I_p>0.9)}{N_c^{\text{tot}}}$. Indeed, the first outbursts of kinetic energy result in building more resilient contact networks with fewer contacts likely to reach Mohr-Coulomb condition ($I_p = 1$), while the second bursts result in less resilient contact networks which eventually fail globally. This explains why failure occurs only after the second outburst of kinetic energy.

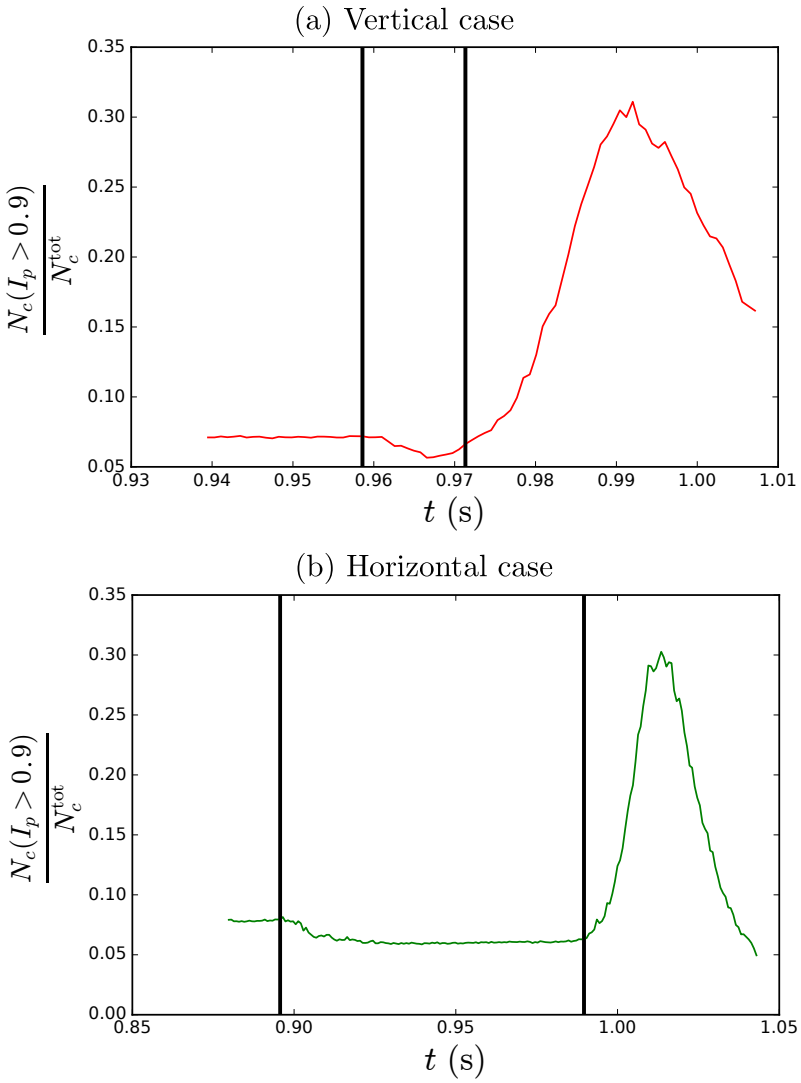

Figure 5.9 – Time evolution of the fraction of contacts close to sliding during the sample collapse for the vertical flow case (a) and the horizontal one (b). The onset of the two outbursts of kinetic energy is shown with vertical solid lines.

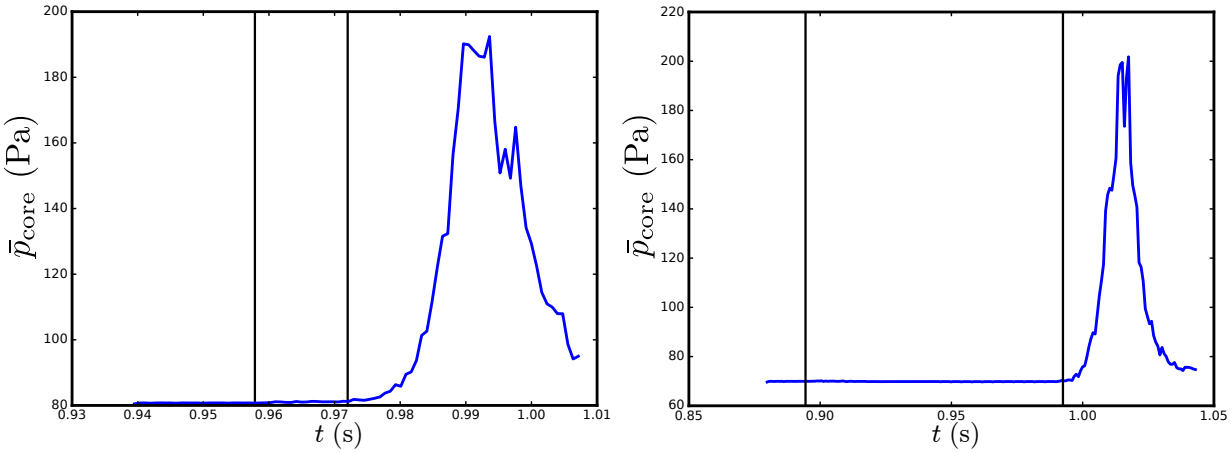

(a)Vertical fow case (b)Horizontal fow case

Figure 5.10 – Time evolution of the average pore pressure in the core of the sample for the two flow cases. The pore pressure is averaged over the domain $[0.45\ell_x, 0.55\ell_x] \times [0.45\ell_y, 0.55\ell_y] \times [0.45\ell_z, 0.55\ell_z]$ where ℓ_x, ℓ_y and ℓ_z are the sample dimensions. The onset of the two outbursts of kinetic energy visible in Figure 5.8 are shown with vertical solid lines.

5.1.6 Collapse and resulting excess pore pressure

Soil liquefaction is one possible phenomenon responsible for granular material failure. In order to precise the failure mechanism leading to the outbursts of kinetic energy shown in Figure 5.8, it is interesting to plot the time evolution of the pore water pressure. In Figure 5.10, the average pore pressure in the core of the sample is plotted during the sample collapse.

In Figure 5.10 the propagation of the two outbursts of kinetic energy are shown by vertical solid lines. For both flow cases, an increase in the central pore pressure is observed only after the onset of the second outburst of kinetic energy. As a result, the observed pore excess pressure is a consequence and not the cause of the observed material failure triggered off by the internal fluid flow. As a result the mechanisms responsible for the observed material failure can be investigated with the micromechanical tools developed in the previous chapters for dry granular materials.

In Figure 5.11 the difference between the pore pressure and the linear approximations of the macroscopic pressure gradient ($p_{\text{macro}} = p_0 - x\frac{p_0}{\ell_x}$ and $p_{\text{macro}} = p_0 - z\frac{p_0}{\ell_z}$) are shown for the two flow cases and at different times during the increase in the central pore pressure shown in Figure 5.10. As in Section 3.4.2, 2D average pore pressures $\bar{p}(x)$ and $\bar{p}(z)$ are computed together with the corresponding standard deviations in the plane perpendicular to the

fluid flow.

In both cases the pressure distributions deviates from the linear approximation of the macroscopic pressure gradient with an increase in the pore pressure in the core of the samples. Close to the boundaries where pressure is imposed, this deviation is less pronounced. In both flow cases the pore pressure increase occurs at the same pace but the maximum increase is located more on the downstream side of the sample in the vertical flow case and more on the upstream side of the sample for the horizontal case.

5.1.7 Driving mesoscale mechanisms

As widely acknowledged in the literature, stresses imposed at the macroscopic scale concentrate locally on only 20 to 30 % of the grains organized in elongated mesostructures commonly called force chains (Liu et al., 1995; Radjai et al., 1998; Bardenhagen et al., 2000; Cambou et al., 2013). The interplay between these chains and the surrounding loosely stressed grains (the non-chained grains) is known to have important implications on force chain stability as loose particles provide lateral support (Tordesillas et al., 2010; Zhu et al., 2016b). By using the force chain definition introduced by Peters et al. (2005) the set of chained particles can be tracked in the considered sample during its flow induced collapse identify in Figure 5.4.

In Figure 5.12, the current set of chained particles is compared to the initial one in terms of:

- *born particles* (N_{born}): current chained particles that were not belonging to initial force chains;
- *died particles* (N_{died}): initially chained particles that does not belong to force chains anymore.

In Figure 5.12, the sample collapse is visible through important modifications in the chained particle populations (after collapse, roughly 70% of the initial chained particles have *died*). A simultaneous increase in N_{born} and N_{died} occurs as outbursts of kinetic energy are observed. In the end, as the sample gets denser, more force chains are built than initially ($N_{\text{born}} > N_{\text{died}}$).

Similarly to Sections 4.3.3 and 4.3.4, elementary force chain bricks composed of three particles can be considered to understand the causes of chained particle population renewal. At some point, these elementary bricks referred to as *3-p groups* in the following may not be identified as such because they do not satisfy anymore one of the three conditions used in the force chain definition (Peters et al., 2005) illustrated in Figure 5.13:

- a contact is lost between the considered three particles;

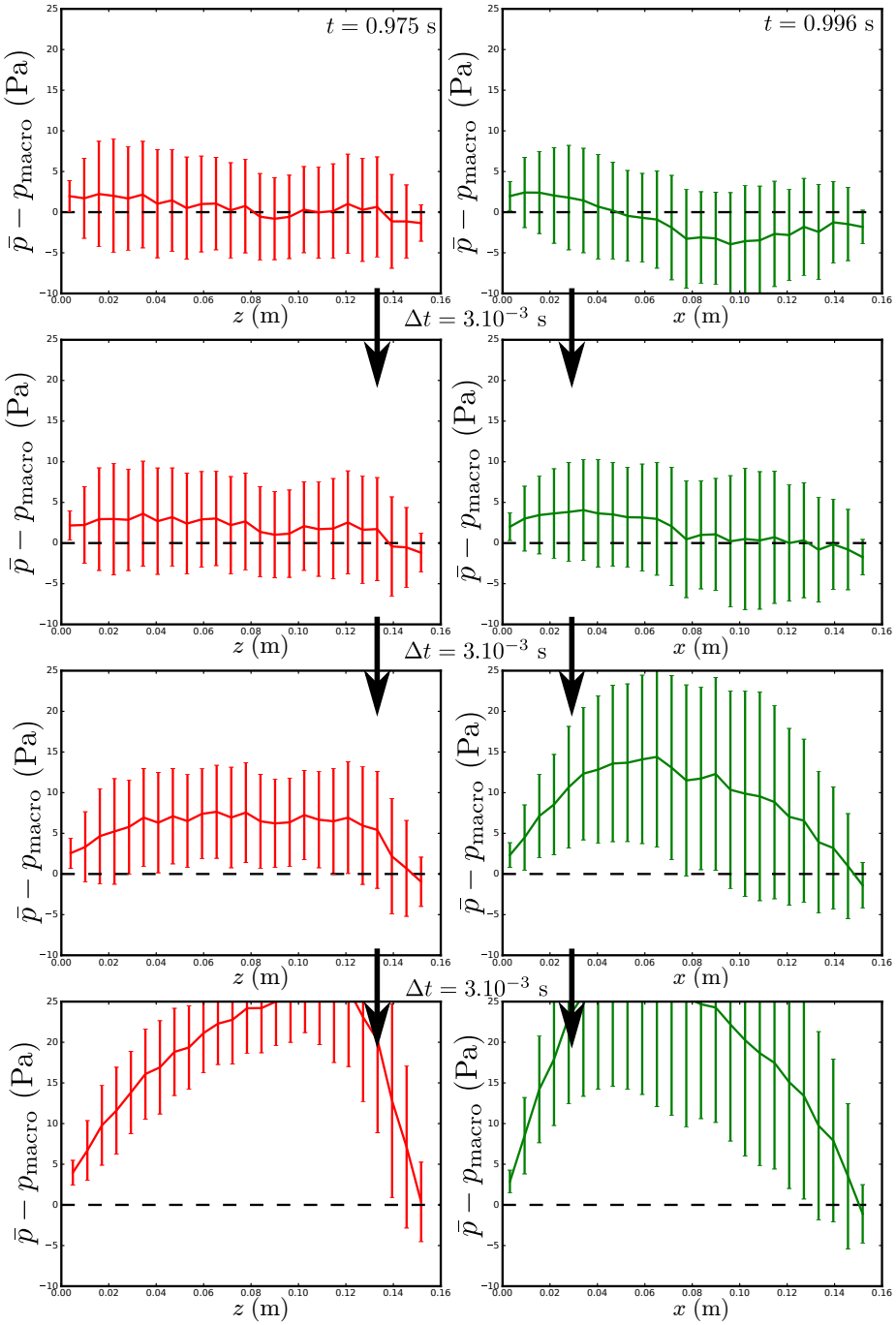

(a)Vertical fow case (b)Horizontal fow case

Figure 5.11 – Differences between the 2D averaged pore pressure and the linear approximations of the macroscopic pressure gradient $p_{\text{macro}} = p_0 - x\frac{p_0}{\ell_x}$ and $p_{\text{macro}} = p_0 - z\frac{p_0}{\ell_z}$ for the two flow cases after the onset of failure. Standard deviations are shown in the form of error bars.

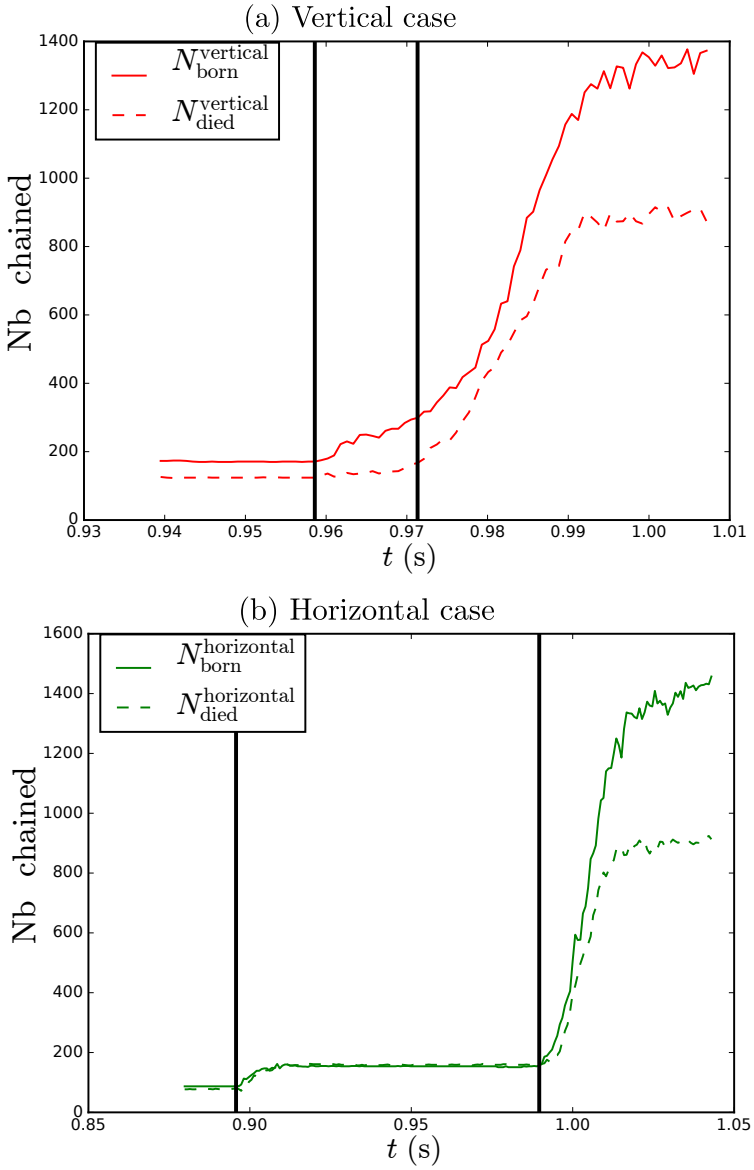

Figure 5.12 – Time evolution of N_{born} (solid) and N_{died} (dashed) during the sample collapse for the vertical flow case (a) and the horizontal one (b). The common reference set of chained particles is defined on the sample prior to impose the horizontal or vertical fluid pressure drop. The onset of the two outbursts of kinetic energy is shown with vertical solid lines.

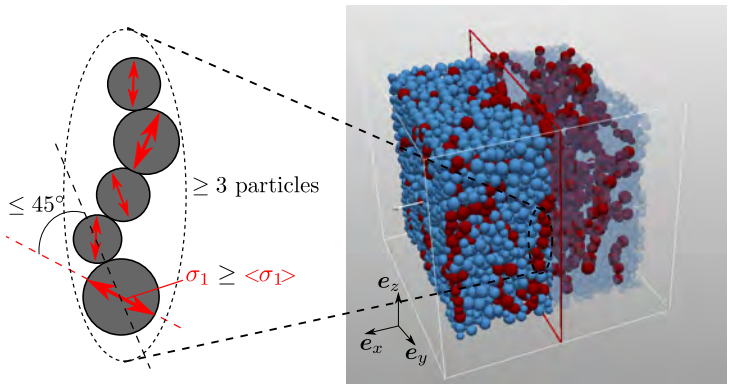

Figure 5.13 – Three criteria force chain definition according to Peters et al. (2005) (left) and force chain visualization in the sample before collapse (right). σ_1 corresponds to the principal compression value of each grain. Grains belonging to force chains are colored in red while non-chained grains are represented in blue or transparent blue.

- one of the particle's principal stress is now lower than the mean principal stress computed for all the sample particles;

- the geometrical direction of the contacts is no more aligned with the principal stress direction (a maximum deviation of 45° is used here).

In Figure 5.14 the relative contributions of the above causes for the disappearing of a 3-p group are given for the current set of 3-p groups that will disappear in the future.

Misalignment between principal stress and contact directions and relative unloading compared to the mean principal stress are the two main cause of the disappearing of initial 3-p groups. On the contrary, contact loss is not a significant mechanism at first. As a result, the changes in force chain populations observed in Figure 5.12 mainly result from force chain bending occurring simultaneously with the second outburst of kinetic energy.

Once the general collapse occurs (after the second outburst of kinetic energy), the remaining force chains will mainly disappear because of stress redistribution (relative unloading compared to the mean principal stress value). Later on, contact loss becomes a non-negligible cause for 3-p groups disappearing. These observations are consistent with previous results found in the literature for dry granular materials describing the micromechanisms responsible for failure in granular materials (Tordesillas et al., 2010; Zhu et al., 2016b; Wautier et al., 2018b). Additional fluid forces induce force chain bending which results in important stress redistribution and eventually some

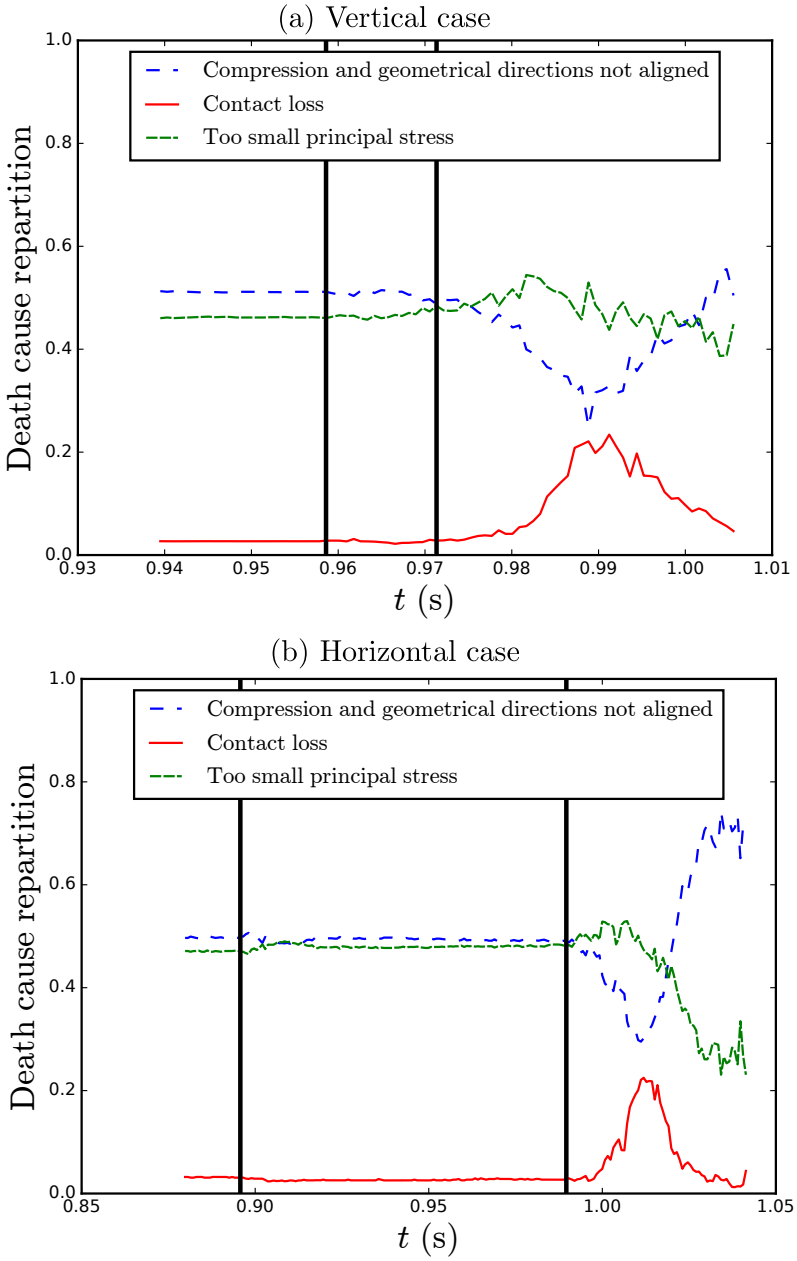

Figure 5.14 – Statistical repartition between the three possible disappearing causes for 3-p groups existing at time t and disappearing at time $t_f < 1.01$ s (vertical flow case (a)) or $t_f < 1.05$ s (horizontal one (b)). A 3-p group may not be identified as such anymore either because of contact loss (solid line), relative unloading (densely dashed line) or geometrical/compression misalignment (dashed line). The onset of the two outbursts of kinetic energy is shown with vertical solid lines.

contact losses. It is important to stress here that the disappearing of 3-p groups through contact loss is a consequence from the global collapse of the contact network and not directly driven by the fluid flow. As a result, grain detachment may not be directly induced by fluid flows but may be a consequence of force chain collapse.

Based on the distinction between chained particles (heavily stressed particles constituting the force chains) and non-chained particles (loosely stressed particles not belonging to force chains), three populations of contacts can be defined, namely chained/chained (cc) non-chained/non-chained (nn) and non-chained/chained (nc) contacts. By tracking the time evolution of these three contact populations, information can be obtained on internal kinematic constraints. In particular, the number of non-chained/chained contacts (N_{nc}) is known to be of fundamental importance with respect to force chain stability (Wautier et al., 2018b; Zhu et al., 2016b). In Figures 5.15(a) and 5.15(b) the time evolution of N_{nc}, N_{nn} and N_{cc} is shown for three control volumes: for the whole sample and for two small volumes around the locations of the two outbursts of kinetic energy. The control volumes located around the positions of the outbursts of kinetic energy are visible in Figures 5.8(b) and 5.8(a).

For the horizontal case in Figure 5.15(b), the first outburst of kinetic energy is followed by a local drop in N_{nn} together with an increase in N_{nc} and N_{cc}. As a result kinematic constraints increase around force chains which is consistent with the sample recovering from a temporary destabilization. This is not the case for the second burst which is accompanied by a drop in N_{nc} which characterizes force chain deconfinement. This drop appears at first locally in the second control volume ($N_{nc}^{b_2}$) before generalizing to the whole sample (N_{nc}). In the end, as the sample densifies and new force chains are build, N_{nn}, N_{cc} and N_{nc} increase again.

For the vertical case in Figure 5.15(a), the two bursts appear in a row with increasing levels of kinetic energy. If the first burst is not accompanied by a drop in N_{nc}, the second one is. As for the horizontal case, the drop in N_{nc} appears at first locally in the second control volume ($N_{nc}^{b_2}$) before generalizing to the whole sample (N_{nc}). As the sample densifies N_{nn}, N_{cc} and N_{nc} increase again in the end.

In both cases, the sample collapse occurs simultaneously with a release in kinematic constraints around force chains which is consistent with previous results found in the literature (Zhu et al., 2016b; Wautier et al., 2018b). However it must be emphasized that this force chain deconfinement does not seem to be the triggering mechanism as it was shown in the case of an incremental stress loading corresponding to a negative second-order work (see Section 4.3). Indeed, for classical stress-controlled directional analysis under

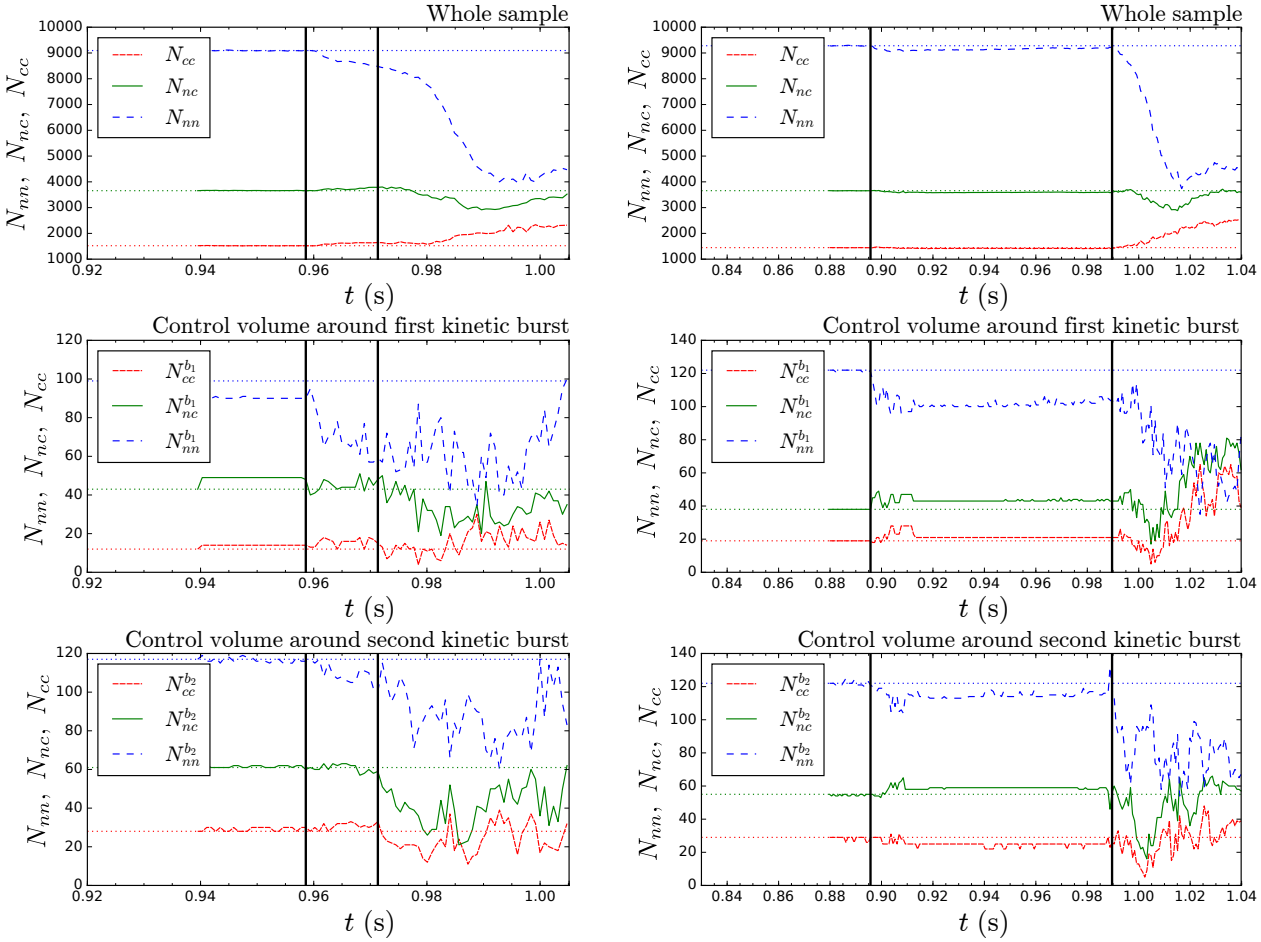

(a) Vertical flow case

(b) Horizontal flow case

Figure 5.15 – Time evolution of the number of chained/chained (densely dashed line) non-chained/non-chained (dashed line) and non-chained/chained (solid line) contacts during the sample collapse for the two flow cases. N_{nc}, N_{nn} and N_{cc} are given for the whole sample and for the two control volumes shown in Figure 5.8. The onset of the two outbursts of kinetic energy is shown with vertical solid lines.

drained axisymmetric conditions, the vanishing of the second-order work is usually observed for loading directions corresponding to a macroscopic dilation (Nicot et al., 2009, 2013a; Wautier et al., 2018b). At the microscale, this dilation results in some contact loss. When occurring around force chains contact loss results in a decrease in kinematic constraints which eventually lead to force chain collapse. In the present case, the perturbation is imposed by the fluid and does not necessarily result in global dilation. As a result, no force chain deconfinement is observed before the onset of the outburst of kinetic energy in Figure 5.15.

5.1.8 Grain detachment as a consequence of force chain collapse

At the microscale, suffusion is reduced to three elementary mechanisms, namely grain detachment, grain transport and clogging (or grain attachment). In the present case, since all rattlers have been removed initially, any transported grains have to be previously detached. As a result, the occurrence of grain detachment can be simply assessed by detecting grains with a coordination $Z_c = 0$. In Figure 5.16, grain detachment events (t, i) are shown by pointing the first moment t at which a grain identified by its index $i \in [\![0; 10,000]\!]$ has a coordination number $Z_c^i(t) = 0$.

In Figure 5.16, grain detachment is found to occur only after each outburst of kinetic energy for the two flow cases. As seen in Figure 5.8, these outbursts of kinetic energy propagate to the whole sample and result in a general rearrangement of the contact force network. As a result, grain detachment *is not* an isolated mechanism in which grains are individually extracted from the primary fabric under the action of a fluid force. Grain detachment is indeed a non-local mechanism which is the consequence of force chain reorganization. This result precises the sequence of mechanisms responsible for grain detachment:

- first the internal fluid flow forces stress reorganization in the granular material

- in case of force chain collapse, grains are then detached from the primary fabric.

This result is backed by the fact that no grain detachment was ever found in all DEM/PFV simulations run during this PhD without any sample collapse.

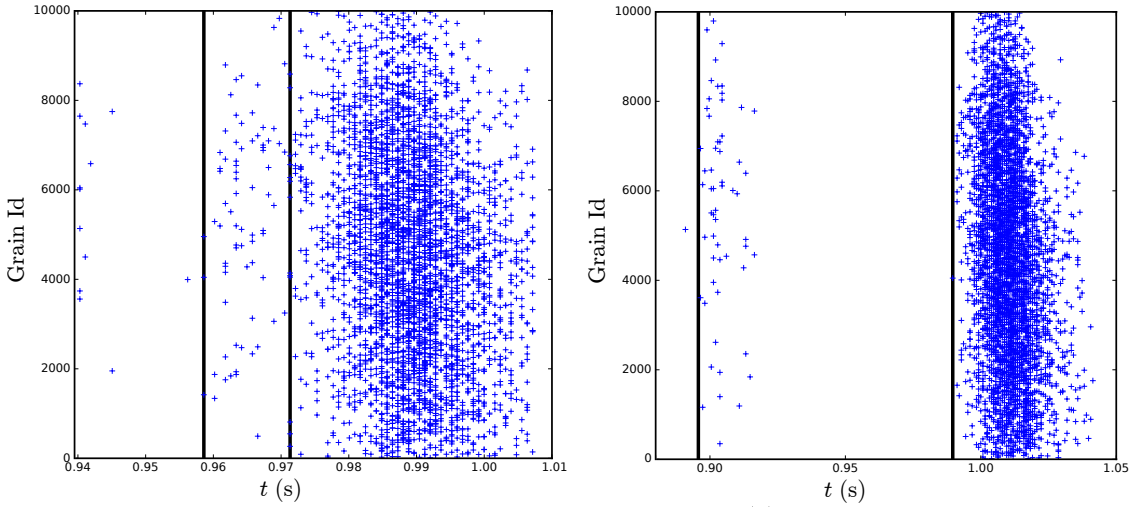

(a) Vertical case (b) Horizontal case

Figure 5.16 – Grain detachment events (t, i) for both flow cases around the collapse of the sample. Point (t, i) corresponds to the first moment t at which a grain identified by its index $i \in [\![0, 10000]\!]$ has a coordination number $Z_c^i(t) = 0$. The onset of the two outbursts of kinetic energy is shown with vertical solid lines.

5.2 Relative influence of flow induced erosion and clogging

In the previous section, a sample in which rattlers are removed was considered to analyze the direct impact of an internal fluid flow on stress transmission. In this section, a sample with a wider PSD is considered and the relative influence of erosion and clogging with respect to mechanical stability is explored in the light of the results from Chapter 4.

5.2.1 Definition of a widely graded sample with significant fine fraction

Similarly to the preparation procedure presented in Section 3.1, a cubic assembly of spheres is generated randomly with a widely graded particle size distribution (PSD) illustrated in Figure 5.17. This PSD is such that the ratio between the largest and smallest particles is 10 and such that the coefficient of uniformity $\mathrm{Cu} = d_{60}/d_{20} = 1.98$ where d_{20} and d_{60} are the particle diameters corresponding respectively 20 % and 60 % of the mass passing fractions.

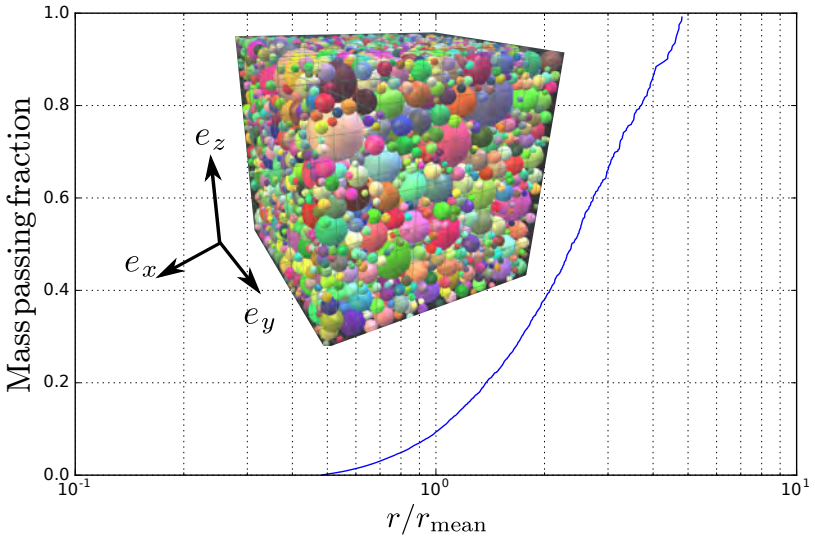

Figure 5.17 – Normalized PSD curve by mass corresponding to the generated sample. Particle radii are normalized by the mean radius value $r_{\text{mean}} = 2.10^{-4}$ m. The generated sample in the isotropic state is shown.

After generating a cloud of 5,000 non-overlapping spheres surrounded by six bounding planes defining a cube, the particles are inflated and allowed to rearrange according to the radius expansion technique. This process is stopped when the confining pressure applied to the bounding planes reaches 20 kPa and the normalized unbalanced force (F_{unb}) of the system decreases below 1.5 10^{-2}. By definition F_{unb} is equal to the mean summary force on the N_p particles divided by the mean contact force magnitude on the N_c contacts:

$$F_{\text{unb}} = \frac{\frac{1}{N_p}\sum_{p=1}^{N_p} ||\sum_{c_p} \boldsymbol{F}_{c_p}||}{\frac{1}{N_c}\sum_{c=1}^{N_c} ||\boldsymbol{F}_c||}. \tag{5.1}$$

During this process, the inter-particle friction angle is maintained to 35° in order to prepare a dense granular material with a void index $e = 0.55$. The resulting sample shown in Figure 5.17 is then rescaled such that $r_{\text{mean}} = 2.10^{-4}$ m.

It should be highlighted here that despite the large aspect ratio between the largest and smallest particles, the used PSD is not identified as internally unstable acording to Kezdi's filter rule (Kézdi, 1979) or Kenney and Lau

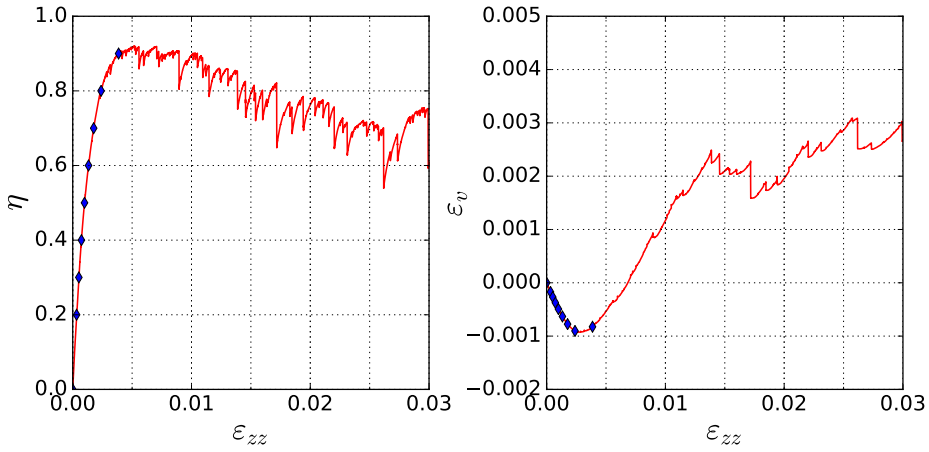

Figure 5.18 – Drained triaxial test response. The diamond points correspond to the mechanical states considered for the stability analysis.

criterion (Kenney and Lau, 1985).

5.2.2 Mechanical stability assessment for different stress states

From the obtained equilibrium state, a drained triaxial loading is then imposed to the sample in the form of a two step procedure as in Section 3.1.2. First, the confining pressure (σ_0) is increased from 20 kPa to 100 kPa by allowing the bounding walls to move. Once a new equilibrium state is reached ($F_{\text{unb}} < 10^{-4}$), a vertical compression strain rate $\dot{\varepsilon}_{zz} = 0.01$ s^{-1} is applied up to 3 % of deformation while keeping the same lateral confining pressure σ_0. This strain rate is chosen similar to the one used in previous numerical studies (Hadda et al., 2013; Nicot et al., 2012) and is supposed to be sufficiently small so that the loading can be considered as quasi-static.

In Figure 5.18, the stress ratio and volumetric strain responses are shown. A typical contractive/dilative behavior of a dense soil is observed. While the stress ratio increases, samples are saved for $\eta \in \{0, 0.2, 0.3, 0.4, 0.5, 0.6, 0.7, 0.8, 0.9\}$. The corresponding states are marked with diamonds in Figure 5.18.

Following the procedure detailed in Section 4.2, directional analyses are performed in Rendulic's plane to assess the mechanical stability of the nine saved samples (dry conditions). In Figure 5.19, the second-order work circular envelopes are shown for the considered stress ratio.

In Figure 5.19, as the stress ratio increases, second-order work decreases for directions around 235°. The second-order work eventually vanishes for

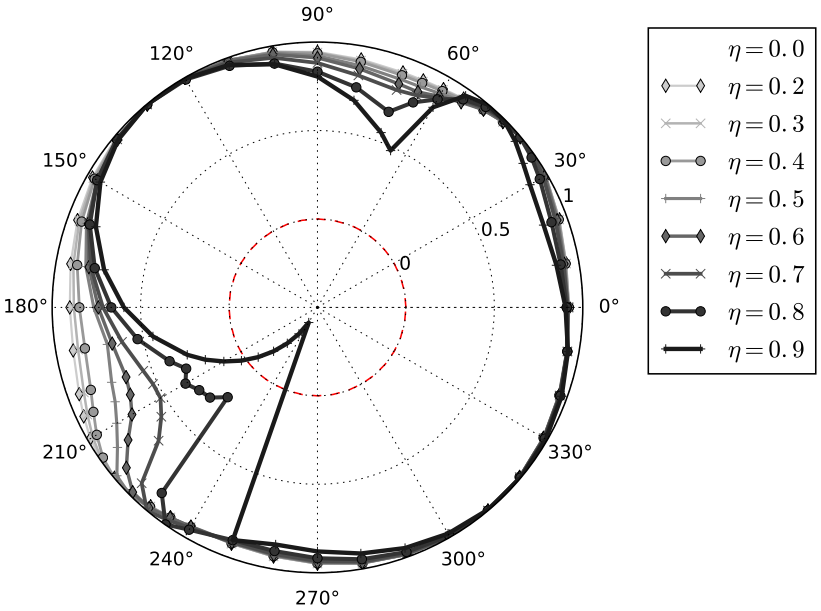

Figure 5.19 – Circular second-order work for different η values. $W_2 = 0$ is indicated by a red dashed circle.

$\eta = 0.9$ in the instability cone $\theta \in [220°, 250°]$. If is interesting to notice that the vanishing of the second-order work occurs after the characteristic point in Figure 5.18 when the volumetric behavior changes from contractancy to dilatancy. This point is also known to correspond to the moment from which the number of chained particles decreases (Liu et al., 2018). This weakening of the contact force network is thus consistent with the existence of an underlying instability.

5.2.3 Flow boundary value problem and bounce back erosion criterion

In the following subsections, DEM/PFV simulations with boundary conditions similar to Section 5.1.2 are considered for the two samples corresponding to $\eta \in \{0.7, 0.9\}$, for the two flow directions $\{\boldsymbol{e}_x, \boldsymbol{e}_z\}$ and for the two flow intensities $I \in \{0.1, 1\}$. The corresponding six DEM/PFV simulations are summarized in Table 5.1.

Since non-periodic boundary conditions are used in the DEM/PFV simulations carried out, transported grains are either i) extracted out from the core of the sample as they reach the downstream wall or ii) filtrated by the primary fabric as they are blocked by a too narrow constriction. In the first

Table 5.1 – The six DEM/PFV simulations carried out in this section.

Stress state	Hydraulic gradient $I = 0.1$	$I = 1$	Flow direction Vertical ($\boldsymbol{e}_z$)	Horizontal ($\boldsymbol{e}_x$)
$\eta = 0.7$	x		x	x
$\eta = 0.9$	x	x	x	x

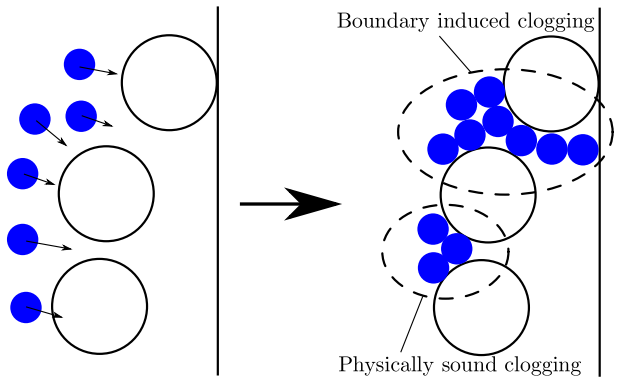

Figure 5.20 – Illustration of the non-physical clogging induced by the downstream wall.

case, the downstream wall induces artificial clogging. If many particles can be extracted, this boundary effect is likely to strongly affect particle transport in the sample as illustrated in Figure 5.20.

To avoid such boundary effects, it is thus important to detect and delete particles reaching the downstream wall. A naive and computationally expensive approach is to check for particles with a single contact with the downstream wall. The main problem with this criterion is that it has to be run at every time step as extracted particles often bounce several times on the downstream wall before stabilizing and the contact with the downstream wall never lasts for long. As a result, a prediction/correction algorithm was preferred to this first approach. This algorithm is illustrated in Figure 5.21 and consists in the following two steps:

- At time t, rattlers are identified. By assuming that their velocity $\boldsymbol{v}(t)$ remains constant over the interval $[t, t+\Delta t]$, rattlers that will virtually go through the downstream wall during this interval are identified as candidates to particle removal. This is the prediction step.

- At time $t+\Delta t$, the scalar product between the updated velocity $\boldsymbol{v}(t+\Delta t)$ and the outward normal to the downstream wall $\boldsymbol{n}$ is computed for rattlers candidates to particle removal. If $\boldsymbol{v}(t+\Delta t)\cdot\boldsymbol{n} < 0$, then the

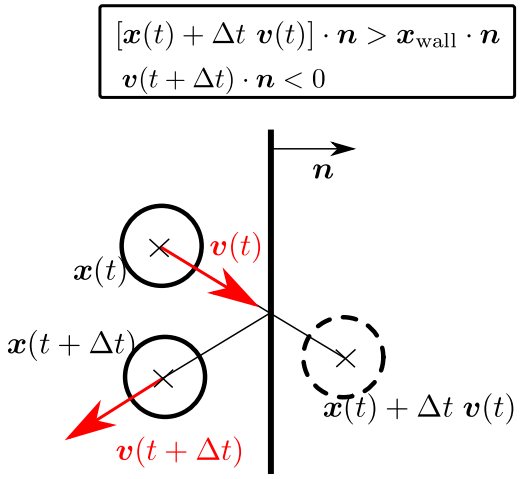

Figure 5.21 – Prediction/correction algorithm used to identify extracted particles.

considered particle bounced back on the downstream wall during the time interval $[t, t + \Delta t]$ and will be removed from the simulation. This is the correction step.

This approach reduces the computational cost needed to detect extracted particles as loops over the number of particles are required only from time to time and not at every DEM time step. In practice, Δt is set to be equal to 1,000 DEM time steps.

To improve computational efficiency, when extracted particles are identified, they are not deleted immediately. Indeed, as the PFV scheme relies on a particle based tessellation of the pore space (see Section 2.4.2), remeshing is needed each time a particle is deleted. As a result, extracted particles are kept in memory and are only deleted after several runs of the prediction/correction algorithm (every 5,000 iterations in practice which is small enough to avoid that particle that bounced back collide with an other particle).

5.2.4 Numerical analysis of directional transport properties

By tracking the positions of all particles during the fluid flow simulations, travel distances are estimated as in Section 3.4.2. In addition, extracted particles that reached the downstream side of the sample during DEM/PFV simulations are identified. The shortest displacements (see definition in Equation (3.18)) of all particles are shown in Figure 5.22 for the initially unstable

sample subjected to a hydraulic gradient $I = 0.1$ either in vertical or horizontal directions.

In Figure 5.22 the clouds of points corresponding to extracted (red diamonds) and non-extracted (blue crosses) particles superimpose, showing that the considered sample is sufficiently large to compute mean travel distances representative of material properties and not influenced by sample boundaries. Compared to the sample dimensions $(\ell_x, \ell_y, \ell_z) = (43.7r_{\text{mean}}, 43.7r_{\text{mean}}, 43.5r_{\text{mean}})$ some particles are transported over quite large distances up to 20 times the mean radius, but the average travel distances are small ($< 2r_{\text{mean}}$). There exist too few pores and constrictions large enough to allow for transport and clogging dominates as expected by the fact that the used PSD is not identified as *internally unstable*.

As in Section 3.4.2, the numerical estimations of the shortest mean travel distances $\bar{D}^{\text{short}}_{\text{num}}$ can be compared to pore network predictions $\bar{D}^{\text{short}}$. To this respect, three predictions of $\bar{D}^{\text{short}}$ are considered and plotted in Figure 5.22. Theses predictions rely on the three weighted pore networks illustrated in Figure 5.23. The first pore network corresponds to the one used in Section 3.3.3 and relies on a triangulation of the pore space based on all particles and a pressure map computed thanks to the PFV scheme (Figure 5.23 (a)). The second pore network was introduced in Section 3.4.2 and relies on a triangulation of the pore space based on all particles and a pressure map computed thanks to the linear approximation of the macroscopic pressure gradient (Figure 5.23 (b)). The third pore network relies on a triangulation of the pore space based only on non-free particles and a pressure map computed thanks to the linear approximation of the macroscopic pressure gradient (Figure 5.23 (c)).

In Figure 5.22, mean shortest travel distances computed thanks to the transport network model of Section 3.3.3 gives indeed lower and upper bounds of the transport distances estimated thanks to fully coupled DEM/PFV simulations. While using the pore network computed with all particles, pore and constriction sizes are underestimated. For instance, for a free particle in a tetrahedron composed of four particles, four small pores are identified in the corresponding pore network whereas the free particle moves in a single large pore (see Figure 5.23). As a result, mean travel distances computed from this pore network provide lower bounds for the effective mean travel distances. While using the pore network computed with only non-free particles, pore and constriction sizes are more relevant but collective motions of the free particles are not accounted for (in particular collective clogging). As a result, mean travel distances computed from this pore network provide upper bounds for the effective mean travel distances. As already seen in Section 3.4.2, the local fluctuations in the pore pressure tend to increase

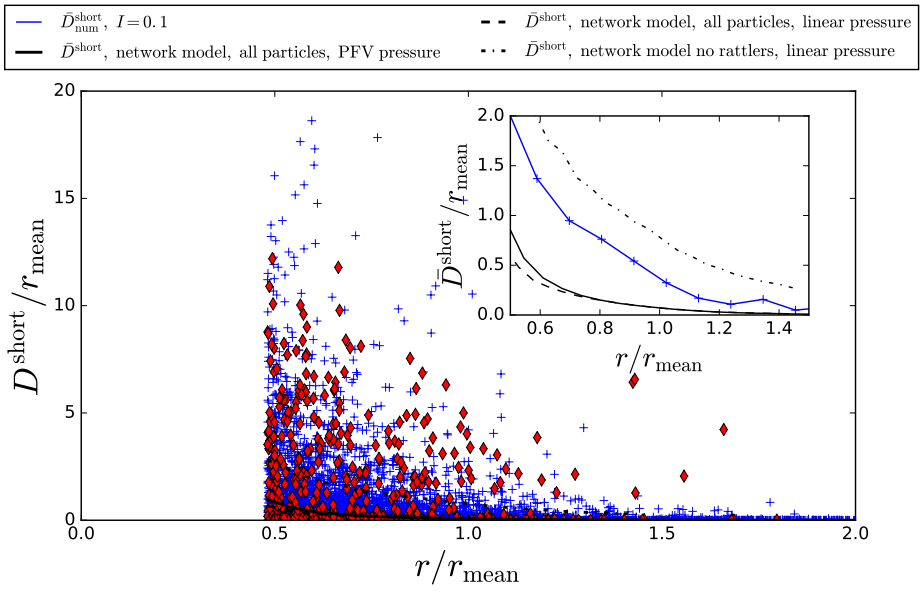

(a) Vertical flow case

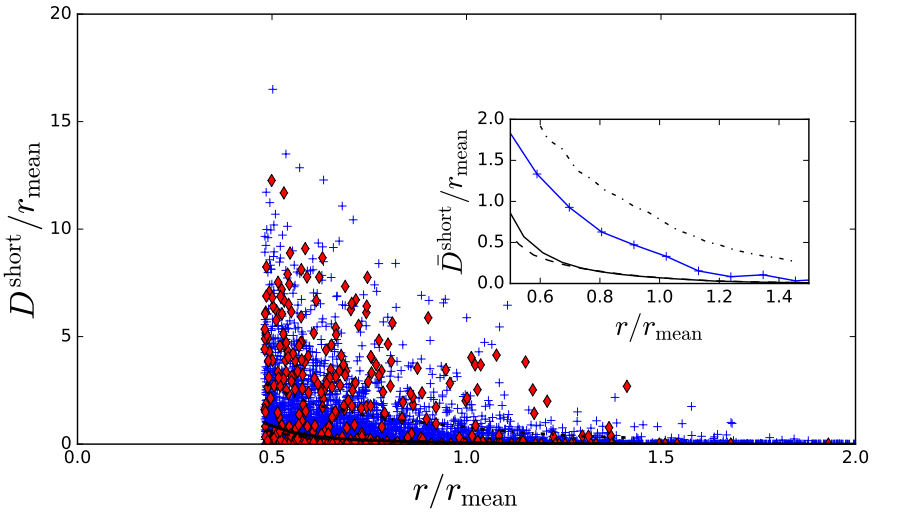

(b) Horizontal flow case

Figure 5.22 – Shortest travel distances of all the particles of the initially unstable sample corresponding to $\eta = 0.9$ subjected to a hydraulic gradient $I = 0.1$ in the vertical (a) or horizontal (b) directions. Extracted particles are identified by red diamonds. The mean transport distances $\bar{D}^{\text{short}}_{\text{num}}$ are shown in blue solid lines. In black solid lines the numerical prediction corresponding the transport model of Section 3.3.3 are shown (pressure map computed thanks to the PFV scheme). Dashed and dot-dashed lines correspond to the predictions computed from the linear approximation of the macroscopic pressure gradient respectively on the pore network computed with all particles and on the pore network computed with only non-free particles.

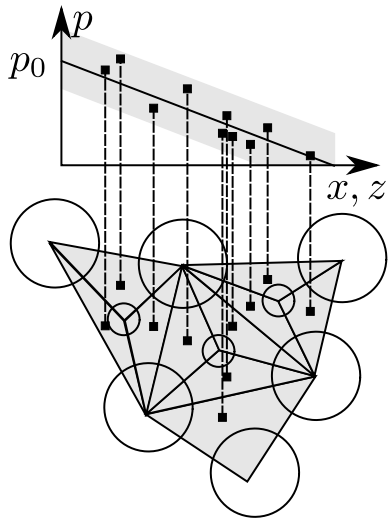

(a) Pore network on all particles, PFV pore pressure map

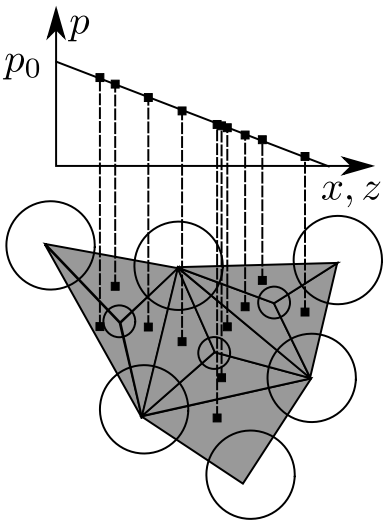

(b) Pore network on all particles, linear pore pressure map

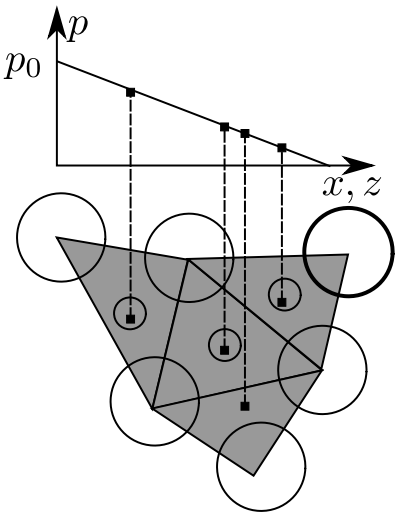

(c) Pore network on non free particles, linear pore pressure map

Figure 5.23 – Three different pore networks used to estimate mean travel distances. The network can be constructed either from all particles ((a) and (b)) or only from non-free particles (c). The pore pressure map can be derived from the use of the PFV scheme (a) or from the linear approximation of the macroscopic pressure gradient ((b) and (c)).

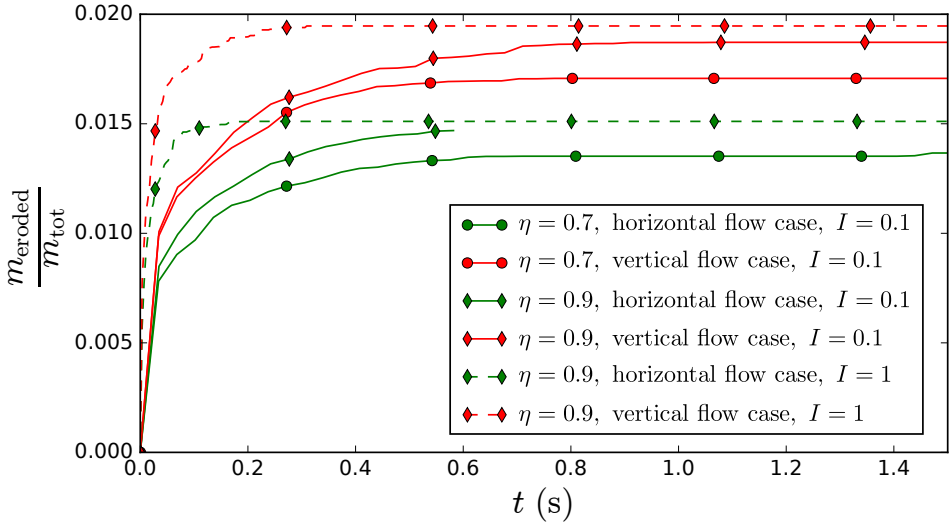

Figure 5.24 – Time evolution of the eroded mass (corresponding to the mass of deleted particles) for the six DEM/PFV simulations considered.

the travel distances as shown by the comparison between the predictions obtained in Figure 5.22 for the two localization schemes of the macroscopic pressure gradient (models (a) and (b) in Figure 5.23).

In Figure 5.22, transport and erosion seem to be more important for the vertical than for the horizontal flow direction. This is quantified in Figure 5.24 by looking at the time evolution of the eroded mass (corresponding to the mass of deleted particles) for the six DEM/PFV simulations considered.

In Figure 5.24, erosion is limited to 1.4-1.9 % of the total mass of the particles, which is consistent with the main occurrence of clogging over erosion. A larger eroded mass is observed i) for the vertical flow case, ii) for the larger hydraulic gradient $I = 1$ and iii) for the largest stress ratio $\eta = 0.9$.

These observations are indeed consistent with micromechanical features highlighted previously in this manuscript, namely:

- for $\eta > 0$ force chains are built aligned with the vertical direction (the major compression direction). This load induced anisotropy explains why more particles are extracted from the sample when the flow is aligned with force chains.

- a larger hydraulic gradient increases the kinetic energy of transported particles that are thus able to explore more transport paths (a larger induced grain detachment has to be excluded as no grains are detached in the six DEM/PFV simulations considered in this section).

- while the stress ratio is increased from $\eta = 0.7$ to $\eta = 0.9$, the sample dilates, which increases pore and constriction sizes. In the meantime the number of chained particles decreases, which increases the number of particles candidate to erosion.

As highlighted in Figures 5.22 and 5.24, transport process is not isotropic in the two samples considered ($\eta = 0.7$ and $\eta = 0.9$). A systematic analysis of this anisotropy can be sought in the form of a directional analysis with respect to the flow direction. In the current form of the PFV scheme implemented in YADE, imposing an arbitrary macroscopic flow direction is however not straightforward and DEM/PFV directional analyses would anyway be computationally expensive. A cheap alternative to fully coupled simulations is to use the transport model of Section 3.3.3 applied to pore networks for which the pressure map consists in the linear approximation of the macroscopic pressure gradient (see Figure 5.23 (b) and (c)). The resulting computed mean travel distances provide thus a lower and an upper bounds for the effective mean travel distances.

For flow directions lying in the plane $(\boldsymbol{e}_x, \boldsymbol{e}_z)$, the flow direction is given by an angle θ ($\theta = 0$ corresponding to $\boldsymbol{e}_x$ and $\theta = 90°$ corresponding to $\boldsymbol{e}_z$). In Figure 5.25, lower and upper bounds of the shortest mean travel distances are computed for $\theta \in [0, 2\pi]$ and for a given particle size $r = r_{\min} = 0.48 r_{\text{mean}}$.

In Figure 5.25, polar plots of the predicted shortest mean travel distances are quite isotropic. Even if these results are not inconsistent with anisotropic effective shortest mean travel distances (the predictions in Figure 5.25 are given by bounds), the transport model of Section 3.3.3 applied to pore networks for which the pressure map consists in the linear approximation of the macroscopic pressure gradient is too rough to capture the anisotropic transport properties highlighted in Figures 5.22 and 5.24. The limitation of the simplified transport model may stem from the fact that for the stress ratios considered, the microstructure geometry is still isotropic while considering all the grains (the triaxial strain ε_{zz} is less than 0.5 %). For the considered samples, only the load bearing mesostructures show a marked anisotropy. This anisotropy is not accounted for in the simplified transport model but may affect the effective transport while considering the fully coupled problem.

5.2.5 Stabilizing effect induced by clogging domination

Compared with the study presented in the first section of this Chapter, the internal fluid flow does not trigger off the collapse of the samples. Even for the instable sample corresponding to $\eta = 0.9$, the observed incremental strain during DEM/PFV simulations are smaller than 2.10^{-5}. As a result,

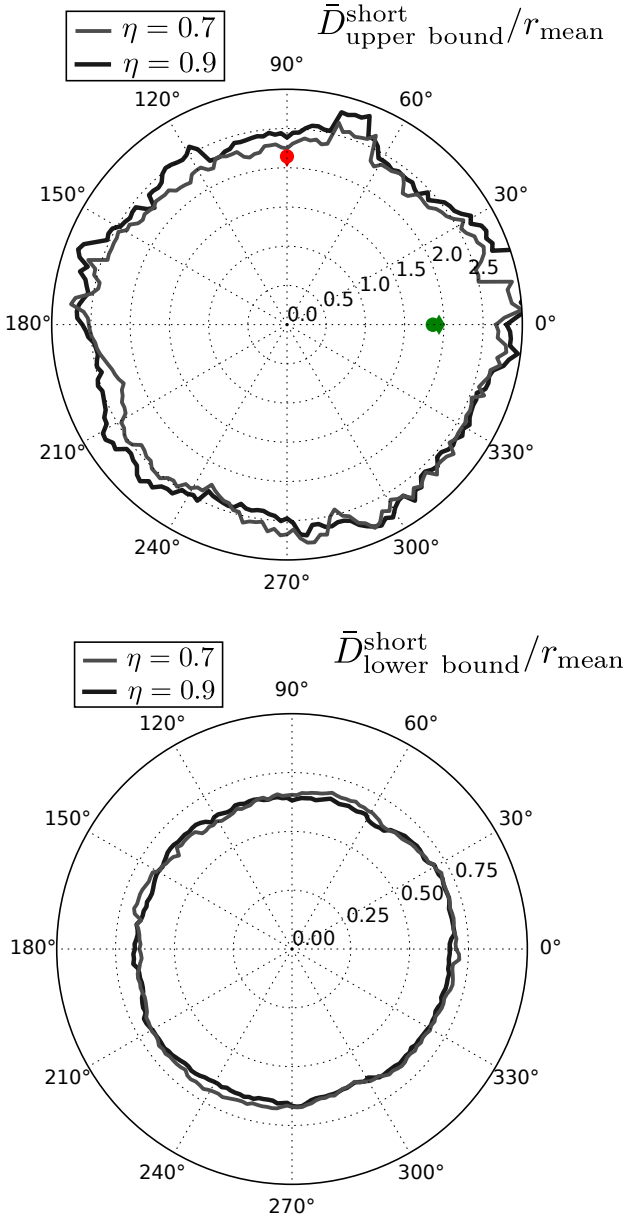

Figure 5.25 – Directional analysis of the lower and upper bounds of the shortest mean travel distances in the plane $(\boldsymbol{e}_x, \boldsymbol{e}_z)$ for the two samples corresponding to $\eta = 0.7$ and $\eta = 0.9$. Bounds are calculated for a given particle size $r = r_{\min} = 0.48 r_{\text{mean}}$. Round ($\eta = 0.7$) and diamond ($\eta = 0.9$) points correspond to effective shortest mean travel distances computed with DEM/PFV simulations.

the suffused samples obtained at the end of DEM/PFV simulations can be used to assess the relative influence of erosion and clogging on the mechanical stability. Similarly to the testing procedure described in Chapter 4, stress-controlled directional analyses are performed in Rendulic's plane on the dry suffused samples with stress increments of $||\mathbf{d}\boldsymbol{\sigma}|| = 5$ kPa imposed in the form of a stress loading rate of $1,558$ kPa.s^{-1} (corresponding to 10 000 numerical time increments) followed by a stabilization phase letting the samples evolve toward a new equilibrium position as $F_{\text{unb}} < 10^{-5}$.

The second-order work envelopes computed from directional analyses performed before and after the application of a macroscopic hydraulic gradient $I = 0.1$ in the horizontal or vertical direction are plotted in Figure 5.26 for the two samples corresponding to $\eta = 0.7$ and $\eta = 0.9$[1].

In all cases, the second-order work computed after the application of an internal fluid flow is larger than the value computed in the initial case. And for the initially unstable sample ($\eta = 0.9$), no cone of instability exists anymore after the application of an internal fluid flow (either vertical or horizontal). As a result, the fluid is shown to have a restabilization effect on the considered samples.

These observations can be explained by recalling the results obtained in Section 4.6 for the particular role played by rattlers with respect to the mechanical stability of a granular material. Indeed, by providing support in case of force chain collapse, rattlers improve the mechanical stability. In the present case, as analyzed in the previous section, clogging dominates over erosion. As a result, rattlers remain trapped in the considered granular samples and are clogged in contact with existing force chains. They are thus ready to prevent the development of plastic strain in case of force chain collapse.

In Figure 5.26 it can be noted that second-order work values are slightly smaller in the vertical flow case which corresponds to larger fraction of eroded rattlers in Figure 5.24. This observation is consistent with the fact that removing rattlers results in larger plastic strain together with a decrease in the second-order work when a stress increment is applied (see Section 4.6).

[1] In both case, dry granular samples are considered in the directional analyses.

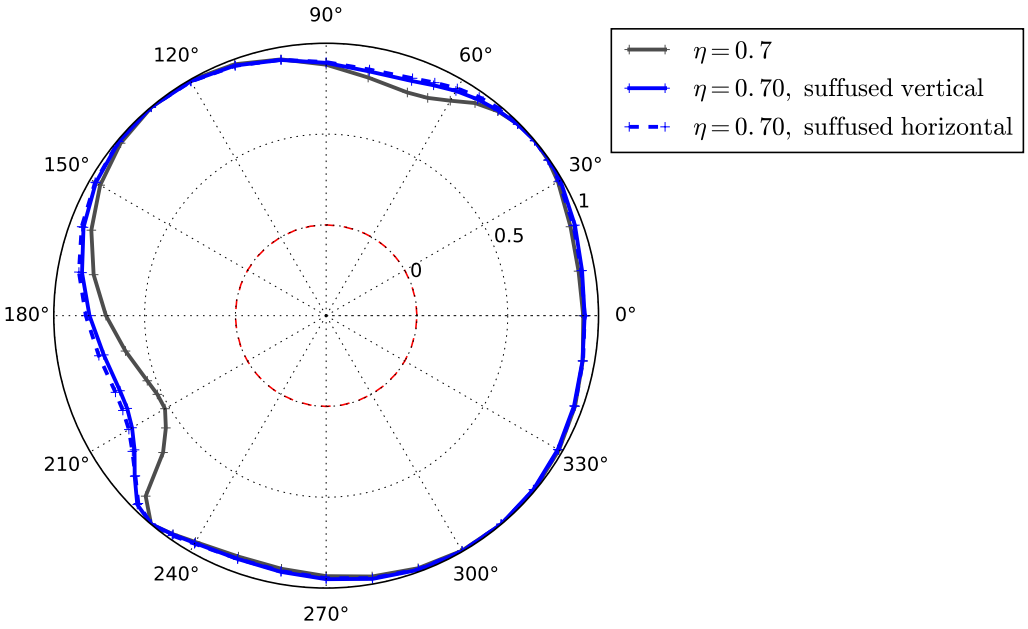

(a) Initially stable sample

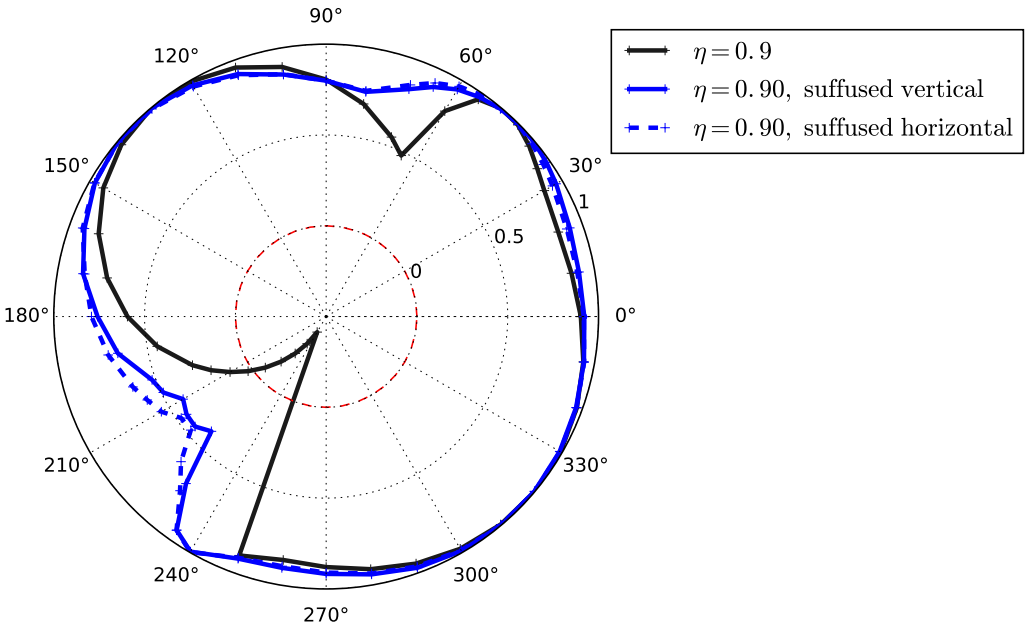

(b) Initially unstable sample

Figure 5.26 – second-order work envelopes corresponding to directional analysis performed before the application of an internal fluid flow (solid black or gray) and after the application of a macroscopic hydraulic gradient $I = 0.1$ in the horizontal (dashed blue) or vertical (solid blue). Two samples corresponding to $\eta = 0.7$ and $\eta = 0.9$ are used. $W_2 = 0$ is indicated by a red dashed circle.

5.3 Summary of the main findings

In the first section of this chapter, the specific impact of a fluid flow on the primary fabric of a granular material was investigated in terms of mechanical stability. For a reference state (stress and microstructure geometry) identified as mechanically unstable, a fluid flow was shown to be able to trigger off the underlying instability on its own (without any change in the external contact forces on the sample boundaries). Thanks to the micromechanical tools developed in the previous chapters, the sudden collapse is shown to result from an outburst of kinetic energy mechanism associated with force chain deconfinement and increase in the number of contacts close to sliding as well. Following, the sample collapse, the pore water pressure increases and grains are detached following force chains reorganization. Because of fluid force fluctuations in directions perpendicular to the macroscopic flow, it is important to notice that the flow direction does not influence the triggering of the underlying instability.

In the second section of this chapter, the relative influence of clogging and erosion was investigated on widely graded samples in stable or unstable states according to the second-order work criterion. For the considered samples, internal fluid flows were not able to trigger off material collapse. While analyzing grain transport for DEM/PFV simulations, it was found that most of the initially free particles got clogged when an internal fluid flow is considered. As predicted by the results from Chapter 4, the microstructure evolutions induced here by internal fluid flows have a restabilization effect for the samples considered.

Chapter 6

General conclusion and perspectives

This PhD work was devoted to the multi-scale analysis of instability in saturated granular materials subjected to an internal fluid flow. The objective of this study was to improve the understanding of the microscale mechanisms leading to the occurrence of material instability thanks to numerical experiments of suffusion at the material point scale taking into account both the hydraulic and mechanical loadings. These mechanisms are of paramount importance in the understanding of the consequences of the suffusion phenomenon affecting earthen hydraulic structures such as river or maritime dikes. To achieve this, we have proposed the following approach which consists of the following steps:

- Define representative elementary volumes of cohesionless granular material subjected to different stress states and different hydraulic gradients.

- Perform directional analyses before and after taking into account fluid/-grain coupling in order to assess mechanical stability at the continuum scale thanks to the second-order work criterion.

- Use micromechanical tools to analyze down to the micro and meso scales the impact of suffusion in terms of grain transport, stress reorganization, grain detachment and grain reattachment. These micromechanical tools, and in particular the definition of force chains, were used to investigate the driving mechanisms leading to material collapse.

The main contribution of this work has been to propose i) fully coupled and resolved simulations of suffusion at the representative elementary volume scale in 3D, ii) use a general definition of mechanical stability at the material point scale to assess suffusion consequences, iii) highlight the micro origin of instability in granular material and iv) link suffusion induced modifications of the microstructure of granular materials to the existence of mechanical instability.

In the following the major results obtained during this PhD are listed. Then several perspectives for future work are proposed.

6.1 Noticeable contributions

6.1.1 Development of versatile micromechanical tools

One of the great advantage of DEM is that individual grain data are accessible such as grain positions and velocities or contact and fluid forces. In order to approach the physics of granular materials, this large amount of raw data has to be organized to become readable. One of the greatest challenge of this PhD work was to find a sensible way to structure the huge amount of data acquired from each DEM simulation and extract the physics out of it.

To this respect, valuable information on the small scale physics of granular materials was extracted thanks to the definition of force chains and pore networks. These tools were used in the present work to define relevant quantities that help understand the micro origin of instability in granular materials and the specific impact of an internal fluid flow. Among micromechanical tools introduced in this manuscript, one can mention the definition of autocorrelation distances between chained particles, force chain bending rate, populations of contacts close to sliding, non-chained/chained contact population, pore and constriction size distributions, transport criterion and travel distance predictions. It should be underlined that these micromechanical tools are not specific to this study and can be used to investigate other features of granular materials such as for instance strain localization mechanisms.

6.1.2 Numerical procedure to assess the mechanical stability of granular materials

Initially developed within continuum mechanics framework, the application of the second-order work criterion to granular materials at the representative elementary volume scale (REV) is not straightforward. In this PhD, a systematic numerical procedure has been provided to assess the mechanical stability of granular materials. This procedure is based on the following three steps:

Pre-stabilization step	The second-order work is linked to the second-order variation of the kinetic energy. In order to interpret the vanishing of the second order work as the possibility to observe an inertial transition, the reference state of the material must be in an equilibrium position ($E_c = 0$ and $\mathrm{d}E_c = 0$) such that $\Delta E_c = W_2^{\mathrm{ext}} - W_2^{\mathrm{int}}$.
Directional analysis step	Contrary to theoretical results derived in the continuum framework, stress probes cannot be infinitely small while considering granular materials. The finite size of the stress probes is linked to the discrete nature of granular materials, the constitutive behavior of which strongly rely on microstructure evolutions. The applied stress probes should be able to generate such microstructure evolutions.
Post-stabilization step	After the application of each loading increment, dynamic evolutions occur in granular materials such that the microstructure adapts to withstand the new imposed load. In order to equal the external second-order work W_2^{ext} computed on REV boundaries with the internal second-order work W_2^{int}, it is important to wait for the material to restabilize after incremental loads are applied ($\Delta E_c = W_2^{\mathrm{ext}} - W_2^{\mathrm{int}} = 0$).

This above procedure is not new but the justification of each of the three steps is hardly ever reported in the literature. Thanks to micro to macro analysis, it was shown that localized micro-inertia crisis occurring during the pre-stabilization step need to be taken into account to interpret the results of the mechanical stability assessment. While looking at the time evolution of the external second-order work, it has been shown that, when plasticity is activated, transient losses of controllability occur. Depending on the level of plastic strain, transient vanishing of the external second-order work can be observed which was never reported in the literature. These observations are strongly linked to the discrete nature of granular materials and cannot be accounted for in a quasi-static continuum mechanics framework. As a result, they should be systematically investigated when assessing the mechanical stability of granular materials.

6.1.3 Multiscale approach of mechanical instability and identification of elementary mechanisms

At the microscale, granular materials are discrete by nature. However, at the macroscale (the scale of the hydraulic structure) they are described within the framework of continuum mechanics. In this PhD work a detailed analysis of the link between the discrete and continuum modelings of granular materials was carried out. In particular, i) the role of rattlers has been highlighted with respect to the development of plastic strain and ii) the elementary mechanisms leading to the vanishing of the second-order work computed at the material point scale have been specified.

The existence of material instability (at the continuum scale) was shown to rely on the possibility to impose locally the deconfinement of force chains. This deconfinement results in force chain bending and collapse. Without pre-existing free particles ready to build new force chains, important microstructure reorganizations occur which results macroscopically in the development of plastic strain. Then, the intensity and the direction of plastic strain controls the vanishing of the second-order work and thus the existence of material instability.

6.1.4 Occurrence of suffusion elementary mechanisms

At the microscale, suffusion is usually decomposed into grain detachment, grain transport and grain reattachment. In this PhD, the use of DEM/PFV simulations was used to investigate the occurrence of these three elementary mechanisms.

The occurrence of grain transport was investigated through the computation of mean travel distances. These distances provide information to assess the relative occurrence of erosion and clogging. Pore network models were used to provide lower and upper bounds for the expected travel distances.

For all the fluid/grain coupled simulations performed in this PhD work, grain detachment was never observed individually but follows force chain collapse and stress reorganization. As a result, no individual grain detachment criterion can be formulated as it is the case for surface erosion. Grain detachment is a non local phenomenon which consists in two steps. Fluid induces stress reorganization which is then followed by the release of new rattlers as microstructure reorganizations occur.

Similarly, grain reattachment is a consequence of microstructure reorganizations. It is not a direct flow induced mechanism, however, clogging facilitate grain reattachement in case of force chain redistribution.

6.1.5 Fluid flow impacts with respect to mechanical stability

Rattlers have been shown in this work to play an important role with respect to mechanical stability. As these particles are also easily transported by an internal fluid flow, clogging and erosion play antagonist roles with respect to mechanical stability through their ability to limit incremental plastic strain development. By removing free particles, internal erosion has a destabilizing effect. On the contrary, by increasing the number of contacts between loosely stressed particles and force chains, clogging facilitates the reconstruction of new force chains. This result shows the importance to account for erosion or clogging of rattlers to assess the consequences of suffusion in terms of mechanical stability.

In addition, it was shown thanks to DEM/PFV simulations that an internal fluid flow can trigger off an underlying mechanical instability by acting directly on the primary skeleton of a granular material. Indeed, by introducing additional forces, the fluid induces stress reorganization. Because of fluid forces fluctuations induced by the local tortuosity of the pore space, the macroscopic flow direction was not shown to influence the triggering of the underlying instability.

6.2 Outlook for future investigations

6.2.1 Towards real particle size distributions

Despite the computational efficiency of the DEM/PFV approach used in this work, simulating real soils at the REV scale is still computationally demanding. Nevertheless, during this PhD exploratory DEM/PFV simulations were performed with a numerical sample corresponding to the soil gradation used in the experimental work of Aboul Hosn (2017) and in the ongoing PhD of Doan Nguyen at IRSTEA. The corresponding gap-graded sample composed of 50,000 particles is shown in Figure 6.1 together with the associated particle size distribution. This sample is on the edge of what can be simulated today with DEM/PFV simulations but is still considered as not so widely graded from an experimental point of view. It should also be underlined that even if 50,000 particles are used, only 200 to 300 particles actually compose the primary fabric which is too small to have a representative elementary volume for the mechanical behavior.

This sample was subjected to a horizontal hydraulic gradient $I = 0.1$ while being prepared under an isotropic confining stress of 20 kPa. Com-

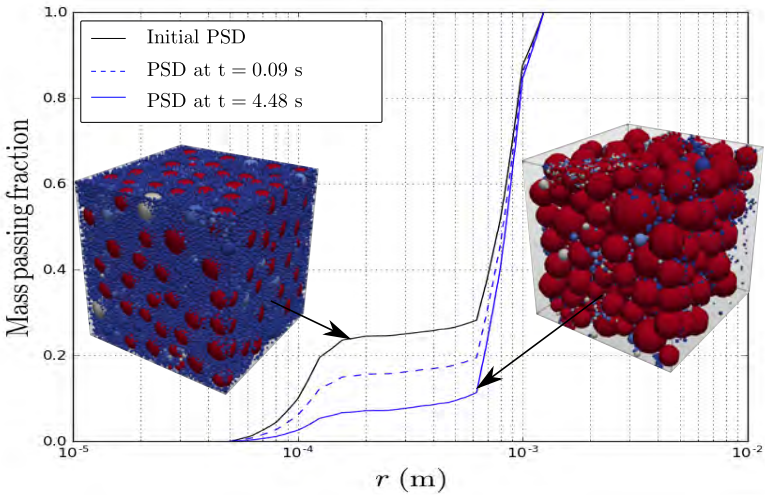

Figure 6.1 – Particle size distributions corresponding to the soil gradation used in the experimental work of Aboul Hosn (2017) before (solid black), during (dashed blue) and after (solid blue) the application of a horizontal hydraulic gradient $I = 0.1$ while imposing an isotropic confining pressure of 20 kPa. The initial and final sample microstructures are shown.

pared to the samples used in this PhD work, erosion largely dominates clogging and in the end of the simulation, most of the fine particles have been eroded as seen in Figure 6.1. Since too few particles compose the primary fabric of this sample, its stability cannot be assessed properly. In order to simulate more efficiently the microstructure evolutions induced by suffusion, a possible option would be to apply the cheaper one way coupling approach developed by Aboul Hosn (2017). The present two ways coupling DEM/PFV simulation will be used to assess the relevance of the erosion criterion used in this approach and possibly improve this criterion. Such a work is currently in progress.

6.2.2 Towards comparison with experimental evidences

In the present PhD, numerical experiments replace real ones and no direct confrontation was attempted simply because both time and length scales accessible numerically and experimentally are not comparable. Indeed, numerical samples represent typically a few cubic centimeters of soil and flow induced microstructure modifications last a few seconds whereas in laboratory experiments, samples are composed of a few cubic decimeters of soil and suffusion experiments last for hours.

However, recent developments of small scale 3D imaging techniques such as X-ray microtomography enable the acquisition of detailed images of soils in which individual grains can be isolated (Fonseca et al., 2014; Hurley et al., 2016; Marteau and Andrade, 2017; Nguyen et al., 2017). By comparing the microstructures before and after erosion, the consistency of the microscale mechanisms highlighted in this work will be strengthened. It should however be underlined that the spatial resolution of X-ray microtomograph images does not allow yet to detect individually both small and large particles over a representative elementary volume of real soil (Nguyen et al., 2017).

At the macroscopic scale, experiments on granular materials in which data are acquired over time steps comparable to the accessible ones in DEM are scarce but exist. In particular, in Doanh et al. (2017) stick-slips and transient liquefactions are observed over short periods (comparable to those simulated with DEM) for saturated granular materials subjected to deviatoric stress loadings. These experimental observations seem similar to the transient losses of controllability observed in Section 4.2.3. The microscale mechanisms responsible for the observed instability in this present thesis are likely to explain the experimental observations of Doanh et al. (2017). The possibility to reproduce the experimental observations with DEM is currently discussed.

6.2.3 Towards enriched micromechanical models

Understanding the elementary micromechanisms presented in this PhD work is of paramount importance while considering the development of micromechanical models in which a model mesostructure is used to represent the microstructure geometry of a granular material (Chang and Hicher, 2005; Zhu et al., 2006; La Ragione et al., 2008; Zhu et al., 2010; Nicot and Darve, 2011; Xiong et al., 2017). In these *bottom-up* models, and contrary to macroscopic phenomenological models, no assumptions are required a priori on the form of the overall constitutive behavior which simply results from the micromechanisms captured in a simplified manner at the micro or mesoscale. As a result, micromechanical models in which mesostructures are rich enough to account for the collapse and rebuilding of force chains incorporating free particles will be able to account for the suffusion induced evolutions in terms of mechanical stability.

The development of enriched versions of micromechanical models such as the one proposed by Nicot and Darve (2011) and recently extended in 3D by Xiong et al. (2017) could thus lead to advanced constitutive modeling of internal processes in soils for engineering applications in which detecting underlying mechanical instability is of paramount importance. A possible

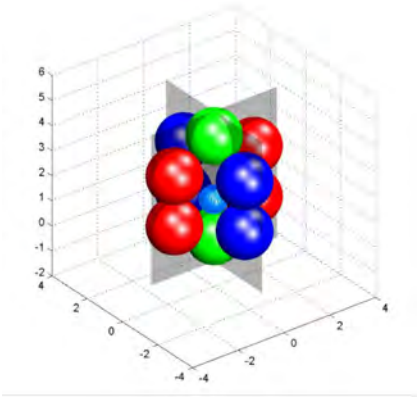

Figure 6.2 – A possible enriched version of the mesostructure of the 3D H-model (Xiong et al., 2017) with a central free particle.

enriched version of the mesostructure of the 3D H-model (Xiong et al., 2017) is shown in Figure 6.2.

The scope of applications of such micromechanical models looks very promising and such models could also provide an elegant way to question to which extent the classical paradigm of single gradient continuum mechanics holds for granular material at the macroscopic scale. To this respect, the confrontation with higher order continuum models might give some micromechanical clues to better assess the relevance of such approaches applied to granular materials.

Appendix A

Résumé étendu en français

A.1 Contexte général

La France dispose d'un important parc d'ouvrages hydrauliques avec plus de 19 000 km de digues fluviales et maritimes, plusieurs dizaines de milliers de petits barrages, et environ 600 grands barrages. Ces ouvrages hydrauliques sont pour la plupart construits à partir de matériaux granulaires compactés. Ce mode constructif en fait des ouvrages perméables qui sont soumis en permanence à des écoulements d'eau dans leur volume pouvant altérer leur structure interne par érosion. Tant que les ouvrages endommagés ne sont pas soumis aux chargements hydrauliques pour lequels ils ont été dimensionnés (crues ou tempêtes par exemple), les conséquences de l'érosion interne peuvent passer inaperçues. Cependant, les infiltrations d'eau sont susceptibles de générer des instabilités mécaniques responsables de ruptures lors de brusques modifications des conditions de chargement. Aujourd'hui, on observe en moyenne une rupture de digue par an en France, dont 45 % sont attribuées à l'érosion interne. Dans un contexte de changement climatique où la fréquence et l'intensité des tempêtes et des crues ne cessent d'augmenter, la compréhension des mécanismes de rupture des digues et barrages devient aujourd'hui un enjeu de plus en plus important.

En reprenant la typologie présentée à Aussois en 2005 (International Workshop on Internal Erosion of Embankment Dams and their Foundations), on distingue aujourd'hui quatre types d'érosion interne :

- l'érosion de conduite reliant l'amont et l'aval ;
- l'érosion de contact, à l'interface entre un sol fin et un sol grossier ;
- l'érosion régressive, par l'entraînement de matériaux qui se déclenche à l'exutoire d'un écoulement d'eau et qui s'auto-entretient jusqu'à déboucher à l'amont ;
- la suffusion, qui est l'entraînement sélectif, par l'eau en mouvement, des petits grains à travers l'espace poreux formé par les grains les plus gros.

De ces quatre mécanismes, la suffusion est le plus complexe et le seul pour lequel il n'a pas encore été possible d'établir des recommandations ex-

ploitables en pratique. Par exemple, les deux principaux critères granulométriques mentionnés dans la littérature manquent de cohérence et se contredisent (Li and Fannin, 2008). De plus, la suffusion apparaît le plus souvent bien en deçà du gradient critique de Terzaghi prédisant la liquéfaction des sols (Skempton and Brogan, 1994). Face à ce constat, une réponse possible consiste en le développement de modèles macroscopiques phénoménologiques. Si cette approche permet de proposer des modèles mécaniques enrichis, ils ne permettent pas toujours de comprendre l'origine physique des phénomènes étudiés et des termes correctifs introduits. Récemment, avec le développement de techniques d'imagerie performantes (comme la micro-tomographie à rayons X) et d'outils de calcul numérique toujours plus puissants, il est possible d'étudier les mécanismes d'érosion interne par une approche micromécanique. Plus rigoureuse mais aussi plus complexe, cette approche permet par exemple de donner un sens physique aux termes correctifs des modèles phénoménologiques et d'étendre leur domaine de validité.

A.2 Objectifs et méthodologie

Les objectifs de ce travail de thèse sont d'une part de comprendre les mécanismes élémentaires responsables des instabilités matérielles dans les matériaux granulaires et d'autre part de relier les changements de microstructure induits par un écoulement interne à l'existence de telles instabilités mécaniques.

Pour atteindre ces objectifs, une approche numérique par homogénéisation est utilisée. Elle consiste à prendre en compte la nature discrète des matériaux granulaires à l'échelle microscopique tout en considérant un nombre suffisamment important de grains pour être représentatif du comportement macroscopique. On se place ainsi à l'échelle d'un volume élémentaire représentatif (VER) de sol de quelques centimètres cubes. À cette échelle, il est possible, d'une part, d'appliquer les outils de la mécanique des milieux continus pour caractériser la stabilité mécanique de l'assemblage grâce au critère du travail du second ordre (Hill, 1958; Nicot et al., 2009; Daouadji et al., 2011; Wan et al., 2016), et d'autre part, d'utiliser des outils micromécaniques pour caractériser le comportement local du milieu.

Dans ce travail de recherche, la géométrie d'un VER est approchée par un assemblage de sphères interagissant par des lois de contact élasto-frictionnelles (Cundall and Strack, 1979). Le comportement mécanique de l'assemblage granulaire saturé est alors modélisé par une méthode aux éléments discrets (DEM) (Šmilauer et al., 2015) et un schéma de couplage fluide/grains aux différences finies de type réseau de pores (PFV) (Chareyre et al., 2012). Grâce

à ces outils numériques, il est possible de simuler le comportement de matériaux granulaires en trois dimensions à l'échelle du point matériel en tenant compte à la fois du chargement mécanique et du chargement hydraulique. On s'affranchit ainsi des contraintes expérimentales (tels que les effets de structure et le nombre limité de chargements possibles) pour analyser de manière très fine tout changement de microstructure tant du point de vue de la cinématique que de la transmission des efforts.

A.3 Définition quantitative d'un VER pour la suffusion grâce à des outils micromécaniques

L'homogénéisation repose sur l'hypothèse forte de séparation d'échelles. Si la taille caractéristique des hétérogénéités à l'échelle microscopique est très petite devant la taille caractéristique du problème d'intérêt à l'échelle macroscopique, il est alors possible de remplacer un milieu hétérogène par un matériau homogène équivalent. Pour l'étude du comportement d'un matériau granulaire soumis à un écoulement d'eau interne, la difficulté est de caractériser les longueurs internes d'intérêt qui ne sont pas forcément celles des grains. En effet, le comportement mécanique d'un matériau granulaire repose en grande partie sur l'arrangement géométrique des grains entre eux qui s'organisent pour former des structures longilignes de quelques grains fortement comprimés que l'on nomme *chaînes de force*. De plus, la présence d'un écoulement interne provoque le transport de grains dans l'espace poral avec des évolutions de microstructure sur des distances caractéristiques qui peuvent être bien plus grande que la taille des grains. Des outils micromécaniques basés sur la définition des chaînes de force (Peters et al., 2005) et de réseaux de pores (Vincens et al., 2015) sont proposés dans ce travail pour donner une définition quantitative de ces longueurs internes associées à la transmission des efforts dans le squelette granulaire ainsi qu'au transport des grains libres dans l'espace poral.

Une analyse des chaînes de force dans les matériaux granulaires montre qu'il est possible de distinguer d'une part, des grains peu nombreux (20 à 30 %) reprennant la majorité des efforts (les grains chaînés), et d'autre part, des grains peu chargés et très nombreux (les grains non-chaînés). En s'intéressant aux distances d'autocorrélation spatiales (Kanit et al., 2003) entre les grains chaînés, il est possible de définir une échelle mésoscopique qui caractérise la dimension des mésostructures responsables du comportement mécanique des matériaux granulaires. Un échantillon de matériau granulaire peut alors être considéré comme un VER vis-à-vis du comportement mécanique s'il est

suffisamment gros par rapport à cette échelle mésoscopique (en pratique 10 fois plus gros).

La définition d'une échelle caractéristique vis-à-vis du transport est traitée dans ce travail i) en réduisant l'espace des vides à un réseau de pores et ii) en décrivant le mécanisme de transport comme un problème de propagation sur un graphe orienté. Pour cela, un critère de propagation est proposé et validé par confrontation avec les résultats de simulations couplées DEM/PFV. Le critère proposé se base sur i) une estimation de l'intensité des forces fluides entre deux pores voisins (deux nœuds du graphe) et ii) sur la taille des constrictions joignant ces pores (les arêtes du graphe). La distance moyenne que les plus petits grains du matériau peuvent parcourir fournit alors une échelle caractéristique associée au phénomène de transport. Elle précise ainsi la taille du VER à considérer pour étudier le phénomène de suffusion.

A.4 Relations micro macro pour une description des instabilités dans les milieux granulaires

Aujourd'hui, la plupart des critères de susceptibilité à la suffusion sont basés sur la notion d'*instabilité interne* définie comme l'incapacité d'un matériau granulaire à s'auto-filtrer (Kenney and Lau, 1985). Toutefois, cette approche n'apporte aucune information sur les conséquences de la suffusion vis-à-vis du comportement mécanique du matériau concerné. C'est pour cette raison que nous avons choisi dans ce travail de préférer la notion d'*instabilité mécanique* à la notion d'*instabilité interne*. Cette notion trouve une définition générale basée sur le critère du travail du second-ordre introduit par Hill (1958) dans le cadre de la mécanique des milieux continus. Un matériau est défini comme instable dans un état donné (caractérisé par sa microstructure et son état de contrainte) s'il existe au moins un chargement incrémental pour lequel le travail du second-ordre est négatif. L'existence d'un tel chemin signifie qu'il existe des conditions de chargement pour lesquelles le matériau peut être continument déformé sans apport extérieur d'énergie et passer d'un comportement quasi-statique à un comportement dynamique (on parle de point de bifurcation).

Il est toutefois à noter que l'application de ce critère (hérité de la mécanique des milieux continus) sur un matériau modélisé par éléments discrets n'est pas sans poser quelques difficultés. Dans cette thèse, une procédure numérique en trois étapes est utilisée afin d'estimer la stabilité mécanique d'un matériau granulaire : pré-stabilisation, chargement incrémental direc-

tionnel et post-stabilisation. Le respect de ces trois étapes est primordial pour pouvoir appliquer un formalisme continu quasi-statique à un matériau dont le comportement provient en grande partie de réorganisations dynamiques locales.

Pour des matériaux granulaires secs identifiés comme instables au sens du critère du travail du second-ordre, les mécanismes élémentaires responsables de ces instabilités sont analysés grâce à des outils micromécaniques s'appuyant en grande partie sur la définition des chaînes de force. Nous avons établi que l'annulation du travail du second-ordre résulte du déconfinement et de la flexion des chaînes de force. Leur effondrement déclenche alors une transition inertielle qui se traduit par un adoucissement transitoire et une perte momentanée de contrôlabilité (i.e. une incapacité temporaire à imposer le chargement incrémental désiré). Ce régime dynamique prend fin lorsque la réorganisation de la microstructure permet de reconstruire de nouvelles chaînes de force stables. Les résultats obtenus dans cette thèse viennent conforter les conclusions de Zhu (2015) issus de travaux en deux dimensions sur le rôle des cycles de grains vis-à-vis de la stabilité des chaînes de force.

D'un point de vue macroscopique, les réorganisations microstructurelles s'interprètent comme des déformations plastiques incrémentales. Pour des matériaux granulaires frictionnels, ces déformations sont souvent décrites par des lois élasto-plastiques non-associées, pour lesquelles le caractère non-associé de la règle d'écoulement plastique est fondamental pour décrire correctement les changements de volume observés. C'est également grâce à ce caractère non-associé que des instabilités mécaniques existent avant même d'atteindre la surface de rupture plastique. En calibrant un modèle élasto-plastique non-associé sur des simulations DEM, il est possible de relier les paramètres phénoménologiques du modèle macroscopique à des caractéristiques microstructurelles. En particulier, nous avons démontré que les grains libres contrôlent le développement des déformations plastiques incrémentales en termes d'intensité et de direction d'écoulement. Ces deux paramètres pilotent à leur tour l'existence d'un cône d'instabilité, c'est à dire l'existence de directions de chargement pour lesquelles le travail du second-ordre s'annule. La présence de grains libres dans un matériau granulaire limite ainsi l'existence d'instabilités matérielles. Ces grains étant par ailleurs potentiellement transportables par un écoulement interne, ce résultat est fondamental pour analyser les conséquences de la suffusion sur la stabilité mécanique d'un matériau granulaire.

A.5 Analyse numérique de l'impact d'un écoulement interne sur la stabilité mécanique des matériaux granulaires

Par rapport aux autres méthodes de résolution numérique de la phase fluide, le schéma PFV utilisé ici (Chareyre et al., 2012) permet de simuler le double impact d'un écoulement interne dans un matériau granulaire à l'échelle d'un VER, en trois dimensions et en tenant compte de la géométrie locale de l'espace poral.

En introduisant des forces additionnelles, le fluide induit une réorganisation de la transmission des efforts dans le matériau. Cet effet sur la microstructure n'induit pas forcément de modifications flagrantes de la géométrie de la microstructure. En revanche, pour un matériau instable au sens du critère du travail du second-ordre, il peut être suffisant pour déclencher l'effondrement du matériau. En effet, si le réseau de contact existant ne permet pas une réorganisation suffisante des chaînes de forces, le matériau n'est alors plus capable de résister au chargement mécanique qui lui est imposé. Afin d'isoler cet effet du fluide, nous avons étudié un échantillon granulaire instable privé de ses grains libres. Les résultats de simulations couplées DEM/PFV montrent que le fluide est capable de déclencher une transition inertielle dans l'échantillon considéré. Dans ce processus, l'importance des fluctuations des forces fluides est mise en évidence car l'effondrement observé ne dépend pas de la direction d'écoulement macroscopique (parallèle ou perpendiculaire à la direction du chargement principal). Cela confirme qu'il est important d'utiliser un schéma local de résolution du fluide et non un schéma à mailles larges (pour lesquels l'impact des grains sur l'écoulement est modélisé par une perméabilité apparente de type Kozeny-Carman par exemple). De manière simultanée avec l'effondrement du matériau, on observe, comme pour le cas sec, un déconfinement et un fléchissement généralisé des chaînes de force.

Le second impact du fluide concerne le transport des grains libres. Selon que ceux-ci se retrouvent colmatés ou érodés, le fluide a un effet stabilisateur ou déstabilisateur sur le matériau granulaire considéré. Grâce à des simulations DEM/PFV sur un VER dans lequel les grains libres sont majoritairement colmatés, nous avons montré que le matériau est plus stable mécaniquement après l'application d'un écoulement interne qu'avant (disparition des directions de chargement pour lesquelles le travail du second-ordre est négatif). Cet effet stabilisateur du fluide s'interprète localement par la mise en contact des grains colmatés avec les chaînes de force. Ceux-ci peuvent alors plus facilement limiter les déformations plastiques en cas d'effondrement des chaînes de force.

A.6 Perspectives

L'approche multi-échelle mise en œvre dans cette thèse a permis d'isoler les mécanismes élémentaires responsables des instabilités mécaniques dans les matériaux granulaires et d'identifier les directions de chargement particulièrements défavorables à leur stabilité. Les résultats obtenus permettent ainsi d'améliorer la compréhension des modes de ruptures liées à l'érosion interne par suffusion dans les digues et les barrages et permettront à l'avenir de mieux anticiper leur rupture éventuelle.

Les analyses présentées dans ce manuscrit aident également à interpréter les expériences de laboratoire. En particulier, les mécanismes mis en évidence viennent confirmer les explications souvent proposées pour interpréter les résultats d'essais triaxiaux sur des échantillons ayant été préalablement érodés (Chang and Zhang, 2011; Ke and Takahashi, 2012; Xiao and Shwiyhat, 2012; Ke and Takahashi, 2014a; Sibille et al., 2015b; Hosn et al., 2017). La résistance maximale au cisaillement dépend d'une part des contributions relatives de l'érosion et du colmatage, et d'autre part d'éventuels tassements résultants de l'effondrement des chaînes de force pendant la phase d'érosion.

Sur le plan de la modélisation, un prolongement naturel de ce travail de thèse concerne le développement de modèles micromécaniques enrichis. Ces modèles constituent une approche alternative pour déterminer les propriétés mécaniques homogènes équivalentes des matériaux granulaires. En effet, elles proposent une description statistique et non volumique du VER par une collection de mésostructures. Le comportement macroscopique est alors obtenu par moyennisation statistique et non spatiale. La difficulté de ces approches réside dans la définition d'une mésostructure simple et non simpliste, capable de rendre compte des mécanismes physiques locaux. Ainsi, un modèle micromécanique basé sur une mésostructure capable à la fois de reproduire l'effondrement des chaînes de force et de tenir compte du rôle clé joué par les grains libres dans l'enrayement des déformations plastiques permettra certainement de reproduire une large gamme de comportements macroscopiques. Le modèle H développé par Nicot and Darve (2011) et récemment étendu en 3D par Xiong et al. (2017) pourrait être enrichi par la présence de grains libres érodables.

Annexe B

Liste de publications

Le présent manuscrit redonne de la cohérence aux différents résultats obtenus au cours des trois ans de thèse. La plupart des résultats présentés peuvent être retrouvés dans les cinq articles de journaux et dans les trois actes de conférence suivants :

Articles de journaux :

Antoine Wautier, Stéphane Bonelli, and François Nicot. Scale separation between grain detachment and grain transport in granular media subjected to an internal flow. *Granular Matter*, 19(2) :22, 2017.

Antoine Wautier, Stéphane Bonelli, and François Nicot. Micro-inertia origin of instabilities in granular materials. *Int J Numer Anal Methods Geomech*, page 19, 2018.

Antoine Wautier, Stéphane Bonelli, and François Nicot. Rattlers' contribution to granular plasticity and mechanical stability. Accepted in *International Journal of Plasticity*, 2018.

Antoine Wautier, Stéphane Bonelli, and François Nicot. Flow impact on granular force chains and induced instabilities. Accepted in *Physical Review E*, 2018.

Antoine Wautier, Stéphane Bonelli, and François Nicot. DEM investigations of internal erosion : grain transport in the light of micromechanics. Accepted in *Int J Numer Anal Methods Geomech*, 2018.

Actes de conférence :

Antoine Wautier, Stéphane Bonelli, and François Nicot. A micromechanical approach of suffusion based on a length scale analysis of the grain detachment and grain transport processes. In *EPJ Web of Conferences*, volume 140, page 09022. EDP Sciences, 2017.

Antoine Wautier, Stéphane Bonelli, and François Nicot. Micromechanical modelling of suffusion : Towards the stability analysis of hydraulic structures. In *International Workshop on Bifurcation and Degradation in Geomaterials*, pages 169–175. Springer, 2017.

Antoine Wautier, Jiaying Liu, François Nicot and Félix Darve. Bifurcation micromechanics in granular materials. In *Tenth US-France symposia of the International Center for Applied Computational Mechanics* (ICACM 2017).

References (170)

Abdoulaye Hama, N.
2016. *Comportement mécanique des sols granulaires et critères de stabilité: Application à l'érosion interne*. PhD thesis, Le Havre. Cited in page 11

Abdoulaye Hama, N., T. Ouahbi, S. Taibi, H. Souli, J.-M. Fleureau, and A. Pantet
2016. Analysis of mechanical behaviour and internal stability of granular materials using discrete element method. *International Journal for Numerical and Analytical Methods in Geomechanics*, 40(12):1712–1729. Cited in page 41

Abichou, T., C. H. Benson, and T. B. Edil
2004. Network model for hydraulic conductivity of sand-bentonite mixtures. *Canadian Geotechnical Journal*, 41(4):698–712. Cited in page 42

Aboul Hosn, R.
2017. *Suffusion and its effects on the mechanical behavior of granular soils: numerical and experimental investigations*. PhD thesis, Grenoble Alpes. Cited in pages 19, 187, 188

Alonso-Marroquín, F.
2004. *Micromechanical investigation of soil deformation: Incremental Response and granular Ratcheting*. PhD thesis, University of Stuttgart, Germany. Cited in page 29

Andrianatrehina, L., H. Souli, J. Rech, S. Taibi, J.-J. Fry, L. Ding, and J.-M. Fleureau
2016. Analysis of the internal stability of coarse granular materials according to various criteria. *European Journal of Environmental and Civil Engineering*, 20(8):936–953. Cited in page 12

Bagi, K.
2007. On the concept of jammed configurations from a structural mechanics perspective. *Granular Matter*, 9(1):109–134. Cited in page 102

Bakke, S., P.-E. Øren, et al.
1997. 3D pore-scale modelling of sandstones and flow simulations in the pore networks. *Spe Journal*, 2(02):136–149. Cited in page 42

Bardenhagen, S., J. Brackbill, and D. Sulsky
2000. Numerical study of stress distribution in sheared granular material in two dimensions. *Physical Review E*, 62(3):3882. Cited in pages 14, 160

Bardet, J.-P.
1994. Numerical simulations of the incremental responses of idealized granular materials. *International Journal of Plasticity*, 10(8):879–908. Cited in pages 94, 117, 118, 120

Beguin, R., P. Philippe, and Y.-H. Faure
2012. Pore-scale flow measurements at the interface between a sandy layer and a model porous medium: Application to statistical modeling of contact erosion. *Journal of Hydraulic Engineering*, 139(1):1–11. Cited in pages 146, 153, 154

Benahmed, N., T. K. Nguyen, P. Y. Hicher, and M. Nicolas
2015. An experimental investigation into the effects of low plastic fines content on the behaviour of sand/silt mixtures. *European Journal of environmental and civil engineering*, 19(1):109–128. Cited in page 12

Bonelli, S.
2012. *Erosion of geomaterials.* John Wiley & Sons. Cited in pages 1, 2, 3

Bonelli, S.
2013. *Erosion in geomechanics applied to dams and levees.* John Wiley & Sons. Cited in page 3

Bonelli, S. and D. Marot
2011. Micromechanical modeling of internal erosion. *European Journal of Environmental and Civil Engineering*, 15(8):1207–1224. Cited in page 6

Bryant, S. L., P. R. King, and D. W. Mellor
1993. Network model evaluation of permeability and spatial correlation in a real random sphere packing. *Transport in Porous Media*, 11(1):53–70. Cited in page 42

Calvetti, F.
2003. A numerical investigation of the incremental behavior of granular soils. *Revista Italiana di Geotechnica*, 37:5–23. Cited in pages 29, 94, 117

Cambou, B., M. Jean, and F. Radjai
2013. *Micromechanics of granular materials.* John Wiley & Sons. Cited in pages 14, 37, 38, 58, 160

Catalano, E.
2012. *A pore-scale coupled hydromechanical model for biphasic granular media. Application to granular sediment hydrodynamics.* PhD thesis, Université de Grenoble. Cited in pages 42, 43, 46, 76

Challamel, N., F. Nicot, J. Lerbet, and F. Darve
2010. Stability of non-conservative elastic structures under additional kinematics constraints. *Engineering Structures*, 32(10):3086–3092. Cited in page 23

Chang, C. S. and P.-Y. Hicher
2005. An elasto-plastic model for granular materials with microstructural consideration. *International journal of solids and structures*, 42(14):4258–4277. Cited in pages 18, 189

Chang, D. and L. Zhang
2011. A stress-controlled erosion apparatus for studying internal erosion in soils. *Geotechnical Testing Journal*, 34(6):579–589. Cited in pages 17, 197

Chang, D. S. and L. M. Zhang
2012. Critical hydraulic gradients of internal erosion under complex stress states. *Journal of Geotechnical and Geoenvironmental Engineering*, 139(9):1454–1467. Cited in pages 6, 17

Chang, D. S. and L. M. Zhang
2013. Extended internal stability criteria for soils under seepage. *Soils and Foundations*, 53(4):569–583. Cited in page 14

Chareyre, B., A. Cortis, E. Catalano, and E. Barthélemy
2012. Pore-scale modeling of viscous flow and induced forces in dense sphere packings. *Transport in porous media*, 94(2):595–615. Cited in pages 41, 42, 43, 44, 45, 46, 67, 135, 147, 192, 196

Chen, F., E. C. Drumm, and G. Guiochon
2011. Coupled discrete element and finite volume solution of two classical soil mechanics problems. *Computers and Geotechnics*, 38(5):638–647. Cited in page 41

Christoffersen, J., M. Mehrabadi, and S. Nemat-Nasser
1981. A micromechanical description of granular material behavior. *Journal of applied mechanics*, 48(2):339–344. Cited in page 15

Corson, P. B.
1974. Correlation functions for predicting properties of heterogeneous materials. ii. empirical construction of spatial correlation functions for two-phase solids. *Journal of applied Physics*, 45(7):3165–3170. Cited in page 61

Cuellar, P., P. Philippe, S. Bonelli, N. Benahmed, F. Brunier-Coulin, J. Ngoma, J.-Y. Delenne, and F. Radjai
2015. Micromechanical analysis of the surface erosion of a cohesive soil by means of a coupled lbm-dem model. In *Proc. 4th Int. Conf. on Particle-based Methods, PARTICLES*. Cited in page 42

Cundall, P. A. and O. D. Strack
1979. A discrete numerical model for granular assemblies. *Geotechnique*, 29(1):47–65. Cited in pages 29, 31, 50, 147, 192

Daouadji, A., F. Darve, H. Al Gali, P. Hicher, F. Laouafa, S. Lignon, F. Nicot, R. Nova, M. Pinheiro, F. Prunier, et al.
2011. Diffuse failure in geomaterials: experiments, theory and modelling. *International Journal for Numerical and Analytical Methods in Geomechanics*, 35(16):1731–1773. Cited in pages 23, 192

Darve, F., E. Flavigny, and M. Meghachou
1995. Constitutive modelling and instabilities of soil behaviour. *Computers and Geotechnics*, 17(2):203–224. Cited in page 22

Darve, F. and F. Nicot
2005. On incremental non-linearity in granular media: phenomenological and multi-scale views (part i). *International journal for numerical and analytical methods in geomechanics*, 29(14):1387–1409. Cited in page 24

Darve, F., G. Servant, F. Laouafa, and H. Khoa
2004. Failure in geomaterials: continuous and discrete analyses. *Computer methods in applied mechanics and engineering*, 193(27):3057–3085. Cited in page 105

di Prisco, C. and S. Imposimato
1996. Time dependent mechanical behaviour of loose sands. *Mechanics of Cohesive-frictional Materials*, 1(1):45–73. Cited in page 93

di Prisco, C. and S. Imposimato
1997. Experimental analysis and theoretical interpretation of triaxial load controlled loose sand specimen collapses. *Mechanics of Cohesive-frictional Materials*, 2(2):93–120. Cited in pages 105, 116

Doanh, T., N. Abdelmoula, L. Gribaa, T. Nguyên, S. Hans, C. Boutin, and A. Le Bot
2017. Dynamic instabilities under isotropic drained compression of idealized granular materials. *Acta Geotechnica*, 12(3):657–676. Cited in page 189

Drescher, A. and G. D. J. De Jong
1972. Photoelastic verification of a mechanical model for the flow of a granular material. *Journal of the Mechanics and Physics of Solids*, 20(5):337–340. Cited in pages 14, 37

Drucker, D. C. and W. Prager
1952. Soil mechanics and plastic analysis or limit design. *Quarterly of applied mathematics*, 10(2):157–165. Cited in page 116

Dubois, F., V. Acary, and M. Jean
2017. The contact dynamics method: A nonsmooth story. *Comptes Rendus Mécanique*. Cited in page 29

Edelsbrunner, H. and N. R. Shah
1996. Incremental topological flipping works for regular triangulations. *Algorithmica*, 15(3):223–241. Cited in pages 43, 67

El Shamy, U. and M. Zeghal
2005. Coupled continuum-discrete model for saturated granular soils. *Journal of engineering mechanics*, 131(4):413–426. Cited in page 41

Fannin, R. and R. Moffat
2006. Observations on internal stability of cohesionless soils. *Geotechnique*, 56(7):497–500. Cited in page 12

Fell, R. and J. J. Fry
2007. *Internal Erosion of Dams and Their Foundations: Selected and Reviewed Papers from the Workshop on Internal Erosion and Piping of Dams and Their Foundations, Aussois, France, 25–27 April 2005*. Taylor & Francis Group. Cited in page 3

Fonseca, J., W. Sim, T. Shire, and C. O'Sullivan
2014. Microstructural analysis of sands with varying degrees of internal stability. *Géotechnique*, 64(5):405–411. Cited in pages 16, 189

Foster, M., R. Fell, and M. Spannagle
2000. The statistics of embankment dam failures and accidents. *Canadian Geotechnical Journal*, 37(5):1000–1024. Cited in page 2

Froiio, F., J.-N. Roux, J. Goddard, P. Giovine, and J. T. Jenkins
2010. Incremental response of a model granular material by stress probing with DEM simulations. In *AIP Conference Proceedings*, volume 1227, Pp. 183–197. AIP. Cited in pages 93, 98, 101

Garner, S. and R. Fannin
2010. Understanding internal erosion: a decade of research following a sinkhole event. *The international journal on hydropower & dams*, 17(3):93. Cited in pages 10, 11

Gudehus, G.
1979. A comparison of some constitutive laws for soils under radially symmetric loading and unloading. *Canadian Geotechnical Journal*, 20:502–516. Cited in pages 24, 117

Hadda, N.
2006. *Aspects micromécaniques de la rupture dans les milieux granulaires*. PhD thesis, Ecole Doctorale Ingénierie - Matériaux Mécanique Environnement Energétique Procédés Production (I-MEP^2). Cited in pages 34, 52

Hadda, N., F. Nicot, F. Bourrier, L. Sibille, F. Radjai, and F. Darve
2013. Micromechanical analysis of second order work in granular media. *Granular matter*, 15(2):221–235. Cited in pages 27, 90, 129, 170

Harthong, B. and R. G. Wan
2013. Directional plastic flow and fabric dependencies in granular materials. In *Powders and grains 2013: Proceedings of the 7th International Conference on Micromechanics of Granular Media*, volume 1542, Pp. 193–196. AIP Publishing. Cited in page 94

Hill, R.
1958. A general theory of uniqueness and stability in elastic-plastic solids. *Journal of the Mechanics and Physics of Solids*, 6(3):236–249. Cited in pages 10, 22, 192, 194

Hill, R.
1963. Elastic properties of reinforced solids: some theoretical principles. *Journal of the Mechanics and Physics of Solids*, 11(5):357–372. Cited in pages 29, 62

Hilpert, M., R. Glantz, and C. T. Miller
2003. Calibration of a pore-network model by a pore-morphological analysis. *Transport in porous media*, 51(3):267–285. Cited in page 42

Hosn, R. A., C. D. Nguyen, L. Sibille, N. Benahmed, and B. Chareyre
2017. Microscale analysis of the effect of suffusion on soil mechanical properties. In *International Workshop on Bifurcation and Degradation in Geomaterials*, Pp. 117–124. Springer. Cited in pages 17, 197

Hosn, R. A., L. Sibille, N. Benahmed, and B. Chareyre
2016. A discrete numerical description of the mechanical response of soils subjected to degradation by suffusion. In *Scour and Erosion: Proceedings of the 8th International Conference on Scour and Erosion (Oxford, UK, 12-15 September 2016)*, P. 397. CRC Press. Cited in page 17

Hosn, R. A., L. Sibille, N. Benahmed, and B. Chareyre
2018. A discrete numerical model involving partial fluid-solid coupling to describe suffusion effects in soils. *Computers and Geotechnics*, 95:30–39. Cited in pages 19, 20, 77, 135

Hurley, R., S. Hall, J. Andrade, and J. Wright
2016. Quantifying interparticle forces and heterogeneity in 3D granular materials. *Physical review letters*, 117(9):098005. Cited in page 189

Indraratna, B., J. Israr, and C. Rujikiatkamjorn
2015. Geometrical method for evaluating the internal instability of granular filters based on constriction size distribution. *Journal of Geotechnical and Geoenvironmental Engineering*, 141(10):04015045. Cited in page 14

Indraratna, B., A. K. Raut, and H. Khabbaz
2007. Constriction-based retention criterion for granular filter design. *Journal of*

Geotechnical and Geoenvironmental Engineering, 133(3):266–276. Cited in page 14

Iwashita, K. and M. Oda
1998. Rolling resistance at contacts in simulation of shear band development by DEM. *Journal of engineering mechanics*, 124(3):285–292. Cited in pages 38, 55

Iwashita, K. and M. Oda
2000. Micro-deformation mechanism of shear banding process based on modified distinct element method. *Powder Technology*, 109(1-3):192–205. Cited in pages 38, 55

Jaeger, R., M. Mendoza, and H. J. Herrmann
2017. Mechanism behind erosive bursts in porous media. *Physical review letters*, 119(12):124501. Cited in pages 42, 146, 147

Jin, C., P. A. Langston, G. E. Pavlovskaya, M. R. Hall, and S. P. Rigby
2016. Statistics of highly heterogeneous flow fields confined to three-dimensional random porous media. *Physical Review E*, 93(1):013122. Cited in page 61

Johns, M., A. Sederman, A. Bramley, L. Gladden, and P. Alexander
2000. Local transitions in flow phenomena through packed beds identified by mri. *AIChE journal*, 46(11):2151–2161. Cited in page 153

Kanit, T., S. Forest, I. Galliet, V. Mounoury, and D. Jeulin
2003. Determination of the size of the representative volume element for random composites: statistical and numerical approach. *International Journal of solids and structures*, 40(13):3647–3679. Cited in pages 53, 60, 61, 193

Kawano, K., T. Shire, and C. O'Sullivan
2017. Coupled DEM-CFD analysis of the initiation of internal instability in a gap-graded granular embankment filter. In *EPJ Web of Conferences*, volume 140, P. 10005. EDP Sciences. Cited in pages 41, 146, 147

Ke, L. and A. Takahashi
2012. Strength reduction of cohesionless soil due to internal erosion induced by one-dimensional upward seepage flow. *Soils and Foundations*, 52(4):698–711. Cited in pages 17, 197

Ke, L. and A. Takahashi
2014a. Experimental investigations on suffusion characteristics and its mechanical consequences on saturated cohesionless soil. *Soils and Foundations*, 54(4):713–730. Cited in pages 17, 18, 197

Ke, L. and A. Takahashi
2014b. Triaxial erosion test for evaluation of mechanical consequences of internal erosion. *Geotechnical Testing Journal*, 37(2):347–364. Cited in page 17

Kenney, T. and D. Lau
1985. Internal stability of granular filters. *Canadian Geotechnical Journal*, 22(2):215–225. Cited in pages 5, 12, 146, 170, 194

Kézdi, A.
1979. Soil physics (selected topics) developments in geotechnical engineering. Technical report. Cited in pages 11, 16, 169

Kishino, Y.
2003. On the incremental nonlinearity observed in a numerical model for granular media. *Italian Geotechnical Journal*, 3:3–12. Cited in pages 94, 117

La Ragione, L., V. C. Prantil, and I. Sharma
2008. A simplified model for inelastic behavior of an idealized granular material. *International Journal of Plasticity*, 24(1):168–189. Cited in page 189

Lallemand, P. and L.-S. Luo
2000. Theory of the lattice boltzmann method: Dispersion, dissipation, isotropy, galilean invariance, and stability. *Physical Review E*, 61(6):6546. Cited in pages 41, 42

Langroudi, M. F., A. Soroush, and P. T. Shourijeh
2015. A comparison of micromechanical assessments with internal stability/instability criteria for soils. *Powder Technology*, 276:66–79. Cited in page 16

Lantuejoul, C.
1991. Ergodicity and integral range. *Journal of Microscopy*, 161(3):387–403. Cited in page 60

Le, V.
2017. *Development of a new device and statistical analysis for characterizing soil sensibility face suffusion process*. PhD thesis, Université Bretagne Loire. Cited in page 11

Li, M. and R. J. Fannin
2008. Comparison of two criteria for internal stability of granular soil. *Canadian Geotechnical Journal*, 45(9):1303–1309. Cited in pages 3, 12, 13, 146, 192

Li, W., E. Vincens, N. Reboul, and B. Chareyre
2014. Constrictions and filtration of fine particles in numerical granular filters: Influence of the fabric within the material. In *Scour and Erosion: Proceedings of the 7th International Conference on Scour and Erosion, Perth, Australia, 2-4 December 2014*, P. 241. CRC Press. Cited in page 146

Liu, C., S. R. Nagel, D. Schecter, S. Coppersmith, S. Majumdar, et al.
1995. Force fluctuations in bead packs. *Science*, 269(5223):513. Cited in pages 14, 37, 160

Liu, J., A. Wautier, S. Bonelli, F. Nicot, and F. Darve
2018. Macroscopic softening in granular materials from a mesoscale perspective. in preparation. Cited in page 171

Locke, M., B. Indraratna, and G. Adikari
2001. Time-dependent particle transport through granular filters. *Journal of geotechnical and geoenvironmental engineering*, 127(6):521–529. Cited in page 14

Love, A.
1927. A treatise on the mathematical theory of elasticity, cambridge university press. *Cambridge,*. Cited in page 15

Luding, S.
2004. Micro–macro transition for anisotropic, frictional granular packings. *International Journal of Solids and Structures*, 41(21):5821–5836. Cited in page 29

Lyapunov, A.
1907. Problème général de la stabilité du mouvement. In *Annales de la Faculté des sciences de Toulouse: Mathématiques*, volume 9, Pp. 203–474. Cited in page 22

Magnico, P.
2003. Hydrodynamic and transport properties of packed beds in small tube-to-sphere diameter ratio: pore scale simulation using an eulerian and a lagrangian approach. *Chemical engineering science*, 58(22):5005–5024. Cited in page 153

Mahabadi, N. and J. Jang
2017. The impact of fluid flow on force chains in granular media. *Applied Physics Letters*, 110(4):041907. Cited in page 146

Maier, R. S., D. M. Kroll, H. T. Davis, and R. S. Bernard
1999. Simulation of flow in bidisperse sphere packings. *Journal of colloid and interface science*, 217(2):341–347. Cited in page 153

Majmudar, T. S. and R. P. Behringer
2005. Contact force measurements and stress-induced anisotropy in granular materials. *Nature*, 435(7045):1079. Cited in pages 37, 38, 55

Mansouri, M., J.-Y. Delenne, M. S. El Youssoufi, and A. Séridi
2009. A 3D DEM-LBM approach for the assessment of the quick condition for sands. *Comptes Rendus Mécanique*, 337(9-10):675–681. Cited in page 41

Marteau, E. and J. Andrade
2017. Measuring force-chains in opaque granular matter under shear. In *International Workshop on Bifurcation and Degradation in Geomaterials*, Pp. 441–444. Springer. Cited in page 189

Matheron, G.
1967. *Eléments pour une théorie des milieux poreux*. Masson. Cited in pages 53, 60, 61

Matheron, G.
1975. *Random sets and integral geometry*. John Wiley & Sons. Cited in page 61

Mcnamara, S., R. García-Rojo, and H. J. Herrmann
2008. Microscopic origin of granular ratcheting. *Physical Review E*, 77(3):031304. Cited in page 35

Mehrabadi, M. M., S. Nemat-Nasser, and M. Oda
1982. On statistical description of stress and fabric in granular materials. *International Journal for Numerical and Analytical Methods in Geomechanics*, 6(1):95–108. Cited in page 15

Ngoma, J., P. Philippe, S. Bonelli, F. Radjaï, and J.-Y. Delenne
2018. Two-dimensional numerical simulation of chimney fluidization in a granular medium using a combination of discrete element and lattice boltzmann methods. *Physical Review E*, 97(5):052902. Cited in page 42

Nguyen, C. D., N. Benahmed, E. Andò, L. Sibille, and P. Philippe
2017. Experiment investigation of micro-structural changes of eroded soil by suffusion using x-ray tomography. Poster- The ph.d. student's day - ed 353, Aix-Marseille University. Cited in pages 6, 20, 21, 189

Nicot, F. and F. Darve
2006a. Micro-mechanical investigation of material instability in granular assemblies. *International Journal of Solids and Structures*, 43(11):3569–3595. Cited in pages 129, 130, 131, 157

Nicot, F. and F. Darve
2006b. On the elastic and plastic strain decomposition in granular materials. *Granular Matter*, 8(3-4):221–237. Cited in page 117

Nicot, F. and F. Darve
2007a. Basic features of plastic strains: from micro-mechanics to incrementally nonlinear models. *International Journal of Plasticity*, 23(9):1555–1588. Cited in page 117

Nicot, F. and F. Darve
2007b. Micro-mechanical bases of some salient constitutive features of granular materials. *International Journal of Solids and Structures*, 44(22):7420–7443. Cited in page 122

Nicot, F. and F. Darve
2007c. A micro-mechanical investigation of bifurcation in granular materials. *International Journal of Solids and Structures*, 44(20):6630–6652. Cited in pages 22, 23

Nicot, F. and F. Darve
2011. The H-microdirectional model: accounting for a mesoscopic scale. *Mechanics of Materials*, 43(12):918–929. Cited in pages 189, 197

Nicot, F., N. Hadda, and F. Darve
2013a. Second-order work analysis for granular materials using a multiscale approach. *International Journal for Numerical and Analytical Methods in Geomechanics*, 37(17):2987–3007. Cited in pages 129, 131, 167

Nicot, F., N. Hadda, M. Guessasma, J. Fortin, and O. Millet
2013b. On the definition of the stress tensor in granular media. *International Journal of Solids and Structures*, 50(14):2508–2517. Cited in page 15

Nicot, F., J. Lerbet, and F. Darve
2017. Second-order work criterion: from material point to boundary value problems. *Acta Mechanica*, Pp. 1–16. Cited in pages 23, 97

Nicot, F., L. Sibille, and F. Darve
2009. Bifurcation in granular materials: An attempt for a unified framework. *International Journal of Solids and Structures*, 46(22):3938–3947. Cited in pages 22, 23, 92, 94, 105, 167, 192

Nicot, F., L. Sibille, and F. Darve
2012. Failure in rate-independent granular materials as a bifurcation toward a dynamic regime. *International Journal of Plasticity*, 29:136–154. Cited in pages 22, 23, 90, 105, 170

Nicot, F., L. Sibille, F. Donze, and F. Darve
2007. From microscopic to macroscopic second-order work in granular assemblies. *Mechanics of materials*, 39(7):664–684. Cited in pages 92, 94, 117, 129

Nova, R.
1994. Controllability of the incremental response of soil specimens subjected to arbitrary loading programmes. *J. Mech. Behav. Mater*, 5(2):193–201. Cited in pages 24, 97

O'Sullivan, C., J. Bluthé, K. Sejpar, T. Shire, and L. Cheung
2015. Contact based void partitioning to assess filtration properties in DEM simulations. *Computers and Geotechnics*, 64:120–131. Cited in page 146

Peck, R. B. and K. Terzaghi
1948. *Soil mechanics in engineering practice*. Cited in page 11

Peters, J. F., M. Muthuswamy, J. Wibowo, and A. Tordesillas
2005. Characterization of force chains in granular material. *Physical review E*, 72(4):041307. Cited in pages 37, 38, 39, 53, 54, 55, 108, 160, 163, 193

Radjai, F., D. E. Wolf, M. Jean, and J.-J. Moreau
1998. Bimodal character of stress transmission in granular packings. *Physical review letters*, 80(1):61. Cited in pages 14, 37, 54, 55, 60, 160

Rashidi, M., L. Peurrung, A. Tompson, and T. Kulp
1996. Experimental analysis of pore-scale flow and transport in porous media. *Advances in Water Resources*, 19(3):163–180. Cited in page 153

Reboul, N., E. Vincens, and B. Cambou
2008. A statistical analysis of void size distribution in a simulated narrowly graded packing of spheres. *Granular Matter*, 10(6):457–468. Cited in pages 63, 67, 73, 146

Reboul, N., E. Vincens, and B. Cambou
2010. A computational procedure to assess the distribution of constriction sizes for an assembly of spheres. *Computers and Geotechnics*, 37(1-2):195–206. Cited in page 14

Robinson, M., M. Ramaioli, and S. Luding
2014. Fluid-particle flow simulations using two-way-coupled mesoscale SPH-DEM and validation. *International journal of multiphase flow*, 59:121–134. Cited in page 147

Royis, P. and T. Doanh
1998. Theoretical analysis of strain response envelopes using incrementally non-linear constitutive equations. *International journal for numerical and analytical methods in geomechanics*, 22(2):97–132. Cited in page 25

Rudnicki, J. W. and J. Rice
1975. Conditions for the localization of deformation in pressure-sensitive dilatant materials. *Journal of the Mechanics and Physics of Solids*, 23(6):371–394. Cited in page 23

Sail, Y., D. Marot, L. Sibille, and A. Alexis
2011. Suffusion tests on cohesionless granular matter: Experimental study. *European Journal of Environmental and Civil Engineering*, 15(5):799–817. Cited in pages 7, 20

Schofield, A. and C. Wroth
1968. Critical state soil mechanics. *McGrow-Hill, London*. Cited in page 53

Scholtès, L., P.-Y. Hicher, and L. Sibille
2010. Multiscale approaches to describe mechanical responses induced by particle removal in granular materials. *Comptes Rendus Mécanique*, 338(10):627–638. Cited in pages 17, 18, 53, 135

Shan, T. and J. Zhao
2014. A coupled CFD-DEM analysis of granular flow impacting on a water reservoir. *Acta Mechanica*, 225(8):2449–2470. Cited in page 41

Shire, T. and C. O'Sullivan
2013. Micromechanical assessment of an internal stability criterion. *Acta Geotechnica*, 8(1):81–90. Cited in page 16

Shire, T., C. O'Sullivan, K. Hanley, and R. Fannin
2014. Fabric and effective stress distribution in internally unstable soils. *Journal of Geotechnical and Geoenvironmental Engineering*, 140(12):04014072. Cited in pages 15, 146

Sibille, L.
2006. *Modélisations discrètes de la rupture dans les milieux granulaires*. PhD thesis, Institut National Polytechnique de Grenoble - INPG. Cited in page 29

Sibille, L., F. Lominé, P. Poullain, Y. Sail, and D. Marot
2015a. Internal erosion in granular media: direct numerical simulations and energy interpretation. *Hydrological Processes*, 29(9):2149–2163. Cited in page 17

Sibille, L., D. Marot, and Y. Sail
2015b. A description of internal erosion by suffusion and induced settlements on cohesionless granular matter. *Acta Geotechnica*, 10(6):735–748. Cited in pages 17, 21, 197

Sibille, L., F. Nicot, F. Donze, and F. Darve
2007. Material instability in granular assemblies from fundamentally different models. *International Journal For Numerical and Analytical Methods in Geomechanics*, 31(3):457–481. Cited in page 27

Sibille, L., F. Nicot, F.-V. Donzé, and F. Darve
2009. Analysis of failure occurrence from direct simulations. *European Journal of Environmental and Civil Engineering*, 13(2):187–201. Cited in pages 92, 94, 98, 101, 105, 117, 122

Silveira, A.
1965. An analysis of the problem of washing through in protective filters. In *Proceedings of the 6th International Conference on Soil Mechanics and Foundation Engineering, Montréal, Que*, Pp. 551–555. Cited in page 14

Sjah, J. and E. Vincens
2013. Determination of the constriction size distribution of granular filters by filtration tests. *International Journal for Numerical and Analytical Methods in Geomechanics*, 37(10):1231–1246. Cited in page 146

Skempton, A. and J. Brogan
1994. Experiments on piping in sandy gravels. *Geotechnique*, 44(3):449–460. Cited in pages 3, 15, 146, 192

Terzaghi, K.
1939. 45$^{\text{th}}$ james forrest lecture. soil mechanics-a new chapter in engineering science. *Journal of the ICE*, 12(7):106–142. Cited in pages 14, 51

Terzaghi, K., R. B. Peck, and G. Mesri
1996. *Soil mechanics in engineering practice*. John Wiley & Sons. Cited in page 53

Thompson, K. E. and H. S. Fogler
1997. Modeling flow in disordered packed beds from pore-scale fluid mechanics. *AIChE Journal*, 43(6):1377–1389. Cited in page 42

To, H. D., S. A. G. Torres, and A. Scheuermann
2015. Primary fabric fraction analysis of granular soils. *Acta Geotechnica*, 10(3):375–387. Cited in page 58

Tordesillas, A., Q. Lin, J. Zhang, R. Behringer, and J. Shi
2011. Structural stability and jamming of self-organized cluster conformations in dense granular materials. *Journal of the Mechanics and Physics of Solids*, 59(2):265–296. Cited in pages 108, 114, 115

Tordesillas, A., D. M. Walker, and Q. Lin
2010. Force cycles and force chains. *Physical Review E*, 81(1):011302. Cited in pages 112, 114, 160, 163

Vincens, E., N. Reboul, and B. Cambou
2012. The process of filtration in granular materials. *Erosion of Geomaterials*, Pp. 81–114. Cited in page 14

Vincens, E., K. J. Witt, and U. Homberg
2015. Approaches to determine the constriction size distribution for understanding filtration phenomena in granular materials. *Acta Geotechnica*, 10(3):291–303. Cited in pages 14, 67, 146, 193

Voivret, C., F. Radjai, J.-Y. Delenne, and M. S. El Youssoufi
2009. Multiscale force networks in highly polydisperse granular media. *Physical review letters*, 102(17):178001. Cited in page 58

Šmilauer et al., V.
2015. *Yade Documentation 2nd ed.* The Yade Project. http://yade-dem.org/doc/. Cited in pages 30, 31, 33, 36, 50, 90, 147, 192

Walker, D. M. and A. Tordesillas
2010. Topological evolution in dense granular materials: a complex networks perspective. *International Journal of Solids and Structures*, 47(5):624–639. Cited in pages 29, 37

Wan, C. F. and R. Fell
2008. Assessing the potential of internal instability and suffusion in embankment dams and their foundations. *Journal of geotechnical and geoenvironmental engineering*, 134(3):401–407. Cited in page 14

Wan, R., F. Nicot, and F. Darve
2016. *Failure in Geomaterials, a contemporary treatise*. ISTE/Elsevier. Cited in pages 24, 192

Wan, R., M. Pinheiro, A. Daouadji, M. Jrad, and F. Darve
2013. Diffuse instabilities with transition to localization in loose granular materials. *International Journal for Numerical and Analytical Methods in Geomechanics*, 37(10):1292–1311. Cited in page 23

Wang, X. and J. Li
2015. On the degradation of granular materials due to internal erosion. *Acta Mechanica Sinica*, 31(5):685–697. Cited in page 53

Wautier, A., S. Bonelli, and F. Nicot
2017. Scale separation between grain detachment and grain transport in granular media subjected to an internal flow. *Granular Matter*, 19(2):22. Cited in pages 8, 50, 108, 135, 146

Wautier, A., S. Bonelli, and F. Nicot
2018a. Flow impact on granular force chains and induced instability. under review. Cited in page 8

Wautier, A., S. Bonelli, and F. Nicot
2018b. Micro-inertia origin of instabilities in granular materials. *International Journal for Numerical and Analytical Methods in Geomechanics*, 42(9):1037–1056. Cited in pages 8, 157, 163, 165, 167

Wautier, A., S. Bonelli, and F. Nicot
2018c. Rattlers contribution to granular plasticity and mechanical stability. under review. Cited in pages 8, 157

Weber, J.
1966. Recherches concernant les contraintes intergranulaires dans les milieux pulvérulents. *Bulletin de Liaison des Ponts-et-chaussées*, 20:1–20. Cited in page 15

Wood, D., K. Maeda, and E. Nukudani
2008. Discrete element modelling of soil erosion. In *Fourth International Conference on Scour and Erosion*. Cited in pages 17, 18

Wood, D. M. and K. Maeda
2008. Changing grading of soil: effect on critical states. *Acta Geotechnica*, 3(1):3. Cited in page 17

Xiao, M. and N. Shwiyhat
2012. Experimental investigation of the effects of suffusion on physical and geomechanic characteristics of sandy soils. *Geotechnical Testing Journal*, 35(6):890–900. Cited in pages 6, 17, 197

Xiong, H., F. Nicot, and Z. Yin
2017. A three-dimensional micromechanically based model. *International Journal for Numerical and Analytical Methods in Geomechanics*, 41(17):1669–1686. Cited in pages 189, 190, 197

Yu, Z. and L.-S. Fan
2010. Lattice boltzmann method for simulating particle–fluid interactions. *Particuology*, 8(6):539–543. Cited in page 42

Zeghal, M. and U. El Shamy
2004. A continuum-discrete hydromechanical analysis of granular deposit liquefaction. *International Journal for Numerical and Analytical Methods in Geomechanics*, 28(14):1361–1383. Cited in page 41

Zhang, L., N. G. H. Nguyen, S. Lambert, F. Nicot, F. Prunier, and I. Djeran-Maigre
2016. The role of force chains in granular materials: from statics to dynamics. *European Journal of Environmental and Civil Engineering*, Pp. 1–22. Cited in page 129

Zhao, J. and T. Shan
2013. Coupled CFD-DEM simulation of fluid–particle interaction in geomechanics. *Powder technology*, 239:248–258. Cited in page 41

Zhu, H.
2015. *Prise en compte d'une échelle intermédiaire dans la modélisation microstructurelle des sols granulaires*. PhD thesis, Grenoble Alpes. Cited in pages 40, 195

Zhu, H., M. M. Mehrabadi, and M. Massoudi
2006. Three-dimensional constitutive relations for granular materials based on the dilatant double shearing mechanism and the concept of fabric. *International journal of plasticity*, 22(5):826–857. Cited in page 189

Zhu, H., H. N. Nguyen, F. Nicot, and F. Darve
2016a. On a common critical state in localized and diffuse failure modes. *Journal of the Mechanics and Physics of Solids*, 95:112–131. Cited in pages 29, 56, 66, 108

Zhu, H., F. Nicot, and F. Darve
2016b. Meso-structure evolution in a 2d granular material during biaxial loading. *Granular Matter*, 18(1):1–12. Cited in pages 40, 114, 115, 160, 163, 165

Zhu, H., F. Nicot, and F. Darve
2016c. Meso-structure organization in two-dimensional granular materials along biaxial loading path. *International Journal of Solids and Structures*, 96:25–37. Cited in page 40

Zhu, Q., J.-F. Shao, and M. Mainguy
2010. A micromechanics-based elastoplastic damage model for granular materials at low confining pressure. *International Journal of Plasticity*, 26(4):586–602. Cited in page 189

Titre : Analyse micro-inertielle des instabilités mécaniques dans les milieux granulaires, application à l'érosion interne.

Mots clefs : Instabilités mécaniques, matériaux granulaires, érosion interne, simulation par éléments discrets, micromécanique.

Résumé : La plupart des digues sont constituées de matériaux granulaires compactés. Elles sont ainsi perméables et constamment soumises à des écoulements d'eau dans leur volume. Dans certaines conditions, ces écoulements sont susceptibles d'altérer leur microstructure par érosion interne et de générer des instabilités mécaniques responsables de ruptures inopinées lors de fortes crues.
Cette thèse s'intéresse à l'analyse multi-échelle des instabilités mécaniques dans les matériaux granulaires soumis au phénomène d'érosion interne. Dans ce travail, le comportement mécanique de ces matériaux est simulé en trois dimensions à l'échelle de volumes élémentaires représentatifs, et ce, pour différents états de contraintes et gradients hydrauliques. Grâce à l'utilisation du critère du travail du second-ordre et d'outils micromécaniques, leur stabilité est analysée avant et après l'application d'un écoulement interne. Il est établi que l'origine micro-inertielle des instabilités observées provient du déconfinement et de la flexion des chaînes de force ainsi que des déformations plastiques importantes résultant de l'effondrement des chaînes de force. Par leur capacité à enrayer rapidement le développement de telles déformations plastiques, il est montré que les particules libres contribuent à assurer la stabilité mécanique des matériaux granulaires. Ce résultat est fondamental pour analyser les conséquences de l'érosion interne sur la stabilité mécanique d'un matériau granulaire car les particules libres sont facilement transportables sous l'action d'un écoulement interne. Selon si elles sont colmatées ou érodées, un écoulement interne aura alors un effet stabilisateur ou déstabilisateur vis-à-vis du comportement mécanique des matériaux granulaires soumis à l'érosion interne.

Title : Micro-inertial analysis of mechanical instability in granular materials with application to internal erosion.

Keywords : Mechanical instability, granular materials, internal erosion, discrete element simulation, micromechanics.

Abstract : Dikes are most of the time built of compacted granular materials that are permeable and continuously subjected to internal fluid flows. In some cases, microstructure modifications resulting from internal erosion generate mechanical instability that will lead to unexpected failures in case of serious flooding.
This thesis focuses on multi-scale analysis of mechanical instability in granular materials subjected to internal erosion. In this work, the mechanical behavior of such materials is simulated in three dimensions at the scale of representative elementary volumes subjected to different stress states and hydraulic gradients. Thanks to the use of the second-order work criterion and micromechanical tools, the mechanical stability of these materials is tested before and after internal erosion. It is established that the micro-inertial origin of the observed instabilities is linked to force chain deconfinement and bending as well as to the development of large plastic strains resulting from force chain collapse. By preventing the development of such plastic strains, it is shown that rattlers contribute to ensure the mechanical stability of granular materials. This key finding is of a particular significance in relation with internal erosion as rattlers can be easily transported under the action of an internal fluid flow. Depending on whether they get clogged or eroded, an internal fluid flow has thus either a stabilizing or a destabilizing effect on the mechanical behavior of granular materials subjected to internal erosion.